DEMONSTRATING OPTOTHERMAL
ACTUATORS FOR AN AUTONOMOUS
MEMS MICROROBOT

THESIS

Francis R. Szabo, SMSgt, USAF

AFIT/GE/ENG/04-23

DEPARTMENT OF THE AIR FORCE
AIR UNIVERSITY

AIR FORCE INSTITUTE OF TECHNOLOGY

Wright-Patterson Air Force Base, Ohio

APPROVED FOR PUBLIC RELEASE; DISTRIBUTION UNLIMITED

DEMONSTRATING OPTOTHERMAL ACTUATORS FOR AN AUTONOMOUS
MEMS MICROROBOT

THESIS

Presented to the Faculty of the

Department of Electrical and Computer Engineering

Graduate School of Engineering and Management

Air Force Institute of Technology

Air University

Air Education and Training Command

In Partial Fulfillment of the Requirements for the

Degree of Master of Science in Electrical Engineering

Francis R. Szabo, BSEE

SMSgt, USAF

March 2004

DEMONSTRATING OPTOTHERMAL ACTUATORS FOR AN AUTONOMOUS
MEMS MICROROBOT

Francis R. Szabo, BS
SMSgt, USAF

Approved:

_____
Capt Paul E. Kladitis (Chairman)

05 MAR 04
date
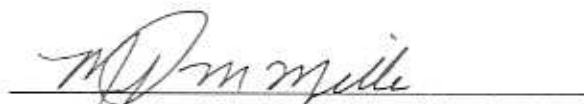
_____
Lt Col James A. Lott (Member)

03 MAR 04
date

_____
Dr. Gilbert L. Peterson (Member)

12 MAR 04
date

_____
Dr. Mikel M. Miller (Member)

15 MAR 04
date

Table of Contents

List of Figures

xiii

xiv

List of Tables

AFIT/GE/ENG/04-23

Abstract

There are numerous applications for microrobots which are beneficial to the Air Force. However, the microrobotics field is still in its infancy, and will require extensive basic research before these applications can be fielded. The biggest hurdle to be solved, in order to create autonomous microrobots, is generating power for their actuator engines. Most present actuators require orders of magnitude more power than is presently available from micropower sources. To enable smaller microrobots, this research proposed a simplified power concept that eliminates the need for on-board power supplies and control circuitry by using actuators powered wirelessly from the environment. This research extended the basic knowledge of methods required to power Micro-Electro-Mechanical Systems (MEMS) devices and reduce MEMS microrobot size. This research demonstrated optothermal actuators designed for use in a wirelessly propelled autonomous MEMS microrobot, without the need of an onboard power supply, through the use of lasers to directly power micrometer scale silicon thermal actuators. Optothermal actuators, intended for use on a small MEMS microrobot, were modeled, designed, fabricated and tested, using the PolyMUMPs silicon-metal chip fabrication process. Prototype design of a MEMS polysilicon-based microrobot, using optothermal actuators, was designed, fabricated and tested. Each of its parts was demonstrated to provide actuation using energy from an external laser. The optothermal actuators provided 2 µm of deflection to the microrobot drive shaft, with 60 mW of pulsed laser power. The results of these experiments demonstrated the validity of a new class of wireless silicon actuators for MEMS devices, which are not directly dependant on electrical power for actuation. The experiments also demonstrated a potentially viable design that could be used to propel the world's smallest autonomous MEMS microrobot.

DEMONSTRATING OPTOTHERMAL ACTUATORS FOR AN AUTONOMOUS MEMS MICROROBOT

1. Introduction

1.1. Motivation

According to Ebefors and Stemme, the ultimate goal in designing microrobots is to "create a fully autonomous, wireless mobile microrobot, equipped with suitable microtools" [1]. Because the field of Micro-Electro-Mechanical Systems (MEMS) microrobotics is in its infancy, extensive basic research will be required by numerous academic groups to achieve this goal. The biggest hurdle to be solved, to enable autonomous microrobots, is the ability to generate onboard power for the actuators that propel microrobots. Most conventional microactuators require orders of magnitude more power than is presently available from micropower sources. Current low-power microactuators require relatively large amounts of chip real estate. Both of these attributes are barriers to further miniaturization. Current researchers have demonstrated several successful locomotive MEMS microrobots, but only one is close to being fully autonomous (locomotion by itself, without attached wires). No small MEMS microrobots (less than 1 cm^2) have shown fully autonomous behavior to date. The immediate goal for my research is the demonstration of optothermal actuators which can be used to propel an autonomous MEMS microrobot without the need for an onboard power supply or attached wires. This research investigated the use of lasers to directly power micrometer scale silicon thermal actuators. Optothermal actuators, intended for use on a small MEMS microrobot, were modeled, designed, fabricated and tested, using the PolyMUMPs silicon-metal chip fabrication process. Prototype designs for MEMS polysilicon-based microrobots, using optothermal actuators, were designed, fabricated and tested. Each of the microrobot's separate parts was demonstrated to provide

actuation using laser power. The results of these experiments demonstrated the validity of a new class of wireless silicon actuators for MEMS devices, which are not directly dependant on electrical power for actuation. They also demonstrated a potential design that could be used to propel the world's smallest autonomous MEMS microrobot to date.

1.2. Background

There are numerous applications of microrobots beneficial to the Air Force that this basic research will support. The Air Force Research Laboratory's Munitions Directorate (AFRL/MNAV) is sponsoring several projects investigating ways to power remote MEMS devices on munitions used by Special Operations Forces. One specific project being researched is the use of microrobots to deliver a small explosive charge into a small area (such as a cable trough or cave), where it can then be detonated to sever communications or power lines [2]. There are many wider Air Force missions where this research knowledge can be used, such as medical microrobots that can be used to perform minimally invasive surgery and diagnostic tests in place of surgery [3], [4]. Swarms of microrobots, equipped with various sensors, could potentially be used to inspect aircraft engines and other large complicated machines without requiring disassembly. With different sensors and propulsion systems, the swarms could be distributed by Unmanned Air Vehicles (UAVs) or infantry troops to greatly extend reconnaissance capabilities into small dangerous places [5]. They can also be used in groups to search large areas for small isolated spills of biological and chemical warfare agents. The applications are unlimited, but the microrobotics field, still in its infancy, will require extensive basic research before these applications can be fielded. This research extends the basic knowledge of methods required to power MEMS devices and reduce MEMS device size.

1.3. Problem Statement

A major with modern microrobots is that more power is required than available onboard power supplies can handle. Also, current low-power actuators require relatively large amounts of chip real estate. Both of these are barriers to further miniaturization, as supplying power through attached wires severely limits autonomous movement at small sub-millimeter robot sizes.

1.4. Research Constraints

The fabrication process for this research was limited to the PolyMUMPs process [6]. A design problem, specific to MEMS PolyMUMPs microrobots, is that silicon beam structures conduct electricity, causing problems when structural connections and electrical isolation are both required. This makes it very hard to simultaneously run more than one physically connected actuator, to allow for combining actuators with multiple degrees of freedom of movement.

1.5. Proposed Solution

The problem to be investigated by this research was to model, design, fabricate and test polysilicon-based optothermal actuators that can be used to drive a MEMS microrobot. Wireless laser microrobots, using combined optothermal actuators, were designed, fabricated and tested. The end goal of this research was to demonstrate designs for a wireless power scavenging microrobot, which could be used to design the smallest autonomous microrobot in the world to date.

1.6. List of Novel Contributions of Work

- Demonstrate a new non-electronic paradigm for powering thermal actuators without wires.

- Modeled, designed, fabricated, and demonstrated laser heated optothermal actuators.

- Demonstrated actuators that could be used in combination for providing multiple degrees of freedom of movement, which is very difficult with PolyMUMPs electrothermal actuators.

- Demonstrated conformally coated drive shaft housings for long drive shafts. This housing limited drive shaft movement in both the X and Z directions, even with nonaxial forces applied to the shaft.

- A temperature dependant model of electrothermal actuators was demonstrated that varied more properties with temperature than any model yet published, and proved fairly accurate at predicting temperature distribution and deflection until the actuator was near burnout.

1.7. Thesis Overview

Chapter 2 covers the background literature search on microrobots and some of the actuators used for microrobot motors. Chapter 3 briefly covers laser heating theory and discusses the wavelength and power of the laser used in this research. Chapter 4 discusses the designs of electrothermal and optothermal actuators used in this research. This research's prototype microrobot designs, based on optothermal actuators, are also covered. Chapter 5 introduces the models for single material optothermal actuators and the approach taken in this

research. Chapter 6 covers experimental procedures, and provides a list of equipment, software, and supplies that were used. Chapter 7 demonstrates the results obtained from the research, and compares experimental results with the predictions of the models developed in Chapter 5. Finally Chapter 8 summarizes the results of this research, and gives recommendations for future research. Appendix A contains large illustrations of all the L-Edit designs of actuators and microrobots submitted for fabrication during this research. Appendix B and Appendix C list the MATLAB computer code for the various models in Chapter 5.

1.8. Bibliography

[1]   M. Gad-el-Hak, et al., "Microrobotics" chapter in *The MEMS Handbook*, CRC Press LLC, 2002, University of Notre Dame, pp. 28-1 to 28-42, 2002.

[2]   C. L. Fowler, AFRL/MNAV, Eglin AFB, FL. Private communications, February 2003.

[3]   http://www.foresight.org/Nanomedicine/Gallery/Captions/index.html.

[4]   S. Fatikow and U. Rembold, *Microsystem Technology and Microrobotics*, Berlin, Springer-Verlag, 1997.

[5]   P. E. Kladitis, Class Notes and Discussion, EENG 636, Micro Elec Mech Sys, Graduate School of Engineering and Management, Air Force Institute of Technology, Wright Patterson AFB, OH, Winter Quarter 2003.

[6]   D. Koester, A. Cowen, R. Mahadevan, B. Hardy, *PolyMUMPs Design Handbook, a MUMPs® process,* Revision 10.0, MEMSCAP, http://www.memscap.com/memsrus/docs/polymumps.dr.v10.pdf, 2003.

2. Background

This background chapter covers what has been accomplished in the microrobotics field to date. Section 2.1 gives a brief overview of the history of the microrobotics field. Section 2.2 discusses possible microrobot applications. Section 2.3 briefly covers theory and operation for different available and proposed microrobotic actuators. Section 2.4 introduces proposals by several researchers to use lasers as a power source for actuation. Section 2.5 provides a summary of performance comparisons of existing small microrobots, and discusses possible performance standards.

2.1. History

In 1959, Richard Feynman, who won the Nobel Prize for his work in nuclear physics at Los Alamos on atomic theory, gave a speech entitled "There's Plenty of Room at the Bottom" [1]. In it he addressed the trend and need toward miniaturization in storing data and creating machines. This speech was a landmark towards creating the microelectronics field. In 1982, Kurt Peterson published "Silicon as a Mechanical Material", which is credited with launching the Micro-Electro-Mechanical Systems (MEMS) field [2]. In 1983, Feynman gave another speech entitled "Infinitesimal Machinery", which emphasized precise machinery through miniaturization. It also foretold such effects as friction and stiction, and predicted computing with single atoms. This speech provided the encouragement for a new MEMS field and microrobotics [3]. In 1987, IEEE organization held the first Micro-Robots and Teleoperators Workshop, officially launching microrobotics as a recognized research field.

2.1.1. Microrobotics History

In 1994, Fukada et al. reported a swimming microrobot [4], Yasudah, from Kagawah Univerisity in Japan, announced a microrobot run by a vibration field [5], and Yeh, from the University of California at Berkeley, published an article entitled "Towards a Silicon Microrobot" [6]. In 1995, Teshigahara published a paper on his work creating a 7-mm micro fabricated car [7]. In 1996, Yeh, et al. published another article, "Surface Micromachined Components for Articulated Microrobots" [8]. In 1997, Kladitis, from the Air Force Institute of Technology, published a thesis on the self assembly of microstructures, which included a PolyMUMPs based, surface micromachined microrobot with 96 legs, based on electrothermal actuators [9], [10]. In 1999 and 2000, Ebefors constructed a very successful microrobot, based on polyimide electrothermal actuators, that had a top speed of 12 mm/sec, and could carry a load of 3500 mg, over 30 times its own weight [11] - [14]. In 2001, Mohebbi, Suh, and Bohringer, from the University of Washington, published papers on a microrobot they created, which was the first to have programmable and accurate movement with three degrees of freedom (DOF) [15] - [18]. Also that year, Linderman and Bright, from University of Colorado, published a paper on a microrobot capable of nanometer length precision movements, based on electrostatic scratch drives [19]. In 2003, Hollar, et al., from the University of California at Berkeley, demonstrated the first autonomous microrobot [20], based on Yeh's electrostatic comb drive microrobot designs [6] and powered by Bellew's solar cells [21]. For a summary of the specifications of the more recent successful MEMS microrobots, see Table 2.1 in section 2.5.

The next steps in microrobotics will be perfecting autonomous locomotion, miniaturization, and adding manipulators and sensors to create more complete microrobots. Once these have been perfected numerous applications exist for microrobots.

2.2. Microrobot Applications

There are almost a limitless number of applications where the use of microrobots would be highly advantageous. As with all robot applications, any task which is dangerous, repetitive, requires high precision, or requires multitasking is tailor made for robotics. Additionally, microrobotics can extend accomplishing these kinds of tasks into the sub-cm^2 and micrometer world. Medical microrobots could perform minimally invasive surgery and diagnostic tests in place of surgery [22], [23]. Steerable catheters using MEMS and microrobot technology have actually been developed and used for remote control surgery. Concepts such as mining and clearing blocked blood vessels of plaque have been proposed. Microrobots could be guided to cancer sites to release medicine to a specific spot, avoiding general poisoning of the body by chemotherapy. In biology and medicine, concepts have been proposed for working with individual cells, performing tasks such as diagnostic sampling tests and gene-splicing. Yabe, et al. have proposed a vehicle that can navigate the blood stream, driven by a low power X-ray laser [24]. Their proposed microrobot would concentrate the X-ray power with a microscopic Freznel lens, and use that power to induce energy to an ablation drive mechanism, which would provide the propulsion for their microrobot.

There are several applications beneficial to the Air Force which microrobotic research will support. Swarms of microrobots, equipped with various sensors, can be used to inspect aircraft engines and other large complicated machines without requiring costly disassembly. With different sensors and propulsion systems, they can be distributed by Unmanned Air Vehicles (UAVs) or infantry troops to greatly extend reconnaissance, security, and surveillance capabilities. They can also be used in groups to search large areas for small isolated spills of

biological, nuclear and chemical warfare agents. Researchers working on special operations

forces equipment are especially interested in flying or crawling microrobots that can explore and

perform reconnaissance inside of caves and bunkers [25]. These types of places have proven

especially dangerous for American forces in Afghanistan.

Japanese researchers have developed an in-pipe wireless microrobot for the purpose of

inspecting the inside of pipes and pipelines in chemical factories and nuclear power plants [26],

[27]. Yabe, et al. have proposed and demonstrated laser driven vehicles that can be used

remotely inside contaminated nuclear power plants and in outer space [24], [28].

The most successful microrobot applications, that are presently being demonstrated, are

for use in microfactories and microassembly in laboratories [23], [22], [15]. Fatikow, et al., at

the University of Karlsruhe in Germany, have developed an extensive desktop microassembly

station used for micromanipulation and assembling microchips and MEMS devices [22], [29].

Santa, et al. have developed an extensive control system for guiding Fatikow's microassembly

robots using laser tracking, optical camera tracking and neural network computer control

programs [30] - [33]. Bohringer, et al. have developed programmable MEMS micromanipulator

arrays for precise computer controlled placement of microelectronic devices under a microscope

[15], [16]. Linderman, et al. have also proposed a scratch drive array driven device that could

possibly provide placement of devices on a workstation with 30 nm accuracy [19]. Aoyama, et

al., at the Tokyo Institute of Technology, have developed a system for using one inch

microrobots inside a vacuum chamber of a scanning electron microscope (SEM) [34]. These

microrobots can move a specimen around and manipulate it, and use a magnetic clamp-down

mechanism to keep themselves stationary when the platform is tilted. Aoyama developed a

magnetic shielding shell on the outside of his microrobots because he found that the magnetic clamp-down mechanism was interfering with the electron beam inside the SEM during imaging.

The possible microrobot applications are unlimited, but there are numerous hurdles to using microrobots commercially. They are fragile and hard to mass produce. Ebefors was able to design the first batch fabrication of microrobots which were mass producible, but they had no manipulators for practical use, nor did they have any onboard circuits or means of control [11]. As Aoyama found with his SEM system, microrobots need to have protective packaging to keep them from adversely affecting the environment where they work [34]. Problems such as heat production in electrothermal actuators and high voltage in electrostatic actuators make microrobots dangerous to their environment without proper packaging. This is especially true in the medical field. Also, because of the extreme fragility, corrosion, and stiction due to humidity, extensive research needs to be done on protective packaging, so that the microrobots can survive large forces, such as can be found in the blood stream. Other problems, such as poor navigability, limited space for on-board control mechanisms, friction and limited durability are all barriers that have to be overcome before commercially feasible microrobots can be marketed [23]. However, all these barriers simply provide a wealth of frontiers for researchers to explore in the field of microrobotics.

2.3. Theory and Operation of Microrobotic Actuators

The most commonly used types of actuators that drive small MEMS microrobots are electrothermal, electro-static, piezo-electric, electromagnetic [35], photothermal and vibration actuators. There are two general types of electrothermal actuators, the bimorph (two materials) actuator and the single material asymmetric actuator. Several new types of photothermal

actuator have been proposed. This thesis proposes a new optical thermal double asymmetric actuator. The theory for that actuator can be found in the actuator design section of Chapter 4 in extensive detail.

The electrothermal polyimide bimorph actuator was used by Ebefors in his Walking Silicon Microrobot [11] - [14]. This actuator is the strongest and most powerful actuator for a microrobot built to date. Ebefors' microrobot carried 3500 mg, or 30 times its own weight. Ebefors was able to get his 15 x 5 mm^2 robot to travel at 12 mm per second. However, his microrobot required 1.1 Watts of power to perform these tasks, a very large amount of power for such a small microrobot.

The actuation principle for Ebefors' polyimide bimorph actuator leg movements is based on the heating and cooling of a polyimide filled four-V-groove joint. Figure 2.1 is a depiction of Ebefors' electrothermal polyimide bimorph actuator, showing the leg is construction and in (a), how it expands when heated, (b), and how electrothermal heating and cooling extend the microrobot's legs (c) [14]. As shown in Figure 2.1 (b), by heating the joint, using a high current through resistive elements, a horizontal displacement is obtained due to greater thermal expansion of the polyimide at the wide part of the V-groove than at the narrow part. Cooling causes the leg to retract.

(a)   **(b)**   **(c)**
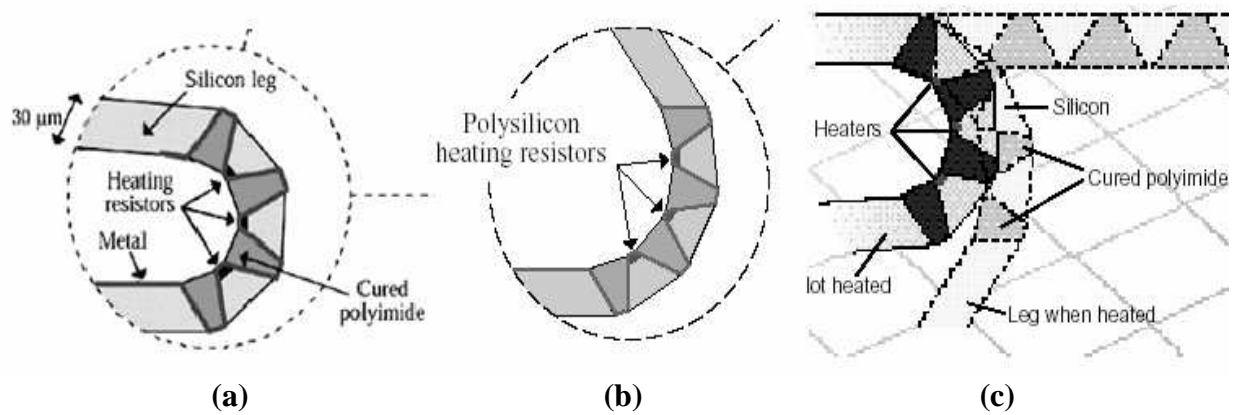
Figure 2.1: Depiction of Ebefors' electrothermal polyimide bimorph actuator, showing the leg is construction and in (a), how it expands when heated, (b), and how electrothermal heating and cooling extend the microrobot's legs (c) [14].

Mohebbi [17], Böhringer [15], and Suh [16], et al., from the University of Washington MEMS lab, designed a programmable mobile MEMS microrobot with three degrees of freedom (DOF). Figure 2.2 is a depiction (a) and a scanning electron microscope (SEM) micrograph (b) of Mohebbi, Böhringer, and Suh's bimorph actuators, showing their construction [18], [36]. As seen in Figure 2.2, they used sets of four orthogonally oriented thermal bimorph actuators, arranged like four leaf clovers. These were arranged into 8x8 arrays of "motion pixels," using a microcilia array concept. Using this concept, they were able to design the first small microrobot with accurate control of a three DOF motion in the x-y plane. They varied the input power, frequency, and gait motion strategy to accurately control the velocity and direction. As seen in Figure 2.2 (a), the TiW resistors, under the high coefficient of thermal expansion (CTE) polyimide, heat up when current is applied, causing the bimorph actuators to bend. The encapsulated stiffening layer acts as a spring to quickly return the leg to its original shape once the current is removed.

| **(a)** | **(b)** |
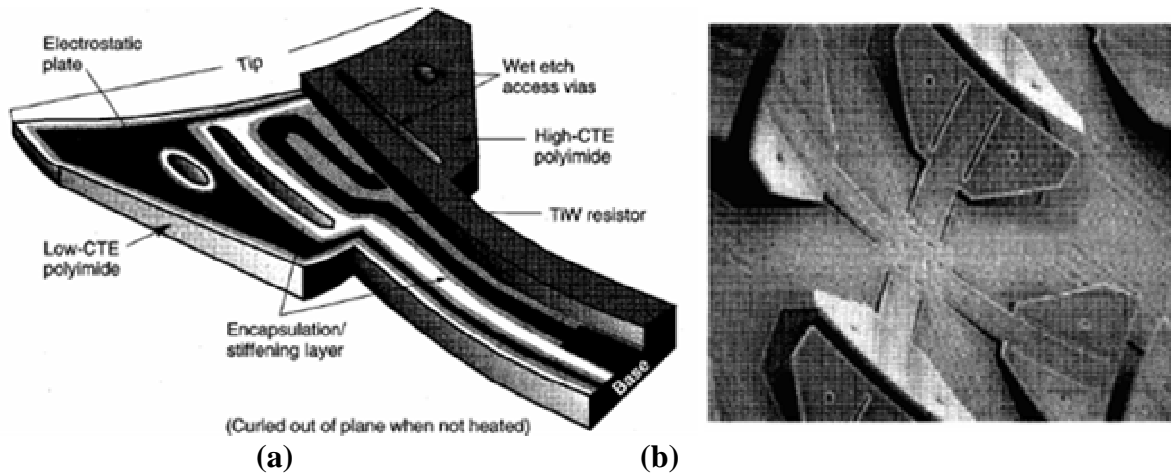
Figure 2.2: Depiction (a) and a scanning electron microscope (SEM) micrograph (b) of Mohebbi, Böhringer, and Suh's bimorph actuators, showing their construction [18], [36].

Bonvilain, et al., from Laboratoire d'Automatique de Besancon in France, have investigated a dual thermal bimorph actuator to produce a real walking motion similar to an insect's walk [37]. Figure 2.3 is a depiction of Bonvilain, et al.'s dual bimorph thermal actuator producing a stepping motion with a pin leg/foot. As shown in Figure 2.3, the left and right bimorph arms are actuated separately to produce stepping motion. Pin leg, mounted between the two arms, does the actual walking. Bonvilain, et al. have been able to successfully demonstrate a step length of 120 µm with single legs, but have yet to assemble a complete microrobot. Their power budget was 1.3 W per leg, which, with a six leg insect gate, using 3 legs at a time, would require 3.9 W to run. This high power requirement may make it very hard to make this microrobot autonomous.
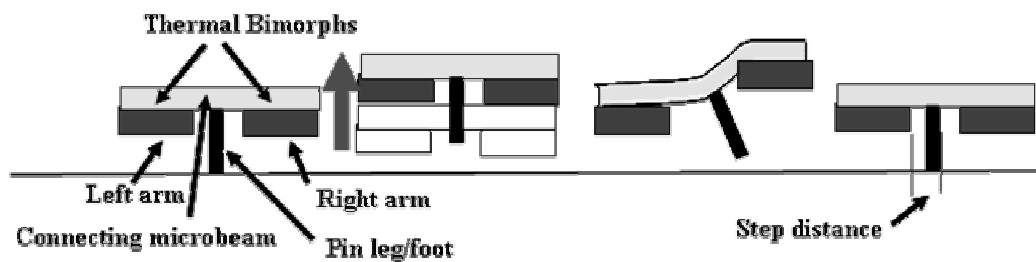
Figure 2.3: Depiction of Bonvilain, et al.'s dual bimorph thermal actuator producing a stepping motion with a pin leg [37].

Djakov, et al. used a combination of residual stress cantilevers and bimorph actuation principles to obtain vertical actuation [38]. Heaters were fabricated into bimorph thin films of polyimide and gold. Djakov, et al. achieved up to 200 μm vertical deflections with 600 μm long by 80 μm wide cantilevers, using 5 mW of power and a 50 Hz signal.

The polysilicon electrothermal asymmetric actuator was used by Kladitis as a leg in his prototype microrobot [9], [10]. Figure 2.4 is a SEM micrograph showing a polysilicon electrothermal asymmetric hot arm actuator used as a leg on the microrobot. When this actuator has electric current applied, the narrow, thin hot arm acts as a resistor, heats up, and thermally expands. In an electrothermal asymmetric actuator, the hot arm is the heated beam which has expansion that is used for actuation. In the hot arm, the small cross sectional area causes high resistance, heating, and thermal expansion [39]. The cold arm has a large cross sectional area, thus low resistance, and thus has little heat or expansion. This differential in expansion causes the arm to deflect laterally, as seen in Figure 2.4. Kladitis was able to obtain 3.75 μm deflections with his erected polysilicon legs. The differential in expansion can cause a lateral deflection as much as 14 µm with a double hot arm actuator [40], [41]. Kladitis used an 8 volt, 2 Hz square wave, with alternating asynchronous voltage to power 96 legs. The current was 74 mA and the power consumed was 2.87 Watts. Electrothermal asymmetric hot arm actuators operate with very high current, low voltage, and high power consumption.

Fatikow [22], [29], Martel [42], [43], Montane [44], and Wörn [45] all chose to use a version of the piezo-electric actuator for the legs on their PROHAM, Nanowalker, and MINIMAN microrobots. The piezo-ceramic leg version was the most efficient. It consists of a hollow tube of ceramic, with one electrode on the inside and one electrode on the outside. Figure 2.5 is a depiction of "slip and stick" actuation movement using piezo electric actuator

legs; variations of this are used by the PROHAM, MINIMAN, and Nanowalker microrobots. When a voltage differential is applied across the inner and outer electrodes, the leg bends as seen in Figure 2.5. This bending can be used for a hopping motion as seen in Figure 2.5 (a), or "slip and stick" actuation as in Figure 2.5 (b). The Nanowalker used from 13 to 15 Watts of power.
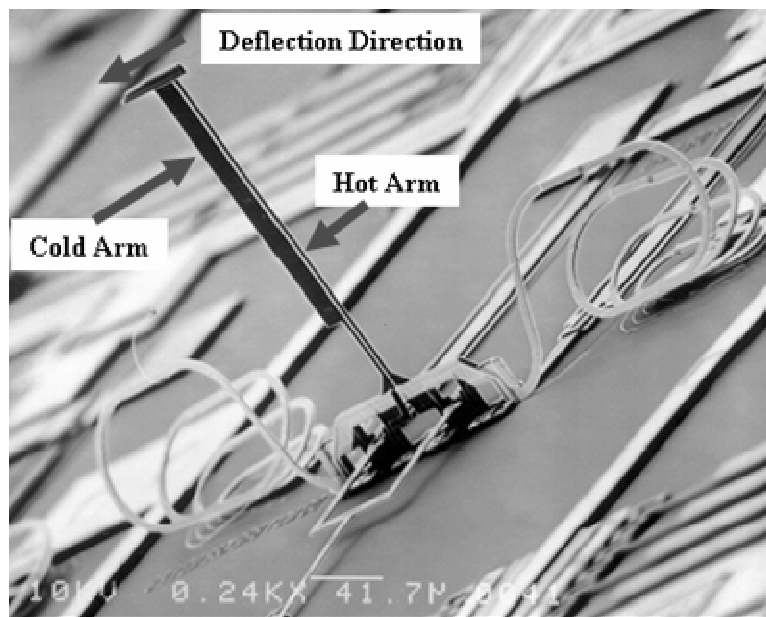
Figure 2.4: SEM micrograph showing polysilicon electrothermal asymmetric hot arm actuator used as a leg on the Kladitis microrobot [10].
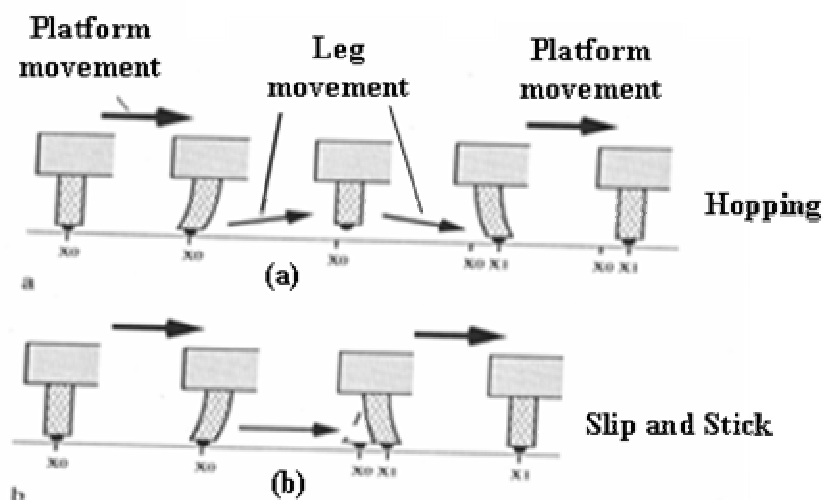
Figure 2.5: Depiction of "slip and stick" actuation movement using piezo electric actuator legs; variations of this are used by the PROHAM, MINIMAN, and Nanowalker microrobots [22].

Figure 2.6 shows illustrations depicting Aoyama and Fuchiwaki's system of flexible micro-assembly microrobots for working inside a SEM [34]. Their robots used piezo-electric actuators for movement, and used a bimorph PZT actuator to run the tweezers, as seen in Figure 2.6. They used a set of electromagnetic legs to clamp down on the SEM stage once they were in position, so the SEM stage could be tilted without the microrobots moving or sliding off.
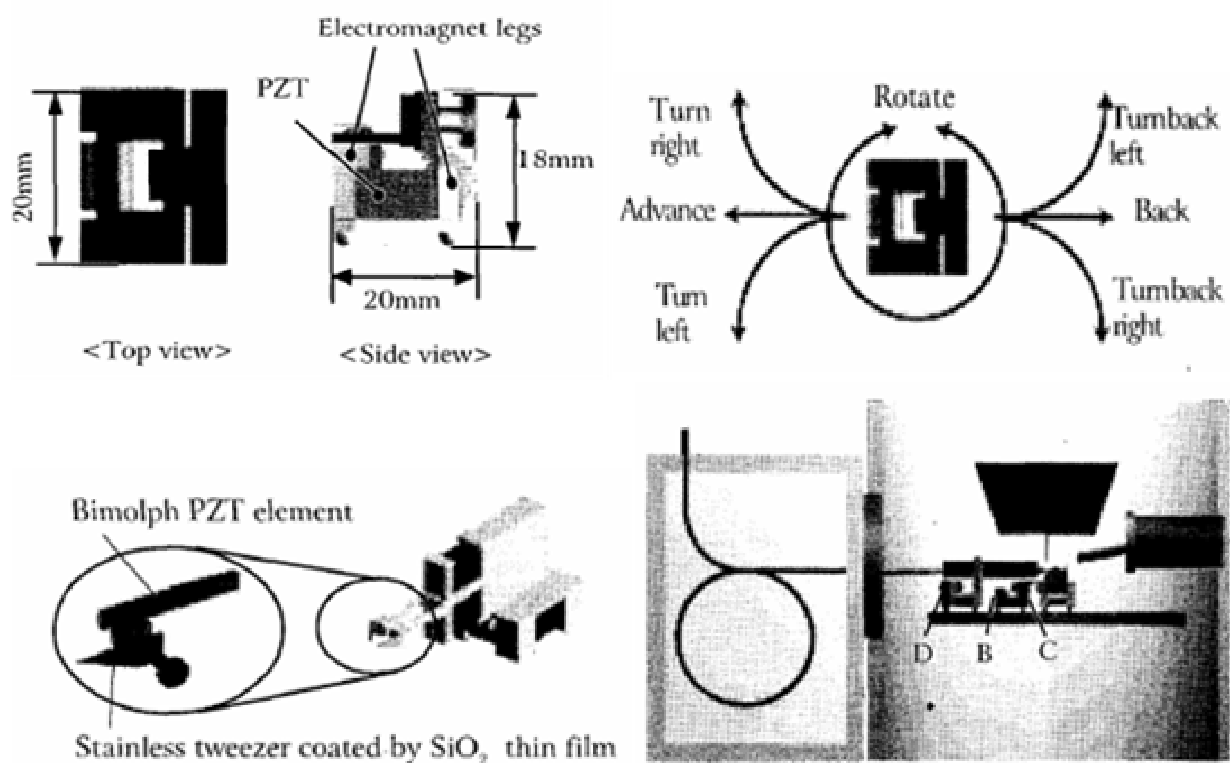
Figure 2.6: Illustrations depicting Aoyama and Fuchiwaki's system of flexible micro-assembly microrobots for working inside a SEM [34].

Baglio, et al. from the University of Catania, Italy, have recently tried an innovative photo-thermal-mechanical actuation method to autonomously power a microrobot [46] - [49]. Their strategy was to improve photo-thermal-mechanical efficiency by using an array of micro-lenses, based on photonic band gap (PBG) materials, to concentrate light on their photo-thermal actuators. They used bimorph (metal-dielectric PBG) cantilever structures as thermal actuators. Figure 2.7 is a depiction of Baglio, et al.'s photo-thermal-mechanical actuator, showing how they

used light to heat a bimorph actuator. They focused light through micro-lenses at the constrained ends of the cantilever legs, as seen in Figure 2.7. They used two types of PBG materials to make two sets of lenses, acting as bandpass filters at two separate laser light wavelengths, so they could separately address the different legs of their proposed microrobot. The light generates heat in the actuators, which were coated with an optical absorber material. The legs were designed to turn heat into mechanical energy. So far they have only a nonworking prototype microrobot, but it is on the order of 3 mm long, much smaller than any presently demonstrated microrobot.
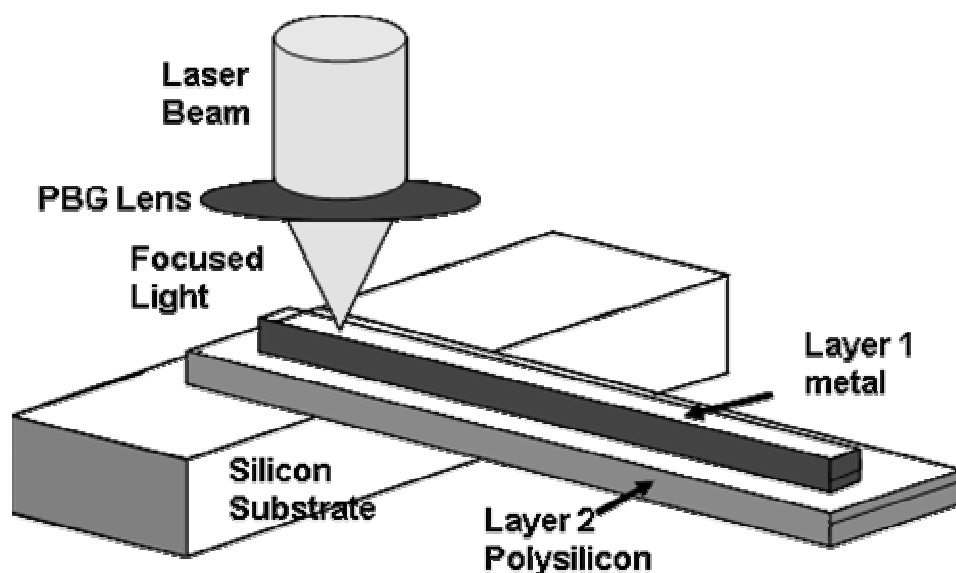
Figure 2.7: Depiction of Baglio, et al.'s photo-thermal-mechanical actuator, showing how they used light to heat a bimorph actuator.

Basset, et al. have experimented with a combination of low power electrostatic actuators, similar in design to those used in scratch drives and electromagnetic induction [50]. Figure 2.8 is an illustration of Basset, et al.'s low power electrostatic actuator, which is similar in design to scratch drives. The actuators are set out in large arrays for use as a distributed ciliary motion system. They designed high **Q** antennas for electromagnetic induction power transfer by sputtering gold on an epoxy film to produce hollow coil antennas with 23 turns in the coil, which

was 15 mm in diameter. They then remotely powered an array of 128 actuators using a 13.56 MHz power signal. They are working on a prototype microrobot based on these designs.
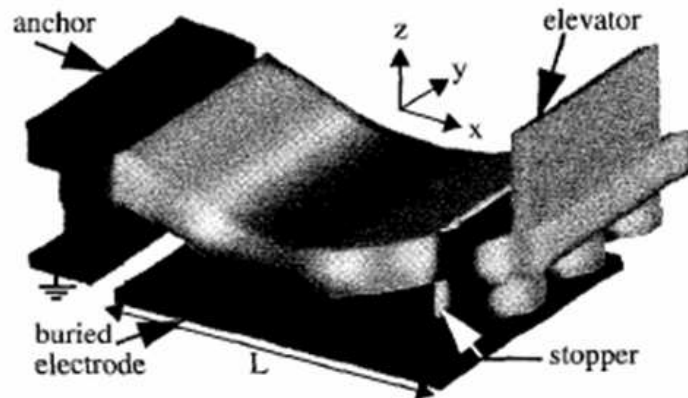
Figure 2.8: Illustration of Basset, et al.'s low power electrostatic actuator, which is similar in design to scratch drives [50].

Hollar [20], Bellew [21], and Yeh [5], et al., from the Berkeley Sensors and Actuators Center at the University of California, used low power electrostatic comb drive actuators and solar cells to power their small size autonomous microrobot. Figure 2.9 is a photograph of the first solar powered autonomous microrobot, presented by Hollar in 2003, which used electrostatic comb drives and gear and clutch combinations to accumulate motion. It was 8.5 mm x 4 mm in size. Figure 2.10 is a SEM micrograph depicting an electro-static comb drive actuator with multiple plates. These actuators move when electrostatic charges attract two sets of plates together, as seen in Figure 2.10. The design ensures that contact is never made. Even though large voltages are used (up to 88.5 volts), there is theoretically no current. By this actuation method, Hollar, et al. were able to obtain deflections of 2 μm. Despite this small deflection, their actuator arrays were capable of moving a shuttle a large distance. This was accomplished by using two large actuator arrays, each with a clutch stage and a drive stage. This system allowed them to "accumulate" the 2 μm deflections into a very large deflection. Their microrobot used 50 V synchronous voltages, with only very small leakage current. The total

power consumed was 2.6 μW; 3 to 4 orders of magnitude less than for electrothermal actuators. However, it should be noted that due to the large surface area required by the capacitive plates, electro-static actuators are much less powerful than electrothermal actuators for the amount of chip surface area they occupy. However, their low current, high voltage characteristics make them ideal for use with solar cells [51].
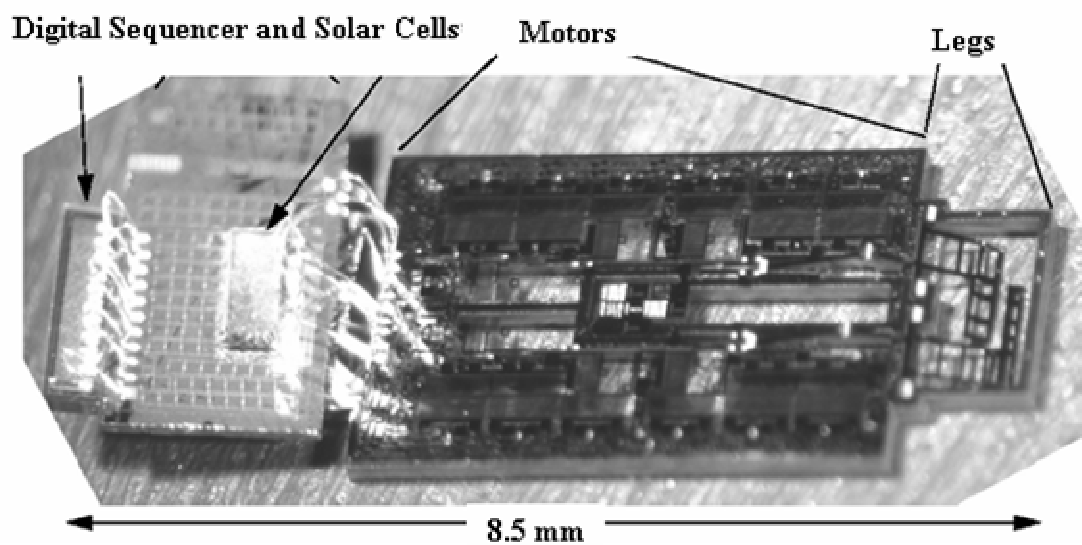
Figure 2.9: Photograph of the first solar powered autonomous microrobot, presented by Hollar in 2003, which used electrostatic comb drives and gear and clutch combinations to accumulate motion [20].
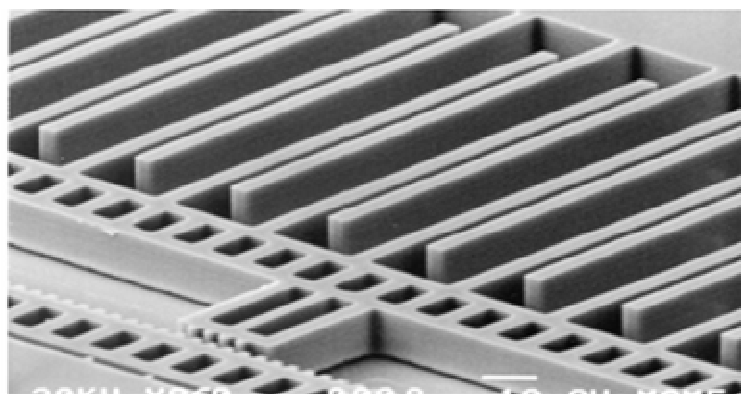
Figure 2.10: SEM micrograph depicting an electro-static comb drive actuator with multiple plates [21].

Linderman and Bright developed a scratch drive array (SDA) which used electrostatic step actuators [19]. Figure 2.11 is a Depiction of Linderman and Bright's Electrostatic Scratch

Drive Actuators, showing the stepping process [19]. To enable the stepping function, a snap through voltage is applied as in Figure 2.11, middle picture. Then an extra electrostatic voltage is applied, storing strain energy into the support arms, plate and bushing, and causing the stepping motion. The stored strain energy is equivalent to energy stored in a spring. When the voltage is removed, the stored strain energy pulls the actuator forward as the energy is released.
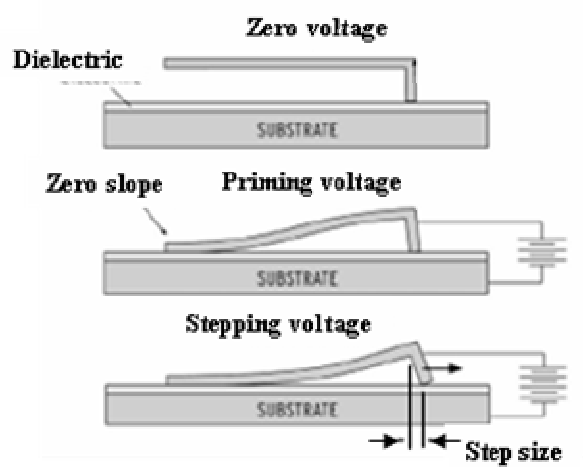
Figure 2.11: Depiction of Linderman and Bright's Electrostatic Scratch Drive Actuators, showing the stepping process [19].

2.4. Lasers as a Power Source for Actuation

Lasers have been used in several ways to power actuating devices. Among the laser actuation methods are ablation, liquid heating and expansion, light trapping, optothermal expansion with bimorph structures, and resonant induction [52], [53]. The most common laser actuator to date is the liquid expansion type.

Nogimori, et al. devised a laser powered microgripper, using a laser beam which was guided down a fiber optic cable to heat and expand fluid in a cylinder [54]. This provided the microgripper with stroke length of 900 μm. Figure 2.12 is a depiction of Nogimori's laser powered microgripper, which uses thermally expanding liquid to provide the power for actuation [54]. Plate-spring in the jaws returned the gripper to the open position when actuation power

was removed as seen in Figure 2.12.
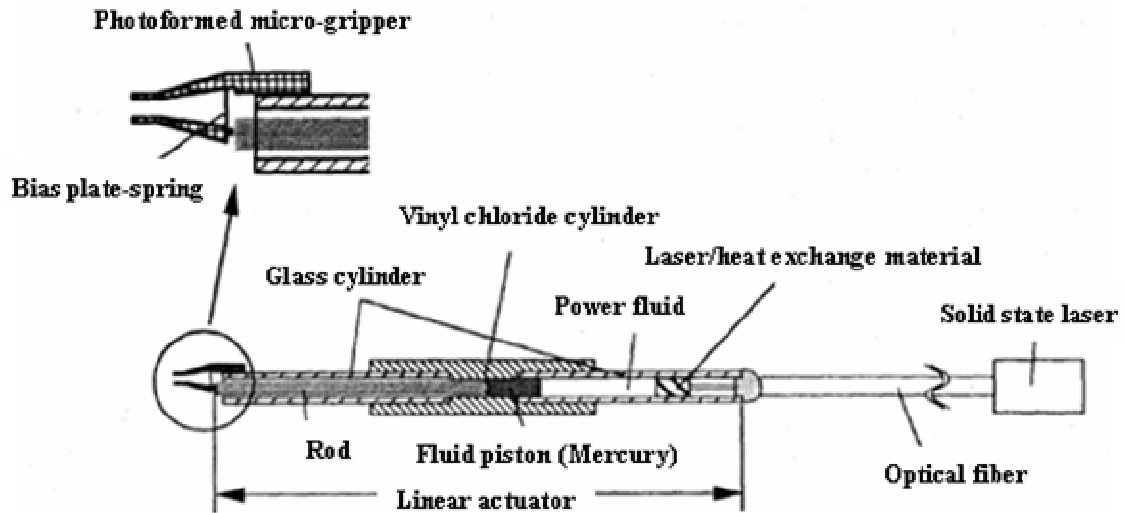
Figure 2.12:   Depiction of Nogimori's laser powered microgripper, which uses thermally expanding liquid to provide the power for actuation [54].

Kirshberg [55] and Pettigrew [56] used a CO_2 laser to power microcapillary pumps by shining a 1 mm diameter dot-size laser on the back of the pump to evaporate liquid, which caused the pumping action. Liwei, et al. used a laser with an extremely fine dot to create a bubble in liquid at a capillary junction, as a switch to turn liquid flow on and off [57]. They also used heated bubbles in a chamber to run a microbubble controlled nozzle-diffuser pump.

Yamagata, et al. used laser heating induced thermal expansion of solid materials to make micro impact drive mechanisms [58], [59]. Depiction of Yamagata's laser driven micro impact drives, using (a) trapped laser light to heat (b) asymmetric block actuators. Figure 2.13 shows how they used optically excited thermal expansion in solid structures to drive their mechanisms. By aiming the laser at a specifically designed mirror light-concentrating surface geometry, as seen in Figure 2.13 (a), they were able to heat a thin long area, analogous to the hot arms previously presented. Using alternating heating and cooling cycles induced an expansion and retraction motion. They were able to obtain forward motion in a similar manner to scratch

drives. Yang, et al. used a 40 μW laser to thermally resonate small (60 μm long) ultra thin cantilevers [60]. They combined photothermal and light pressure effects to match the Q of the cantilevers, causing them to resonate.
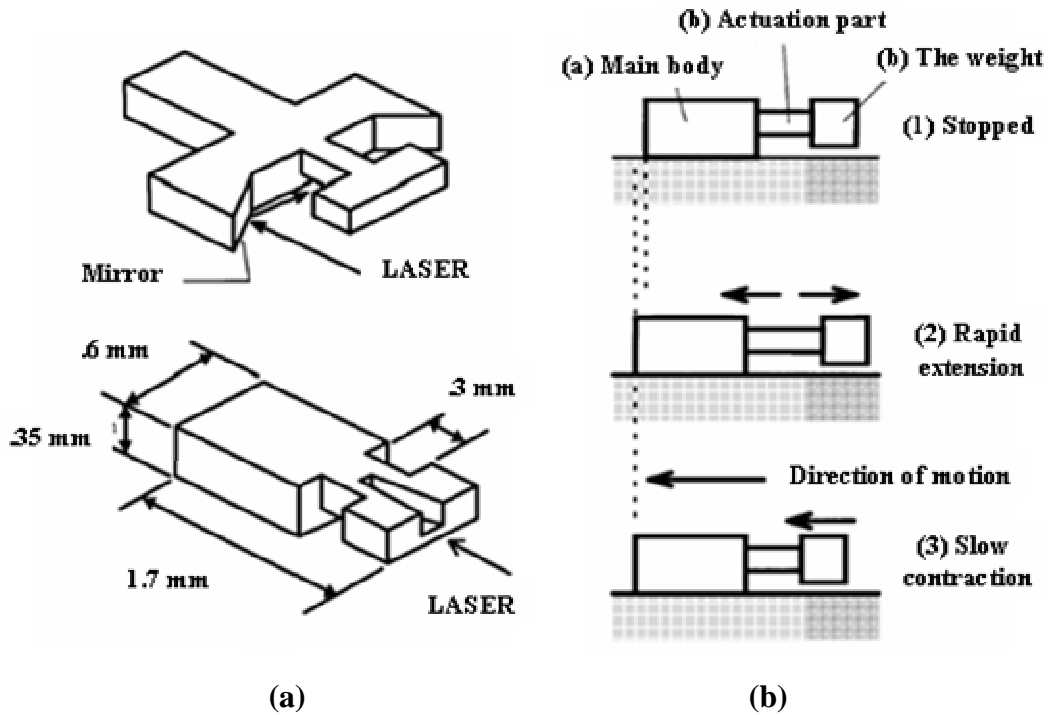
Figure 2.13: Depiction of Yamagata's laser driven micro impact drives, using (a) trapped laser light to heat (b) asymmetric block actuators [58], [59].

Aoki [28] and Yabe [24] used laser ablation explosions to power a micro airplane and other devices. They claimed this drive mechanism could work on anything from microrobots to large space ships. The theoretical idea is to release some kind of heavy liquid into a nozzle type area behind the vehicle, then hit the liquid with a very high powered laser, causing an instant explosion by ablation. The force of this ablation explosion would then drive the vehicle forward.

Tzou and Chou took advantage of the opto-electro-mechanical properties of light sensitive, photostrictive materials to design opto-piezoelectric actuators that worked by inducing photo-deformation [61]. Figure 2.14 is a depiction of Tzou and Chou's laser driven opto-piezoelectric actuators, which use light sensitive, photostrictive materials to provide

asymmetrical expansion. They used four regions of two-layer photosensitive materials, as seen

in Figure 2.14, which are bonded together in opposite polarity to make a two dimensional

photostrictive optical actuator system. The top surface is irradiated by a laser and the absorbed

light energy photovoltaicly induces a current in the top layer, which flows opposite to the

polarized direction, as seen in Figure 2.14. The induced current builds up a charge which

generates an in-plane electric field. This creates a positive strain in the top layer, while a

negative strain is generated in the bottom dark layer due to the converse piezoelectric effect.

This causes the photostrictive optical actuator to deform, providing controllable actuation. The

advantage of this system was remote actuation, while the disadvantage was that it was very slow

compared to standard piezoelectric actuators. It only had a maximum frequency response of

around 100 Hz.
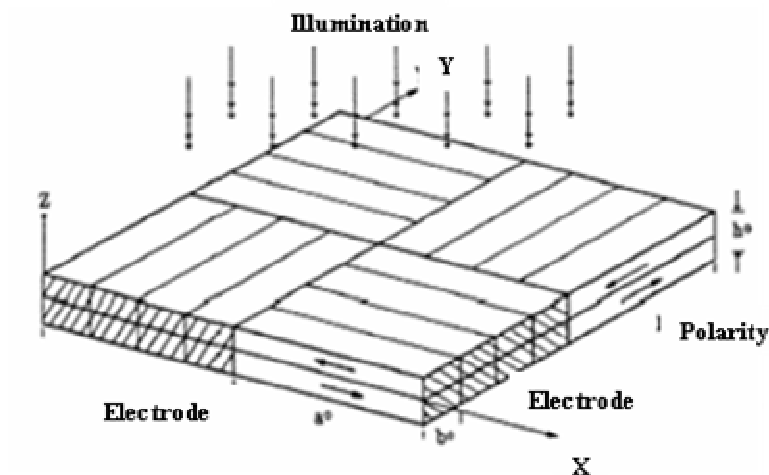
Figure 2.14: Depiction of Tzou and Chou's laser driven opto-piezoelectric actuators, which uses light sensitive, photostrictive materials to provide asymmetrical expansion [61].

2.5. Performance Comparisons of Small Microrobots

Table 2.1, Summary of Specifications for Small MEMS Microrobots, is a summary of

comprehensive descriptions of recent successful MEMS microrobots. Table 2.1 provides

comparisons of performance and characteristics of each microrobot. The first column lists the author(s) who designed the microrobots. The second column is Actuation Principle, which gives the type of actuator used. The third column is Max Velocity, or speed, and Load, or how much weight it could carry. The fourth column is Power Budget / Type, which are the power requirements for the microrobot. The last column is Size, which gives the dimensions of the microrobot. Under each row listing the microrobot is a row detailing the advances and shortcomings of each microrobot design.

The various benchmarks, used by different authors to test their microrobots and compare them, were speed, controllability, payload, power requirements and autonomy. There are no universal testing standards for microrobots, and each author used their own benchmarks that displayed their design advances in the best advantage.

Speed and controllability were tested by some authors using video cameras and running the microrobot on a background, with pre-measured, marked distance increments. Because of power wires acting as tethers, the microrobots could only be run back and forth over short distances, and their speed calculated from the distance increment marks. Some of the earlier models, which were too encumbered by wires to walk, were turned upside down and tested as conveyers, "walking" or conveying large object across their legs.

Payload was tested two ways. The first was to load the robot until the legs broke. The second was to load the microrobot and attempt movement, repeating this with increasing weights until it could no longer move. Power requirements were determined by test equipment hooked up to their power supplies, usually at a probe station. As microrobots get smaller, load capacity can probably be compared as a function of the nicrorobot's weight (i.e. 30 times its own weight).

Autonomous movement can be determined by a large movement (large in comparison to

the robot's size), without any wires attached. Once a microrobot is presented which can travel a distance many times its length, the amount of time it can move before it runs out of power or fails mechanically can be used as a comparison factor. Finally, durability will also be an important comparison factor before these microrobots can be deployed commercially. A couple of the authors performed actuator durability tests, but there was no set test standard.

The Ebefors microrobot, using electrothermal actuators, was by far the fastest and could carry the heaviest payload, but also consumed the largest amount of power. The Hollar microrobot was the first, so far, to move autonomously. The Mohebbi microrobot was the first microrobot with programmable controls. It was also the first, at such a small size, to have three degrees of freedom of movement in a plane.

Table 2.1: Summary of Specifications for Small MEMS Microrobots.

Author(s)	Actuation Principle	Max Velocity, Load	Power Budget / Type	Size
Bohringer, Suh, et al. 1997 [15], [36], [16].	Arrays of four orthogonal **electrothermal** bimorph polyimide legs	0.2 mm/s, carried 3x3x.5 mm silicon chip, (est. 20 mg)	(f = 1 Hz, **30-38 mW** per set of 4 legs, **6.7 W** per array per gait cycle) fc =30 Hz	total area: 10×10 mm^2 $8 \times 8 \times 4$ legs (64 sets of 4) each 430 μm long
Advances: This conveyer worked upside down (legs in air) and conveyed parts across its legs in a controlled manner. It showed great promise to be redesigned into a walking microrobot. The legs were configured in a four-leaf clover configuration and gave good programmable three degree of freedom (DOF) control. The authors used surface micromachining fabrication methods. **Shortcomings:** This device was not a true microrobot and could not walk on its legs. An extremely large power budget of 6.7 Watts indicates it is not a good candidate for autonomous locomotion.				
Kladitis, et al. 1997 [9], [10].	Large array of erected polysilicon legs; **electrothermal** single hot arm actuators, 2 and 3 DOF.	453 μm/min, step size: 3.75 μm, carried 68 mg load	**2.87 W** fc = 2 Hz, 10V, 287 mA for 2 DOF, **592 mW** fc = 2 Hz, 8V, 74 mA for 3 DOF: square wave voltage	total area: 10×10 mm^2 96 legs each 270 μm long; weight: 32 mg
Advances: Kladitis introduced the six leg insect-style tripod walking gate. This conveyer was tested upside down (legs in air) and conveyed parts across its legs in a controlled manner. It was also able to stand on its legs. Kladitis used PolyMUMPs surface micromachining fabrication methods and solder surface-tension-based self assembly. **Shortcomings:** This microrobot was extremely limited in its mobility because the three attached power wires. A very large power budget of 2.87 Watts indicates it is not a good candidate for autonomous locomotion.				
Ebefors, et al. 1999, 2000 [11], [12], [13], [14].	Array of erected silicon legs; **electrothermal** actuation of bimorph polyimide joints (asynchronous)	12 mm/s, step size: 175 μm, carried 3500 mg load	**1.3 W,** fc = 3 to 250 Hz, 18-23V, alternating asynchronous voltage	total area: 15×5 mm^2 2×6 legs each 500 μm long; weight: 115 mg
Advances: Fastest and most powerful (in terms of payload) small microrobot to date. Ebefors used both bulk and surface micromachining fabrication methods. Author listed possibility for 3 DOF and demonstrated transverse and rotational movement. **Shortcomings:** A large power budget of 1.3 Watts indicates this microrobot is not a good candidate for autonomous locomotion. This microrobot was limited in motion length due to three attached power wires. Ebefor's microrobot had strong transverse and rotational movement, but little accuracy. Only 1 DOF was accurately demonstrated.				

Table 2.1: Summary of Specifications for Small MEMS Microrobots (continued).

Author(s)	Actuation Principle	Max Velocity, Load	Power Budget / Type	Size
Mohebbi, Bohringer, Suh, et al. 2001 [17], [16], [36].	Microcilia array, four orthogonally oriented **electrothermal** bimorph actuators	635 μm/s, step size: 5 μm, carried 1448 mg load	Wattage not specified 7.5V-60V, 10 Hz, 30, 60, 90, and 120 Hz	3 cm length, 1 cm width, 1 mm height; weight, 457 mg
Advances: Mohebbi's device is the first MEMS microrobot with accurate and repeatable 3 DOF movement. It was also controllable with a programmable computer control system. Mohebbi used surface micromachining fabrication methods. **Shortcomings:** Mohebbi's microrobot was limited in motion length due to **nine** attached power wires. It was able to travel around a 10 cm x 10 cm plate. While Mohebbi did not give power requirement for his microrobot, it is based on Bohringer and Suh's actuators, which used 6.7 W of power. His device is three times the size of their device. This microrobot is not a good candidate for autonomous locomotion.				
Hollar, Bellew, Yeh,, et al. 2003 [20], [21], [5], [6].	Large arrays of **electrostatic** actuators, inchworm motor, using clutch and shuttle technique to drive two large legs on front of microrobot (dragging style)	3 mm (total), zero payload, no step size	**2.6 μW,** 50 V synchronous voltage, zero static current (leakage current only)	total area: 8.6 x 3.1 mm^2; 2 large legs; weight, 10 mg
Advances: Hollar's microrobot is the first autonomous small MEMS microrobot to successfully move with no wires attached. It used solar cells for power. Hollar and Yeh used surface micromachining fabrication methods with Silicon on Insulator (SOI) technology for 30 μm thick layers. Tall layers increased surface area and power of electrostatic comb drives. **Shortcomings:** Because of its dragging style and the fact that the solar cells were attached at the dragging end of the device, this microrobot was unable to sustain forward motion or carry a payload. The two front legs were unable to gain any traction to overcome the friction on the back end, and produced a wobbling sideways motion like a fishtailing car.				
In 2001, Linderman and Bright produced a scratch drive array microrobot, which could push a 2 x 2 x .5 mm chip a distance of 8 mm, with a possible accuracy of 30 nm [19]. The robot size, from one of their figures, appears to be 3 mm by 8 mm. They claimed it required much less power than previously published microrobots, but provided no specifications for velocity, payload, power, current, weight or size. They used a 200 V, 0 to peak drive signal.				
Note: This table was adapted from Table 1, page 338 from Thorbjörn Ebefor's paper "A Robust Micro Conveyer Realized by Arrayed Polyimide Joint Actuators" [12], with new information added from the references listed above.				

2.6. Summary

This background chapter covered what has been accomplished in the microrobotics field so far. A brief overview of the history of the microrobotics field was given and possible microrobot applications were discussed. Different available and proposed microrobotic actuators and proposals for lasers as an actuation power source were reviewed. A summary of performance comparisons of existing small microrobots was given.

However, none of these actuators or laser heating proposals found in literature fit well with using lasers to heat actuators fabricated in PolyMUMPs. Therefore, a new type of actuator or laser actuation paradigm, not previously used on microrobots, must be found. Chapter 3 discusses laser heating theory and the required wavelengths of laser light that can be used to heat polysilicon actuators. Chapter 4 discusses the actuator designs that I finally came up with to use for laser heating.

2.7. Bibliography

[1]   R. P. Feynman, "There's Plenty of Room at the Bottom," *Journal of Microelectromechanical Systems*, vol. 1, no. 1, pp. 60-66, March 1992.

[2]   K. E. Peterson, "Silicon as a Mechanical Material," *Proceedings of the IEEE*, vol. 70, no. 5, pp. 420-457, March 1992.

[3]   R. P. Feynman, "Infinitesimal Machinery," *Journal of Microelectromechanical Systems*, vol. 2, no. 1, pp. 4-14, March 1993.

[4]   S. Guo, T. Fukada, K. Asaka, "Fish-like Underwater Microrobot with 3 DOF," *Proceedings of the 2002 IEEE International Conference on Robotics & Automation*, pp. 738-743, 2002.

[5]   T. Yasuda, I. Shimoyama, H. Miura, "Microrobot Actuated by a Vibration Energy," *Sensors and Actuators*, part A, vol. 43, pp. 366-370, 1994.

[6]   R. Yeh, S. Hollar, K. S. J. Pister, "Design of Low-Power Silicon Articulated Microrobots," *Journal of Micromechatronics*, vol. 1, no. 3, pp. 191-203, 2002.

[7]   R. Yeh, E. J. Kruglick, K. S. J. Pister, "Surface Micromachined Components for Articulated Microrobots, *Journal of Microelectricalmechanical Systems,* vol. 5, no. 1, 1996.

[8]   A. Teshigahara, M. Watanabe, N. Kawahara, I. Ohtsuka, T. Hattori, "Performance of a 7-mm Microfabricated Car**,**" *Journal of Microelectromechanical Systems*, vol. 4, issue 2 , pp. 76 -80, 1995.

[9]   P. E. Kladitis, V. M. Bright, "Prototype Microrobots for Micro Positioning and Micro Unmanned Vehicles," *Sensors and Actuators*, vol. 80, pp. 132-137, 2000.

[10]   P. E. Kladitis, *Self Assembly of Microstructures*, Masters Thesis, Air Force Institute of Technology, 1997.

[11]   T. Ebefors, J. U. Mattsson, E. Kälvesten and G. Stemme, "A Walking Silicon Micro-Robot," *10th International Conference on Solid-State Sensors and Actuators Proceedings*, pp. 1202-1205, 1999.

[12]   T. Ebefors, J. U. Mattsson, E. Kälvesten, and G. Stemme, "A Robust Micro Conveyer Realized by Arrayed Polyimide Joint Actuators," *Journal of Micromechanical Microengineering*, vol. 10, pp. 337-349, 2000.

[13]   T. Ebefors, J. U. Mattsson, E. Kälvesten, and G. Stemme, "3D Micromachined Devices Based on Polyimide Joint Technology," *Conference on Devices and Process Technologies for MEMS and Microelectronics, SPIE* vol. 3892, pp. 118-132, 1999.

[14]   T. Ebefors, *Polyimide V-Groove Joints For Three – Dimensional Silicon Transducers – Exemplified Through A 3-D Turbulent Gas Flow Sensor And Micro-Robotic Devices*, Doctoral Dissertation, Royal Institute of Technology (KTH), Stockholm, Sweden, 2000.

[15]   K. F. Bohringer, B. R. Donald, N. C. MacDonald, G. T. A. Kovacs, J. W. Suh, "Computational Methods for Design and Control of MEMS Micromanipulator Arrays," *IEEE Computational Science and Engineering*, January – March 1997, pp. 17-29.

[16]   J. W. R. Suh, B. Darling, K. F. Bohringer, B. R. Donald, H. Baltes, G. T. A. Kovacs, "CMOS Integrated Ciliary Actuator Array as a General-Purpose Micromanipulation Tool for Small Objects," *Journal Of Microelectromechanical Systems*, vol. 8, no. 4, pp. 483-496, 1999.

[17]   M. H. Mohebbi, M. L. Terry, K. F. Bohringer, G. T. A. Kovacs, J. W. Suh, "Omnidirectional Walking Microrobot Realized By Thermal Microactuator Arrays," *Proceedings of 2001 ASME International Mechanical Engineering Congress and Exposition,* pp. 1-7, 2001.

[18]   J. W. R. Suh, R. B. Darling, K.-F. Bohringer, B. R. Donald, H. Baltes, G. T. Kovacs, "Fully Programmable MEMS Ciliary Actuator Arrays for Micromanipulation Tasks," *IEEE International Conference on Robotics and Automation. Symposia Proceedings*, vol. 2, pp. 1101-1108, 2000.

[19]   R. J. Linderman and V. M. Bright, "Nanometer Precision Positioning Robots Utilizing Optimized Scratch Drive Actuators," *Sensors and Actuators, A: Physical*, vol. 90, no. 3, pp. 292-300, 2001.

[20]   S. Hollar, A. Flynn, C. Bellew, and K. S. J. Pister, "Solar Powered 10 mg Silicon Robot," *MEMS IEEE Conference Proceedings Paper*, 706-711, 2003.

[21]   C. L. Bellew, A. P. Pisano, K. S. J. Pister, R. T. Howe, "*An SOI Process for Integrated Solar Power, Circuitry and Actuators for Autonomous Microelectromechanical Systems.*" Doctoral Dissertation. Berkeley Sensor and Actuator Center, University of California, Berkeley, Berkeley, CA, 2002.

[22]   S. Fatikow, U. Rembold, *Microsystem Technology and Microrobotics*, Berlin, Springer-Verlag, 1997.

[23]   M. Gad-El-Hak, T. Ebefors, and G. Stemme, "Microrobotics" chapter in *The MEMS Handbook*, CRC Press LLC, 2002, University of Notre Dame, pp. 28-1 - 28-42, 2002.

[24] T. Yabe, P. Claude, A. Keiichi, Y. Masashi, O. Youichi, S. Makoto, I. Gen, O. Masahiko, H. Kazuhiko, K. Itsuro, Y. Kunio, "Laser-Driven Vehicles - from Inner-Space to Outer-Space," *Proceedings of SPIE, The International Society for Optical Engineering*, vol. 4760, no. II, pp. 867-878, 2002.

[25] C. L. Fowler, AFRL/MNAV, Eglin AFB, FL. Private communications, February 2003.

[26] T. Sakakibara, I. Hiroaki, S. Takayuki, T. Hisaki, S. Kenichi, K. Seiichi, K. Nobuaki, "Multi-Source Power Supply System Using Micro-Photovoltaic Devices Combined with Microwave Antenna," *Sensors and Actuators, A: Physical*, vol. 95, no. 2-3, pp. 208-211, 2002.

[27] T. Shibata, T. Sasaya, N. Kawahara, "Development of In-Pipe Microrobot Using Microwave Energy Transmission," *Electronics and Communications in Japan*, part 2, vol. 84, no. 11, 2001, Translated from Denshi Joho Tsushin Gakkai Ronbunshi, Vol. J83-B-II, No. 5, pp. 704-710, 2000.

[28] K. Aoki, T. Yabe, R. Nakagawa, M. Yamaguchi, C. Baasandash, "Numerical and Experimental Studies of Laser Propulsion Toward a Micro-Airplane," *Proceedings of SPIE, The International Society for Optical Engineering,* vol. 4760, no. II pp., 918-928, 2002.

[29] S. Fatikow, U. Rembold, H. Woern, "Design And Control Of Flexible Microrobots For An Automated Microassembly Desktop-Station," *Microrobotics and Microsystem Fabrication, Society of Photo-Optical Instrumentation Engineers, SPIE Proceedings,* vol. 3202, p. 66-77, 1998.

[30] K. Santa, S. Fatikow, "Development of a Neural Controller for Motion Control of a Piezoelctric Three-Legged Micromanipulation Robot," *Proceedings, 1998 IEEE/RSJ International Conference on Intelligent Robots and Systems*, pp. 788–793, 1998.

[31] K. Santa, S. Fatikow, G. Felso, "Control Of Microassembly-Robots by Using Fuzzy-Logic And Neural Networks," *Computers in Industry*, vol. 39, pp. 219–227, 1999.

[32] K. Santa, S. Fatikow, "Control System For Motion Control Of A Piezoelectric Micromanipulation Robot," *Advanced Robotics*, vol. 13, issue 6, pp. 577-589, 2000.

[33] O. Manolov, Sv. Noikov, P. Bison, G. Trainito, "Indoor Mobile Robot Control for Enviroment Information Gleaning," *Proceedings, IEEE Intelligent Vehicles Symposium 2000*, pp. 602-607, 2000.

[34] H. Aoyama, O. Fuchiwaki, "Flexible Micro-Processing by Multiple Micro Robots in a SEM," *Proceedings IEEE International Conference on Robotics and Automation*, vol. 4, pp. 3429-3434, 2001.

[35]   M. Norihisa, S. Isao, "Micro-Flight Mechanism with Rotational Wings," *Proceedings of the IEEE Micro Electro Mechanical Systems (MEMS)*, pp. 158-163, 2000.

[36]   J. W. Suh, R. B. Darling, K.-F. Bohringer, B. R. Donald, H. Baltes, G. T. Kovacs, "Fully Programmable MEMS Ciliary Actuator Arrays for Micromanipulation Tasks," *IEEE International Conference on Robotics and Automation. Symposia Proceedings*, vol. 2, pp. 1101-1108, 2000.

[37]   A. Bonvilain, N. Chaillet, "Fabrication and Experiment of Microlegs for an Insect-Like Microrobot," *Proceedings of SPIE,* vol. 4568, pp.163-174, 2001.

[38]   V. Djakov, S.E Huq, "Bimorph Actuators for MOEMS," *Proceedings of SPIE, The International Society for Optical Engineering*, vol. 4655, pp. 804-814, 2002.

[39]   J. T. Butler, V. M. Bright, W. D. Cowan, "Average Power Control and Positioning of Polysilicon Thermal Actuators," *Sensors and Actuator*s, vol. 72, pp. 88–97, 1999.

[40]   D. Yan, A. Khajepour and R. Mansour, "Modeling of two-hot-arm horizontal, thermal actuator," *Journal of Micromechanics and Microengineering*, vol. 13 pp. 312–322, 2003.

[41]   E. S. Kolesar, M. D. Ruff, W. E. Odom, J. A. Jayachadran, J. B. McAllister, S. Y. Ko, J. T. Howard, P. B. Allen, J. M. Wilken, N. C. Boydston, J. E. Bosch, R. J. Wilks, "Single- and Double-Hot Arm symmetrical Polysilicon Surface Micromachined Electrothermal Microactuators Applied to Realize a Microengine," *Thin Solid Films*, vol. 420-421, pp. 530-538, 2002.

[42]   S. Martel, M. Szabelski, A. Leija, P. Madden, S. Lafontaine, I. Hunter, "Initial Results Of A New Type Of Locomotion For A Wireless Instrumented Robot Capable Of Subatomic Movements," *Proceedings of the Biomedical Engineering Society and the 21st Annual International Conference of the IEEE Engineering in Medicine and Biology Society*, 1999.

[43]   S. Martel, P. Madden, L. Sosnowski, I. Hunter and S. Lafontaine, "Nanowalker: A Fully Autonomous Highly Integrated Miniature Robot For Nano-Scale Measurements," *Proceedings of the European Optical Society (EOS) and SPIE International Symposium on Envirosense, Microsystems Metrology and Inspection*, Vol. 3825, pp. 409-21, 1999.

[44]   E. Montane', P. Miribel-Catala, J. Lopez-Sanchez, M. Puig-Vidal, S. Bota, J. Samitier, "High Voltage Smart Power Integrated Circuits to Drive Piezoceramic Actuators for Microrobotic Applications," *IEEE Proceedings, Circuits, Devices and Systems*, vol. 148, no. 6, pp. 343-347, 2001.

[45] H. Wörn, F. Schmoeckel, A. Buerkle, J. Samitier, M. Puig-Vidal, S. Johansson, U. Simu, J.-U. Meyer, M. Biehl, "From Decimeter- To Centimeter-Sized Mobile Microrobots The Development Of The MINIMAN System," *Proceedings of the SPIE - The International Society for Optical Engineering,* vol.4568, pp. 175-86, 2001.

[46] S. Baglio, S. Castorina, L. Fortuna, N. Savalli, "Modeling and Design of Novel Photo-Thermo-Mechanical Microactuators," *Source: Sensors and Actuators, A: Physical*, vol. 101, no. 1-2, pp. 185-193, 2002.

[47] S. Baglio, S. Castorina, L. Fortuna, N. Savalli, "Novel Microactuators Based on a Photo-Thermo-Mechanical Actuation Strategy," *Sensors, 2002. Proceedings of IEEE*, vol. 1, pp. 192 -197, 2002.

[48] S. Baglio, S. Castorina, L. Fortuna, N. Savalli, "Technologies and Architectures for Autonomous "MEMS" Microrobots," *Proceedings, 2002 IEEE International Symposium on Circuits and Systems,* vol. II, pp. 584-587, 2002.

[49] S. Baglio, S. Castorina, L. Fortuna, N. Savalli, "Development of Autonomous, Mobile Micro-electro-mechanical Devices," *Proceedings, 2002 IEEE International Symposium on Circuits and Systems*, vol. 4, pp. IV-285-288, 2002.

[50] P. Basset, A. Kaiser, P. Bigotte, D. Collard, Lionel Buchaillot, "A Large Stepwise Motion Electrostatic Actuator for a Wireless Microrobot," *Fifteenth IEEE International Conference on Micro Electro Mechanical Systems*, vol. II pp. 606-609, 2002.

[51] J. B. Lee, C Zhizhang, M. G. Allen, R. Ajeet, A. Rajeewa, "Miniaturized High-Voltage Solar Cell Array as an Electrostatic MEMS Power Supply," *Journal of Microelectromechanical Systems*, vol. 4, no. 3, pp. 102-108, 1995.

[52] H. Yu, Y. Wang, C. Ding, Y. Wang, Y. Xu, "The Characteristics of Point-Heating Excitation in Silicon Micro-Mechanical Resonators", *Sensors and Actuators*, vol. 77, pp. 187–190, 1999.

[53] P. Katila, P. Heimala, J. Aarnio, "Thermo-optically Controlled Ring Resonator on Silicon," *Electronics Letters*, vol. 32, no. 11, pp. 1005-1006, 1996.

[54] W. Nogimori, K. Irisa, M. Ando, Y. Naruse, "A Laser-Powered Micro-Gripper," *Proceedings IEEE, The Tenth Annual Workshop on Micro Electro Mechanical Systems, An Investigation of Micro Structures, Sensors, Actuators, Machines and Robots,* pp. 267-71, 1997.

[55] J. Kirshberg, K. L.Yerkes, D. Liepmann, "Demonstration of a Micro-CPL Based on MEMS Fabrication Technologies," *Proceedings of the Intersociety Energy Conversion Engineering Conference*, vol. 2, pp. 1198-1204, 2000.

[56] K. Pettigrew, J. Kirshberg, K. Yerkes, D. Trebotich, D. Liepmann, "Performance of a MEMS Based Micro Capillary Pumped Loop for Chip-Level Temperature Control," *Proceedings of the IEEE Micro Electro Mechanical Systems (MEMS)*, pp. 427-430, 2001.

[57] L. Liwei, "Thermal Challenges in MEMS Applications: Phase Change Phenomena and Thermal Bonding Processes," *Microelectronics Journal*, vol. 34, pp. 179–185, 2003.

[58] Y. Yamagata, O. Ohmichi, T. Higuchi, "Micro Impact Drive Mechanisms Using Optically Excited Thermal Expansion**,**" *Journal of Microelectromechanical Systems*, Volume: 6 Issue: 3, Page(s): 200 -207, 1997.

[59] Y. Yamagata, H. Toshiro, N. Naoto, H. Sho, "Micro Mobile Mechanism Using Thermal Expansion and Its Theoretical Analysis," *Proceedings of the IEEE Micro Electro Mechanical Systems, An Investigations of Micro Structures, Sensors, Actuators, Machines and Robotic Systems*, pp. 142-147, 1994.

[60] J. Yang, O. Takahito, E. Masayoshi, "Energy Dissipation in Submicrometer Thick Single-Crystal Silicon Cantilevers," *Journal of Microelectromechanical Systems*, vol. 11, no. 6, pp. 775-783, 2002.

[61] H. S. Tzou, C.-S. Chou, "Nonlinear Opto-Electromechanics and Photodeformation of Optical Actuators," *Smart Materials and Structures*, vol. 5, no. 2, pp. 230-235, 1996.

3. Laser Heating Theory

This chapter will cover the design theory involved in using a laser to heat up a thermal actuator. Since none of the microrobot actuators or laser heating proposals discussed in the last chapter work well, within this research's constraints of using the PolyMUMPs fabrication processes, a new type of actuator or laser actuation paradigm must be found. Since this research's actuators were fabricated from heavily doped polysilicon, great care was taken to choose the proper wavelength of light, making trade-offs between the absorption of light in the polysilicon, which is required for heating, and the reflectivity of gold, which is used as shielding. Section 3.1 gives a brief description of the different reactions of a material to light hitting a surface at an angle. Section 3.2 describes the trade-off in parameters for reflectivity and absorption. Section 3.3 covers the literature which was reviewed to choose the required laser power.

3.1. Light Impinging on a Semiconductor

To understand how much thermal power can be obtained from laser light for actuation, this section explains the three reactions to incident photon power in a semiconductor material. Figure 3.1 is an illustration depicting three reactions to light impinging on a semiconductor. The picture shows a block of semiconductor material, and the theory is the same as that used for solar cells.

The first reaction in Figure 3.1 is (1), reflection, where no power is absorbed. The reflectivity of light increases at large angles (past 45 degrees for polysilicon [1]). Reflectivity also increases when the surface of the material is highly reflective [1] - [5]. Figure 3.2 is a plot of the reflectivity of PolyMUMPs polysilicon versus laser beam incident angle, with a

wavelength of .6328μm [1]. It shows a reflectivity of around 30 percent, at an incident angle of 45 degrees.

The second reaction in Figure 3.1 is (2), transmission, is when the wavelength energy of the photon is much less than the material bandgap energy. The light passes through the material. This typically happens at longer wavelengths; and the longer the wavelength, the more photonic power is passed through the material. A thin material becomes increasingly transparent at longer wavelengths.

The third reaction in Figure 3.1 is (3), is where the photon energy is absorbed in the material. There are two effects which happen when photons are absorbed in a material. The first effect is the production an electron-hole pairs, and happens when the wavelength energy level of the photon matches or exceeds the bandgap energy of the material. The second effect is when the wavelength energy level of the photons exceeds the bandgap energy of the material. This causes a photonic interaction with the atoms that generates heat in the material. This is the effect we are looking for in an optothermal actuator. A laser used to produce optimal thermal power has to have a wavelength (λ) with its associated photon energy far enough above the bandgap energy level of the material to produce absorption with heat generation in the actuator.
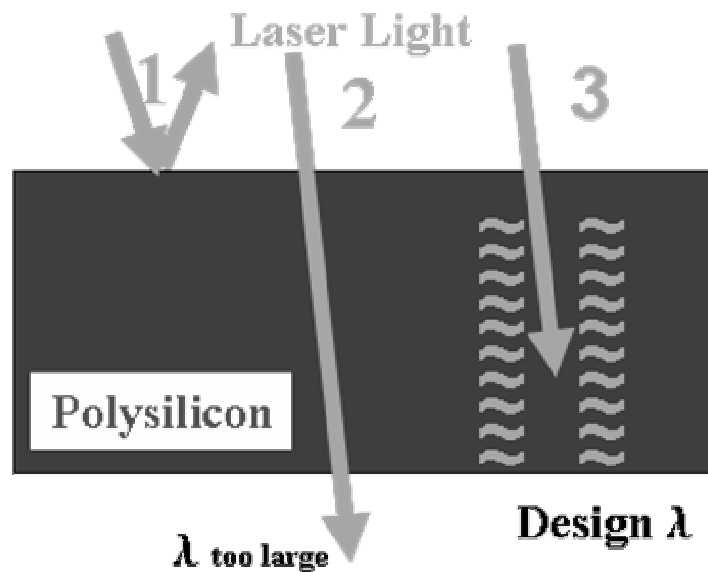
Figure 3.1: Illustration depicting the three reactions to light impinging on a semiconductor.
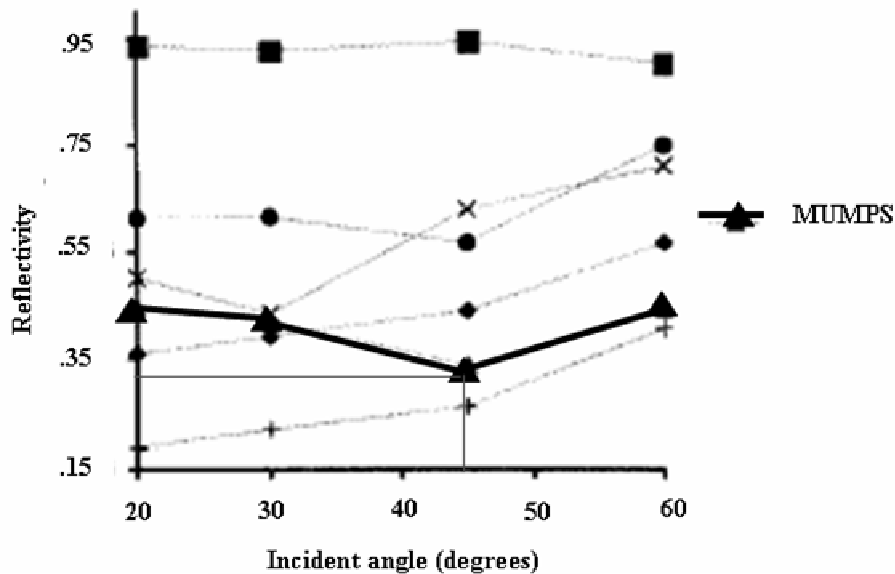
Figure 3.2: Plot of the reflectivity of PolyMUMPs polysilicon versus laser beam incident angle, with a wavelength of .6328μm [1].

3.2. Parameters for Reflectivity and Absorption

In designing a laser actuator, there are several optical-material parameters that must be considered in choosing a proper wavelength of laser to match the materials used in the actuator.

Figure 3.3 is a plot of the relationship between photon energy and wavelength versus light penetration depth and the absorption coefficient for several materials [2]. Figure 3.4 is a plot from a different source and with different materials, showing the relationship between photon energy and wavelength versus the absorption coefficient [4]. As seen in Figure 3.3 and Figure 3.4, each material reacts differently to different wavelengths of light. Since published absorption parameters for heavily phosphorous-doped polysilicon were not available, approximations were made using the values for silicon. As can be seen from Figure 3.3 and Figure 3.4, there are differences in curves between amorphous Silicon (a-Si) and crystal silicon (Si), so these parameter estimates may be very rough approximations.

The PolyMUMPs process limits actuator heating arms to three thicknesses, 1.5 μm, 2 μm and 3.5 μm [6]. So a critical optical design material parameter that needs to be considered is the depth of light penetration into the silicon. As seen in Figure 3.3, these properties are closely related to the photon wavelength energy. The shorter the wavelength, the shallower the light penetrates into the material. If the wavelength is too long, it penetrates too deeply and the energy will pass through 2 μm actuator without producing significant amounts of heat energy, and will heat the substrate, not the actuator. If the penetration is too shallow, the heat will be too high on the top surface of the actuator, causing it too warp out of plane. The Y-axis in Figures 3.3 and 3.4 is on a logarithmic scale. From this plot, the wavelength needed for 2 µm of penetration into crystalline silicon is approximately 0.66 µm. The critical bandgap energy matching wavelength that must be exceeded, in order to generate heat, is labeled λ_C in Figure 3.3
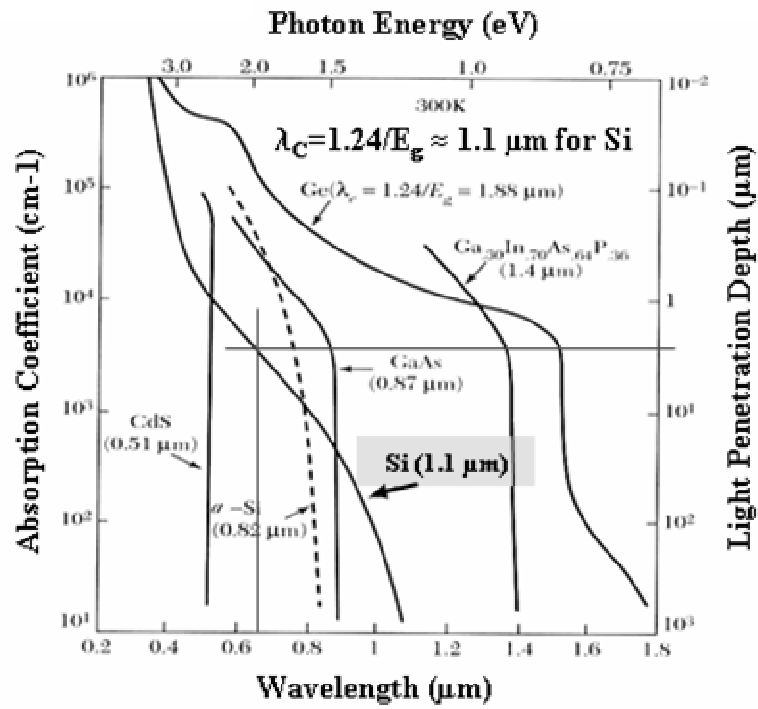
Figure 3.3: Plot of the relationship between photon energy and wavelength versus light penetration depth and the absorption coefficient for several materials [2].
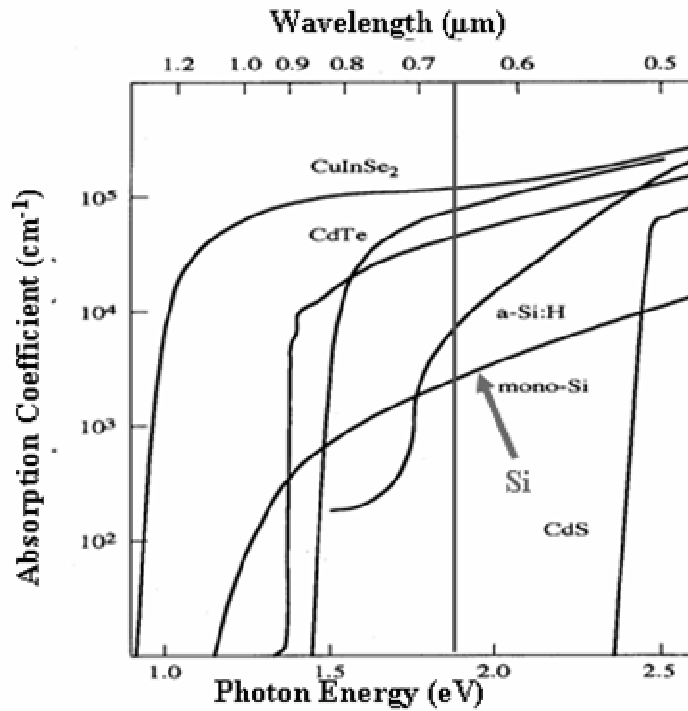
Figure 3.4: Plot of the relationship between photon energy and wavelength versus the absorption coefficient [4].

Another material parameter that is needed is the reflectivity of the gold. It is important that a wavelength be chosen where gold has a high reflectivity, because gold is being used as a shield. The trade-off in determining the required light wavelength will be between a very high reflectivity of gold, and an acceptable depth of light penetration in polysilicon.

The values for the reflectivity of gold were obtained from a table on page 25.15 in the Handbook of Optics, Volume II [7]. Figure 3.5 is a plot for the reflectivity of gold at normal incidence, as a function of wavelength, with a value of 94.5% reflectivity at $\lambda = 0.66\,\mu$m. Figure 3.6 is a plot which shows depth of light penetration into silicon as a function of wavelength, with $2\,\mu$m depth penetration at $\lambda = .66\,\mu$m [2], [4]. The values for light penetration into silicon for Figure 3.6 were approximated from the chart in Figure 3.3, above. The values were then plotted in order to compare them to the gold reflectivity. The two plots in Figure 3.5 and Figure 3.6 show that at a wavelength of 0.66 μm, the reflectivity of gold is 94.5 percent, while the absorption depth for silicon is approximately the desired 2 μm depth. The use of any wavelengths of light less than 0.6 μm will cause a dramatic drop in the reflectivity of the gold. This means that the gold would be absorbing more of the incident energy. Since the purpose of the gold is to shield the devices that should not be heated, this is undesirable. Wavelengths longer than 0.7 μm will cause too much of the energy to pass through the actuator and be absorbed in whatever material is under the actuator.

The final wavelength that was chosen was 0.66 μm, because this wavelength of laser diode was the only one available with an output power over 20 mW. This gave a gold reflectivity of around 95% and a light penetration depth in silicon of around 2.3 μm. Since the final design for the actuators was chosen as 3.5 μm thick, this wavelength was a very good one. A more ideal one would be closer to $\lambda = 0.70\,\mu$m, which would give a gold reflectivity of 96%

and a light penetration depth in the silicon of 3 µm. However, the absorption coefficient goes down with an increase in light wavelength, which is not desirable, because it reduces the power absorbed by the silicon.
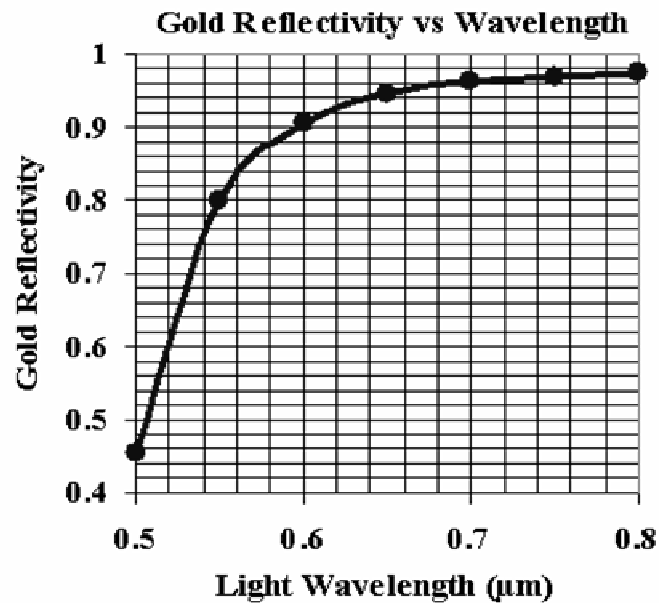
Figure 3.5: Plot showing the reflectivity of gold at normal incidence, as a function of wavelength, with a value of 94.5% reflectivity at $\lambda = 0.66 \, \mu$m.
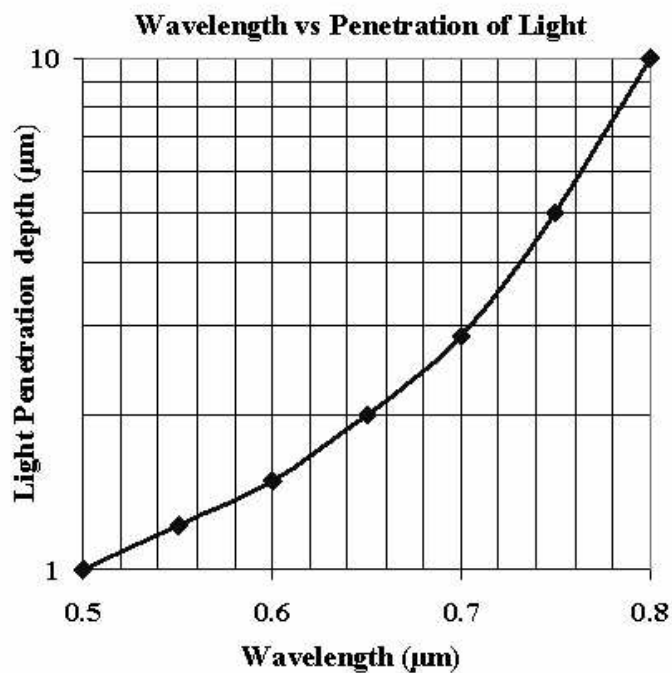
Figure 3.6: Plot showing the depth of light penetration into silicon as a function of wavelength, with 2 μm depth penetration at $\lambda = 0.66 \, \mu$m.

When incident photons interact with atoms, part of the energy produces an electron-hole pair, and part of the energy produces heat. This heat will be used for the thermal expansion of the actuator. Equations 3.1 through 3.5 are the equations needed to calculate the amount of energy that will become heat, and are fractions of the incident energy of the laser. These equations were used to create the plots in Figure 3.7 and Figure 3.8. The photon energy (in Joules) of the incident light is

$$E = hc/\lambda \tag{3.1}$$

where h is Planck's constant, c is the speed of light, and λ is the wavelength of the light. This equation can be restated in terms of energy in electron-volts in the following equation,

$$E\,(eV) \approx 1.24/\lambda \quad (\lambda \text{ in } \mu m) \tag{3.2}$$

The photon power passing into the polysilicon (not reflected) is,

$$P_{li} = P_i\,(1\text{-}R) \tag{3.3}$$

where P_{li} is the power of the incident light beam that is not reflected, P_i is the power of the incident light beam, and R is the reflection coefficient, which, from Figure 3.2 is 0.3. The photon power absorbed by the polysilicon (not reflected or passed through) is,

$$P_{abs} = P_{li}\,(1\text{-}e^{-(\alpha t)}) \tag{3.4}$$

where P_{abs} is the power absorbed, α is the absorption coefficient, which is a function of wavelength, and t is the thickness of the material. The portion of the power absorbed that actually generates heat instead of electron hole pairs is,

$$P_h = P_{abs}\,((hv - E_g)\,/\,hv) \tag{3.5}$$

where P_h is the portion of power turned into heat, hv is the energy of the photon in electron-volts, and E_g is the bandgap of the material [2].

Figure 3.7 is a pair of plots which show the silicon absorption coefficient (a) and the

power absorbed (b) as a function of wavelength. Below is an example problem using 10 mW of incident power, in order to illustrate how much heating power is generated, versus initial incident power. The photon energy level (*hv*) is approximately 2.0 eV at $\lambda = 0.66\ \mu$m and exceeds the bandgap energy of silicon (1.12 eV), which will induce heat generation. The values for the absorption coefficient for silicon in Figure 3.7 (a) were approximated from the plot in Figure 3.3, above [2]. Equation 3.3, gives the amount of incident photon power which is absorbed by the silicon. This is plotted in Figure 3.7 (b) (using a penetration depth of 2 μm in silicon and an incident laser power of 10 mW). At $\lambda = 0.66\ \mu$m, 6.3 mW is absorbed into the silicon out of the 10 mW incident power.

Equation 3.4 gives the portion of absorbed photon power that actually generates heat. Figure 3.8 is a plot of the calculated power absorbed and converted to heat in silicon as a function of wavelength; 2.6 mW is used to produce heat (with 10 mw incident) at $\lambda = 0.66\ \mu$m. These plots were made from data obtained from plots and the equations used by Sze [2].
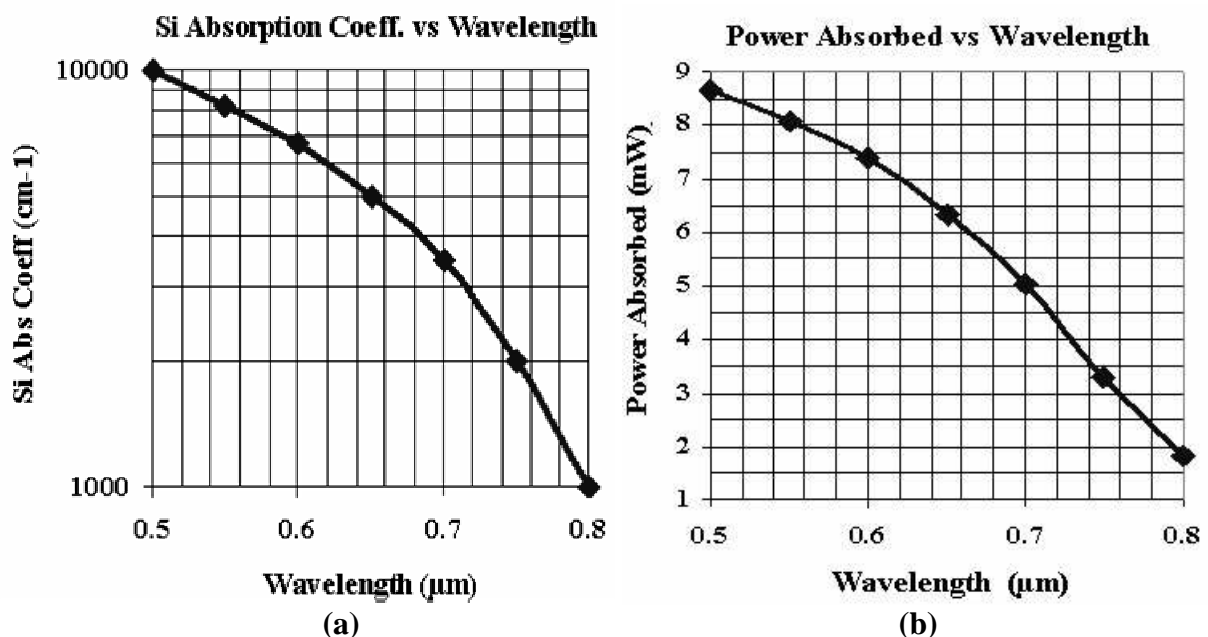
Figure 3.7: Plots showing the silicon absorption coefficient (a) and the power absorbed (b) as a function of wavelength.
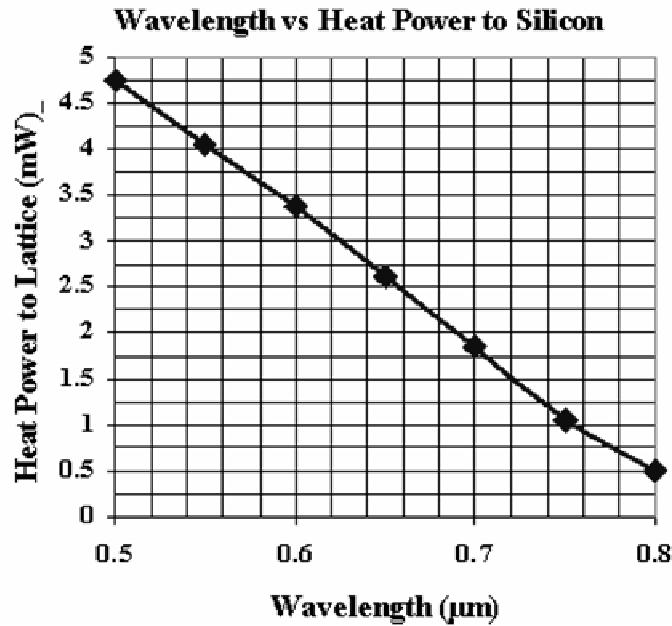
Figure 3.8: Plot of the calculated power absorbed and converted to heat in silicon as a function of wavelength; 2.6 mW is used to produce heat (with 10 mw incident) at $\lambda = 0.66\,\mu$m.

To examine the tradeoff in power absorbed versus reflectivity, Figure 3.5 and Figure 3.8 are compared. At $\lambda = 0.60\,\mu$m, 3.4 mW is absorbed as heat into the silicon, out of the 10 mW incident power, but the gold reflectivity is down to 90.5%. At $\lambda = 0.70\,\mu$m, only 1.85 mW out of the 10 mW incident power is absorbed as heat, but the gold reflectivity is up to 96.4%. The choice of wavelength depends on how much gold reflectivity can be sacrificed for increased heating efficiency.

3.3. Required Laser Power

To find out how close these approximated theoretical values compare to the values for the actual PolyMUMPs materials, and determine the power required, the theoretical values were compared to values obtained by Burns when he was testing PolyMUMPs fabricated MEMS mirrors for laser damage and temperature damage [9] - [11].

Burns observed damages to gold plated PolyMUMPs mirrors at temperatures of 225 ^{0}C to

280 ^{0}C, with an incident laser power of between 4.5 mW and 12 mW. He used a He-Ne laser with a λ of 0.6328 μm. He measured PolyMUMPs gold reflectivity at 91.5%, slightly below the values for gold obtained from the Handbook of Optics, which gave an approximate value of 93.5% at λ = 0.6328 μm [7]. The maximum temperature which Burns gives as 225 ^{0}C (498 K), is the temperature at which the PolyMUMPs gold starts to slightly deform and lose its reflectivity. The loss became more apparent at 250 ^{0}C (523 K), causing a 25% loss in the reflectivity of the gold (which would be disastrous if the gold is being used to shield devices from heat). This loss of reflectivity leads to greater absorption of power by the gold and catastrophic device failure. Early in my research I estimated that the actuators could be heated to a temperature of 300 ^{0}C (573 K), closer to the Au/Si eutectic bonding temperature of 363 ^{0}C [12], but this may not be possible. One of the reasons Burns gives for this the loss of reflectivity of gold at temperatures lower than the eutectic bonding temperature is that the PolyMUMPs polysilicon is heavily doped with phosphorus (10^{20} cm^{-3}), which sublimates out of the polysilicon at around 280 ^{0}C [11], [12]. Also, there is a thin adhesion layer of chromium under the gold [6]. One or both of these may combine with the start of eutectic bonding to ruin the reflectivity of gold and well below the eutectic temperature for normal crystal silicon and gold.

Burns found that the maximum calculated incident power he could use (from his equations), with his maximum temperature set to 225 ^{0}C, depending on the geometry of the mirrors he tested, ranged from 4.25 mW to 7.49 mW [9] - [11]. Figure 3.9 is a pair of SEM micrographs from Burn's paper depicting laser damage to PolyMUMPs gold mirrors at the low power level of (a) 12.35 mW and (b) 9.35 mW.

A measure which Burns left out, but which will be more important for this research's design of optothermal actuators than for mirrors, is the reflectivity of the polysilicon. A more

complex model will need to be built to allow for this factor. Another factor that must be taken into account is Burns used a continuous wave (CW) mode for his laser, whereas tests of this research's designs will experiment with pulsed modes and duty cycles. The pulsed modes are needed because our object is the thermal expansion and contraction of the actuators. Pulsed modes may allow higher power use. Also, Burns' tests were conducted in a vacuum; while this research's tests will be conducted in normal atmosphere. Another problem, which led to an overestimation of heating power of the laser, was that Burns did not mention laser beam size, or power per area. Because this factor was not taken into account early in this research, designs were used which counted on large laser beam dot sizes, which ended up being impossible to use, due to lack of power per area. This is important because the exposed actuators take up very little of the actual surface area where the laser beam is aimed at. So a large percentage of the power is wasted on bare substrate. Also, Burn's did not mention the power profile of the beam, which will be important, as most focused beams have a Gaussian power distribution, with more power at the center and less power near the edges of the beam.

(a)   **(b)**
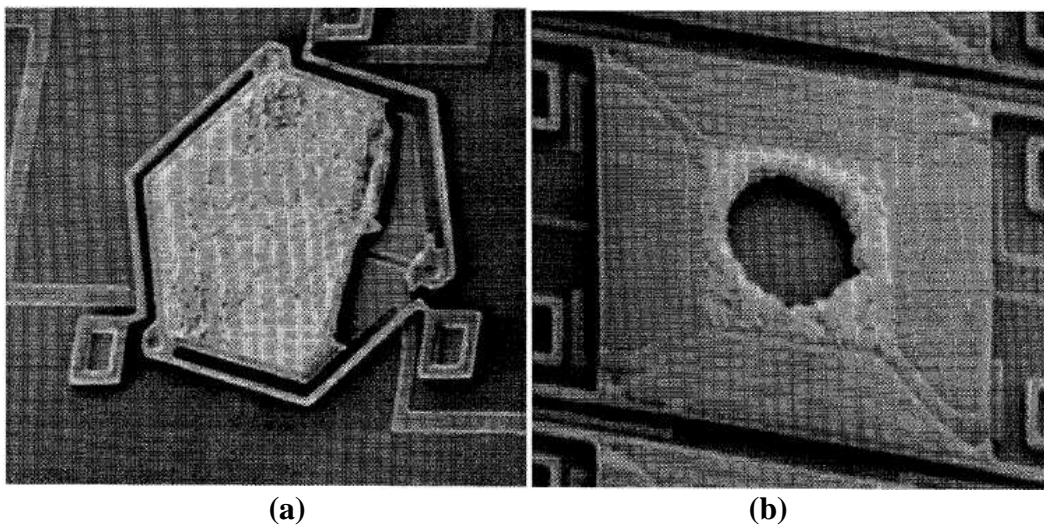
Figure 3.9: SEM micrographs from Burn's paper depicting laser damage to PolyMUMPs gold mirrors at low power level of (a) 12.35 mW and (b) 9.35 mW [7].

3.4. Conclusion

In this chapter a brief description was given of the different reactions of a material to light hitting a surface at an angle. The trade-off in parameters for reflectivity and absorption were discussed. The literature that the required laser power was chosen from was briefly reviewed.

The topic of power per area and beam dot size will be covered extensively in Chapter 5 on modeling. In the next chapter on design, the type of actuators chosen, the chevron actuator, will be discussed. The reason chevron actuators were chosen is that they provide the most concentrated surface area for laser absorption and power generation. The next chapter shows how the knowledge gained reviewing laser light absorption in this chapter was used in designing the optothermal actuators. The key concepts will be actuator thickness and the amount of actuator surface area that can be placed in a small area to absorb the most laser power.

3.5. Bibliography

[1] J. Zou, M. Balberg, C. Byrne, C. Liu, and D. J. Brady, "Optical Properties of Surface Micromachined Mirrors with Etch Holes" *Journal of Microelectromechanical Systems*, vol. 8, no. 4, 1999.

[2] S. M. Sze, *Semiconductor Devices, Physics and Technology*, New York, John Wiley & Sons Inc., 2002.

[3] S. M. Sze, *Physics of Semiconductor Devices*, New York, John Wiley & Sons Inc., 1981.

[4] H. J. Moller, *Semiconductors For Solar Cells*, Boston: Artech House, 1993.

[5] E. Hecht, *Optics, Fourth Edition,* San Francisco, Addison Wesley, 2002.

[6] D. Koester, A. Cowen, R. Mahadevan, B. Hardy, *PolyMUMPs Design Handbook, a MUMPs® process,* Revision 10.0, MEMSCAP, http://www.memscap.com/memsrus/docs/polymumps.dr.v10.pdf, 2003.

[7] J. A. King, *Materials Handbook for Hybrid Microelectronics*, Artech House, London, UK, 1988.

[8] M. Bass, *Handbook of Optics, Volume II, Devices, Measurements, and Properties,* New York, McGraw Hill, 1995.

[9] W. D. Cowan, *Foundry Microfabrication of Deformable Mirrors for Adaptive Optics*, Doctoral Dissertation, Air Force Institute of Technology, 1998.

[10] D. M. Burns and V. M. Bright, "Investigation of the Maximum Optical Power Rating for a Micro-Elctro-Mechnical Device", *International Conference on Solid State Sensors and Actuators*, pp. 335-338, 1997.

[11] D. M. Burns, *Microelectricalmechanical Optical Beam Steering Systems*, Doctoral Dissertation, Air Force Institute of Technology, 1998.

[12] Y. T. Cheng, L. Liwei, N. Khalil, "Localized Silicon Fusion and Eutectic Bonding for MEMS Fabrication and Packaging", *Journal of Microelectromechanical Systems*, vol. 9, no. 1, pp. 4-14, March 2000.

4. Device Design

This chapter discusses the designs for optothermal test actuators and laser microrobot designs based on optothermal actuators. The last chapter discussed laser heating theory and laser light absorption in a semiconductor material. The amount of power used in heat generation was found to be a small fraction of the incident power, ranging from 26% at $\lambda = .66\,\mu$m to 18.5% at $\lambda = .70\,\mu$m. The key concepts in capturing this power were actuator thickness and the amount of actuator surface area thatcan be placed in a small area to absorb the most laser power.

The designs in this research were all developed in L-Edit layout design software [1]. They were designed for fabrication with the MEMSCAP PolyMUMPs process [2]. The results are presented in Chapter 7 for the devices that were fabricated and tested. The tested devices came from PolyMUMPs runs 57 and 58 as shown in Appendix A, Figures A.1 through A.14.

Section 4.1 briefly discusses the PolyMUMPs design process. Section 4.2 explains the designs used for the optothermal tests actuators. Section 4.3 discusses the details of the basic wireless laser microrobot designs used in this thesis. Section 4.4 introduces alternate microrobot designs based on the same basic principles discussed in Section 4.3. All design equations are included in Chapter 5, on device modeling.

4.1. PolyMUMPs Design Process

The fabrication process that will be used with the designs presented in this research will be the Polysilicon Multi-User MEMS Processes or PolyMUMPs, which is a form of surface micromachining with sacrificial layers [2]. Figure 4.1 is an illustration of the layers in the PolyMUMPs process; Poly1 and Poly2 are the two releasable layers. Figure 4.1 also shows the thickness of the structural layers. Figure 4.2 is an illustration of the fabrication and release of the

layers in the PolyMUMPs process, with (a) depicting all the deposition and etching completed at the foundry, and (b) depicting the release of oxide layers in post processing performed by the user. Figure 4.2 shows the structural and releasable layers fabricated by the layering of silicon and silicon oxide. The oxide is the sacrificial layer, which is etched away with 49% HF acid as shown in Figure 4.2 (b). The PolyMUMPs process from MEMSCAP provides two releasable layers. MEMSCAP PolyMUMPs uses eight lithography masks and uses seven material layers, with the last metal layer actually consisting of two metals, one to provide adhesion, and one of gold.

Figure 4.3 is a scanning electron microscope (SEM) micrograph of fabricated and released PolyMUMPs layers. It shows an example of how the layers appear after fabrication and release. Table 4.1, PolyMUMPs Layout Design Specifications, lists the various the PolyMUMPs layer thicknesses and layout design specifications and limitations. The first column lists the design layer names and the second column lists the material layer names. The third column lists the layer thicknesses. The last three columns list the design limitations such as the minimum feature size and spacing

	Poly0		Poly1		Poly2		Metal
	Nitride		1st Oxide		2nd Oxide		
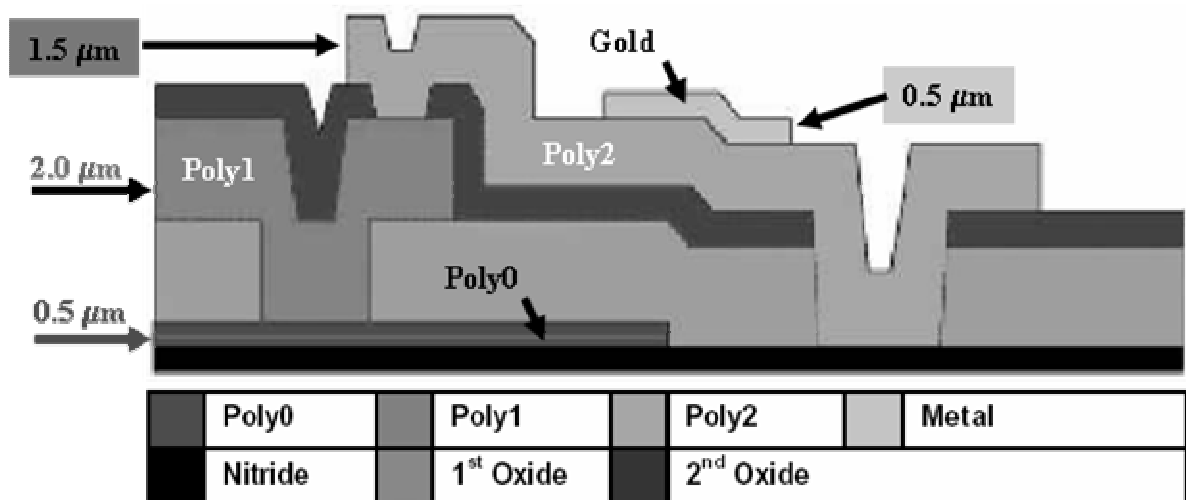
Figure 4.1: Illustration of the layers in the PolyMUMPs process; Poly1 and Poly2 are the two releasable layers [2].

(a)

(b)
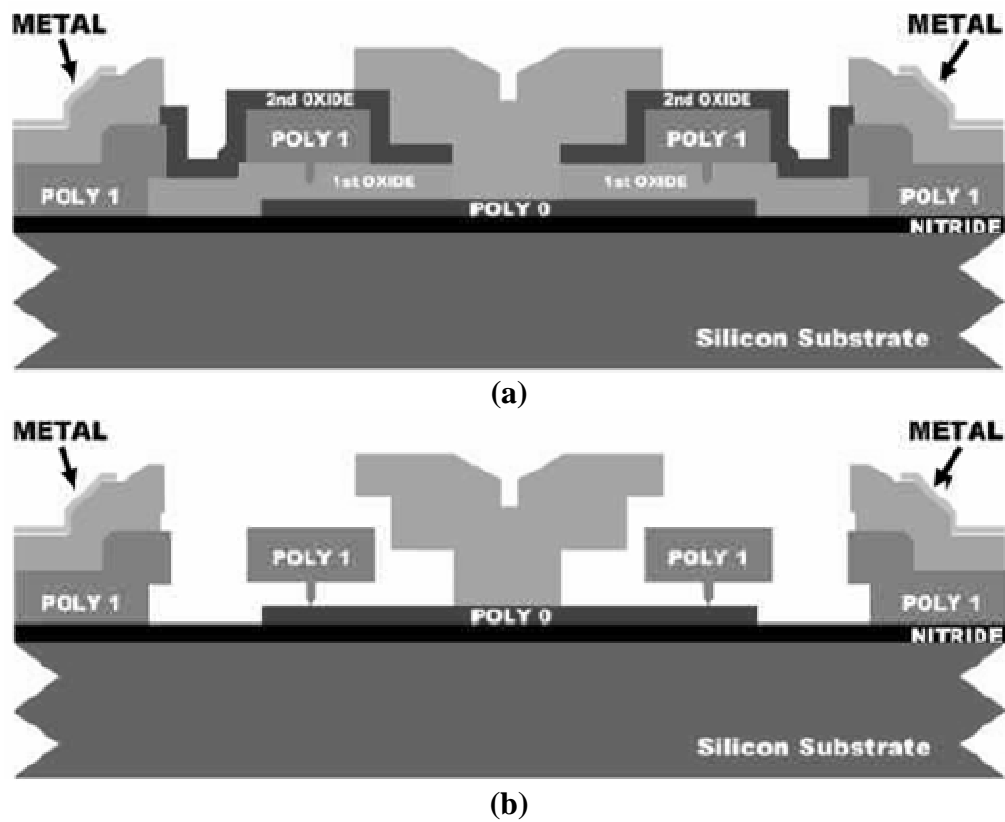
Figure 4.2: Illustration of the fabrication and release of the layers in the PolyMUMPs process, with (a) depicting all the deposition and etching completed at the foundry, and (b) depicting the release of oxide layers in post processing performed by the user [2].
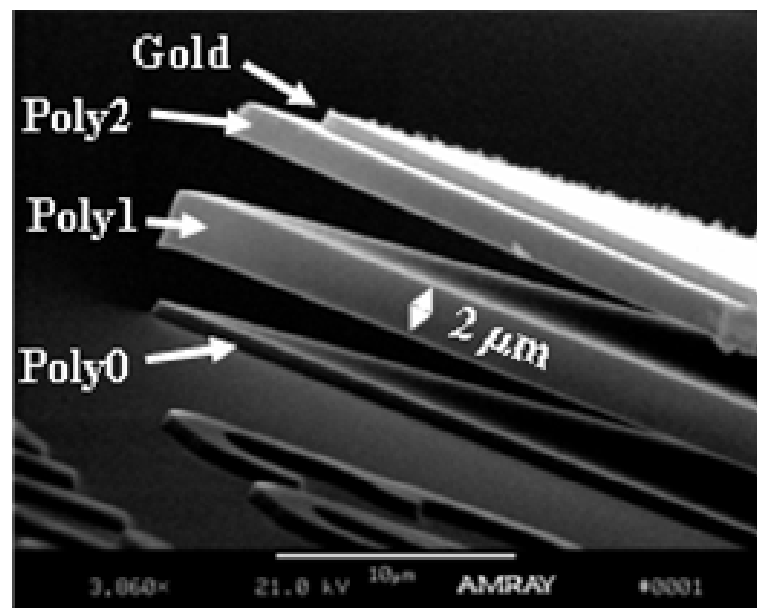
Figure 4.3: SEM micrograph of fabricated and released PolyMUMPs layers.

Table 4.1: PolyMUMPs Layout Design Specifications.

Mnemonic level name	Material Layer	Material Thickness (μm)	Nominal line/space (μm)	Minimum Feature size (μm)	Minimum Object Spacing (μm)
NITRIDE	Nitride	0.6			
POLY0	Poly 0	0.5	3.0	2.0	2.0
(Sacrificial Layer)	First Oxide	2.0			
ANCHOR1			3.0	3.0	2.0
DIMPLE			3.0	2.0	3.0
POLY1	Poly 1	2.0	3.0	2.0	2.0 / 2.25
(Sacrificial Layer)	Second Oxide	0.75			
POLY1_POLY2_VIA			3.0	2.0	2.0
ANCHOR2			3.0	3.0	2.0
POLY2	Poly 2	1.5	3.0	2.0	2.0 / 2.251
METAL	Metal	0.5	3.0	3.0	3.0
HOLE0			3.0	2.0	2.0
HOLE1			4.0	3.0	3.0
HOLE2			4.0	3.0	3.0
Note: Compiled from Tables 2.1, 2.2, and 2.3 in PolyMUMPs Manual [2]					

4.2. Test Actuators

After researching numerous actuators based on thermal expansion principles, the chevron or bent buckle actuators were chosen, because their geometry of close packed thermal arms allows the most surface area for laser absorption with a small beam size [3]. Figure 4.4 is an illustration of two thermal actuators showing how much actuator surface area can be placed under the laser beam; where (a) is a bent beam or chevron thermal actuator and (b) is a double hot arm actuator. In both of these actuators, the hot arm(s) is the heated beam(s) which has expansion that is used for actuation. Figure 4.4 illustrates this concept of packing the most actuator surface area under the laser beam as possible. Figure 4.4 (a) shows four arms fitting under the laser dot, and this number is expandable. A chevron actuator with as many as 16 arms was successfully tested in this research. Figure 4.4 (b) shows that the double hot arm actuator can only fit two thermal arms under a small concentrated beam. Figure 4.4 (a) also illustrates the size nomenclature that will be used throughout this research. A 250 µm chevron actuator will

refer to the length of the beams on one side of the actuator. The actual physical size of the

actuator will vary and will be both sides added together, plus the size of the center piece.

(a)   **(b)**
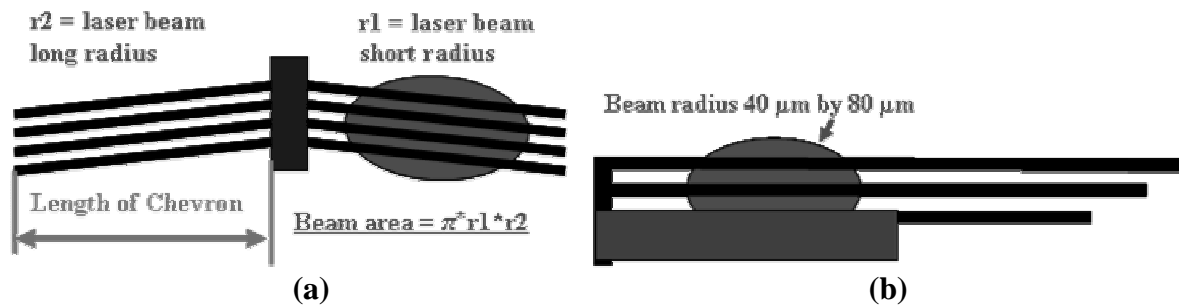
Figure 4.4: Illustration of two thermal actuators showing how much actuator surface area can be placed under the laser beam; where (a) is a bent beam or chevron thermal actuator and (b) is a double hot arm actuator.

Figure 4.5 is an illustration of how thermal expansion causes chevron or bent beam

thermal actuators to operate [3] - [9]. In their traditional use, chevron actuators have thermal

expansion induced electrically by resistive heating, similar to that used for light bulb filaments.

This heating causes thermal expansion, the useful part which is along the length of the beam

(long arrows). The expansion of the two opposing sets of beams causes the beams to bend and

buckle (curling arrows), translating into rectilinear actuation (thick arrow pointing up).
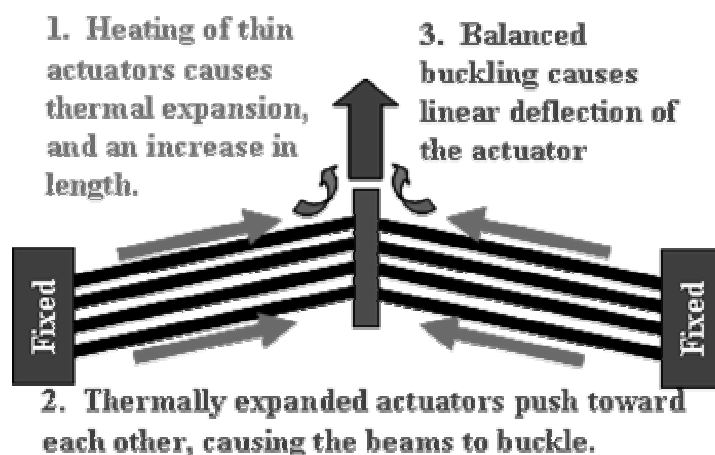
Figure 4.5: Illustration of how thermal expansion causes chevron or bent beam thermal actuators to operate.

This research induced thermal expansion by laser energy absorption. Figure 4.6 is an illustration depicting laser beam heating schemes; with (a) being the original large dot scheme and (b) being the final asymmetric scheme with small elliptical dot. The final scheme was chosen because of the increased power per area imparted to the actuator. The idea for using a laser to power an actuator for a microrobot was proposed by Baglio, [10] - [13], but was developed in a different way in this research. Baglio used MEMS lenses on his devices to filter and concentrate laser power on one end of a bimorph cantilever. This research used only a single material asymmetric actuator, with a laser shining directly on as much surface area of it as possible.

Since laser energy is proportional to the square of the radius of the beam, the smaller the beam radius, the more power can be induced into the actuators. Any part of the laser beam landing on open areas (anywhere but on the beams intended for heating) is wasted energy. In Figure 4.6 (a), the areas marked A and B where laser energy is wasted. Figure 4.6 (b) shows the laser illuminating scheme that produced the best heating and the greatest deflection. This asymmetric illumination scheme was used in all the testing and verification experiments.

(a)   **(b)**
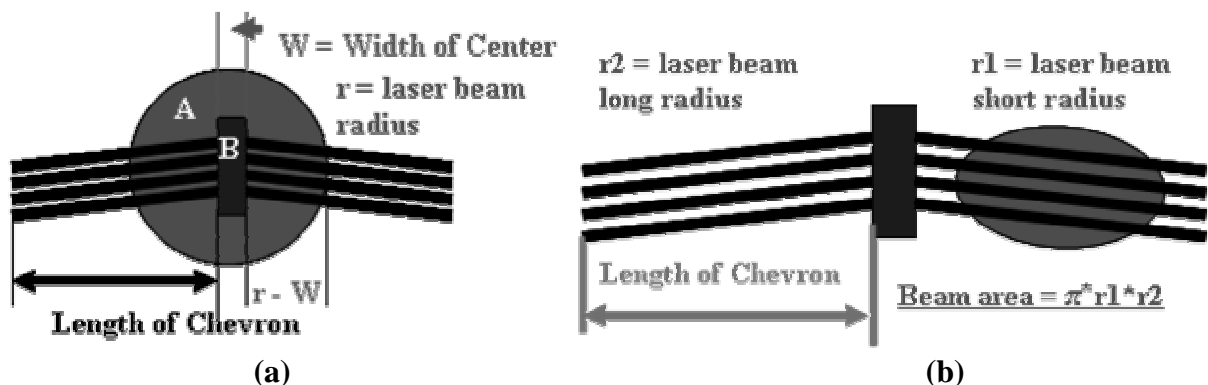
Figure 4.6: Illustration depicting laser beam heating schemes; with (a) being the original large dot scheme and (b) being the final asymmetric scheme with small elliptical dot.

Figure 4.7 is a captured frame from a digital video of a PolyMUMPs 57 chevron test actuator with 250 μm long by 4-beam chevrons used for electrical and laser testing. It displays

the probe pads used to place the probes on for electrical testing on the left. A measuring scale was designed in Poly0 on the substrate, which, along with a Poly1 pointer was designed to measure deflection.
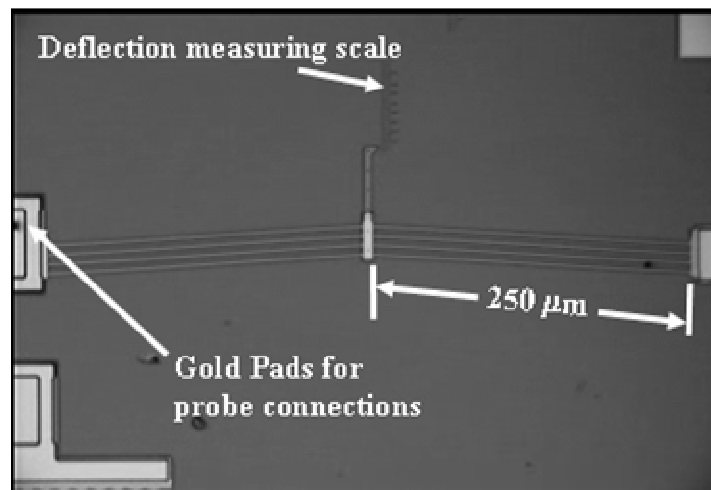
Figure 4.7: Captured frame from a digital video of a fabricated PolyMUMPs 57 chevron test actuator with 250 μm long by 4-beam chevrons used for electrical and laser testing.

4.2.1. Physical Actuator Design Considerations

The more beams the actuators have, the more force they can produce [3], [9]. However, the more beams there are, the stiffer the actuator is and the more power is required to cause deflection, as will be seen later in the experimental electrical power results of the 16 beam versus the 8 beam actuators. The chevron actuator with the largest deflection, tested in this research, had 8 beams. A 16-beam actuator was also successfully tested. The most successful chevron actuator had beams that were 3.5 μm thick and 2.5 μm wide, and were 2.5 μm apart. Sinclair tested deflection versus the pre-bending angle of his actuators and found that a one degree angle was the optimum pre-bending angle for maximum deflection, without out-of-plane movement [3]. Figure 4.9 is an excerpt from an L-Edit layout design for 4-beam chevron web on a test actuator, showing the physical dimensions. It shows the one degree pre-bending angle that was used on all the chevron actuators in this research. The dimensions for the test and microrobot

actuators are listed in Table 4.2, Electrical and Laser Test Chevron Actuators. The columns show the chevron length, the number of chevrons, the chevron width, the chevron single beam thickness, and the spacing between beams. Notice the spacing reduction between the PolyMUMPs 57 and PolyMUMPs 58 designs. Experiments showed that The PolyMUMPs 57 designs were failures as optothermal actuators. The key to a successful optothermal actuator was densely packed hot arms, providing lots of surface area for the laser energy to absorb.
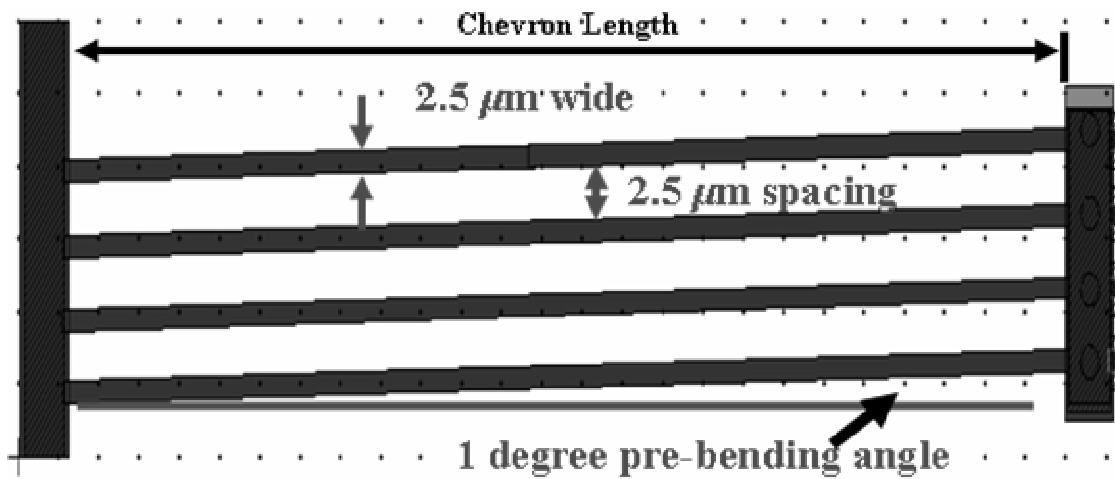
Figure 4.8: Excerpt from an L-Edit layout design for 4-beam chevron web on a test actuator, showing the physical dimensions used on the PolyMUMPs 58 designs.

Table 4.2: Electrical and Laser Test Chevron Actuators.

PolyMUMPs RUN	Chevron Length (μm)	Number of Chevron Beams	Chevron Width (μm)	Chevron Thickness (μm)	Spacing Between Beams (μm)
M57 (Fig A1.14)	250	4	3	3.5	7
M57 (Fig A1.14)	350	8	3.5	3.5	13
M57 (Fig A1.14)	400	4	4	3.5	6
M58 (Fig A1.12)	250	8	2.5	3.5	2.5
M58 (Fig A1.12)	350	16	2.5	3.5	2.5
M58 (Fig A1.12)	400	8	2.5	3.5	2.5

Figure 4.9: is a series of captured frames from digital videos, showing PolyMUMPs 58 test actuators under laser testing, with (a) 250 μm by 8-beam chevron, (b) showing a 350 μm by 16-beam chevron and (c) showing a 400 μm by 8-beam chevron. These test actuators were

designed to test their response to both electrical and laser actuation, so that deflection and frequency response could be directly compared.
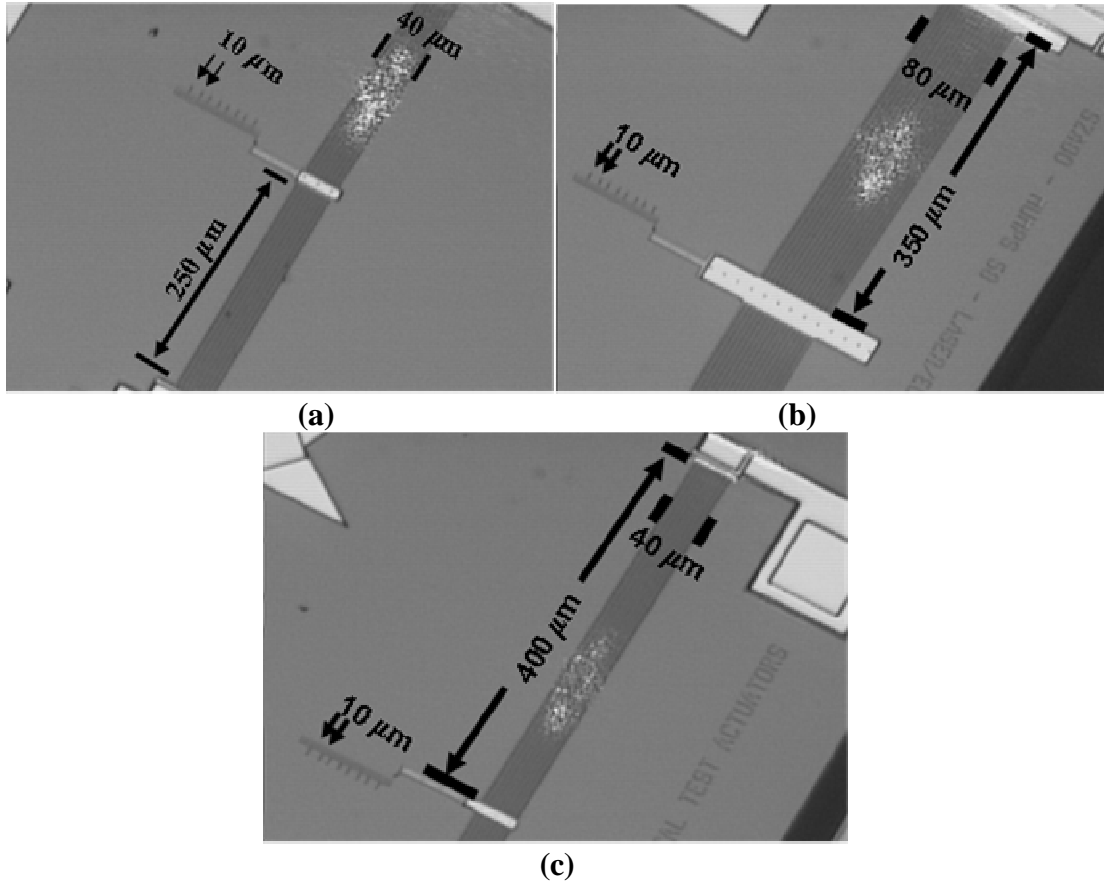
Figure 4.9: Digital photographs, showing PolyMUMPs 58 test actuators under laser testing, with (a) 250 μm by 8-beam chevron, (b) showing a 350 μm by 16-beam chevron and (c) showing a 400 μm by 8-beam chevron.

Figure 4.10 shows two pointers for measuring deflection on test actuators, with (a) being a SEM micrograph and (b) being a digital photo, with the colors reversed in a graphics program for clarity. The deflection scale was laid down on the chip surface in Poly0. The markers were 2 μm wide and 2 μm apart. A longer line was placed every 10 μm. This allowed digital photographs to be taken to measure deflection, as seen in Figure 4.10 (b). The scale is only accurate to at best plus or minus 0.5 μm. The deflection measured in Figure 4.10 (b) would be approximately 16.5 μm. The pointer in Figure 4.10 (b) is from the PolyMUMPs 58 run, and is missing part of its tip, due to a design error.

(a)　　　　　　　　　　　　**(b)**
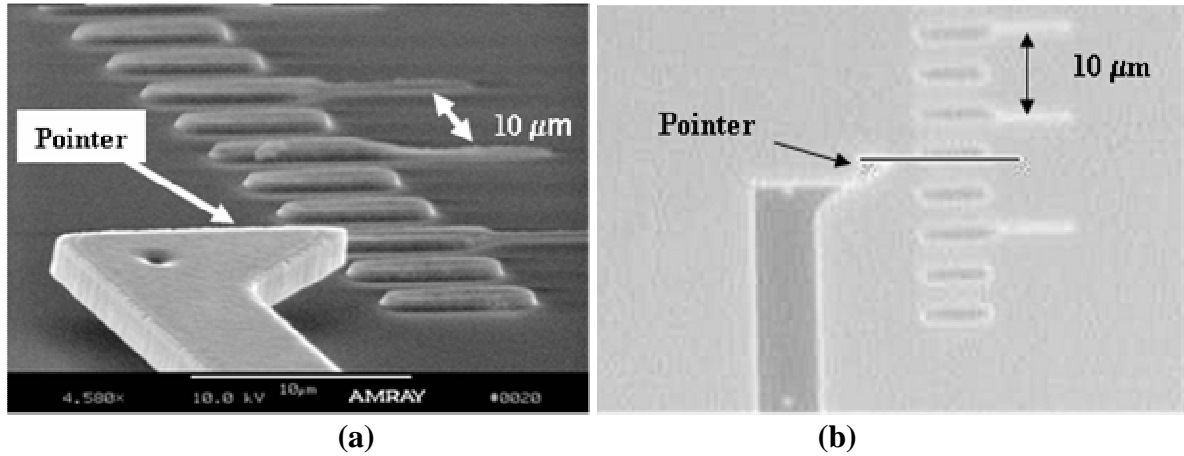
Figure 4.10: Pointers for measuring deflection on test actuators, with (a) being a SEM micrograph and (b) being a digital photo, with the colors reversed in a graphics program for clarity.

4.3. General Wireless Laser Microrobot Design

Figure 4.11 is a digital photograph illustrating the 250 μm by 8-beam chevron laser microrobot and blowups showing its separate parts, with (a) being a SEM micrograph showing the down thermal actuator, and (b) a SEM micrograph showing the chevron beams that are heated for expansion, and (c) and (d) being digital photographs showing the conformal coating driveshaft housings at both ends of the driveshaft. Figure 4.12 shows illustrations taken from L-Edit layouts of the 250 μm by 8-beam chevron laser microrobot, with (a) showing the original laser beam heating scheme, and (b) showing two degrees of freedom movement concept. The main microrobot design used in this research was a 710 μm by 760 μm design shown in Figure 4.11. Some of the innovations introduced during the development of this design are shown in Figure 4.12 (b). These innovations include two degrees of freedom movement and conformally coated drive shafts.

(a)

27 μm

(b)

Gold coating

Housing

Polysilicon drive shaft
12 μm wide

760 μm

(c)

Polysilicon drive shaft
12 μm wide

Housing

Gold coating as a
reflective material

(d)

Chevron
beams

3.5 μm
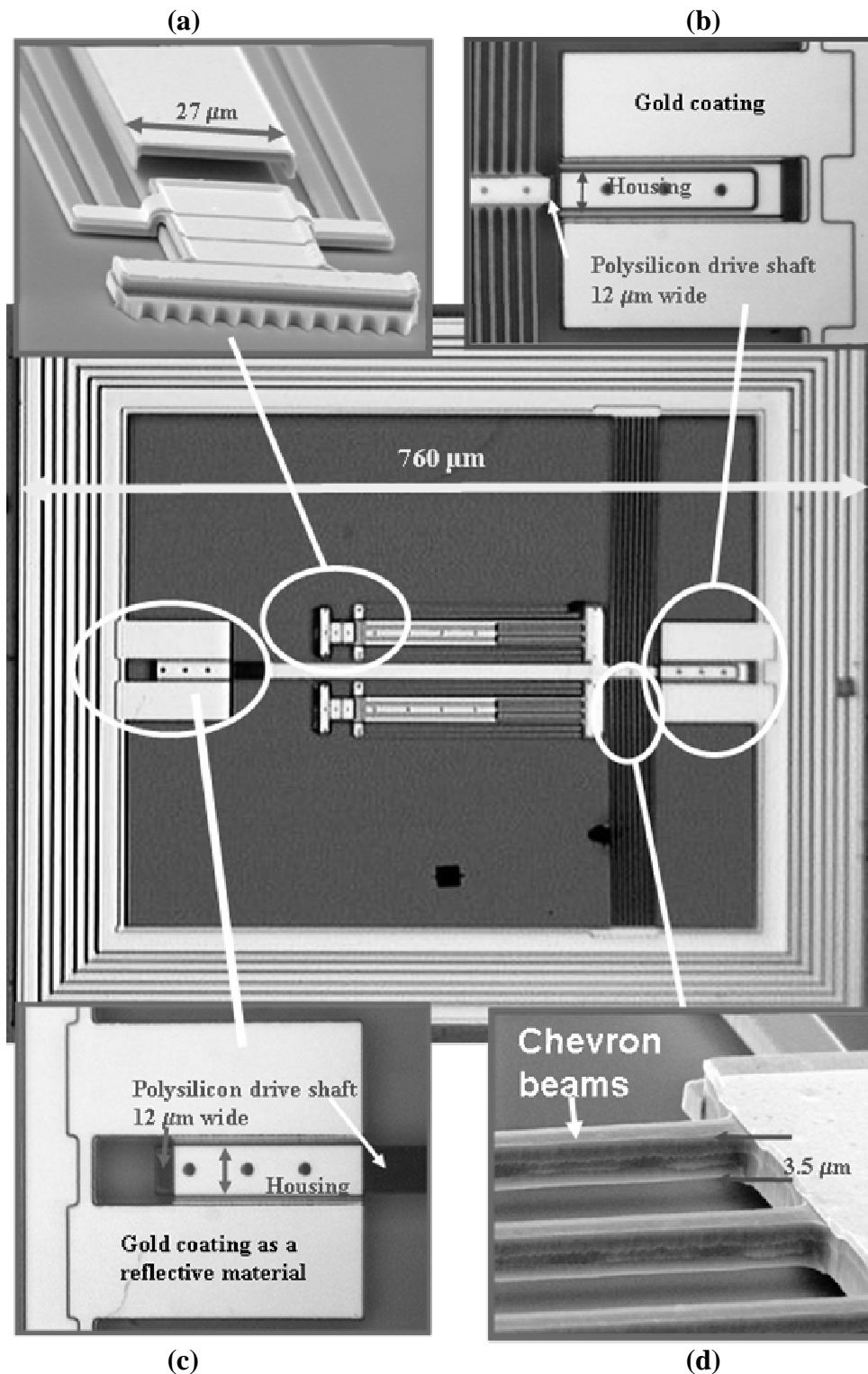
Figure 4.11: Digital photograph illustrating the 250 μm by 8-beam chevron laser microrobot and blowups showing its separate parts, with (a) a SEM micrograph showing the down thermal actuator, and (b) a SEM micrograph showing the chevron beams that are heated for expansion, and (c) and (d) being digital photographs showing the conformal coating driveshaft housings at both ends of the driveshaft.

4.3.1. Multiple Actuators for Multiple Degrees of Freedom

The wireless laser microrobot was designed with 250 μm by 8-beam chevron actuators to provide rectilinear (straight line, parallel to the substrate) motion as seen in Figure 4.12 (b). The two down motion thermal actuators provide a downward movement. These two sets of actuators, when combined together, provide a two-degrees-of-freedom stepping motion. This innovation of using multiple optothermal actuators to give a microrobot multiple degrees of freedom of movement is not easily attainable with electrical activation in a PolyMUMPs fabricated structure. This is because highly doped polysilicon beam structures conduct electricity, causing problems when structural connectivity and electrical isolation are both required. For instance, in Figure 4.12 (a), just the frame around the side would carry most of any current applied, due to its large cross-sectional size and thus low resistance. Very little would take the parallel path through the highly resistive actuators.

(a)	**(b)**
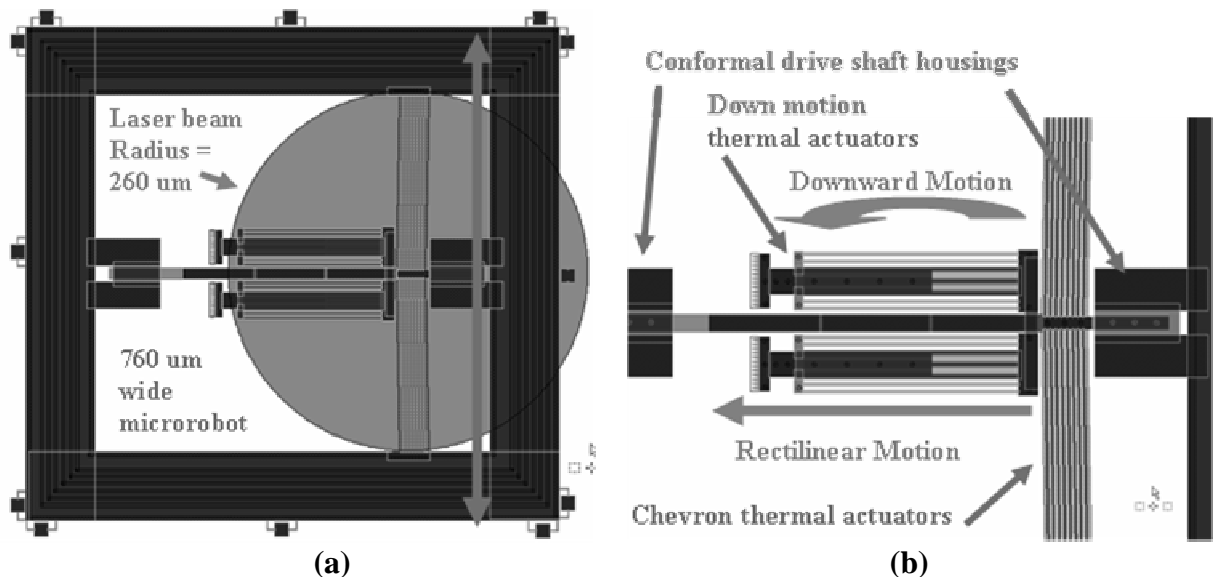
Figure 4.12: Illustrations taken from L-Edit layouts of the 250 μm by 8-beam chevron laser microrobot, with (a) showing the original laser beam heating scheme, and (b) showing two degrees of freedom movement concept.

4.3.2. Conformal Drive Shaft Housings

Another innovation, used on the microrobot prototype, is the use of conformal deposition as a housing for a drive shaft. Figure 4.13 is a SEM micrograph showing the conformal coating drive shaft housing concept. Figure 4.14 shows digital photographs of the conformal coating drive shaft housings used for rectilinear operation, with (a) showing the housing at the base of the shaft and (b) showing the housing at the tip of the shaft. This drive shaft housing ensured rectilinear motion, even with distinctly nonlinear actuation. Because the down thermal actuators provide upward force on the drive shaft, the shaft stays in the housing. The circular holes in the top of the housing ensure the HF acid can properly remove the oxide during the release step, and ensures full freedom of movement for the drive shaft.
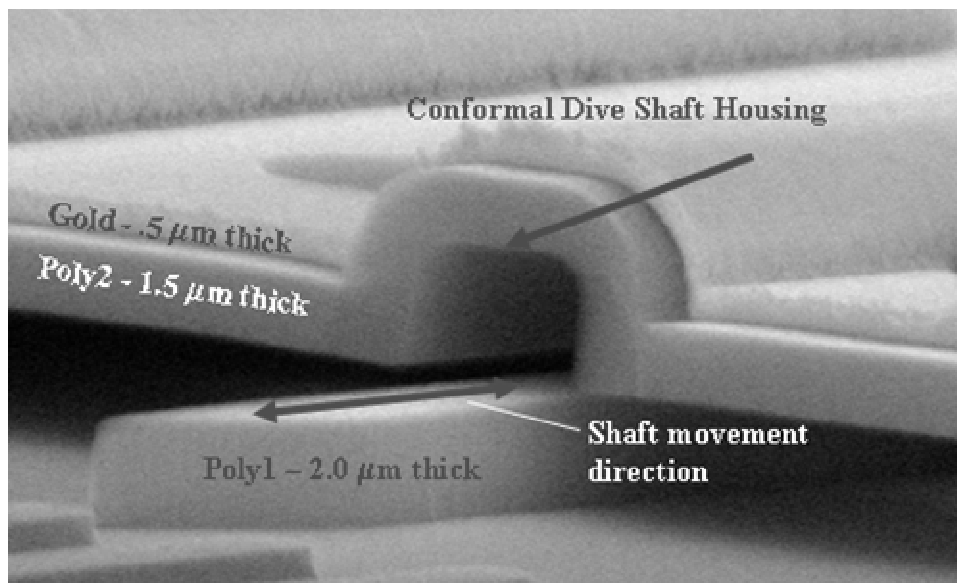
Figure 4.13: SEM micrograph showing the conformal coating drive shaft housing concept.
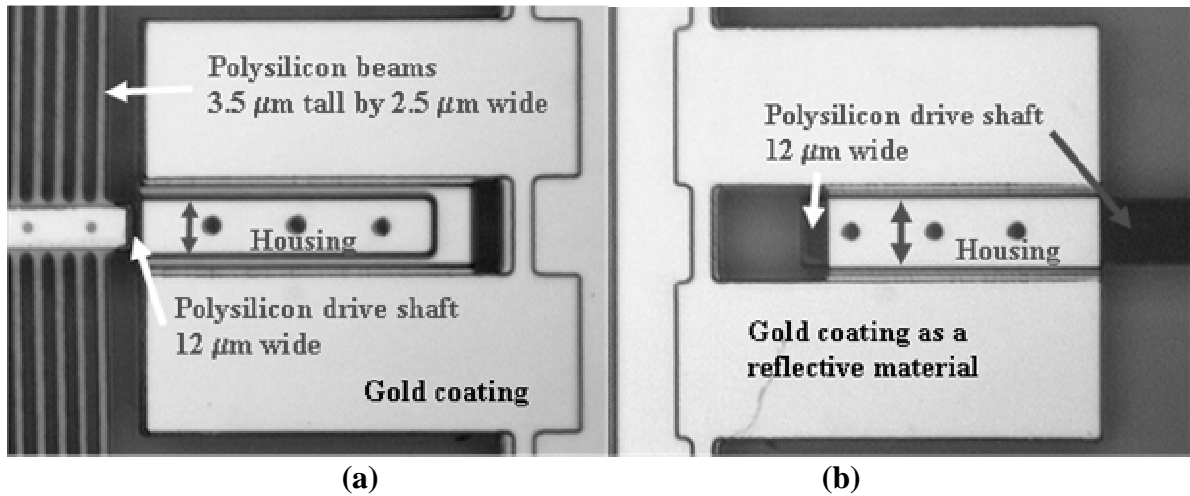
Figure 4.14: Digital photographs of the conformal coating drive shaft housings used for rectilinear operation, with (a) showing the housing at the base of the shaft and (b) showing the housing at the tip of the shaft.

4.3.3. Down Thermal Actuators

The downward optothermal actuator is designed to use a dual downward action. Figure 4.15 is an L-Edit layout design of a downward optothermal actuator with dual action. The standard thermal downward actuator action is provided by the two outside pairs of Poly2 thermal arms. They are 3.5 μm wide by 1.5 μm thick, so when they are heated and expand thermally, they will deflect up (resting position) and down (when heated). The 2 μm thin Poly1 springs at the base allow the actuator to deflect downwards. The second part of the dual downward action is provided by the bimorph thermal action of the gold strips that protect the Poly1 springs from heating. When these bimorphic gold/Poly2 strips are heated, the gold, with its greater coefficient of thermal expansion [14], is designed to bend the whole Poly2 shielding beam down, adding extra force to the downward push of the actuator. So this actuator combines hot arm thermal and bimorph thermal down actuation. The teeth on the end of the feet are all dimpled at the end, so they extend 0.75 μm below the rest of the actuator. This was done so that they would dig into a surface and provide traction for the microrobot. Figure 4.16 shows digital photographs of down

thermal actuators, with (a) showing the dimensions for thermal and spring beams and (b) showing a close-up of the foot. There were two versions of these actuators made, one with 200 μm hot arms that went on the smallest microrobot, the 250 μm by 8-beam chevron wireless laser microrobot. A down thermal actuator with 250 μm hot arms went on the larger microrobot, the 400 μm by 8-beam chevron wireless laser microrobot.
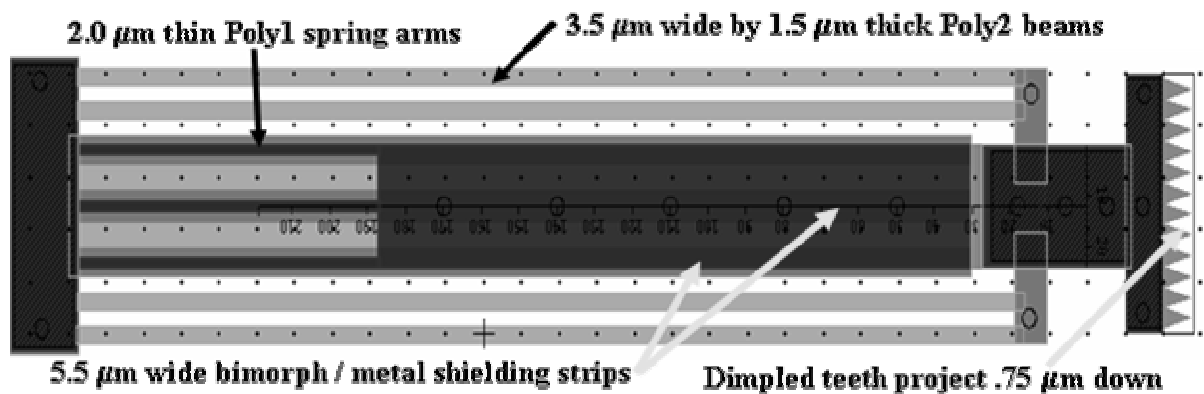
Figure 4.15: L-Edit layout design of a downward optothermal actuator with dual action.
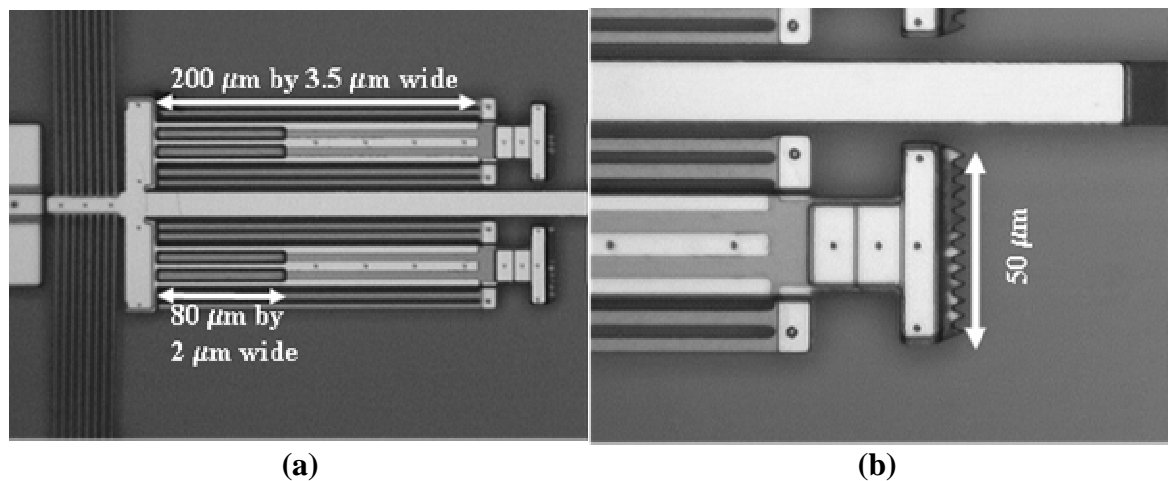
Figure 4.16: Digital photographs of down thermal actuators, with (a) showing the dimensions for thermal and spring beams and (b) showing a close-up of the foot.

4.3.4. The Microrobot Frame

The frame of the microrobot has four layers of material and is 5.5 μm thick. The microrobot is designed to be detached from the substrate, so 5.5 μm is also the thickness of the

entire microrobot. The top layer is gold, to reflect any laser light and stay cool. The next three layers are Poly2, trapped oxide2, and Poly1. The dimpled channels are used for stiffening, in a concept similar to corrugated cardboard. Figure 4.17 shows depictions of the laser microrobot frame, illustrating the corrugation stiffening structure, with (a) being an L-Edit cross-section from the side and (b) being a digital photograph from the top. The frame has a Poly1-Poly2 via only at the edges, but in a manner to provide a seal all the way around, to allow the retention of the trapped oxide during release.

(a)

(b)
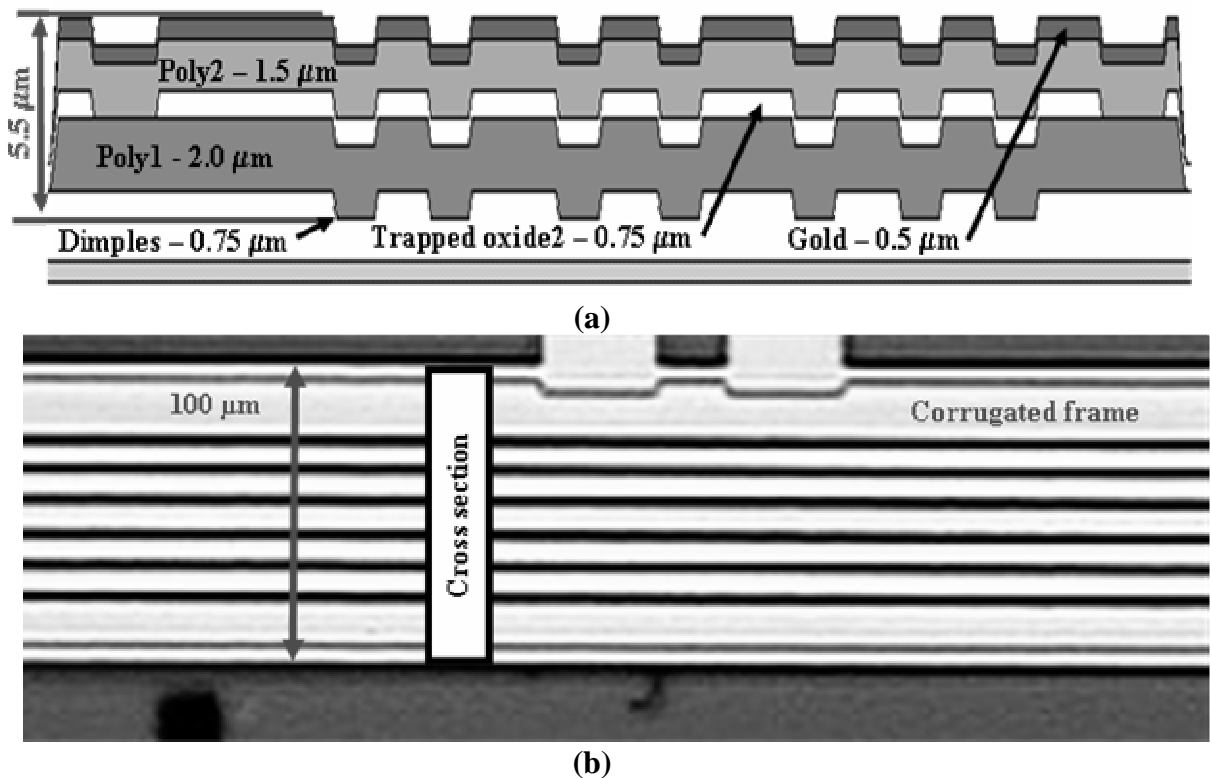
Figure 4.17: Depictions of the laser microrobot frame, illustrating the corrugation stiffening structure, with (a) being an L-Edit cross-section from the side and (b) being a digital photograph from the top.

4.4. Specific Wireless Laser Microrobot Designs

This section will cover the three specific wireless laser microrobot designs based on the general designs in the previous section. The general specifications and name designations for the

prototypes can be found in Table 4.3, PolyMUMPs 58 Prototype Microrobot Designs and Specifications. Other designs were made in the PolyMUMPs 56 and PolyMUMPs 57 fabrication runs, but after experimentation none of them turned out to be workable or realistic. This was because the optothermal actuators did not have densely packed hot arms, and did not provide enough surface area for the laser energy to absorb. However, the designs can be found in Appendix A. Two other PolyMUMPs 58 miscellaneous prototype wireless laser microrobot designs were developed with radically different designs than the those of the previous section. The first was 990 μm by 1120 μm wireless laser microrobots based on a cascaded chevron actuator design. The second was based on double hot arm actuators rather than chevron actuators.

Table 4.3: PolyMUMPs 58 Prototype Microrobot Designs and Specifications.

Prototype Name	Appendix Figure	Overall Size (μm by μm)	Chevron Actuator Length (μm)	Number of Chevron Beams	Down Thermal Actuator Number, Size (μm)	Tested (Y/N)
LR250-8	A1.1	760 by 710	250	8	2, 200	Y, parts only
LR400-8	A1.2	990 by 1120	400	8	2, 250	Y, parts only
LR400-24	A1.3	990 by 1120	400	24	4, 250	N
Cascade-LR400-8	A1.4	990 by 1120	400, 300	8, 4	8, 250	N
Laser Spider	A1.5	1360 by 560	440, Double Hot Arm Actuators	Not Applicable	8, 120	N

4.4.1. LR250-8 Microrobot Design

Figure 4.18 shows digital photographs of the LR250-8 microrobot, with (a) showing the dimensions of the whole microrobot and (b) showing a close-up with the dimensions of down thermal actuator. The left and right down thermal actuators in Figure 4.18 (b) could be actuated separately to provide a means of controlling the direction of the microrobots movement.

(a)　　　　　　　　　　　　　　　**(b)**
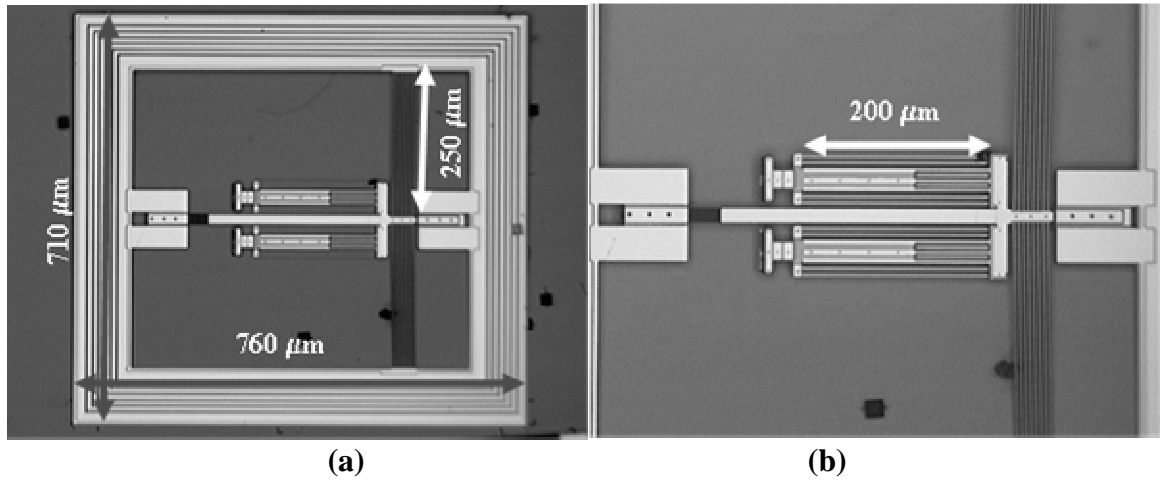
Figure 4.18: Digital photographs of the LR250-8 microrobot, with (a) showing the dimensions of the whole microrobot and (b) showing a close-up with the dimensions of down thermal actuator.

4.4.2. LR400-8 and LR400-24 Microrobot Design

Figure 4.19 shows an L-Edit layout showing the dimensions of the LR400-8 Laser Microrobot. Figure 4.20 shows an L-Edit layout showing the dimensions of the LR400-24 Laser Microrobot. These designs are simply larger versions of the previous design, using longer hot arms on both the chevron and down thermal actuators..
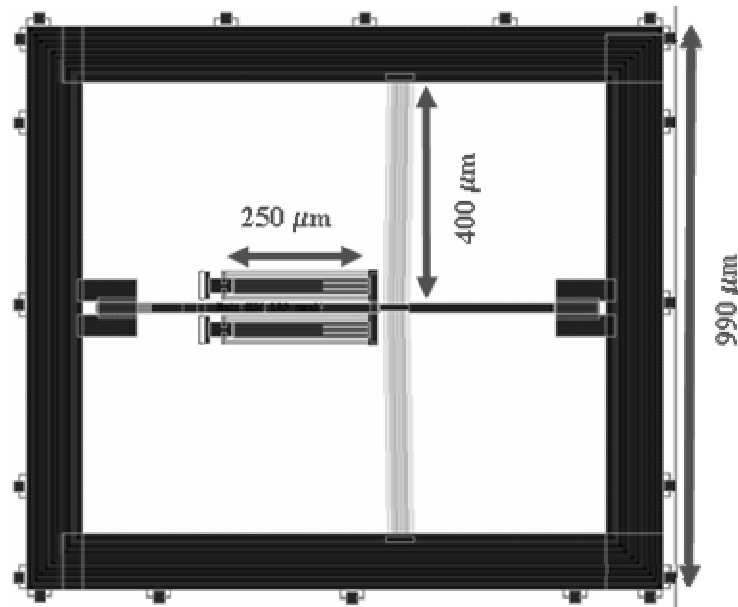
Figure 4.19: L-Edit layout showing the dimensions of the LR400-8 Laser Microrobot.
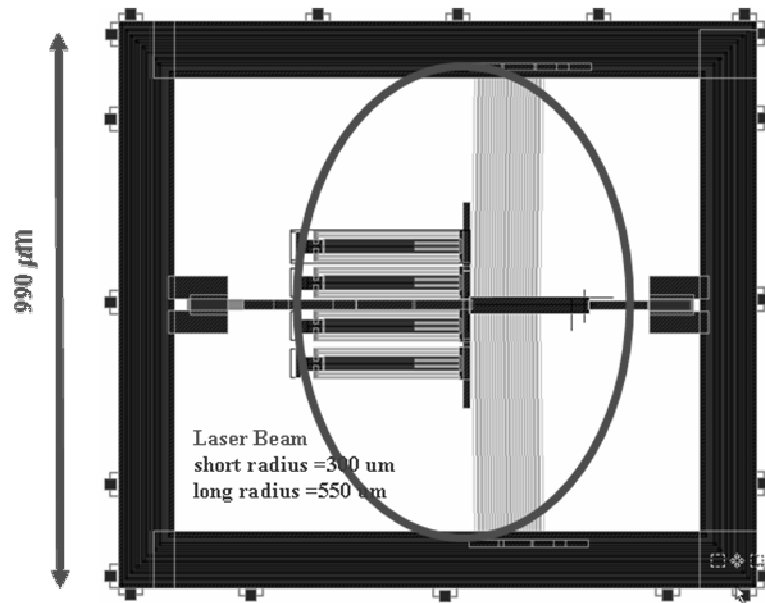
Figure 4.20: L-Edit layout showing the dimensions of the LR400-24 Laser Microrobot.

These two microrobots were based around 400 μm chevron actuators, instead of 250 μm chevron actuators. In experiments with test actuators, longer chevrons provided more maximum deflection with slightly less power, so these were designed to possibly take larger steps than the smaller microrobot. Another difference in these designs was that the down thermal actuators were 250 μm long instead of the 200 μm used on the LR-250 design. Again, the idea was to gain more deflection by using a longer length hot arm for thermal expansion. Figure 4.21 shows digital photographs of the larger laser microrobots, with (a) being the LR400-8 with two down actuators and (b) being the LR400-24 with four down actuators. Figure 4.22 shows a close-up digital photograph of the LR400-24 design with four down actuators. Sinclair noted that the amount of force in a chevron actuator is proportional to the number of beams in the actuator [3], so LR400-24 version, with 24 chevron beams, was designed to be a higher force version. While the smaller microrobot was designed to be used with a 260 μm radius laser beam, these microrobots would require a 400 μm radius laser beam dot size. Because the laser power per

meter squared decreases as the square of the radius, these designs will require a much more

powerful laser to operate than the smaller design.

(a)   **(b)**
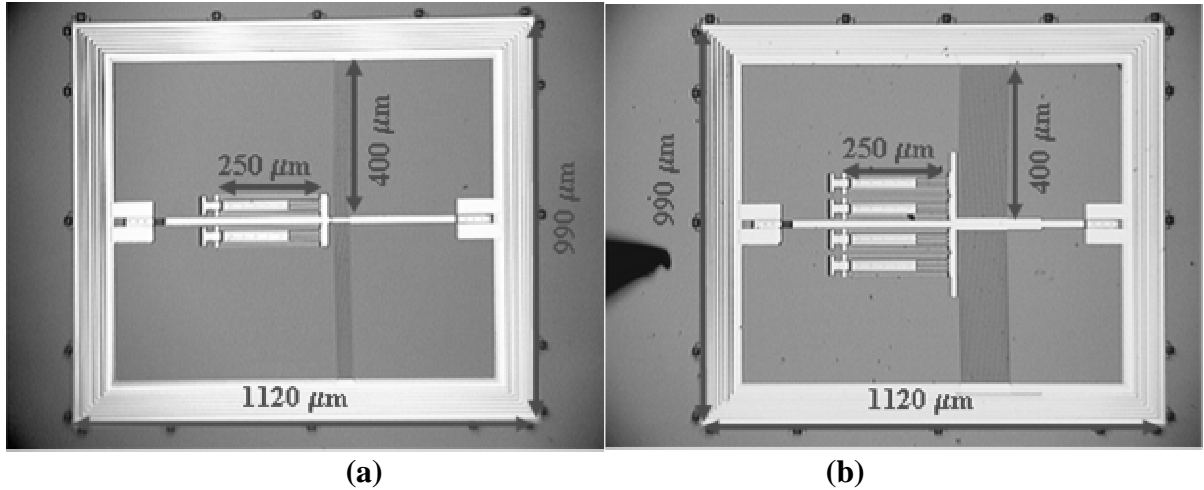
Figure 4.21: Digital photographs of the larger laser microrobots, with (a) being the LR400-8 with two down actuators and (b) being the LR400-24 with four down actuators.
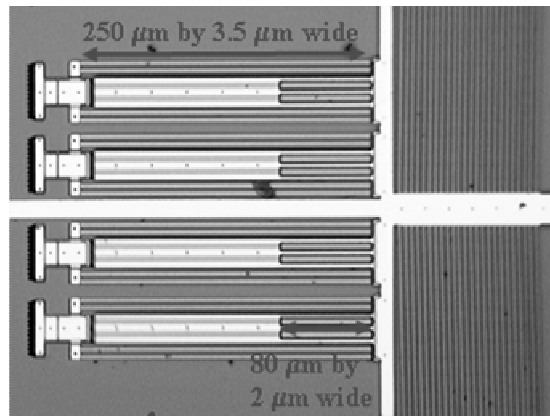
Figure 4.22: Close-up digital photograph of the four down actuators on the LR400-24 design.

4.4.3. Cascade-LR400-8 Microrobot Design

Based on an idea for cascaded bent beam actuators proposed by Que and Park [4], [5], [11], the next microrobot was based around 400 μm and 300 μm chevron actuators, cascaded to provide amplification of deflection. Figure 4.23 shows an L-Edit layout of the Cascade-LR400-8 Microrobot Design with amplified cascade bent beam laser actuators. These cascaded chevron actuators were reported to provide upwards of 30 μm of deflection in the literature [4]. Figure

4.24 shows a CoventorWare simulation depiction of the amplified cascaded bent beam concept. The idea behind the cascaded chevron actuators is illustrated in Figure 4.24. The outer web of actuators thermally expand, (long outside arrows, A), causing buckling, and deflection toward the middle (short outside arrows, B). This inward pushing force is combined with the thermal expansion on the center or inner web of chevron actuators (parallel inner long arrows, C). This combined action causes a large buckling force and a large deflection toward the end, as shown by the large arrow, D. As with the other large actuators, this setup requires a very large laser beam spot size (about 500 μm radius), thus a much more powerful laser diode. This research was constrained to the use of a 60 mW laser, which could not provide enough power per area for a large dot size.
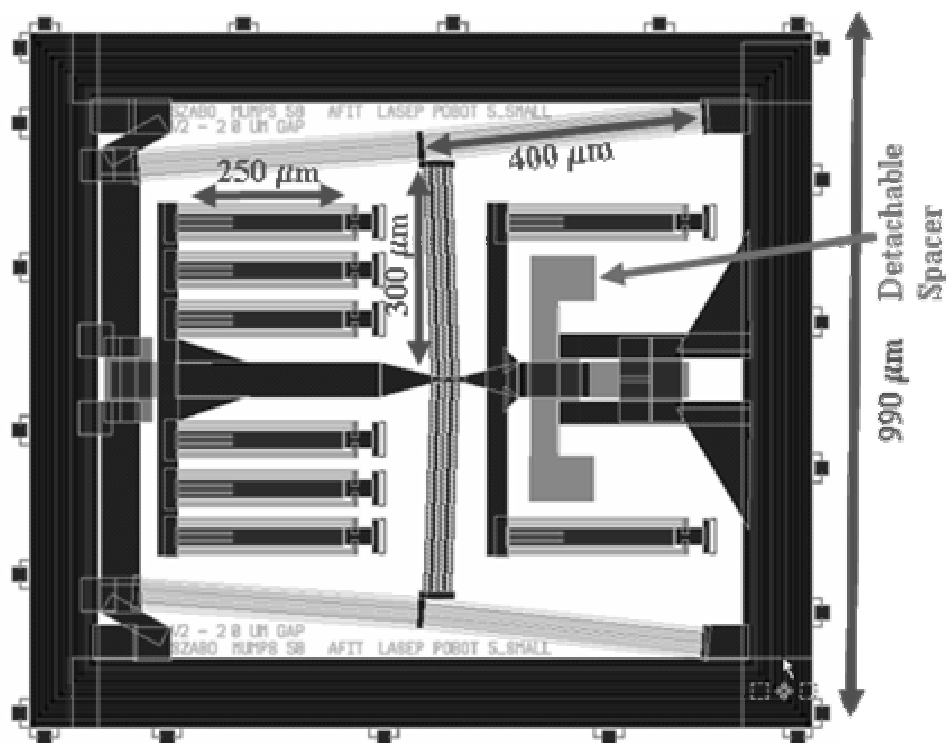
Figure 4.23: L-Edit layout of the Cascade-LR400-8 Microrobot Design with amplified cascade bent beam laser actuators.
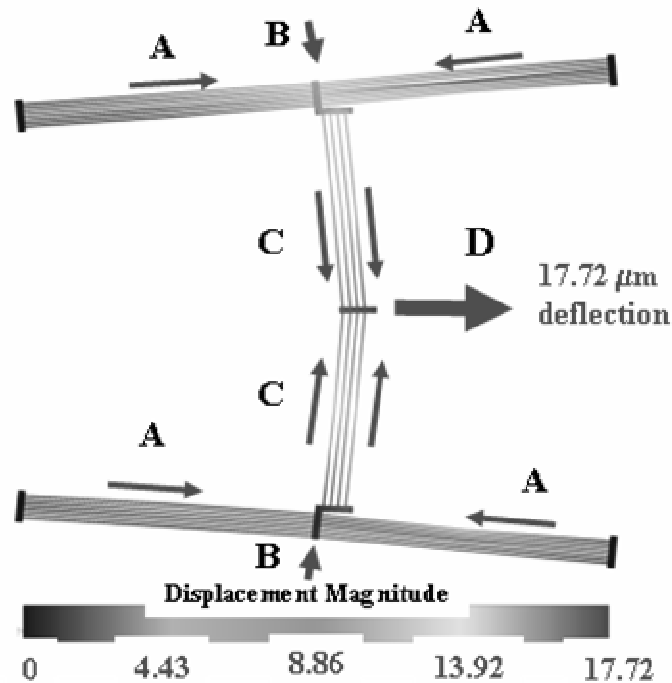
Figure 4.24: CoventorWare simulation depiction of the amplified cascaded bent beam concept.

4.4.4. Laser Spider Microrobot Design

The final design was the laser spider microrobot design which was based on double hot arm actuators and bimorph down thermal actuators. Figure 4.25 is an L-Edit layout of the laser spider microrobot with double hot arm actuators and bimorph down thermal actuators. Figure 4.26 is a digital photograph of the PolyMUMPs 57 laser spider microrobot with double hot arm actuators. As with the other large actuators, this setup requires a very large laser beam spot size (about 600 μm radius), thus a much more powerful laser diode laser source than is presently available.
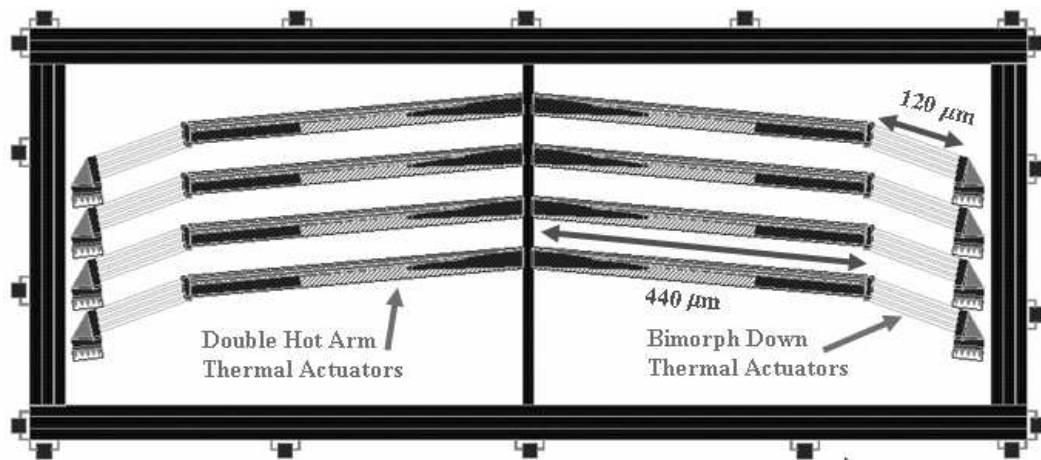
Figure 4.25: L-Edit layout of the PolyMUMPs 58 laser spider microrobot with double hot arm actuators and bimorph down thermal actuators.
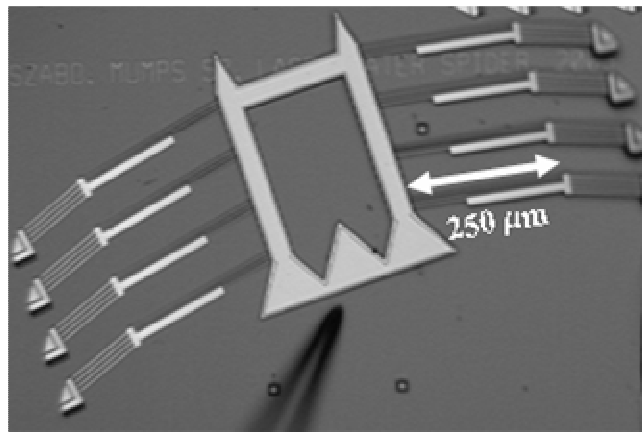
Figure 4.26: Digital photograph of the PolyMUMPs 57 laser spider microrobot with double hot arm actuators.

4.5. Conclusion

This chapter discussed the designs for optothermal test actuators and laser microrobot designs based on optothermal actuators. In Chapter 3, two of the key concepts in capturing laser power were actuator thickness and the amount of actuator surface area that can be placed in a small area to absorb the most laser power. This chapter discussed chevron thermal actuators, which could take the best advantage of these concepts to absorb the maximum amount of laser energy.

The PolyMUMPs design process was briefly discussed. The test actuators of the bent buckle or chevron designs were discussed for use as optothermal tests actuators. Then the details and principles of the basic wireless laser microrobot designs used in this research were presented. Alternate microrobot designs based on those same principles were discussed. Chapter 5 presents the design equations used for the chevron actuators. They will be modeled first as electrothermal actuators, then as optothermal actuators. Chapter 6 explains the experiments used to electrically and optically test the actuators. These actuators were fabricated and the models will be compared against the actual experimental results in Chapter 7.

4.5. Bibliography

[1]   "L-Edit: The Layout Editor, Win32 version 10.00." Computer Software. Tanner Research, Inc. 2650 East Foothill Boulevard Pasadena, CA 91107, USA.

[2]   D. Koester, A. Cowen, R. Mahadevan, B. Hardy, *PolyMUMPs Design Handbook, a MUMPs® process,* Revision 10.0, MEMSCAP, http://www.memscap.com/memsrus/docs/polymumps.dr.v10.pdf, 2003.

[3]   M. J. Sinclair, "A High Force Low Area MEMS Thermal Actuator," *2000 Inter Society Conference on Thermal Phenomena*, pp. 127-132, 2000.

[4]   L. Que, J. Park, and Y. B. Gianchandani, "Bent-Beam Electrothermal Actuators—Part I: Single Beam and Cascaded Devices," *Journal Of Microelectromechanical Systems*, Vol. 10, No. 2, pp. 247-254, June 2001.

[5]   L. Que, J. Park, and Y. B. Gianchandani, "Bent-Beam Electrothermal Actuators for High Force Applications," *IEEE Proceedings*, pp. 31-36, 1999.

[6]   M. Chiao, L. Lin, "Self-Buckling of Micromachined Beams under Resistive Heating," *Journal Of Microelectromechanical Systems*, Vol. 9, No. 1, pp. 146-151, March 2000.

[7]   J. Park, L. L. Chu, A. D. Oliver, and Y. B. Gianchandani, "Bent-Beam Electrothermal Actuators—Part II: Linear and Rotary Microengines," *Journal Of Microelectromechanical Systems*, Vol. 10, No. 2, pp. 255-261, June 2001.

[8]   R. Hickey, D. Sameoto, T. Hubbard and M. Kujath, "Time and Frequency Response of Two-Arm Micromachined Thermal Actuators," *Journal of Micromechanics and Microengineering*, Vol. 13, pp 40-46, 2003.

[9]   Y. Lai, J. McDonald, M. Kujath and T. Hubbard, "Force, Deflection and Power Measurements of Toggled Microthermal Actuators," *Journal of Micromechanics and Microengineering*, Vol. 14, pp 49-56, 2004.

[10]   S. Baglio, S. Castorina, L. Fortuna, N. Savali, "Modeling and Design of Novel Photo-Thermo-Mechanical Microactuators," *Source: Sensors and Actuators, A: Physical*, vol. 101, no. 1-2, pp. 185-193, 2002.

[11]   S. Baglio, S. Castorina, L. Fortuna, N. Savali, "Novel Microactuators Based on a Photo-Thermo-Mechanical Actuation Strategy," *Sensors, 2002. Proceedings of IEEE*, vol. 1, pp. 192 -197, 2002.

[12]   S. Baglio, S. Castorina, L. Fortuna, N. Savali, "Technologies and Architectures for Autonomous "MEMS" Microrobots," *Proceedings, 2002 IEEE International Symposium on Circuits and Systems,* vol. II, pp. 584-587, 2002.

[13]   S. Baglio, S. Castorina, L. Fortuna, N. Savali, "Development of Autonomous, Mobile Micro-electro-mechanical Devices", *Proceedings, 2002 IEEE International Symposium on Circuits and Systems*, vol. 4, pp. IV-285-288, 2002.

[14]   G. T. A. Kovacs, *Micromachined Transducers Sourcebook,* WCB/McGraw-Hill, Boston, Stanford University, 1998.

5. Modeling

In Chapter 3, two of the key concepts in capturing laser power were actuator thickness and the amount of actuator surface area that can be placed in a small area to absorb the most laser power. Chapter 4 discussed chevron actuators which could take the most advantage of these concepts to absorb the maximum amount of laser energy. This chapter presents the design equations used to characterize the chevron actuators. They are modeled, first as electrothermal actuators, then as optothermal actuators. These actuators were fabricated and the models will be tested against the actual experimental results in Chapter 7.

Section 5.1 covers the electrothermal chevron actuator heating model. Section 5.2 discusses the thermal expansion and mechanical modeling. Section 5.3 discusses the extension of the model for use with temperature dependant variables. The last section of this chapter, Section 5.4, discusses the laser heating model used to characterize the optothermal chevron actuators. The MatLab code for the chevron optothermal actuator model is given in Appendix B. The MatLab code for the chevron electrothermal actuator model is given in Appendix C.

5.1. Electrothermal Chevron Actuator Model

Dong, et al. presented a thermal model for PolyMUMPs fabricated asymmetrical double hot arm electrothermal actuators, which uses the same general modeling geometry as the optothermal chevron designs proposed in this paper [1]. The difference between their actuator model and the models proposed in this research is that theirs is a highly simplified three part model, and this research's model will be a five part model. This allows better analysis of optothermal heating when a laser beam is applied to only part of the actuator. Figure 5.1 is a plot of the temperature distribution along the outer and inner hot arms of a polysilicon double hot arm electrothermal actuator, with 5 volts applied, as predicted by the model of Dong, et al. This

electrothermal model was based on polysilicon, which was resistively heated by current passing through the hot arms, causing the uneven temperature profile seen in Figure 5.1. The chevron actuator designs will also be modeled using resistive electrothermal heating. The model presented in this research uses electrical power applied to predict temperature distribution. This temperature distribution will be used to predict thermal expansion, which in turn will be used to predict actuator deflection. The model will have to be adapted to use optothermal heating to predict the temperature. Butler, Bright and Cowan published a similar model for a single asymmetrical hot arm actuator that used as input the total electrical power to predict temperature [2]. Figure 5.2 is a plot of experimental data of electrical power versus deflection for single asymmetrical hot arm electrothermal actuators obtained by Cowan, et al. They used their temperature model data to predicted deflection. Parts of these two models will be modified and used, along with an adaptation of an unpublished thermal conduction model derived by Kladitis [3], to make a final model for the optothermal designs in this research.
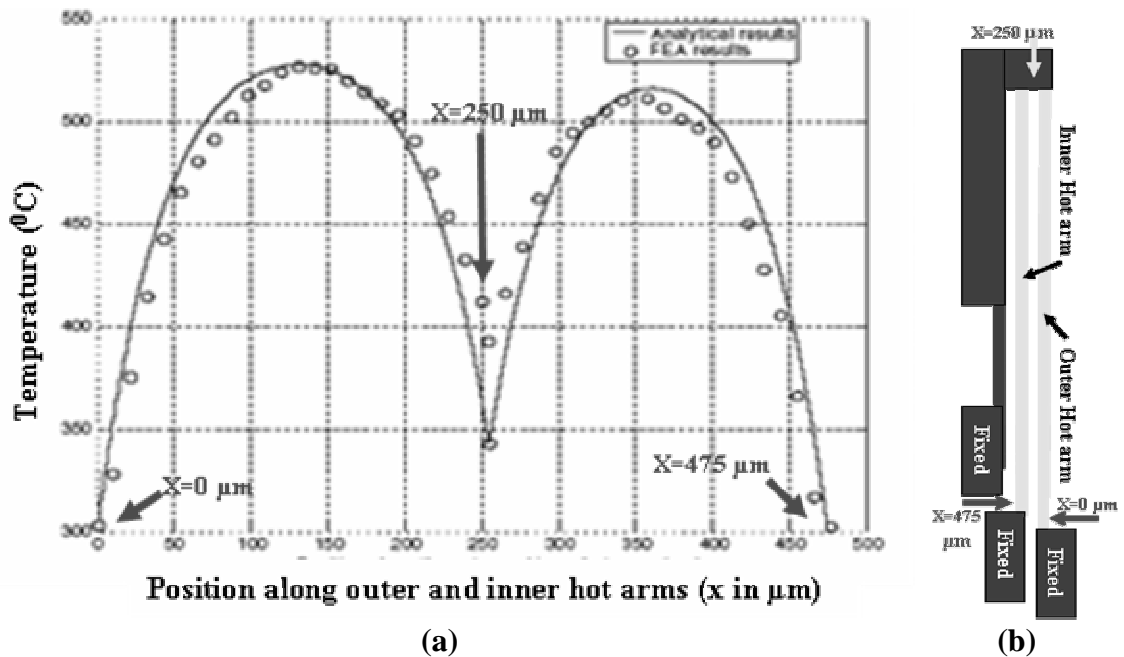
Figure 5.1: Plot of the temperature distribution, (a) along the outer and inner hot arms of a (b), polysilicon double hot arm electrothermal actuator, with 5 volts applied, as predicted by the model of Dong, et al. [1].
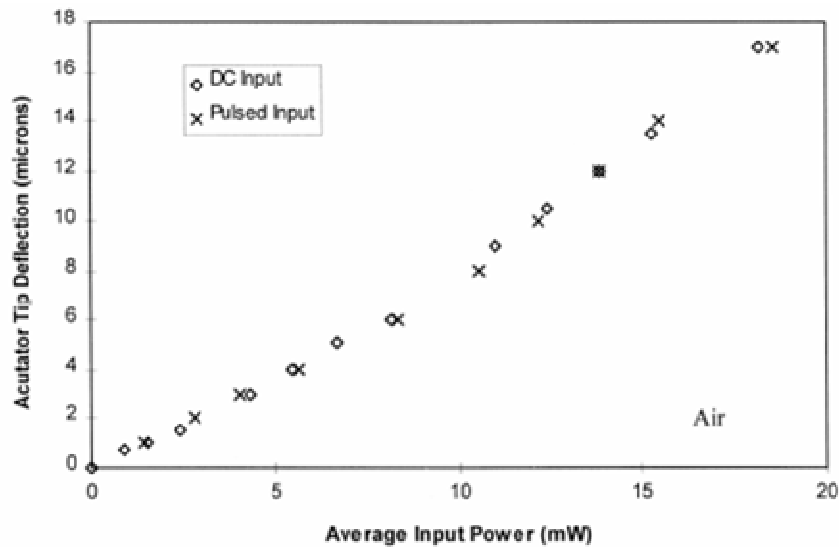
Figure 5.2: Plot of experimental data of electrical power versus deflection for single asymmetrical hot arm electrothermal actuators obtained by Cowan, et al. [2].

This research's chevron model analyzes the temperature profile, thermal expansion and tip deflection of a chevron electrothermal actuator. Figure 4.5 illustrated the thermal actuation principles for the chevron thermal actuator. These devices are fabricated so that current passes through the two opposing hot arms, resistively generating heat in them. This heat generation will produce a temperature distribution similar to Figure 5.1, and causes thermal expansion in the hot arms.

The model is divided into three sections. Figure 5.3 is an illustration of the three part thermal mechanical model. The first part of the model, covered in this section, takes electrical power as input, and gives, as an output, a temperature distribution. The second part of the model takes the temperature as an input and gives an output that is the change in length due to thermal expansion. The third part of the model takes the thermal expansion as an input and translates it into mechanical deflection.
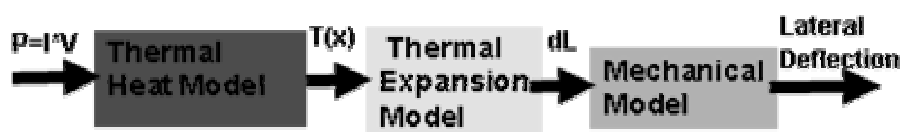
Figure 5.3: Illustration of the three part thermal mechanical model.

5.1.1. The Five Piece Thermal Heat Model

The chevron actuator was divided into five pieces for modeling in this research. Figure 5.4 is an illustration of the five piece thermal model of a chevron thermal actuator, with the light colored pieces being the heated areas, showing the thermal model boundary conditions. These boundary conditions are used in the thermal model equation derivations that follow. The boundary condition, T_0, represents room temperature (293 K). The thermal energy flow is shown as q_n, ($n = 1, 2, 3, 4, 5$), with units of Watts/m^2, and is shown flowing across the model section boundaries. Heat generation, or Joule heating, is shown as $\dot{q}_n$, ($n = 1, 2, 3, 4, 5$), with units of Watts/m^3. In the electrothermal model, Joule heating is caused by electrical resistive heating. In the optothermal model, Joule heating will come from the heat generated by the photons interacting with the atoms in the material. The Joule heating of the center piece $\dot{q}_3$ is assumed to be negligible in both the electrothermal and optothermal models, because it is coated by .5 μm of gold. This greatly reduces resistive heating in the electrothermal model, and shields the material from laser light in the optothermal model.
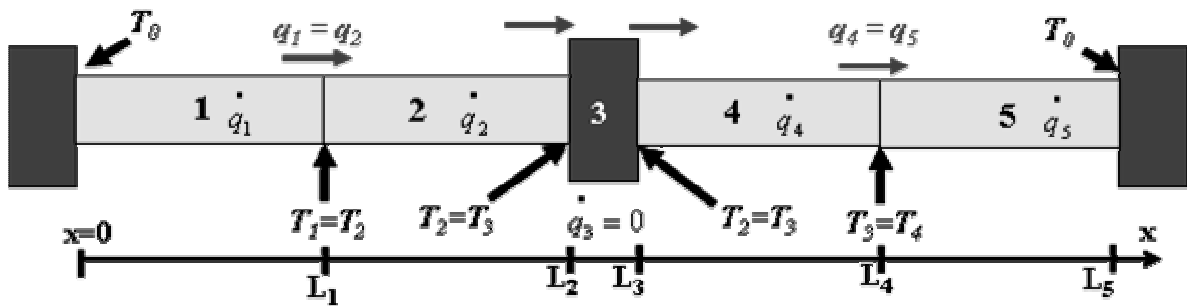
Figure 5.4: Illustration of the five section thermal model of a chevron thermal actuator, with the light sections being the heated areas, showing the thermal model boundary conditions.

Table 5.1, Model Assumptions, lists the assumptions used in this model.

Table 5.1: Model Assumptions.

1. Assume homogeneous material properties. For example, assume that doping and resistivity are uniform.
2. Assume balanced architecture and geometry make twisting, torsion and out-of-plane deflection negligible.
3. Assume polysilicon thickness and density are uniform for the length of the beam. The PolyMUMPs data sheet for run 57 lists the polysilicon thickness for Poly1 as 20095.933 Angstroms with a standard deviation of 327.58, and Poly2 as 15036.67 Angstroms with a standard deviation of 253.56 [3].
4. Assume steady state reactions to temperature changes.
5. Beam bending is assumed to be elastic. This assumption will break down at the higher temperatures, just before it melts.
6. This model will only consider the gradient of temperature in the x direction, and assume it is uniform in the y and z directions.

Three modes of heat transfer are considered in this model. Figure 5.5 is an illustration of the three modes of heat transfer; conduction, convection, and radiation. q_{cond} is the heat flow, P is the perimeter for heat loss conduction out of the material and T_X is the temperature at a point.
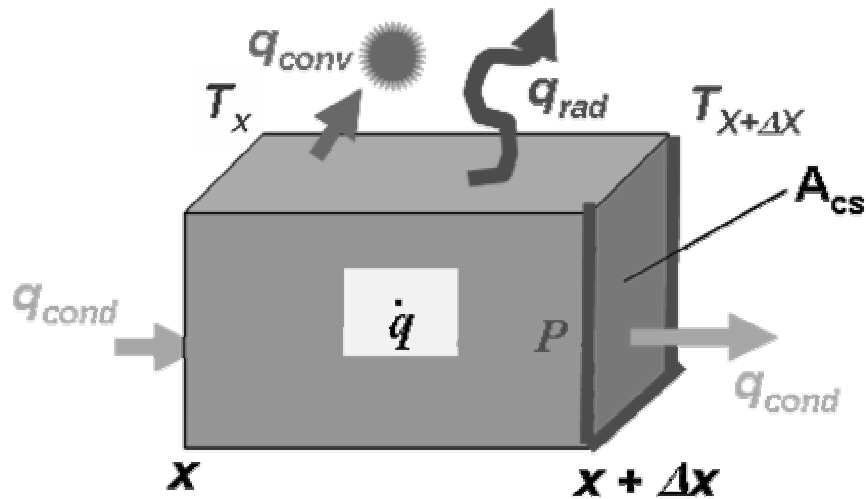
Figure 5.5: Illustration of the three modes of heat transfer; conduction, convection, and radiation.

Equation 5.1 shows Fourier's Law of heat transfer (conduction),

$$q_{cond} = -\kappa A_{CS} \frac{dT}{dx} \tag{5.1}$$

where q_{cond} is the heat flow, κ is the thermal conductivity of the material, A_{cs} is cross sectional area, T is the temperature, and x is the coordinate axis for this one-dimensional model.

Convection is caused by the heat exchange between the material and particles in a gas or liquid and is given by,

$$q_{conv} = hA_{CS}(T_{surface} - T_{\infty})$$ **(5.2)**

where h is the heat transfer coefficient in W/m^2 K, $T_{surface}$ is the surface temperature and T_{∞} is assumed to be room temperature. The heat transfer coefficient, h, is usually found from experimental approximation and correlations. Convection can be natural or forced.

For this model I am simplifying the convection as conduction from the heated actuator beam, through the air, to the substrate. Therefore, the average heat transfer coefficient, h, is can be approximated by,

$$h = \frac{\kappa_{air}}{d}$$ **(5.3)**

where κ_{air} is the thermal conductivity of air (temperature dependant) and d is a distance between the actuator and the substrate.

Radiation occurs when heat is transferred radiatively from one body to another, even in a vacuum. In this model, heat loss due to radiation is assumed to be small with respect to convection, and its effects will lumped in with the convection term.

Using Figure 5.5, the conservation of energy or total change in system energy equation for a cube of length Δx can be expressed as,

$$q_{cond_{in}} + \dot{q} A_{cs}\Delta x - q_{cond_{otu}} - q_{conv} = 0$$ **(5.4)**

where $\dot{q}$ is the internal heat generation term, $q_{cond_{in}}$ is the heat conducting into the block at *X*, and $q_{cond_{otu}}$ is the heat conducting out at *X*+Δ*X* and assuming steady state conditions. For the surface area used for the convection term in Equations 5.2 and 5.4, the perimeter, *P*, times the length, Δ*x*, is substituted. Figure 5.6 is an illustration of the three cases of calculating perimeter, *P*, for the convective heat loss, q_{conv}. For this model, case (b), using the width of the bottom of the beam and half of each side, was used. It was assumed that the majority of the heat is lost due to convection from the bottom and lower sides of the beam to the substrate, which provides a very close heat sink at 2 μm away. On the sides of the hot arms facing each other, they are both sending out heat towards each other, canceling any cooling effect. So for simplicity, all heat loss will be lumped into convection from the bottom and lower part of the sides of the hot arms.

(a)   **(b)**   **(c)**
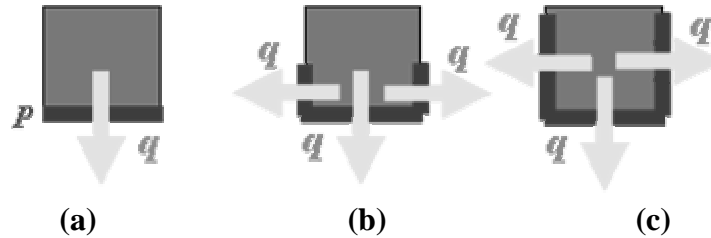
Figure 5.6: Illustration of the three cases of calculating perimeter, *P*, for the convective heat loss, *q*, with (a) having *P* = length of the bottom, and (b) having *P* = length of the bottom plus half the sides, and (c) having *P* = length of the bottom plus the length of both sides.

Substituting Equations 5.1, 5.2, and 5.3 into 5.4, and dividing through by the area (A_{cs}), thermal conductivity (κ), and the differential element in length (Δ*x*), gives us

$$\frac{\partial^2 T}{\partial x^2} + \frac{\dot{q}}{\kappa} - \frac{hP}{\kappa A_{cs}}\left(T - T_\infty\right) = 0 \tag{5.5}$$

where $T_{surface}$ is in Equation 5.2 is equal to the temperature, *T*, of the element for this 1-D model.

The heat generation term, $\dot{q}$, is produced by the resistive heating caused by the electrical power dissipated in the element; in the form of $P = I^2 R$,

$$\dot{q} = \frac{I^2 \rho_e}{A_{cs}^2} \qquad\qquad (5.6)$$

where I is the current, ρ_e is the resistivity of the polysilicon.

For simplicity, in Equation 5.8 let

$$\beta = \frac{\dot{q}}{\kappa} \qquad\qquad (5.7)$$

$$\gamma = \sqrt{\frac{hP}{\kappa A_{cs}}} \qquad\qquad (5.8)$$

and $\qquad\qquad \varepsilon = \frac{\beta + \gamma^2 T_\infty}{\gamma^2} = \frac{\dot{q} A_{cs}}{hP} + T_\infty . \qquad\qquad (5.9)$

For the steady state and substituting Equations 5.7, 5.8, and 5.9; Equation 5.5 reduces to

$$\frac{\partial^2 T}{\partial x^2} + \beta - \gamma^2 (T - T_\infty) = 0 . \qquad\qquad (5.10)$$

This can be rearranged to give us a simple form of a differential equation,

$$\frac{\partial^2 T}{\partial x^2} - \gamma^2 T = -\beta - \gamma^2 T_\infty . \qquad\qquad (5.11)$$

The total solution to this differential equation will combine a homogenous and particular solution as follows,

$$T_H + T_P = C_1 e^{\gamma x} + C_2 e^{-\gamma x} + \varepsilon \qquad\qquad (5.12)$$

where C_1 and C_2 are constants of integration that need to be solved. This equation is used for each section of the actuator, to build a matrix of equations to solve for each of the constants. The constants have to be solved using boundary conditions. The thermal boundary conditions are that $T_\infty = T_0$, or room temperature, is used at the end of each hot arm where it attaches to the substrate with an anchor. The temperature is assumed equal at each boundary between sections.

The heat conducted along x, out of one section, equals the heat conducted into the connecting end of the next section, as was seen above in Figure 5.5.

For sections 1 through 5 the following equations are used,

$$T_1(x) = C_1 e^{\gamma_1 x} + C_2 e^{-\gamma_1 x} + \varepsilon_1, \quad (0 \le x \le L_1) \tag{5.13}$$

$$T_2(x) = C_3 e^{\gamma_2 x} + C_4 e^{-\gamma_2 x} + \varepsilon_2, \quad (L_1 \le x \le L_2) \tag{5.14}$$

$$T_3(x) = C_5 e^{\gamma_3 x} + C_6 e^{-\gamma_3 x} + \varepsilon_3, \quad (L_2 \le x \le L_3) \tag{5.15}$$

$$T_4(x) = C_7 e^{\gamma_4 x} + C_8 e^{-\gamma_4 x} + \varepsilon_4, \quad (L_3 \le x \le L_4) \tag{5.16}$$

$$T_5(x) = C_9 e^{\gamma_5 x} + C_{10} e^{-\gamma_5 x} + \varepsilon_5, \quad (L_4 \le x \le L_5) \tag{5.17}$$

where $T_i(x)$ is the temperature distribution along each length between L_i and L_{i+1}. Given the above boundary conditions, the following equation is obtained from Equation 5.13,

$$T_1(0) = C_1 + C_2 + \varepsilon_1, \tag{5.18}$$

and the following equation is obtained from Equations 5.13 and 5.14,

$$T_1(L_1) = T_2(L_1) = C_1 e^{\gamma_1 L_1} + C_2 e^{-\gamma_1 L_1} + \varepsilon_1 = C_3 e^{\gamma_2 L_1} + C_4 e^{-\gamma_2 L_1} + \varepsilon_2 \tag{5.19}$$

and the following equation is obtained from Equations 5.14 and 5.15,

$$T_2(L_2) = T_3(L_2) = C_3 e^{\gamma_2 L_2} + C_4 e^{-\gamma_2 L_2} + \varepsilon_2 = C_5 e^{\gamma_3 L_2} + C_6 e^{-\gamma_3 L_2} + \varepsilon_3 \tag{5.20}$$

and the following equation is obtained from Equations 5.15 and 5.16,

$$T_3(L_3) = T_4(L_3) = C_5 e^{\gamma_3 L_3} + C_6 e^{-\gamma_3 L_3} + \varepsilon_3 = C_7 e^{\gamma_4 L_3} + C_8 e^{-\gamma_4 L_3} + \varepsilon_4 \tag{5.21}$$

and the following equation is obtained from Equations 5.16 and 5.17,

$$T_4(L_4) = T_5(L_4) = C_7 e^{\gamma_4 L_4} + C_8 e^{-\gamma_4 L_4} + \varepsilon_4 = C_9 e^{\gamma_5 L_4} + C_{10} e^{-\gamma_5 L_4} + \varepsilon_5 \tag{5.22}$$

and the following equation is obtained from Equation 5.17,

$$T_5(L_5) = T_5(0) = C_9 e^{\gamma_5 L_5} + C_{10} e^{-\gamma_5 L_5} + \varepsilon_5 \tag{5.23}$$

where each of these equations uses the stated temperature boundary conditions.

Next, the heat conduction or heat flow boundary conditions will be used to create more equations to solve the unknowns. The following equation is obtained from Equations 5.13 and 5.14,

$$q_1 = q_2 = -\kappa A_{CS_1} \left.\frac{dT_1(x)}{dx}\right|_{x=L_1} = -\kappa A_{CS_2} \left.\frac{dT_2(x)}{dx}\right|_{x=L_1} \tag{5.24}$$

which gives,

$$C_1 A_{CS_1} \gamma_1 e^{\gamma_1 L_1} - C_2 A_{CS_1} \gamma_1 e^{-\gamma_1 L_1} = C_3 A_{CS_2} \gamma_2 e^{\gamma_2 L_1} - C_4 A_{CS_2} \gamma_2 e^{-\gamma_2 L_1} \tag{5.25}$$

Similarly, using boundary conditions $q_2=q_3$ and $q_3=q_4$, and $q_4=q_5$, the following equations are obtained from Equations 5.14 through 5.17:

$$C_3 A_{CS_2} \gamma_2 e^{\gamma_2 L_2} - C_4 A_{CS_2} \gamma_2 e^{-\gamma_2 L_2} = C_5 A_{CS_3} \gamma_3 e^{\gamma_3 L_2} - C_6 A_{CS_3} \gamma_3 e^{-\gamma_3 L_2} \tag{5.26}$$

$$C_5 A_{CS_3} \gamma_3 e^{\gamma_3 L_3} - C_6 A_{CS_3} \gamma_3 e^{-\gamma_3 L_3} = C_7 A_{CS_4} \gamma_4 e^{\gamma_4 L_3} - C_8 A_{CS_4} \gamma_4 e^{-\gamma_4 L_3} \tag{5.27}$$

$$C_7 A_{CS_4} \gamma_4 e^{\gamma_4 L_4} - C_8 A_{CS_4} \gamma_4 e^{-\gamma_4 L_4} = C_9 A_{CS_5} \gamma_5 e^{\gamma_5 L_4} - C_{10} A_{CS_5} \gamma_5 e^{-\gamma_5 L_4} \tag{5.28}$$

yielding 10 equations and 10 constants of integration, C_n, to solve as unknowns. Equations 5.18 through 5.23 and 5.25 through 5.28 are combined into a matrix in MatLab, and the unknown constants are solved for.

Once the constants of integration, C_n, are solved for, they are plugged back into Equations 5.13 through to 5.17 to solve for the temperature distribution. Figure 5.7 is a plot of the temperature distribution predicted by the model, from Equations 5.16 through to 5.20, at different voltages, along the hot arms of an electrically powered 250 μm long chevron actuator designed for the PolyMUMPs 58 fabrication run. It should be noted that this actuator burnt out at around 15 volts, so the 1500 K prediction for 15 volts is fairly close.
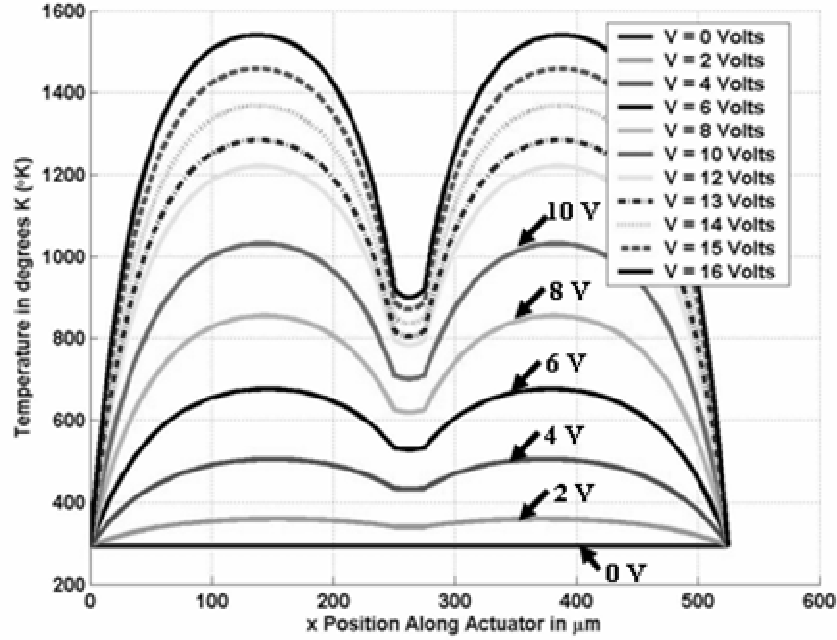
Figure 5.7: Plot of the temperature distribution predicted by the model, from Equations 5.16 through to 5.20, at different voltages, along the hot arms of an electrically powered 250 μm long chevron actuator designed for the PolyMUMPs 58 fabrication run.

5.2. Thermal Expansion and Mechanical Modeling.

Now that the temperature distribution has been obtained, the second part of the model (the second block in Figure 5.4), the thermal expansion model, is now developed. This model uses the average temperature of the hot arms, and uses the thermal coefficient of expansion of the material to determine the new length. The change in length is simply found by multiplying the original length of arm, at T_0, times the thermal coefficient of expansion times the average change in temperature [6]:

$$\Delta L = L\alpha_{CTE}\left(T_{average} - T_0\right) \qquad \textbf{(5.29)}$$

where α_{CTE} is the thermal coefficient of expansion, L is the original length, $T_{average}$ is the average of the temperature distribution along the length of the arm, and T_0 is room temperature.

Once a change in length due to thermal expansion is obtained, the deflection model (the third block in Figure 5.4) must be obtained. Sinclair gives a deflection equation for bent beam chevron actuators that was used in this model [7]. The deflection for a bent beam chevron actuator is given by the following equation,

$$defl = \sqrt{[L^2 + 2L(\Delta L) - L\cos^2(\theta)]} - L\sin(\theta) \qquad \textbf{(5.30)}$$

where θ is the pre-bend angle in the chevron deflectors, which for all this research's actuators was one degree. Figure 5.8 is an example plot of deflection obtained from the model as compared to experimental deflection of an electrically powered 250 μm by 8-beam chevron actuator designed for the PolyMUMPs 58 fabrication run. The code used to produce Figures 5.7 and 5.8 is in Appendix C starting on page C1.
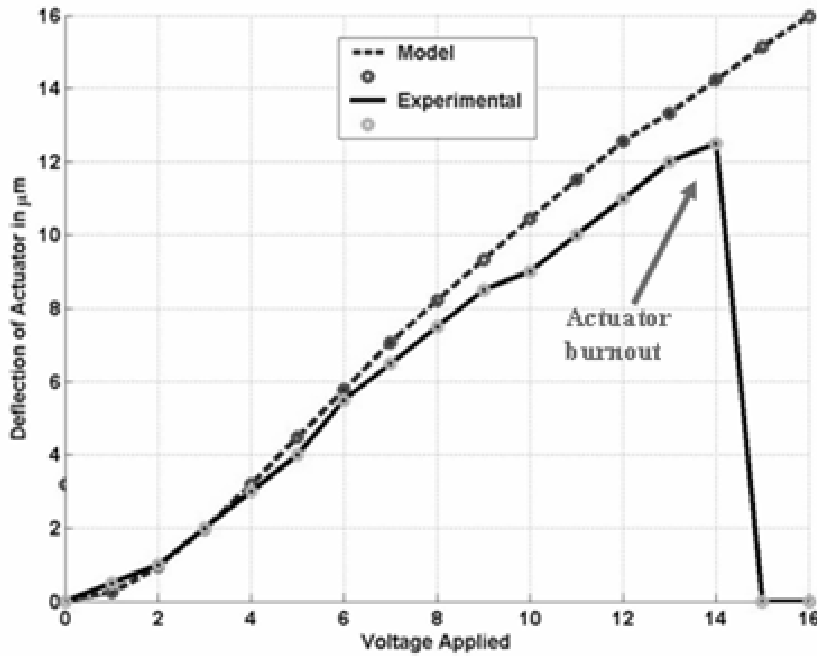
Figure 5.8: Example plot of deflection obtained from the model as compared to experimental deflection of an electrically powered 250 μm by 8-beam chevron actuator designed for the PolyMUMPs 58 fabrication run.

The dimensions, parameters and constants used in the electrothermal chevron actuator model are listed in Table 5.2. All these parameters and values are listed in the references as at "room temperature", (300 K). The first column lists the parameter and its value, named as closely as possible to the variable name used in the MatLab code. The second column gives the description, units, and a reference.

Table 5.2: Electrothermal Chevron Actuator Physical Parameters.

Parameter	Description and Reference
$t\_poly1 = 2.0 \times 10^{-6}$	thickness of polysilicon 1, in m [PolyMUMPs data sheet, run 57][3]
$t\_poly2 = 1.5 \times 10^{-6}$	thickness of polysilicon 2, in m [PolyMUMPs data sheet, run 57] [3]
$d1 = 2.0 \times 10^{-6}$	distance of Poly1 from substrate in m [PolyMUMPs data sheet run 57] [3]
$\alpha_{poly} = 2.33 \times 10^{-6}$	coefficient of thermal expansion, in K^{-1} [5, pg 558] (at 300 K)
$E_{poly} = 169 \times 10^{9}$	Young's Modulus for poly, in Pa [5, pg 201] (at 300 K)
$\nu_{poly} = 0.22$	Poisson's Ratio for polysilicon (unitless) [5, pg 201] (at 300 K)
$K_{poly} = 29$	Thermal conductivity, polysilicon in W/(m K) [10, pg 337] (300 K)
$K_{poly} = 41$	Thermal conductivity of polysilicon, in W/mK [1, pg 315] (at 300 K)
$K_{air} = .026$	Thermal conductivity of air, in W/mK [11, pg 66] (at 300 K)
$p_{e\_poly} = 1.97 \times 10^{-5}$	resistivity Poly1, in ohm-m [PolyMUMPs data sheet, run 57] [3] (300 K)

5.3. Temperature Dependent Variables

The next part of the model deals with the temperature dependencies of the material properties. The coefficient of thermal expansion, the thermal conductivity of polysilicon, the thermal conductivity of air, Young's Modulus, and the resistivity of the polysilicon all vary with temperature and will change as the polysilicon is heated. As noted above in Table 5.1, these parameter values are listed at 300 K in most literature. However, the actual operating temperature can range from 300 K to over 1500 K. This radically changes the material properties. The model in this research will vary these five properties with the average temperature at each voltage step.

One problem in formulating this model was determining the average operating temperature at each operating voltage. Experimentally determining the average operating temperature was not completely possible without complex temperature measuring equipment that could measure on the micron scale. Such equipment was not immediately available for this research. Therefore, I used iteration within my models to converge on an average temperature used to estimate a value for my temperature dependent model. An initial average temperature was found by dividing the operating range in one volt increments between zero and the voltage that the actuator melted at. A corresponding initial temperature was found by dividing (1500 K – 300 K) by the number of voltage steps. For example, if the actuator melted at 15 volts, 1200 K was divided by 15 voltage increments to find a temperature increment of 80 K. The initial "guess" average temperature was then started at room temperature (300 K) and incremented by adding 80 K for each operating voltage up to 15 volts. Average temperatures usually converged after five iterations, to within five percent. The resulting temperature distribution model was then partially verified experimentally using a gold dot test that observed the change in color of gold dots due to eutectic formation with polysilicon. This verification test and its results will be covered later in this section.

Next, the temperature dependant variable equations will be covered. The first to be covered will be the thermal coefficient of expansion (TCE), $\alpha(T)$, for polysilicon. From Butler, et al. an equation was obtained for the coefficient of thermal expansion for polysilicon [2], as a function of temperature,

$$\alpha(T) = 3.725(1 - e^{(-5.88x10^{-3}[T-124])} + 5.548x10^{-4}T)x10^{-6}, \quad (K^{-1}) \tag{5.31}$$

where T is the average temperature along the hot arm. According to the graph for the coefficient of thermal expansion for silicon in the King's *Materials Handbook for Hybrid Micro*

Electronics, the TCE increases with temperature until it levels off in an asymptotic curve near $5\,x10^{-6}\ K^{-1}$ [14].

For the thermal conductivity of polysilicon, a line fitting equation was used, using values from the highest found in the literature (41 W/mK [1]), to the lowest found in King's Materials Handbook, (25 W/mK) [14]. King shows a curve that is nearly linear and steadily decreasing as temperature increases. The thermal conductivity of polysilicon was found using a line fitting equation

$$Kpoly(T) = 41 - 2.65*T \quad \text{W/mK}. \tag{5.32}$$

For the thermal conductivity of air, an equation was found at the Worcester Polytechnic Institute web site, which they used for modeling high temperature effects in fire models, for use in researching firefighting methods [15]:

$$Kair\_t(T) = \left(1.5207x10^{-11}\right)T^{3} - \left(4.8574x10^{-8}\right)T^{2} + \left(1.0184x10^{-4}\right)T - \left(3.9333x10^{-4}\right) \quad \text{(W/mK)}.$$

$$\tag{5.33}$$

Young's Modulus was found by using a line fitting equation from the normal published value at 300 K, 169 GPa [5, pg 201] down to the lowest found in King's for silicon (142 GPa) [13]. King shows a curve that is nearly linear and steadily decreasing as temperature increases:

$$E\_poly1(T) = \left(-2.652x10^{-2}T + 179.5\right)x10^{9}; \quad \text{Pascals} \tag{5.34}$$

The final parameter that was varied with temperature is the resistivity of the polysilicon. Huang and Lee present an equation that approximates the changes in resistivity with temperature as follows [12, pg 66],

$$p_{e}(T) = p_{e}\left(1 + 1.25x10^{-3}\left(T\text{-}T_{0}\right)\right); \quad \text{ohm} \bullet \text{m} \tag{5.35}$$

5.3.1. Gold Silicon Eutectic Temperature Discoloration Experiment

As mentioned earlier, an experiment was conducted to help verify a correct temperature distribution. The experiment was based on the eutectic temperature of polysilicon and gold, which is approximately 636 K [5]. A test actuator was made of Poly2 in PolyMUMPs, and gold dots were deposited at set intervals along the length of the hot arm. Figure 5.9 is a depiction from an L-Edit layout of the Poly2 double hot arms with gold temperature test dots. This was the actuator used for the temperature verification experiments. Anywhere the temperature exceeded 636 K, the gold should change color, due to eutectic formation with the polysilicon, providing a general idea of the temperature distribution when different voltages were applied. Figure 5.10 is a digital photograph showing an example of the gold-polysilicon eutectic temperature used to test temperature distribution in an electrothermal actuator (at 10 volts).
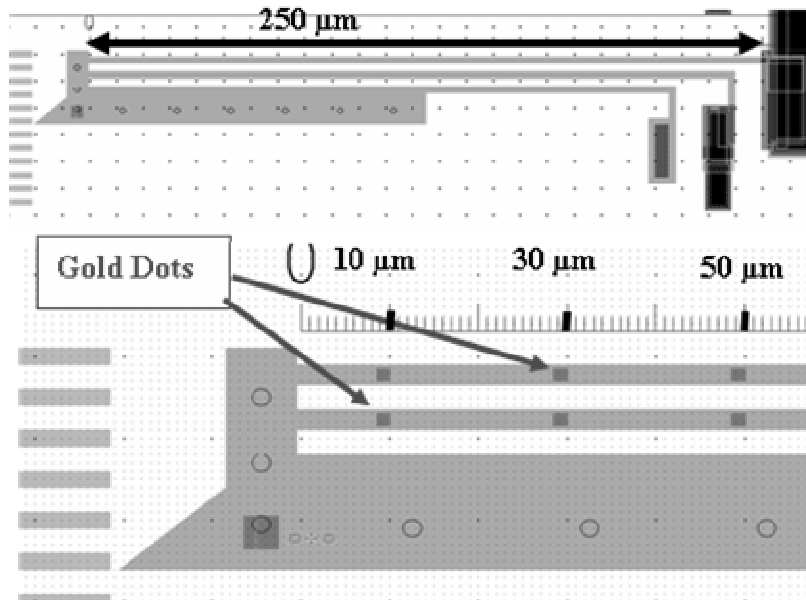
Figure 5.9: Depiction from an L-Edit layout of the Poly2 double hot arms with gold temperature test dots.

One can see from Figure 5.10 that the gold dots on the left (pointed to by the large dark arrow), have not yet exceeded 636 K at 10 volts, and they are 10 microns from the tip (which is

just off the picture's left end). Even the next pair of dots, which are 30 microns from the end are not fully color changed, showing they have also not exceeded 636 K.
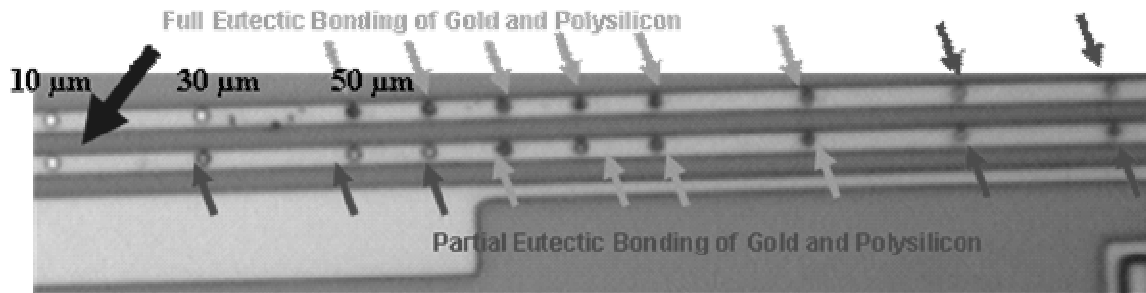
Figure 5.10:   Digital photograph showing an example of the gold-polysilicon eutectic temperature used to test temperature distribution in an electrothermal actuator (at 10 volts).

Figure 5.11: is a plot from the model, upon which the results of the eutectic gold dot experiment have been superimposed, verifying modeled temperature distribution along an arm of a double hot arm electrically powered actuator. The rings in Figure 5.11 show the position of the gold dots and the voltage at which they changed colors due to eutectic forming. The large perpendicular arrows show where the temperature has not exceeded 636 K. For example, at the right-most large perpendicular arrow, the 8 volt step temperature line is below the 636 K line at 80 μm. The gold dot has not changed color, as expected. However, the 9 volt step temperature curve has a value just above the 636 K line at 80 μm, and the gold dot is just beginning to change color, as expected.
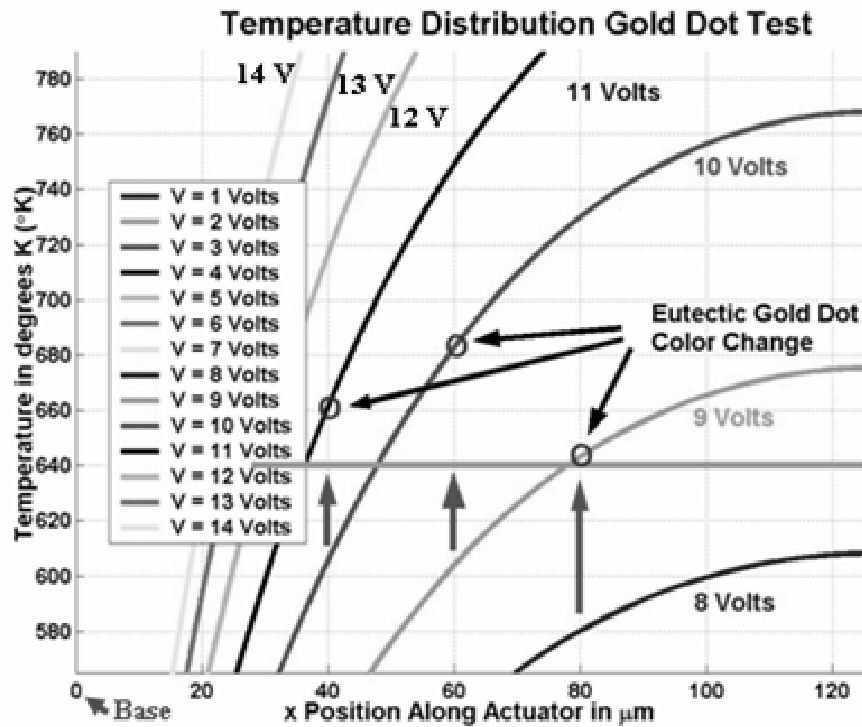
Figure 5.11: Plot from the model, upon which the results of the eutectic gold dot experiment have been superimposed, verifying modeled temperature distribution along an arm of a double hot arm electrically powered actuator.

An example of the temperature-varying parameters used in the Chevron Electrothermal Actuator model is listed in Table 5.3. The first column shows the operating voltage and the second column shows the matching converged average temperature. The succeeding columns show the values of the five temperature-varying parameters matching the operating temperature.

Table 5.3: Physical Parameters Varying with Temperature.

Vo Step (Volts)	Top Avg. Step (K)	α, Butler's Equ. for TCE (10^{-6} K^{-1})	E_{poly} Young's Modulus (10^{11} Pa)	K_{poly} Thermal Conduct-ivity. (10 W/ mK)	K_{air} Thermal Conduct-ivity. (10^{-2} W/ mK)	p_{e_poly1} resistivity (10^{-5} ohm-m)
0	293	2.3365	1.6904	4.1000	2.5700	1.9700
1	301.3	2.4147	1.6876	4.0340	2.6300	1.9900
2	324.8	2.6188	1.6796	3.9680	2.8100	2.0480
3	358.2	2.8668	1.6682	3.9020	3.0600	2.1310
4	399.3	3.1163	1.6642	3.8360	3.3500	2.2320
5	440.3	3.3171	1.6403	3.7700	3.6300	2.3330
6	485	3.4924	1.6251	3.7040	3.9300	2.4430
7	522.4	3.6123	1.6124	3.6380	4.1700	2.5350
8	572.9	3.7437	1.5952	3.5720	4.4900	2.6690
9	620.5	3.8432	1.5790	3.5060	4.7700	2.7770
10	662.8	3.9164	1.5647	3.4400	5.0200	2.8810
11	703.4	3.9764	1.5508	3.3740	5.2500	2.9810
12	742.2	4.0263	1.5376	3.3080	5.4700	3.0760
13	800.3	4.0905	1.5179	3.2420	5.7800	3.2190
14	844.1	4.1326	1.5030	3.1760	6.0100	3.3270
15	883.9	4.1673	1.4895	3.1100	6.2200	3.4250
16	927.3	4.2022	1.4747	3.0440	6.4400	3.5320
17	969.5	4.2339	1.4604	2.9780	6.6600	3.6360
18	1010.3	4.2627	1.4465	2.9120	6.8600	3.7360
19	1054.8	4.2926	1.4314	2.8460	7.0800	3.8460
20	1137.3	4.3451	1.4033	2.7800	7.5000	4.0490

5.4. Laser Heating Expansion Model

Once an electrothermal model was developed for the chevron actuators and verified experimentally, an optothermal laser heating model was developed. Equation 5.6, which gave $\dot{q}$, or internal power generation, in terms of current and resistivity, was replaced with absorbed optical power. The laser heating expansion model used all of the other equations developed previously for temperature distribution, thermal expansion, and deflection unchanged. Only the $\dot{q}$ power generation term is developed differently. Figure 5.12 shows illustrations of the five

piece thermal model of a chevron optothermal actuator, with (a) using elliptical beam centered on actuator and (b) using a more concentrated laser beam for an asymmetrical heating model. The model shown in Figure 5.4 was used and adapted as shown in Figure 5.12.

(a)

(b)
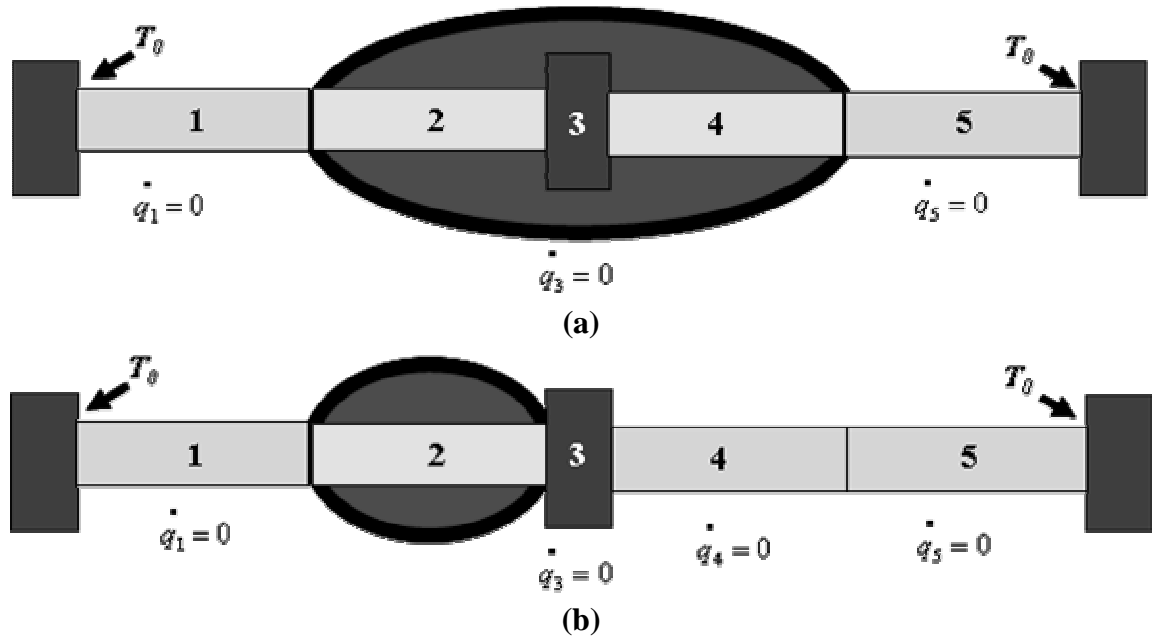
Figure 5.12: Illustrations of the five piece thermal model of a chevron optothermal actuator, with (a) using elliptical beam centered on actuator and (b) using a more concentrated laser beam for an asymmetrical heating model.

As chosen in Chapter 3, Laser Heating Theory and Design, the wavelength of the laser used in this research was $\lambda = 0.660$ μm. This gave an absorption coefficient of $\alpha = 4.63\mathrm{x}10^5$ m^{-1} ($4.63 \mathrm{x}10^3$ cm^{-1}), as read from a graph in a text by Sze, in Figure 5 [13, pg 287]. This model also was used to run a test at a wavelength of $\lambda = 0.632$ μm, with an absorption coefficient of $\alpha_{ac} = 5.63\mathrm{x}10^5$ m^{-1} ($5.63\mathrm{x}10^3$ cm^{-1}). The amount of energy absorbed in the material is shown by the following equation,

$$PE_{abs} = I_{PE}(1 - e^{(-\alpha_{ac}th)}) \tag{5.36}$$

where I_{PE} is the incident photon power, PE_{abs} is the photon energy absorbed per second (in mW), α_{ac} is the absorption coefficient, and th is the chevron thickness.

An equivalent bandgap energy is imparted to a lattice by photons. This energy is governed by the equation,

$$E_{g\,Light} \approx 1.24/\lambda \text{ (in eV)} \tag{5.37}$$

where λ is the wavelength of the light in μm. Only part of the light that is absorbed generates heat energy as shown in Figure 3.1. To calculate the percent of energy that is absorbed as heat, the equivalent bandgap energy of the light, $E_{g\,Light}$, is compared with the bandgap of the absorbing material, silicon (Eg_{sil} = 1.12 eV). To calculate percentage of photon energy converted to heat, the following equation is used.

$$Percent_{Heat} = (E_{g\,Light} - E_{gSil})/E_{Light} \tag{5.38}$$

The power absorbed in material as heat is (P_{abs}) calculated by multiplying Equations 5.36 and 5.38,

$$P_{abs} = PE_{abs}Percent_{Heat} \tag{5.39}$$

The area of laser beam spot used to calculate power per area is

$$A_{spot} = \pi r_1 r_2 \tag{5.40}$$

where is r_1 the short radius of the ellipse and r_2 is the long radius of the ellipse, as was shown back in Figure 4.4(a).

The heating power per area is given by the equation,

$$P_{area} = P_{abs}/Area_{spot} \text{ (W}/\mu\text{m}^2) \tag{5.41}$$

The surface area of the actuator that is absorbing photon energy/heat is given by the equation,

$$SA = N_C r_2 w_C \tag{5.42}$$

where *SA* is the surface area of the actuator under the laser beam, N_C is the number of beams in the chevron, r_2 is the long radius of the elliptical beam, and the w_C is the width of each chevron beam.

The actual heating power absorbed by the actuator arms is given by,

$$Pac_{abs} = P_{area}SA .$$ **(5.43)**

The $\dot{q}_{laser}$, or heat power generated in the actuator is given by,

$$\dot{q}_{laser} = Pac_{abs}/(SAth) \quad (\text{W}/\mu\text{m}^3)$$ **(5.44)**

where *SA*th* is the volume of the chevron beams under the laser beam. The magnitude of the internal heat generation is governed by the size of the laser beam dot. The smaller the beam, the more intense the energy, and thus the more internal energy is generated (higher $\dot{q}_{laser}$). Figure 5.14 is a plot from the model illustrating the qdot, or energy per volume, induced into chevron actuator arms by a laser beam with an elliptical dot shape varying in radius. The smaller the radius (to the left of the plot) the more heating power is generated in the actuators.
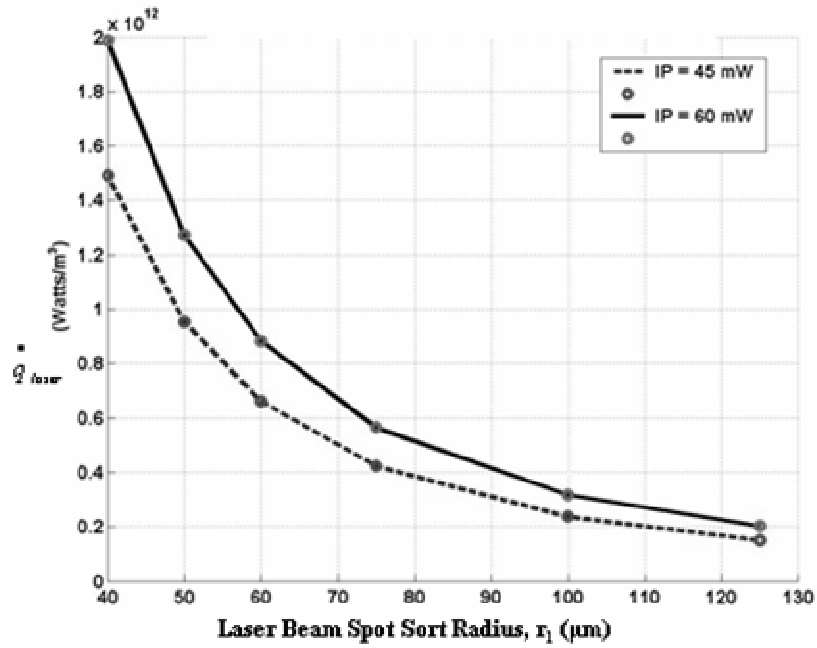
Figure 5.13: Plot from the model illustrating the $\dot{q}_{laser}$, or energy per volume, induced into chevron actuator arms by a laser beam with an elliptical dot shape varying in radius.

Figure 5.15 (a) is a model temperature distribution plot for a chevron actuator arm induced by a laser beam with an elliptical dot shape centered on the actuator, and (b) is a captured image from digital video of corresponding illuminated actuator. The temperature distributions curves induced by the laser generated qdot shown above in Figure 5.14 are seen in Figure 5.15. The MatLab code for Figure 5.14, Figure 5.15 and Figure 5.16 is in Appendix B, MatLab Code for Chevron Hot Arm Actuator Laser Ellipse Beam Simulation, starting on page B1.
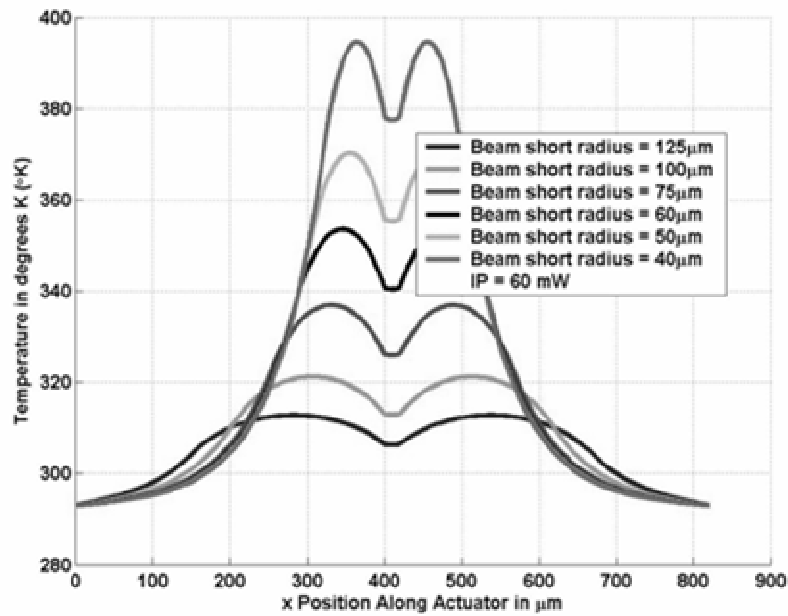
(a)
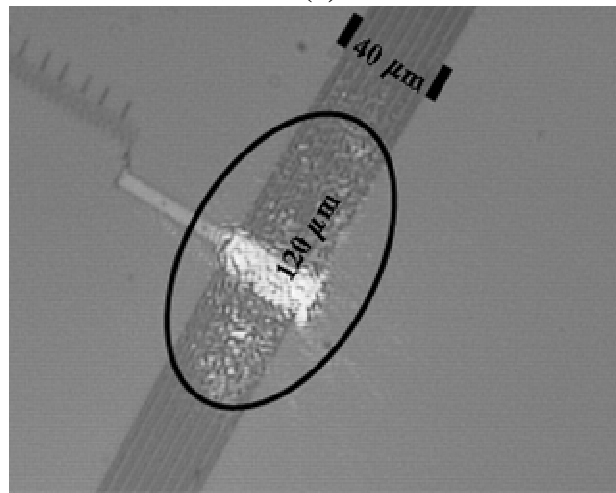
(b)

Figure 5.14: (a) Model temperature distribution plot for a chevron actuator arm induced by a laser beam with an elliptical dot shape centered on the actuator, and (b) is a captured image from digital video of corresponding illuminated actuator.

Figure 5.16 is a plot of the predicted deflection for a chevron actuator corresponding to the temperature distribution graph in Figure 5.16 (a), varying the deflection with the laser beam dot size. Notice that at a laser beam dot radius of 40 µm (far left of plot), the model predicts a deflection of about 1.5 µm for a pulsing laser power of 60 mW. The plots have two curves, one at 45 mW initial laser power, which is what the laser diode used in this experiment is rated for in

continuous wave (CW) mode. The other curve is for 60 mW of initial laser power, which is what

the laser diode is rated for in pulsed mode.
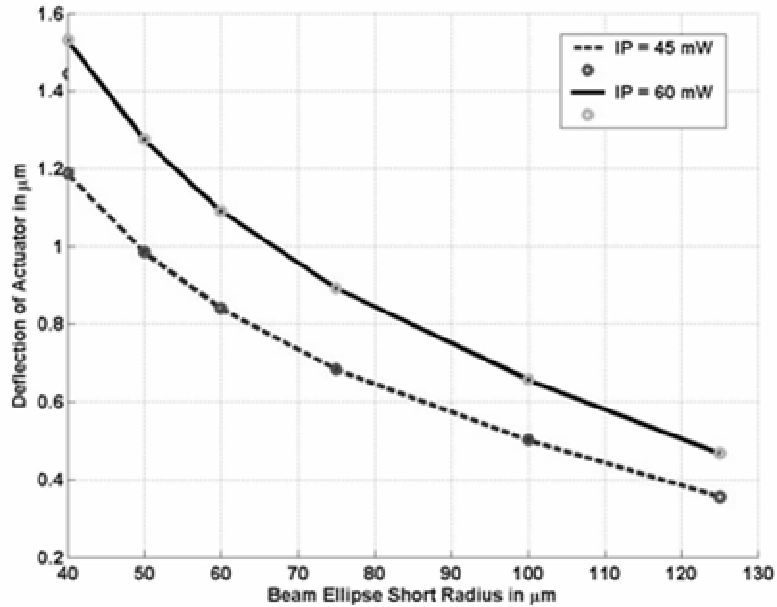
Figure 5.15: Plot of the predicted deflection for chevron actuator corresponding to the temperature distribution graph in Figure 5.16 (a), varying the deflection with the laser beam dot size.

Figure 5.17 (a) is a modeled temperature distribution plot for a chevron actuator arm

induced by a laser beam with an elliptical dot shape asymmetrically illuminated on one side of

the actuator, and (b) is a captured image from digital video of corresponding illuminated

actuator. When the laser illuminates the actuator in an asymmetric fashion as shown in Figure

5.17 (b), a temperature distribution is generated as seen in Figure 5.17 (a). This asymmetric

heating was seen, during experimentation, to cause out of line of the axis of symmetry of the

chevron actuators. But this was compensated for in the actual microrobot designs by the

conformal coating drive shaft housings, which enforced a rectilinear motion.
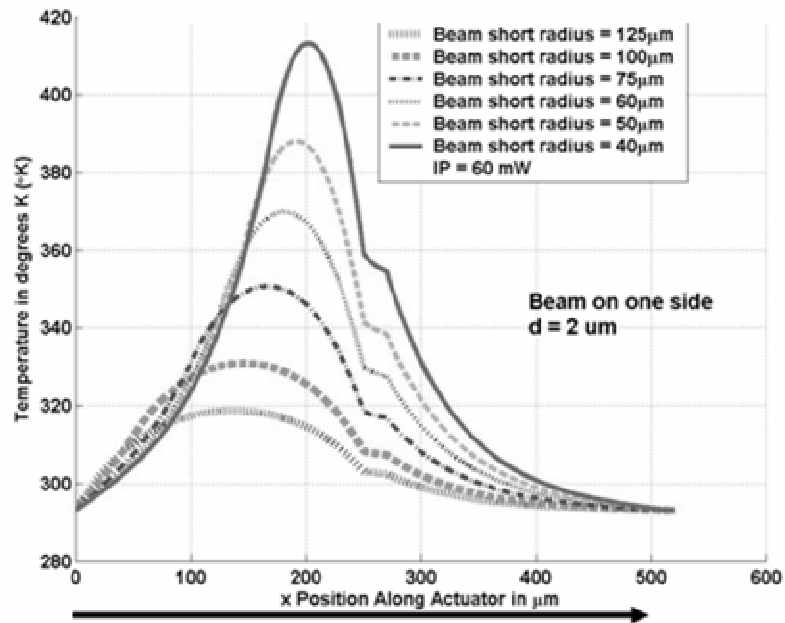
(a)
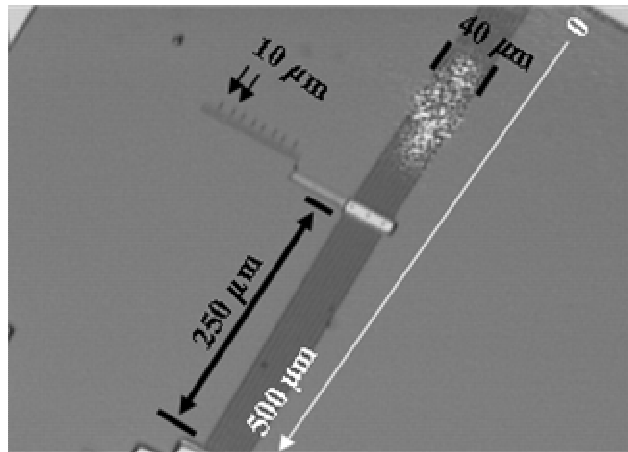
(b)

Figure 5.16: (a) Modeled temperature distribution plot for a chevron actuator arm induced by a laser beam with an elliptical dot shape asymmetrically illuminated on one side of the actuator, and (b) is a captured image from digital video of corresponding illuminated actuator.

The model allows the distance from the actuator to the substrate to be varied, so the effect of events that cause a shortening of the distance to the bulk substrate heat sink can be predicted. Figure 5.18 is a plot showing the temperature distribution in chevron actuator arms with the actuator closer to the surface, as would happen with a released microrobot. The reduction in temperature caused by shortening the distance to the substrate can be seen by comparing the

maximum temperature in Figure 5.18, (358 K) with the maximum temperature in Figure 5.17 (415 K). This shows the effect of bringing the actuator from 2 µm from the surface, closer, down to 0.75 µm from the surface.
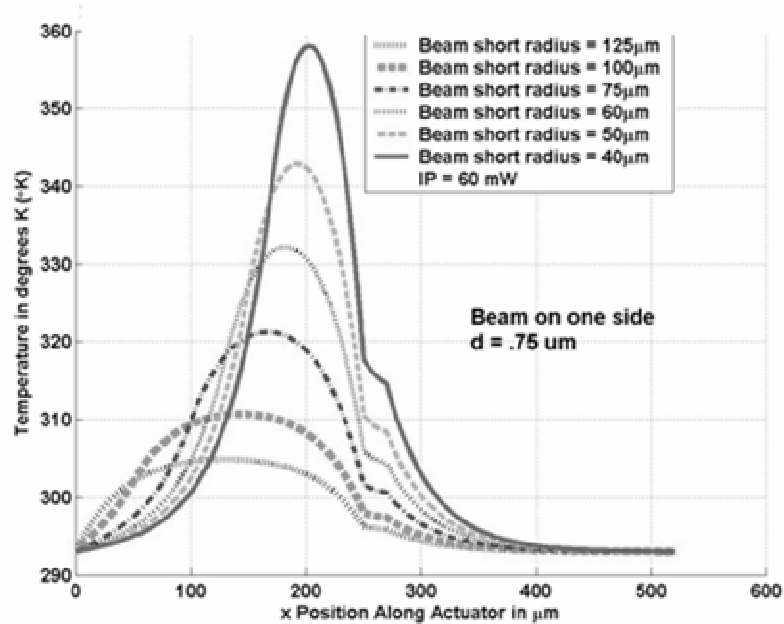
Figure 5.17: Plot showing the temperature distribution in chevron actuator arms with the actuator closer to surface, as would happen with a released microrobot.

5.5. Conclusion

In conclusion, an electrothermal model was developed to predict temperature distribution, thermal expansion and deflection. This model was developed with five temperature dependant parameters, which were varied with temperature. This model was verified by a gold-silicon eutectic temperature experiment and by the actual deflection predicted as compared with experimental deflection. An optothermal model was developed from the electrothermal model by substituting the laser heat generating term, or $\dot{q}$, for the electrical heating. These models predict the deflection of chevron actuators under electrothermal or optothermal actuation.

In the next chapter, Chapter 6, the experimental procedures used to test the fabricated test chevron actuators and prototype microrobots from the designs in Chapter 4 will be detailed. The experimental results gained from experiments in the next chapter verify the models introduced in this chapter. The experimental results and the model results are compared in Chapter 7.

5.5. Bibliography

[1] Y. Dong, A. Khajepour and R. Mansour, "Modeling of two-hot-arm horizontal, thermal actuator," *Journal of Micromechanics and Microengineering*, vol. 13 pp. 312–322, 2003.

[2] J. T. Butler, V. M. Bright, and W. D. Cowan, "Average Power Control and Positioning of Polysilicon Thermal Actuators," *Sensors and Actuator*s, vol. 72, pp. 88–97, 1999.

[3] P. E. Kladitis, Class Notes and discussion, EENG 777, Advanced MEMS, Graduate School of Engineering and Management, Air Force Institute of Technology, Wright Patterson AFB, OH, Summer Quarter 2003.

[4] http://www.memscap.com/memsrus/svcsdata.php.

[5] Y. T. Cheng, L. Lin, K. Najafi, "Localized Silicon Fusion and Eutectic Bonding for MEMS Fabrication and Packaging," *Journal of Microelectromechanical Systems*, vol. 9, no. 1, pp. 4-14, March 2000.

[6] G. T. A. Kovacs, *Micromachined Transducers Sourcebook,* WCB/McGraw-Hill, Boston, Stanford University, 1998.

[7] M. J. Sinclair, "A High Force Low Area MEMS Thermal Actuator," *2000 Inter Society Conference on Thermal Phenomena*, pp. 127-132, 2000.

[8] Y. Lai, J. McDonald, M. Kujath and T. Hubbard, "Force, Deflection and Power Measurements of Toggled Microthermal Actuators," *Journal of Micromechanics and Microengineering*, Vol. 14, pp 49-56, 2004.

[9] M. Chiao, Li. Lin, "Self-Buckling of Micromachined Beams under Resistive Heating," *Journal Of Microelectromechanical Systems*, Vol. 9, No. 1, pp. 146-151, March 2000.

[10] L. Que, J. Park, and Y. B. Gianchandani, "Bent-Beam Electrothermal Actuators—Part I: Single Beam and Cascaded Devices," *Journal Of Microelectromechanical Systems*, Vol. 10, No. 2, pp. 247-254, June 2001.

[11]   D. M. Burns, V. M. Bright, "Investigation of the Maximum Optical power Rating for a Micro-Elctro-Mechnical Device," *International Conference on Solid State Sensors and Actuators*, pp. 335-338, 1997.

[12]   Q. Huang, N. Lee, "Analysis and Design of Polysilicon Thermal Flexure Actuator," *Journal of Micromechanical and Microengineering*, vol. 9, pp. 64–70 1999.

[13]   S. M. Sze, *Semiconductor Devices, Physics and Technology*, New York, John Wiley & Sons Inc., 2002.

[14]   J.A. King, *Materials Handbook for Hybrid Microelectronics*, Artech House, London, UK, 1988.

[15]   http://users.wpi.edu/~ierardi/FireTools/air_prop.html.

6.   Experimental Procedures

This chapter discusses the experimental procedures and equipment used to test and characterize the optothermal actuators and microrobots. This chapter explains the experiments used to test the designs and concepts from Chapter 4 and the models in Chapter 5.

Section 6.1 covers the post processing and release of PolyMUMPs chips. Section 6.2 discusses the video capture equipment used in the collection of data. Section 6.3 discusses electrical power and frequency testing of the optothermal actuators. The last section of this chapter, Section 6.4, discusses laser power and frequency testing used to characterize the optothermal actuators and laser powered microrobots.

6.1. Post Processing and Release of PolyMUMPs Chips

PolyMUMPs chips come from the foundry covered with a protective photoresist layer. The polysilicon devices on the chips are surrounded by highly phosphorous-doped silicon dioxide (PSG) sacrificial layers which must be dissolved to release the devices. The release process uses assorted chemicals to remove the photoresist and silicon dioxide.

The release process was performed in a class 10,000 Clean Room. Figure 6.1 is a photo graph of the clean room acid chemical station, with a venting hood. Because of the dangerous chemicals used in the release process and the dangerous vapors they can give off, all steps of the process but step 7 were performed under the protective hood as shown in Figure 6.1. Figure 6.2 shows photographs of the PolyMUMPs HF release setup, with (a) being the chemicals and safety equipment and (b) being the CO2 critical point dryer. Hydrofluoric acid (HF) could cause grave injury if it is allowed to contact the skin. Therefore, acid resistant laboratory apron, rubber gloves and eye/face protection are worn, as seen on the right side of Figure 6.2. Figure 6.2 also illustrates the experimental setup used throughout the release process. Table 6.1, PolyMUMPs

Chip Release Steps, list the steps used in the process. These steps were adapted from those used by Kladitis [2] and Caffey [3]. Column one lists the release steps, column two lists the time required for that step, and column three lists the purpose of each step.

Figure 6.1: A photo graph of the clean room acid chemical station, with a venting hood.

(a)   (b)
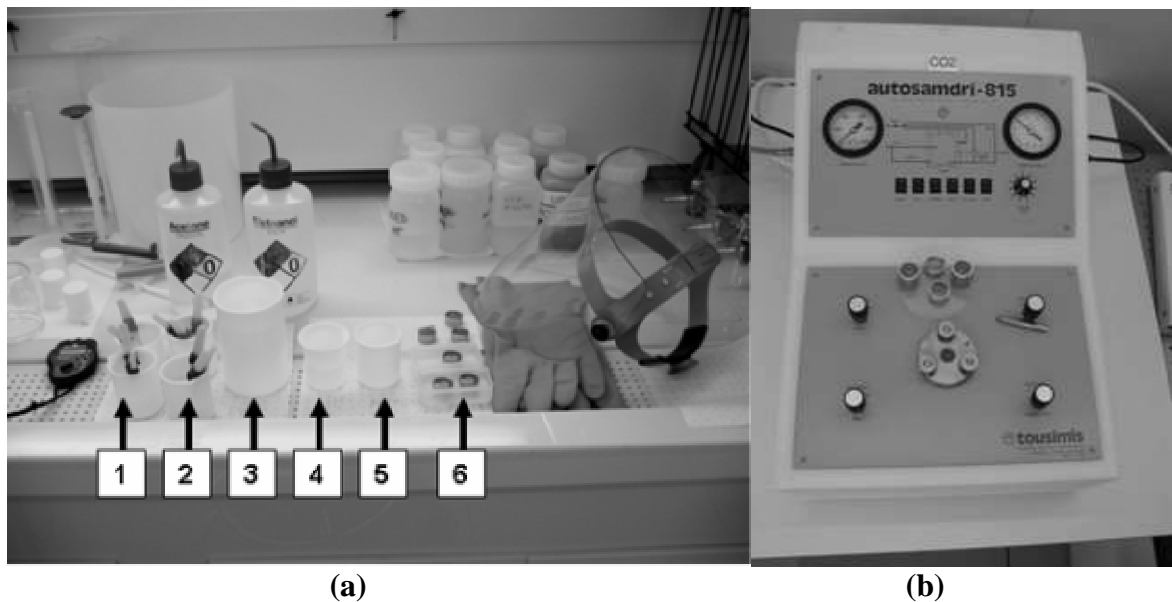
Figure 6.2: Photographs of the PolyMUMPs HF release setup, with (a) being the chemicals and safety equipment and (b) being the CO_2 critical point dryer.

Table 6.1: PolyMUMPs Chip Release Steps.

Step	Time	Purpose
Pre-step: Mount chips in acid resistant tweezers, as seen in Figure 6.2.		Restrain chips from falling to bottom of chemical baths and allow easy transfer between chemicals.
1. Soak chips in 50 ml of acetone. See square 1 in Figure 6.3.	15 minutes.	Removes the protective layer of photoresist.
2. Soak chips in 50 ml of methanol. See square 2 in Figure 6.3.	15 minutes.	Used to rinse any acetone and photoresist residue that may remain from step 2.
3. Soak/stir chips in 500 ml of deionized water. See square 3 in Figure 6.3.	30 seconds	Displace the methanol from the chip to prepare for HF bath.
4. Soak chips in 50 ml 49% HF. See square 4 in Figure 6.3.	4-5 minutes.	Etch sacrificial PSG layers, releasing the mechanical devices on the chip.
5. Dip/lightly stir chips in 50 ml, 5:1, methanol:deionized water solution. See square 5 in Figure 6.3.	5 seconds.	Stop etching by diluting/removing the HF acid. Very slight stirring helps release structures, but hard stirring can break them.
6. Soak chips in methanol, placing them in screened containers used for critical CO_2 drying. See square 6 in Figure 6.3.	5 minutes or until ready for CO2 dryer.	Keep released structures wet without water until ready for drying process. Warning, allowing exposure to air at this point will cause severe stiction.
7. Place chips (already in screened container) in Autosamdri-815 automatic CO_2 critical point dryer. See Figure 6.2 (b).	About 30 minutes.	Dries devices at a supercritical CO_2 temperature and pressure point, removes all H_2O, and prevents stiction. Follow instructions in 815 manual.
Note: After the chips are removed from the dryer, they should immediately be tested, or else placed in dry gel packs and stored in humidity free nitrogen charged storage boxes. This will allow devices to remain free from stiction.		

6.2. Video Capture Setups

Devices were examined under a microscope with digital cameras at both the probe station and the laser table. The images from the cameras were fed both into television monitors and an ATI video capture card on a computer. Figure 6.3 shows photographs of the probe station and digital camera setup, with (a) being the microscope, digital camera and stage, and (b) being a

digital video capture picture used to measure actuator deflection. The digital cameras, as seen in square A, Figure 6.3, allow digital video to be captured into still images and movies that can be used to observe and measure actuator deflection, as seen in Figure 6.3 (b).

| (a) | (b) |
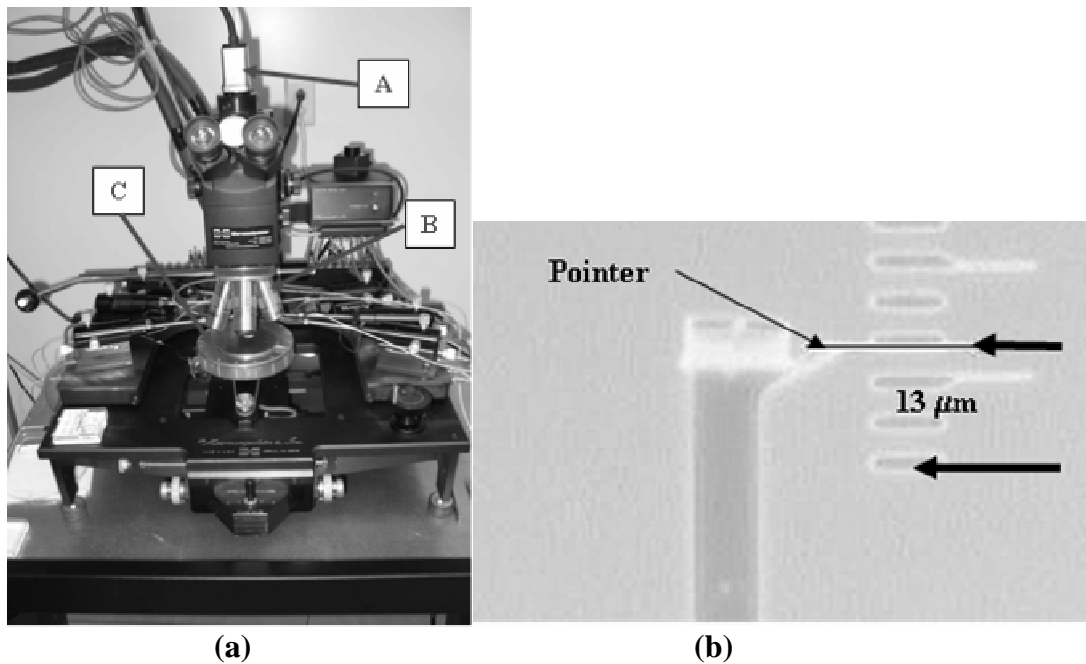
Figure 6.3: Photographs of the probe station and digital camera setup, with (a) being the microscope, digital camera and stage, and (b) being a digital video capture picture used to measure actuator deflection.

For eye safety reasons, digital cameras and television monitors are the only way to examine device reaction at the laser table, because the class 3b laser, amplified through a microscope magnifying lens, could easily and quickly blind the user. Therefore all eyepieces were taped over with black tape, and only the monitors were used for observation. Figure 6.4 shows photographs of the laser table camera and test equipment setup, with (a) cameras and test equipment, (b) being the laser driver, cooler and signal generator. As seen in Figure 6.4, two cameras and two monitors were used to observe the laser devices and steer the laser beam. The camera designated by square B1 in Figure 6.4 (a) was used in concert with the monitor designated by square E in Figure 6.4 (b) to steer the laser beam and give a macro view to what was happening with the chip. The camera designated by square A1 in Figure 6.4 (a) was used in

concert with the monitor designated by square A2 in Figure 6.4 (a) to observe a highly magnified picture of the devices. Camera A1 was also hooked to an ATI video capture card on the computer to record deflections of the actuators and microrobots. The bundled ATI MultiMedia Center, version 7.7, software was used for capturing digital photographs as jpeg files and movies as mpeg files.

(a) **(b)**
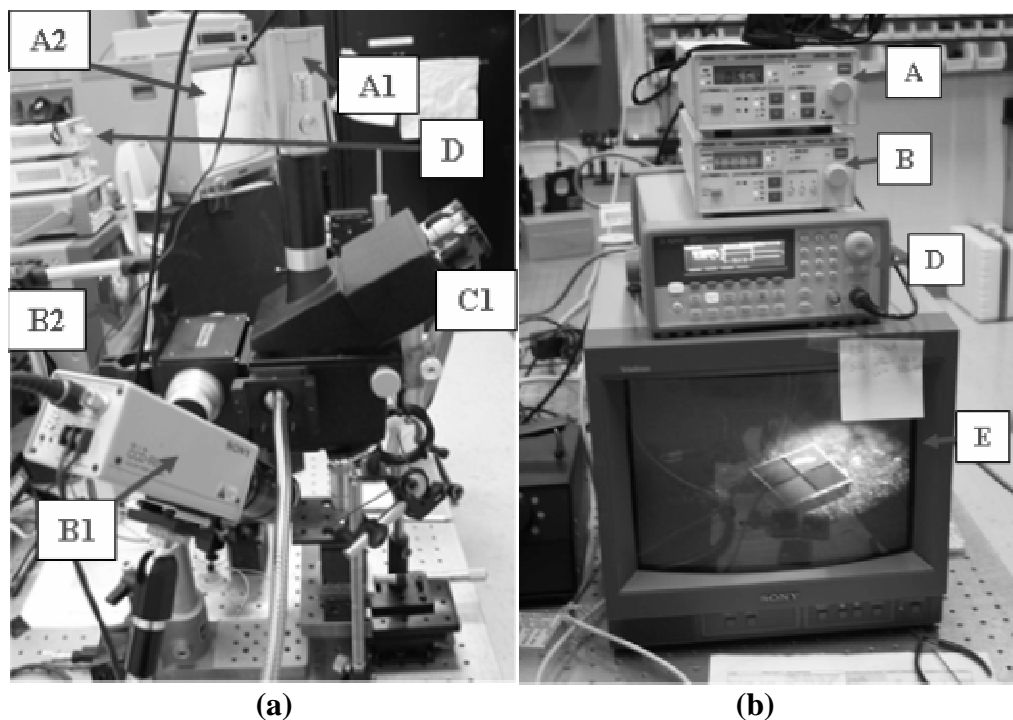
Figure 6.4: Photographs of the laser table camera and test equipment setup, with (a) cameras and test equipment, (b) being the laser driver, cooler and signal generator.

An AMRAY 1810 scanning electron microscope (SEM) was very useful to examine very small details on the devices, especially with side views. Figure 6.5 shows photographs of the scanning electron microscope (SEM) and computer for digital SEM micrograph capture, with (a) being the SEM setup, and (b) being the SEM micrograph captured by SEM and computer for device side view and examination. The software used for video capture was the Orion version 5.20 Digital image Capture software. Minor discrepancies, with disastrous operational effects, which may be undetectable under a regular microscope, are more easily found using the SEM for

examination. Procedures for turn-on, turn-off, loading, operation and unloading the SEM can be found in the AMRAY manual and directions notebook provided with the SEM. One word of caution, it was found that devices that were exposed under the SEM were no longer usable in actuation tests, as the electron beam in the SEM left a huge static charge on the chip, causing devices to adhere to each other and the surface of the chip.

(a) **(b)**
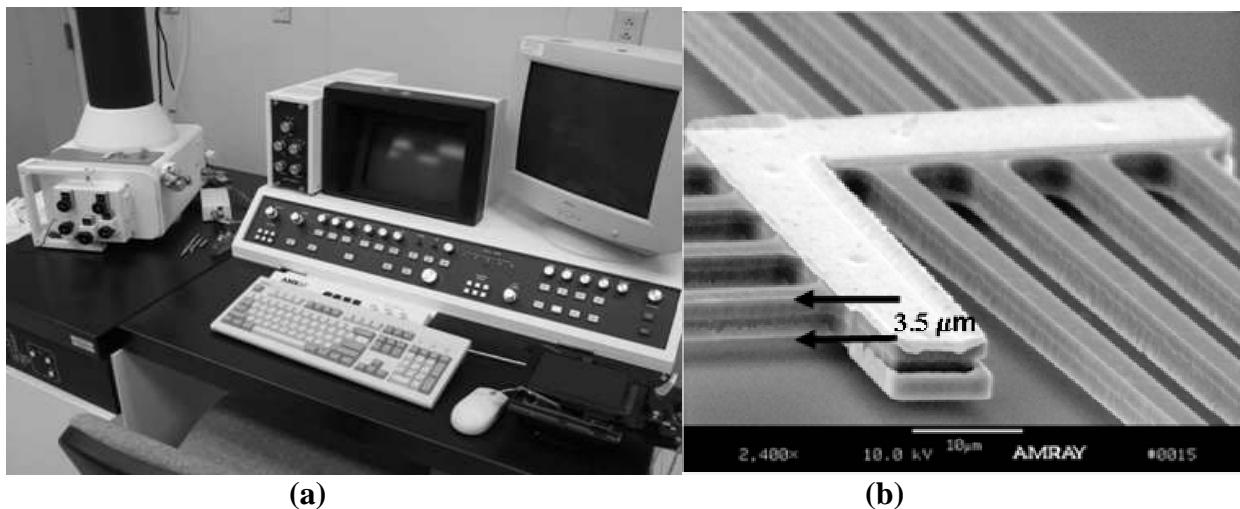
Figure 6.5: Photographs of the scanning electron microscope (SEM) and computer for digital SEM micrograph capture, with (a) being the SEM setup, and (b) being the SEM micrograph captured by SEM and computer for device side view and examination.

6.3. Electrical Experimental Setups

Electrical experiments and frequency characterizations of test actuators were carried out at the probe station. Figure 6.6 shows photographs of the probe station test equipment, with (a) being the voltmeter, amp meter and DC voltage Source, and (b) being the probe station with a vacuum stage to hold chips. Table 6.2, MEMS Video Capture and Electronic Test Equipment, lists the equipment used in these experiments. The columns list the exact model number used, the pertinent specifications, and the purpose for which each piece of test equipment was used. A rack of test equipment, seen below in Figure 6.6 (a) was used to electrically test all the actuators for comparison with laser actuation. Voltage versus deflection, power versus deflection, and

frequency versus deflection tests were all performed with this equipment. Figure 6.7 shows a photograph of the probe station connections to voltage and signal sources. Figure 6.8 shows a photograph of the test actuators at probe station as observed with video capture camera. Probes would be attached to voltage or signal sources at one end, and connected to gold bonding pads at the other end. All deflections were captured with digital video, and test equipment readings were manually recorded for later comparison and plotting.

Table 6.2: MEMS Video Capture and Electronic Test Equipment.

Model Number	Specifications	Application
MicroManipulator Probe Station. See Figure 6.6 (b).	4 probes, with voltage, signal attachments, video camera, microscope - 5x, 10x, 20x, 50x magnification.	Electronically test MEMS devices, perform manipulation and assembly, take photos and videos.
Optronics video camera and interface box, with ATI video card in computer. See square A in Figure 6.6 (b).		Record MEMS testing videos, record digital photographs through microscope
AMRAY 1810 Scanning Electron Microscope (SEM). See Figure 6.5 (a).	Greater than 20,000X magnification.	3D views of MEMS devices, including side views.
Fluke 8600A Digital Multimeter. See square A in Figure 6.6 (a).	DC, AC (RMS value), Ohms.	Measure voltage, current and resistance.
HP 6236B Triple Output DC Power Supply. See square C in Figure 6.6 (a).	0 - 6 V @ 2.5 A 0 - 20 V @ 0.5 A	DC power supply
Lecroy 9324 Quad 1 Ghz Oscilloscope	Signals to 1 GHz	Measure on observe voltage signals, especially periodic wave signals.
Agilent 33250A Function Waveform Generator. See square D in Figure 6.4 (b)	AC waveforms, fully programmable	Provide programmable signals for device testing
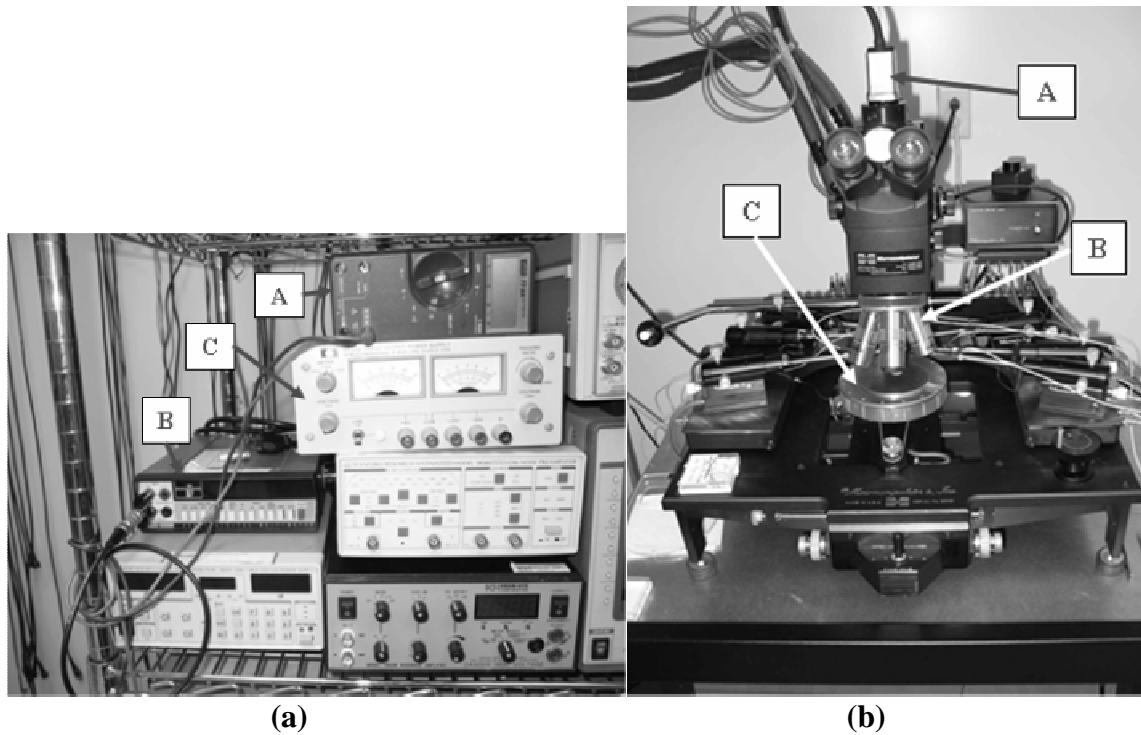
Figure 6.6: Photographs of the probe station test equipment, with (a) being the voltmeter, amp meter and DC voltage Source, and (b) being the probe station with a vacuum stage to hold chips.
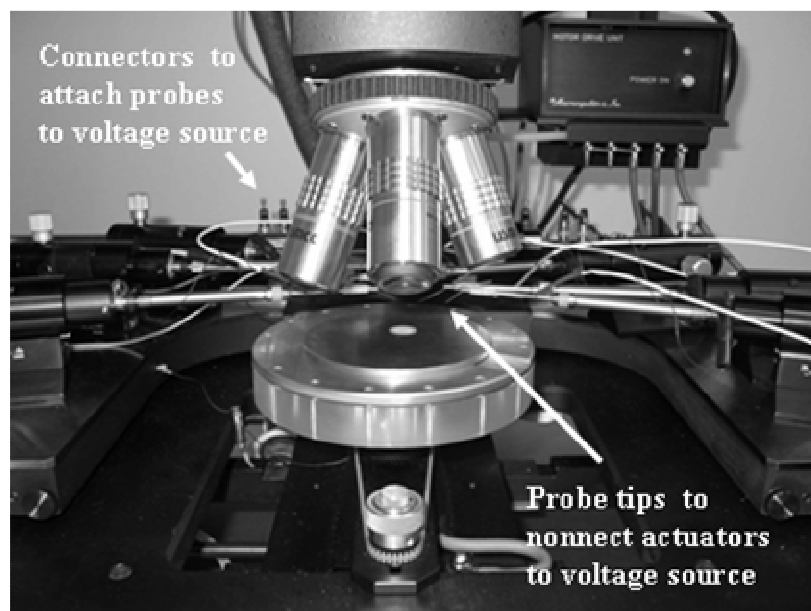
Figure 6.7: Photograph of the probe station connections to voltage and signal sources.
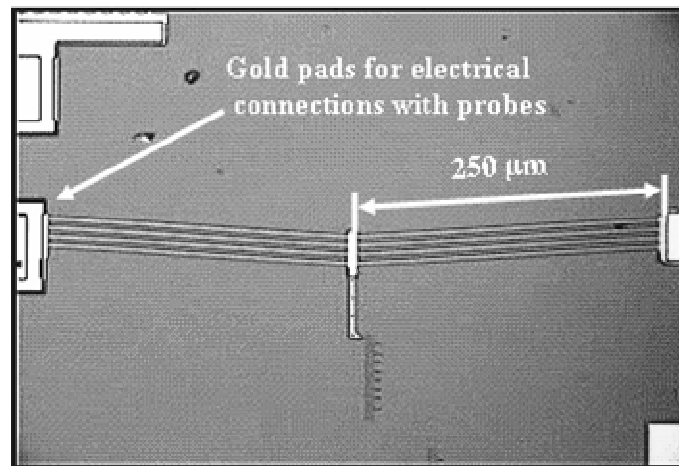
Figure 6.8: Captured video image of a test actuator at probe station as observed with video capture camera.

6.4. Laser Experimental Setups

The actual laser experiments involved setting up a laser to illuminate a 2 mm by 2 mm chip under a microscope. Figure 6.9 is a block diagram of the experimental setup for heating an optothermal actuator with a laser. More details can be found in the next section. A cooled diode laser, with a maximum power output of 45 mW continuous wave (CW) and 60 mW pulsed, and a wavelength of .660 µm, was used. The microscope had a CCD camera attached, and all illuminated surfaces were observed on a monitor. The eye lenses were removed for safety and the holes were taped over with black electrical tape. Laser safety goggles were worn any time laser power was over 5 mW (56.4 mA on laser driver. The laser beam was aligned with 5 mW of power. Figure 6.10 is a plot of driver current versus laser power and was used as a calibration chart. The chart in Figure 6.10 was developed to approximate power readings on the fly, as the power meter used would interrupt the beam, and real power could not be read directly from the power meter anyway (a voltmeter reading had to be converted and calculated.) Power meter readings were recorded from the voltmeter and calculated for each laser driver current level, and the equivalent power versus driver current reading was recorded on the chart. This process

would have to be repeated for each diode placed in the laser driver, due to variations in power

output between diodes.
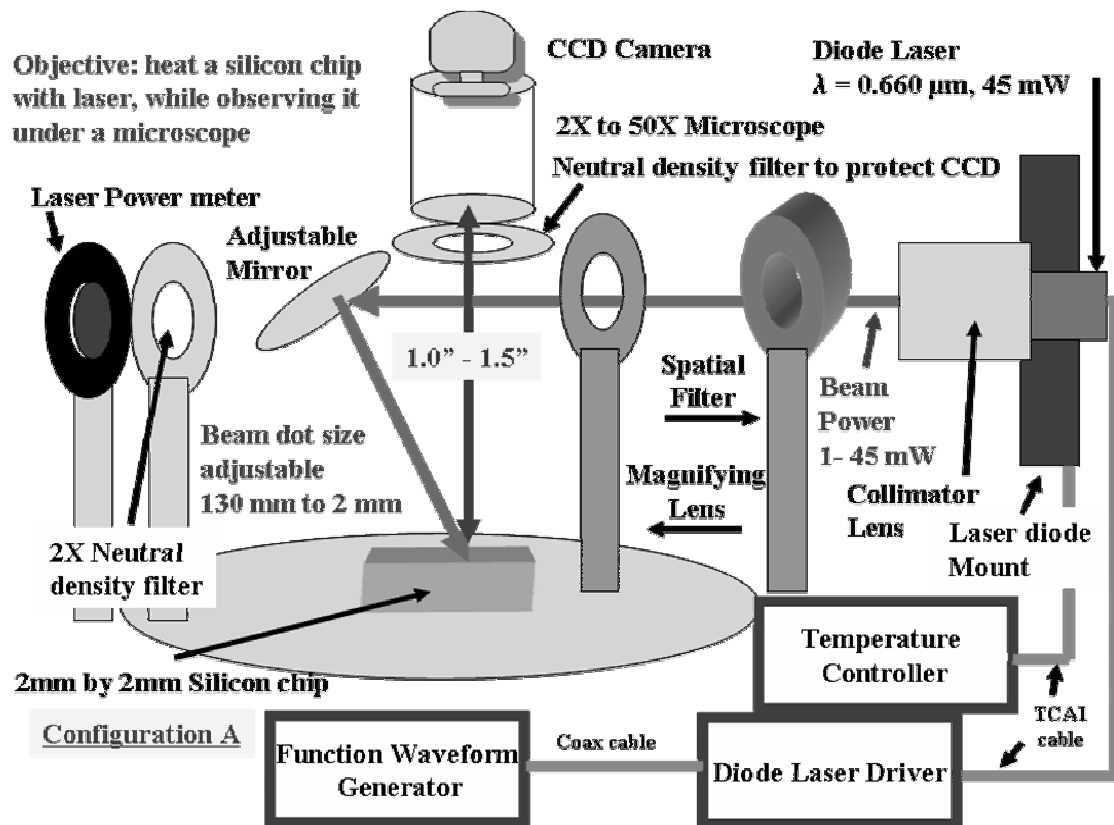
Figure 6.9: Block diagram of the experimental setup for heating an optothermal actuator with a laser.
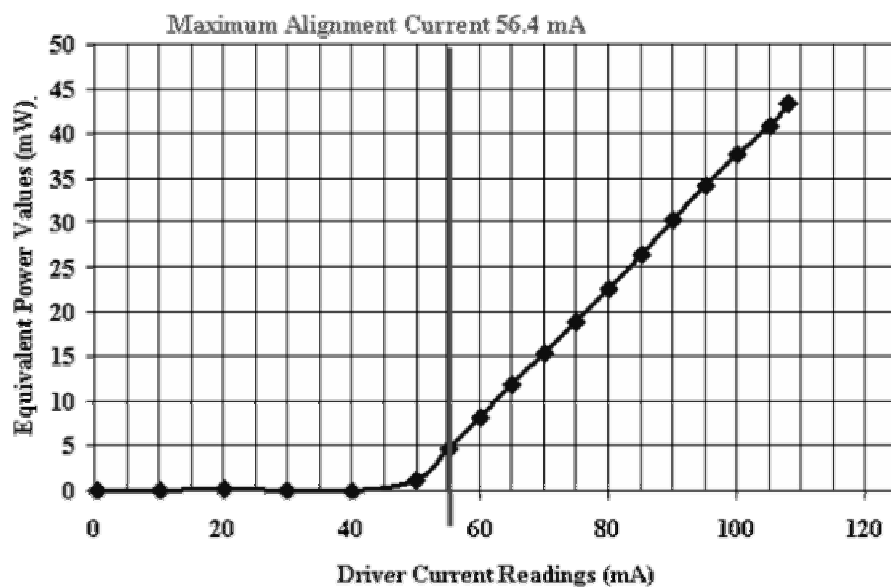
Figure 6.10: Plot showing the current versus laser power calibration chart.

The laser illuminated the target under the microscope at an angle of 45 degrees out from orthogonal to the chip surface (the beam coming from the side of the microscope). A shroud was built around the microscope laser setup to prevent stray laser light from leaving the experiment platform area, as a safety precaution. The laser was pulsed using a sine wave and other waveforms from the signal generator. All optothermal actuator and microrobot behavior was recorded on video.

First the laser beam power was set to 5 mW of continuous wave power, as measured on the power meter. The beam was then focused and aligned on the target using the collimator lens, magnifying lens and the adjustable mirror. Safety goggles were then donned, and the signal generator was turned on, using a 0-950 mV 0-pk sine wave, with a varied frequency. The period and magnitude of the sine wave and other waveforms were varied during the experiment. This signal was fed into the laser driver, and the driver adjusted until the diode driver current reached its maximum of 125 mA at the peak of the sine wave. This equated to the 60 mW maximum power that the laser diode was rated for under pulsed conditions. The laser cooler was kept at 12 ^{0}C for all experiments. The test equipment used is listed below in Table 6.3, Laser Test Equipment. The columns list the exact model number used, the pertinent specifications, and the purpose for which each piece of test equipment was used.

The video of any deflection was then recorded using an ATI video capture card on a PC, which was hooked up to the CCD camera.

Table 6.3: Laser Test Equipment.

Model Number	Specifications	Application
Optronics color video camera and interface box, with ATI video card in computer.		Record MEMS testing videos, record digital photographs through microscope.
EMcal Scientific microscope color video camera.		Camera mounted on microscope.
Function Waveform Generator Agilent 33250A.	AC waveforms, fully programmable.	Provide programmable signals for device testing.
Diode laser driver, ThorLabs LDC500.		Provide programmable signal voltage for driving Laser.
Diode laser mount ThorLabs TCLDM9		Mount and cool diode
Laser diode, Mitsubishi ML101J8.	λ=.660 μm, 45 mW at CW, 60 mW pulsed.	Laser diode for experiments.
Temperature Controller, ThorLabs TEC2000.		Provide cooling for Laser.
Laser Power Meter, ThorLabs S20MM.	20 mW max rating.	Measure laser output power.
Fluke 8600A Digital Multimeter.	DC, AC (RMS value), Ohms	Measure laser output power in concert with Power S20MM meter.
Laser goggles, LG4.	625-830 nm OD3+.	Eye Protection.
WESCO 50X Microscope Assembly.	50X Magnification.	Examine experiments.
ISO 9001 Fiber Optics Illuminator.		Provides light for microscope.
Collimator Lens, Mounted Geltech™ Aspheric Lens, C230TM-B	f=4.5mm 0.55NA, AR Coating: 600-1050 nm	Collimate laser beam.
Spatial Filter, Thor Labs KT310 and P25S	20 X magnifying lens, 25 μm filter hole size.	Concentrate laser beam dot size.
Magnifying lens, Newport BK-7 Precision Bi-Convex Lens.	125 mm focal length.	Concentrate laser beam dot size and adjust dot size.
Adjustable Mirror: Kinematic mirror mount, with mirror; ThorLabs KM100-E02	Steering optic holder with 400-800 nm reflective range mirror	Steer laser beam
Neutral density filters, ThorLabs NE03A.	2X	Absorptive neutral density filter, cuts transmitted power by 50% for power meter measurements.
Sony Trinitron Television.		Monitor for laser experiments.

6.4.1. Laser Table Experimental Setup

Figure 6.11 is a photograph of the laser table setup, showing the complete test equipment, camera and monitor setup. Figure 6.11, squares A1 and A2 show the camera and monitor combination used for steering the laser beam on the chip. Figure 6.11, squares B1 and B2 show the camera and monitor combination used for observing deflection through the microscope. Square B3 is the computer with an ATI video capture card that was used to record video and pictures. Square C shows the laser beam path through the optics.
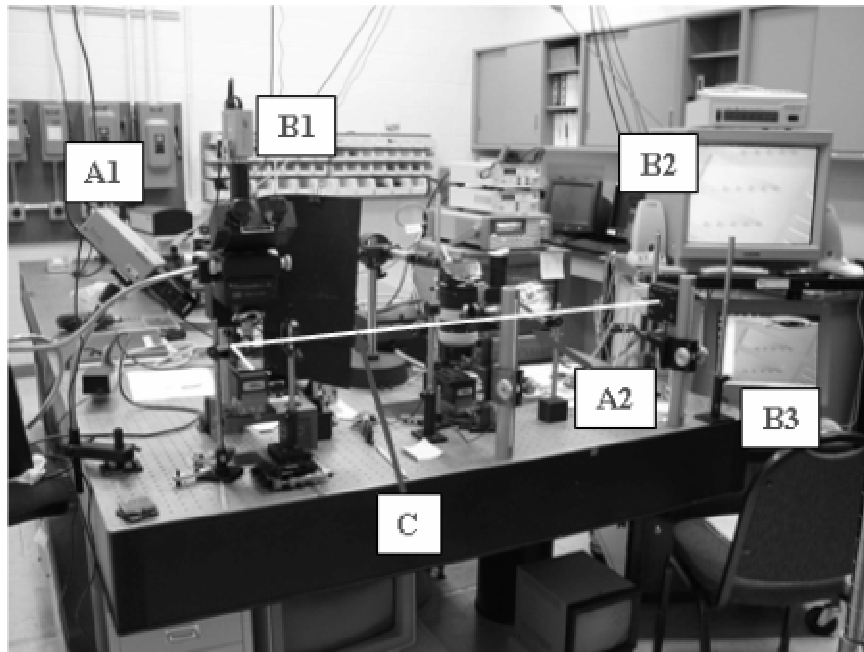
Figure 6.11: Photograph of the laser table setup, showing the complete test equipment, camera and monitor setup.

Figure 6.12 is a photograph of the laser table camera and stage setup showing the different parts of the video and microscope lens setup. Figure 6.12, shows a close-up of the stage area where the specimens were tested. Figure 6.12, square A, shows the camera used to monitor laser beam steering. Figure 6.12, Square B, is the camera for monitoring magnified views of the actuators through the microscope. Square C is the light source for the microscope. It had to be kept on a platform separate from the table, due to the vibration its cooling fan introduced to the

camera picture. Square D is the microscope itself. The microscope magnifying lenses had to be changed out manually each time magnification was changed, because the extra lenses interfered with the laser optics devices and the laser beam path when they were rotated to an off position. Square E is the stage on which test chips were placed. It has micrometer adjustments for the X, Y, and Z directions to provide maximum flexibility. Square F is the mirror used to direct the laser beam toward the chip. It has two adjustment screws that allow the laser beam to be steered in the X and Y directions on the target stage. Square G is the spatial filter, an optics device used to help concentrate the laser beam for focusing a small dot size.
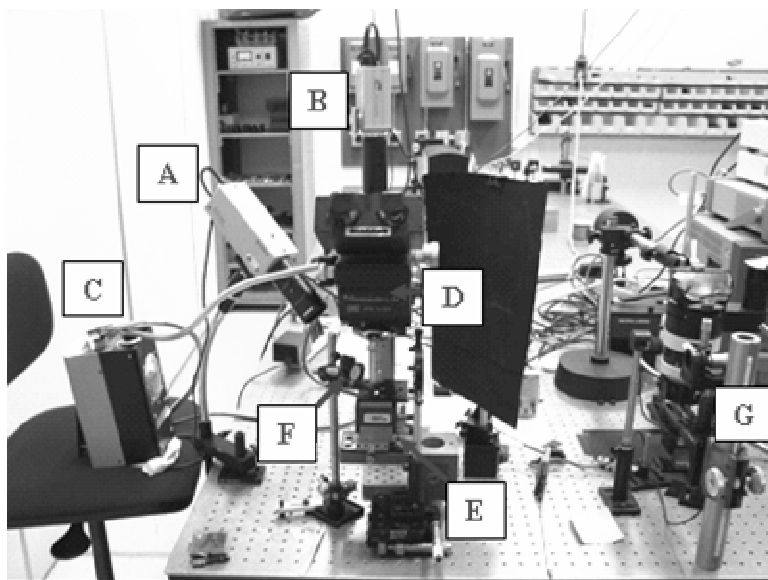
Figure 6.12: Photograph of the laser table camera and stage setup showing the different parts of the video and microscope lens setup.

Figure 6.13 shows photographs of the laser table optics equipment setup, with (a) being the laser driver and laser diode setup and (b) being the spatial filter. Figure 6.14 shows the laser diode assembly and the spatial filter. Figure 6.13 (a), square A shows the collimator lens that is mounted over the laser diode. This lens sends the laser beam out in a straight parallel 150 μm radius beam. Square B is the laser driver input signal that drives the diode with whatever input is produced by the signal generator. Square C is the cooler input that keeps the laser diode at a

constant 12 ^{0}C temperature, thus also at a constant light frequency and steady power level.

Figure 6.13 (b), square A shows the 20X magnifying lens of the spatial filter, which

concentrates the beam to send it through a 25 μm pinhole, then spreads it out to the two inch

magnifying lens. This purifies and concentrates the beam at the expense of some power loss.

This spatial filter was measured to cause a 9.1 percent power loss. However, it allowed the beam

to be concentrated from a minimum 150 μm radius beam dot size, from the original

configuration with only a collimator lens, down to a 40 μm radius beam dot size. This allowed

the laser power to be highly concentrated on the actuator arms, with much less power lost to

illuminating bare substrate.

(a)   **(b)**
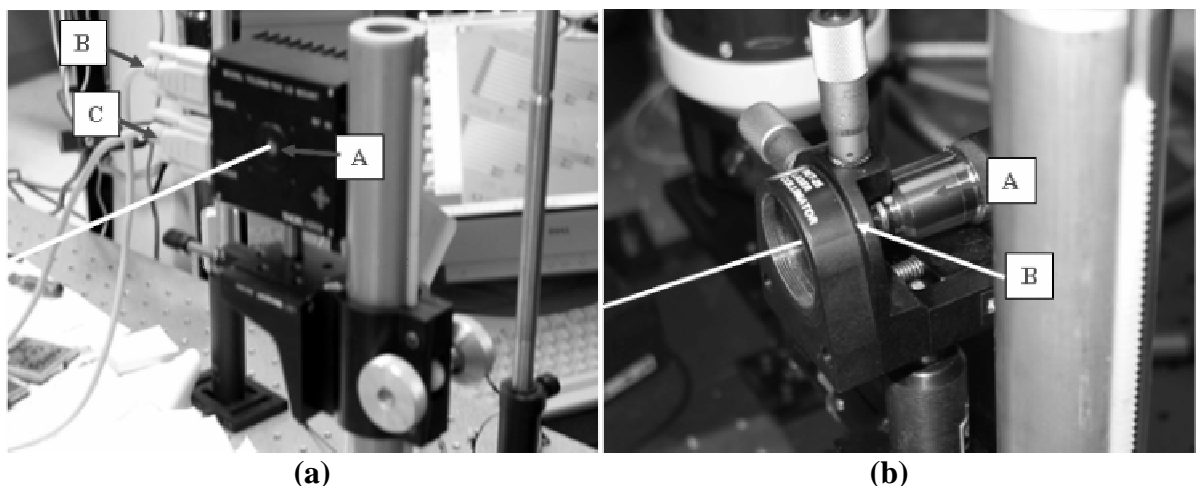
Figure 6.13: Photographs of the laser table optics equipment setup, with (a) being the laser driver and laser diode setup and (b) being the spatial filter.

Figure 6.14 shows photographs of the laser optics equipment setup at microscope, with

(a) being the microscope, optics and stage side view and (b) being the front view, showing the

laser beam path and light concentration. Figure 6.14 shows the final focusing and laser beam

steering optics used to target and illuminate the devices under the microscope. Square A (in both

Figure 6.14 (a) and (b)) shows the stage, with its three micrometers for X, Y, and Z adjustment.

Square B shows the mirror, with it two adjustment screws, one for the X direction and one for

the Y direction, which are used to steer the laser beam to the target. Square C shows the microscope magnifier lens used by the video camera to observe the device actuation. Square D shows the two inch concave magnifying lens used to concentrate the laser beam down to a 40 μm radius beam dot size. An adjustment micrometer at its base adjusts its distance from the mirror and the stage, adjusting the focal distance, and thus allowing the operator to vary the spot size.

Figure 6.15 is an illustration of the laser optics beam focusing, with (a) showing using the collimator lens alone and (b) showing using spatial Filter and two inch magnifying lens. Figure 6.15 shows the effects on the laser beam with two of the optics configurations that were tried. With just the collimator lens alone, the beam dot size could be adjusted down to 150 μm, but never smaller than that. With a spatial Filter and two inch magnify lens, the laser beam dot size could be adjusted down to 40 μm. Note that in Figure 6.15 (a), the beam comes in at a shallow angle, but does not concentrate as much. In Figure 6.15 (b), the beam comes in from a wider angle, but concentrates to a smaller dot size.

(a)　　　　　　　　　　　　**(b)**
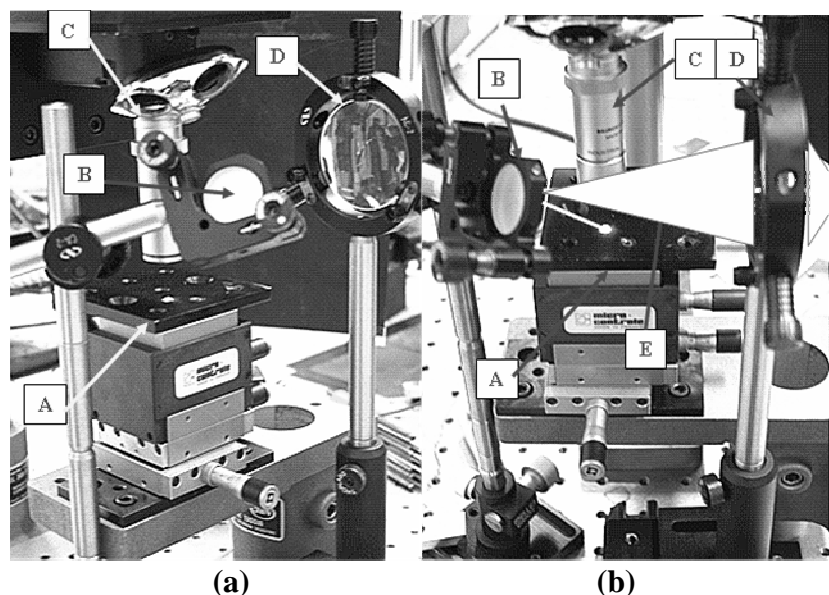
Figure 6.14: Photographs of the laser optics equipment setup at microscope, with (a) being the microscope, optics and stage side view and (b) being the front view, showing the laser beam path and light concentration.

150 *μ*m radius dot size   40 *μ*m radius dot size

(a)   **(b)**
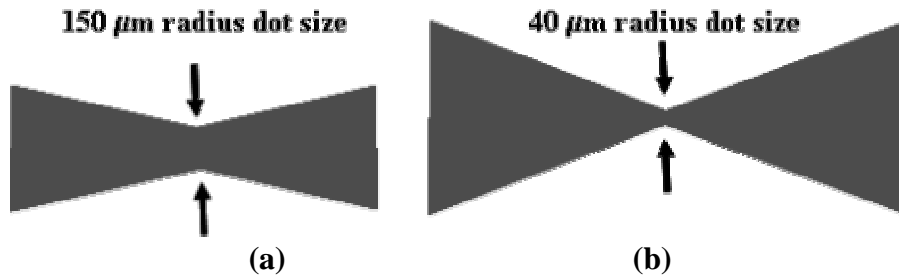
Figure 6.15: Illustration of the laser optics beam focusing, with (a) showing using the collimator lens alone and (b) showing using spatial Filter and two inch magnifying lens.

Figure 6.16 is a photograph illustrating the optics focusing the laser beam with A, the collimator lens, B, the spatial filter and C, the two inch magnifying lens. Figure 6.16 shows how the concentration of the beam size is accomplished. The beam comes out of the collimator lens (square A) at 150 μm. The spatial filter (square B) spreads the beam out wider than the collimator lens, but this allows the magnifying lens (square C) to concentrate the beam to a smaller spot size. In square C of Figure 6.16 one can see how the beam is spread out to a wide angle, and then concentrated quickly to a small dot size by the two inch magnifying lens. The critical distances, L_1, L_2, and L_3 in Figure 6.16 are governed by the following equation,

$$(1/(L_2 + L_3)) + (1/L_1) = 1/F_L \tag{6.1}$$

where L_1 is the length from the spatial filter to the magnifying lens , L_2 is the distance from the magnifying lens to the mirror, L_3 is the distance from the mirror to the specimen, and F_L is the focal length of the magnifying lens. The focal length, F_L, of the magnifying lens used in this experiment was 125 mm.
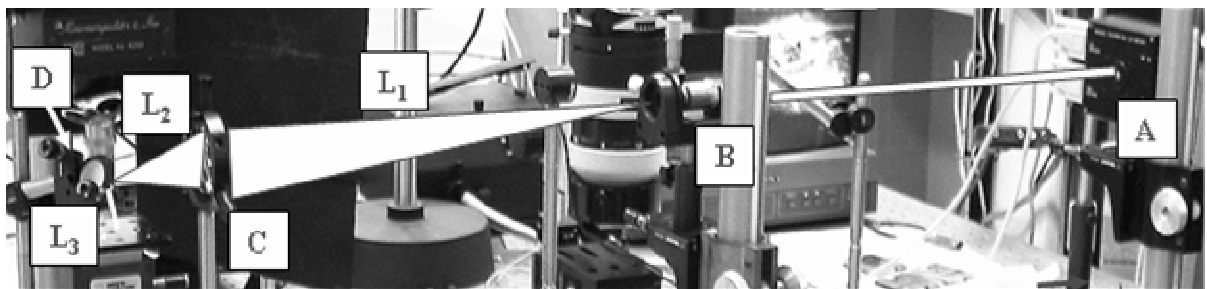
Figure 6.16: Photograph illustrating the optics focusing the laser beam with A, the collimator lens, B, the spatial filter and C, the two inch magnifying lens.

Figure 6.17 is a photograph of the laser power meter equipment setup with A, the 50%
neutral density filter, B, power meter head, C, the power meter head, D, the voltmeter for taking
readings, and E, the chart for interpreting the readings. Figure 6.17 shows the equipment
required to measure the power of the laser beam. Square A shows the power meter head, which
is covered by a 2X density filter lens (square B), because it could only handle 20 mW of power.
This feeds into the power meter (square C), which turns it into a voltage reading, which is
displayed on the voltmeter (square D). The reading on the voltmeter is multiplied by the setting
on the power meter, and then multiplied by two to account for the 2X filter. Because this was
too complicated a process for taking fast readings, numerous readings were taken, and compared
to the current on the laser driver. A chart was prepared (square E) so that power levels could be
estimated directly from the driver current. These were checked on a regular basis to ensure
accuracy.
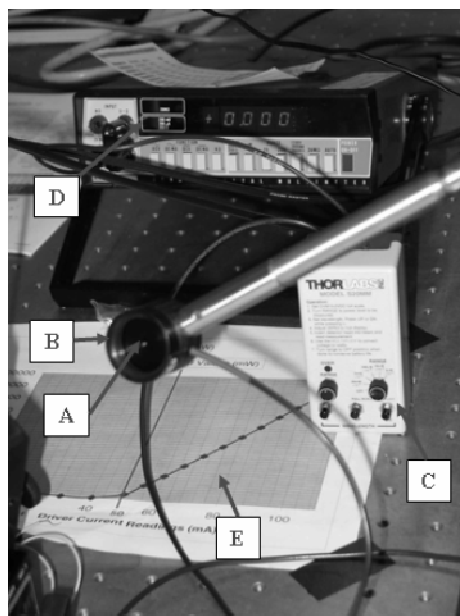
Figure 6.17: Photograph of the laser power meter equipment setup with A, the 50% neutral
density filter, B, power meter head, C, the power meter head, D, the voltmeter for taking
readings, and E, the chart for interpreting the readings.

6.5. Device Characterization

The chevron test actuators were designed so that they could be activated both electrothermally and optothermally. This was done so that their operation under electrical activation could be directly compared with their operation using laser power activation. As much as possible, all tests, especially the frequency response tests, were performed exactly the same. In the following section, all tests regimens are assumed to be used for both electrical and laser actuation unless otherwise specified. Because of the design with a gold frame, the actual microrobots could not be activated electrically, so were only tested by manual probing and under laser actuation.

6.5.1. Laser Testing

Before laser tests could be performed, the laser dot size had to be calibrated to match the laser dot size radius with that of the model. This was accomplished by shining the laser beam on an array of reflective structures of a known length. Figure 6.18 shows digital images illustrating the calibration of the laser dot size using reflective structures of known length, with (a) being the reflective residual stress structures, (b) being the 80 μm diameter laser dot size (40 μm radius), (c) being the 100 μm diameter laser dot size (50 μm radius) and (d) being the 160 μm diameter laser dot size (80 μm radius). The dot size adjustment was accomplished by adjusting the micrometer at the base of the two inch magnifying lens. For most tests, the 80 μm diameter (40 μm radius) dot size was used, as this gave the most concentrated power on the 250 μm x 8 beam and 400 μm x 8 beam chevron actuators. Figure 6.19 shows captured digital video images illustrating the concentrated laser dot used for PolyMUMPs 58 test actuators in asymmetric illumination operation with (a) being the 250 mμ by 8-beam chevron, (b) being the 350 μm by 16-beam chevron, (c) being the 400 μm by 8-beam chevron, and (d) showing the laser dot focused on the center of the actuator. The laser beam was purposely distorted into an elliptical

shape using the collimator lens in front of the diode. This elliptical shape was further enhanced by the beam shining on the actuator at a 44 degree angle. Figure 6.19 (b) shows a very good picture of the complete 80 μm diameter dot size. All pictures are taken at 5 mW of laser power to prevent the camera from being made nonfunctional by the bright flashing of the laser. The dot size increased about 25% under full power, due to the size of the beam coming out of the diode under full power.

(a)   **(b)**

(c)   **(d)**
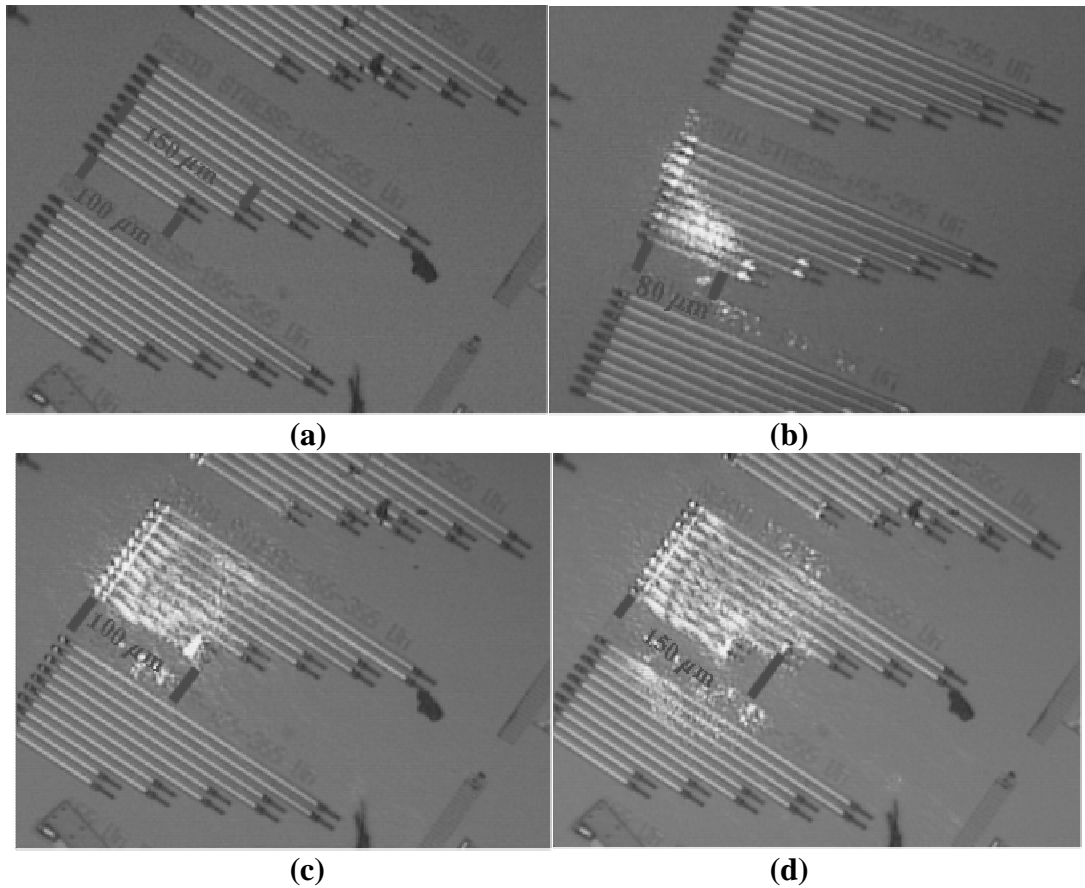
Figure 6.18: Digital images illustrating the calibration of the laser dot size using reflective structures of known length, with (a) being the reflective residual stress structures, (b) being the 80 μm diameter laser dot size (40 μm radius), (c) being the 100 μm diameter laser dot size (50 μm radius) and (d) being the 160 μm diameter laser dot size (80 μm radius).

The brightness of the laser at full power overcomes the synchronization pulse in the video signal, and makes the video components, especially the digital VCR non-operational. This was compensated for by brightening the light fed through the microscope and putting the main part of

the laser dot out of the picture during full power pulsed operations. This generally made it easier to detect the difference between flashing video appearing like deflection or movement of parts, and actual physical deflection.

Figure 6.19 shows the actual test actuators being illuminated by the laser. Figure 6.19 (d) shows the original concept of shining the laser on the center of the actuator. Too much power was lost due to reflection with this method; therefore the method of shining the entire beam on the arms on just one side of the actuator was used.
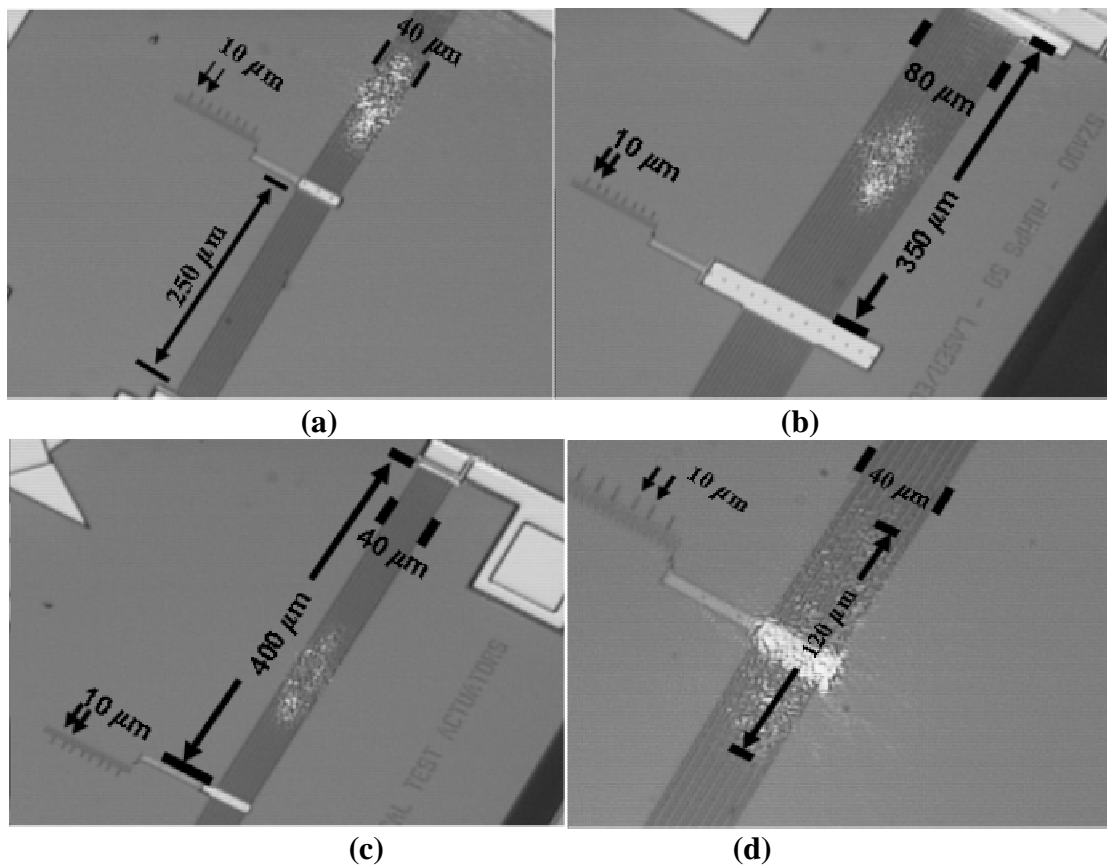
Figure 6.19: Captured digital video images illustrating the concentrated laser dot used for PolyMUMPs 58 test actuators in asymmetric illumination operation with (a) being the 250 mμ by 8- beam chevron, (b) being the 350 μm by 16- beam chevron, (c) being the 400 μm by 8-beam chevron, and (d) showing the laser dot focused on the center of the actuator.

6.5.2. Material Reflectivity Test

A PolyMUMPs chip, with Poly0, Poly1, Poly2 and gold areas, was tested for reflectivity. Figure 6.20 shows illustrations of the PolyMUMPs material reflectivity test, with (a) showing the measurement of incident power and (b) showing the measurement of reflected power. The power meter head was placed near the chip surface facing toward the mirror to measure incident power, and then just off the surface facing the reflected beam to measure the reflected power.

(a)   **(b)**
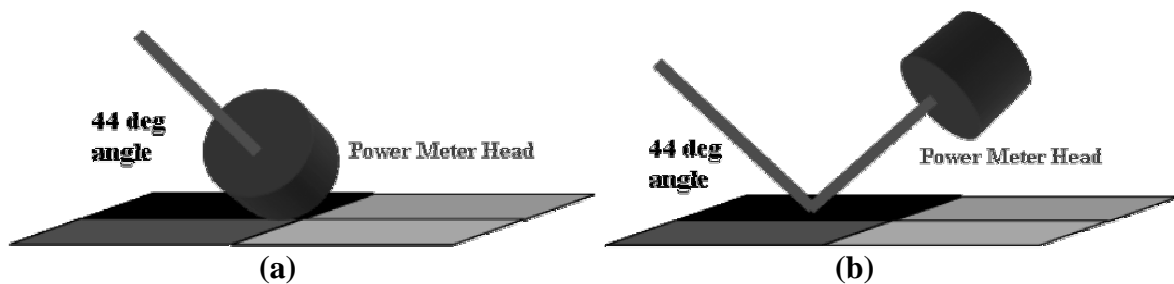
Figure 6.20: Illustrations of the PolyMUMPs material reflectivity test, with (a) showing the measurement of incident power and (b) showing the measurement of reflected power.

6.5.3. Electrical Testing Of Actuators

The first deflection experiment to characterize the actuators was conducted electrically to determine the amount of power required for minimum deflection, the power applied versus deflection, and the maximum amount of power each actuator could handle. Figure 6.21: This is an illustration of the test equipment setup for the test actuator electrical power test showing the wiring connections. Figure 6.21 shows how the experiment was set up at the probe station. Voltage was applied in one volt increments. Current and voltage readings were taken at each step, and a picture was taken to record the deflection. This was repeated three times for each actuator configuration. The deflection was so small under laser power that deflection was only recorded for laser actuation at maximum power.
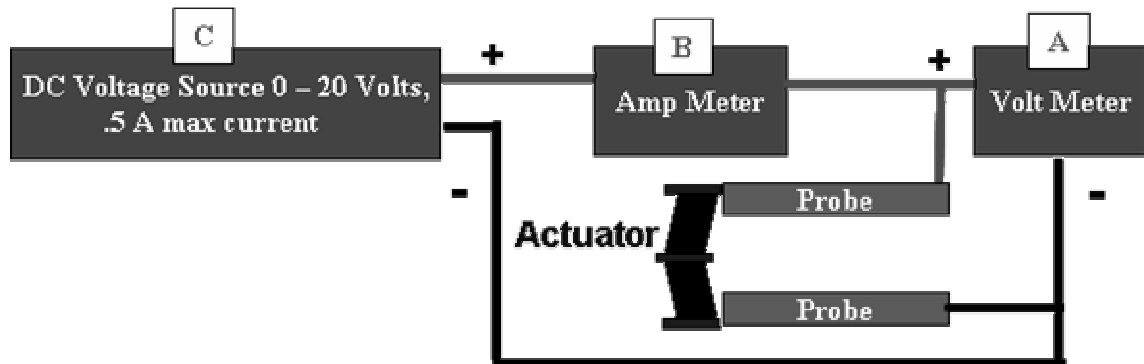
Figure 6.21: Illustration of the test equipment setup for the test actuator electrical power test showing the wiring connections.

Another non-actuation test was performed electrically to verify the temperature distribution part of the deflection model. This involved the use of double hot arm electrothermal actuators, along which gold dots had been placed at regular predetermined intervals, as was discussed in section 5.3.1. These dots change color at the eutectic temperature (approximately 636 K) [1]. The test setup used was the same as in Figure 6.21, above. Voltage readings were taken at each step, and a picture was taken to record the change in gold dot color.

Figure 6.22 shows an illustration of the test equipment setup for the test actuator electrical frequency-response test. The test frequencies are listed below in Table 6.4. The columns list the frequencies for each test. Three sets of tests were performed, a frequency ranging test to determine the maximum response limits, a high frequency range response to determine the best frequency for use in high frequency operation, and an amplitude versus frequency response test to determine the amplitude response at different frequencies. The last test was conducted at an offset frequency because the frame rate for the video was 30 frames per second, and high frequency ranges were found to be un-measurable unless on offset frequency was found that was one Hertz off a frequency that was a factor of 30. This was because all frequencies faster than the frame rate produced only an un-readable blur on the video screen. A considerable number of trial and error tests had to be conducted to find frequencies near those of

interest and observable using the video equipment with its handicapping frame rate problems. Video was recorded for all tests, and the microscope light was blinked between each frequency change to indicate a change had taken place on the video.

The voltage on the function waveform generator, as shown below in Figure 6.22, was 5 Volt peak to peak, with a 2.5 Volt offset. This setup assured the voltage was always positive and was used to prevent perceived frequency doubling during frequency testing.
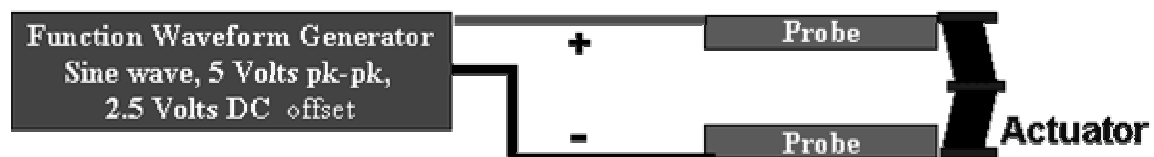
Figure 6.22: Illustration of the test equipment setup for the test actuator electrical frequency-response test.

Table 6.4: Frequencies Used in Testing.

Frequency Ranging Test (Hertz)	High Frequency Range Response Test (Hertz)	Amplitude versus Frequency Response Test (Hertz)
10	2.0 k	61
100	2.51 k	1020
500	3.01 k	1980
1.0 k	3.51 k	2511
1.51 k		
2.0 k		
2.51 k		
3.01 k		
3.5 k		
4.0 k		
4.51 k		
5.0 k		

The waveforms and duty cycles are listed below in Table 6.5, Laser Driver Signal Types. Each of the signal types was tried with each of the duty cycles, and all these combinations were tried at each of the frequencies in column 3 of Table 6.4. These tests were performed both on the PolyMUMPs 58 test chevron actuators and on the LR250-8 laser microrobot.

Table 6.5: Laser Driver Signal Types.

Wave Type	Duty Cycle
Sine	20%
Triangle	30%
Ramp	40%
Square	50%
	60%
	70%
	80%

Figure 6.23 shows digital images of the steps in releasing a LR250-8 laser microrobot for testing, with (a) illustrating the use of probes to break it free and position it and (b) illustrating the microrobot in the "launch" position the microrobot on PolyMUMPs chip surface. The microrobots were held by numerous 2 μm tabs, each held to the substrate by a 10 by μm Poly0/Poly1 square (small black squares in Figure 6.25) to hold the microrobot in place during HF release. These had to be broken loose to "launch" release the microrobot to be free on the substrate. Several robots were lost by launching into space when the force used to break the tabs also threw the microrobot off the chip surface. Figure 6.25 (a) shows the two probe method used to successfully launch the microrobots. The large probe on the left was used to break the tabs, while the thin probe on the right was placed in an empty spot in the middle of the microrobot to contain it if it tried to launch off the surface

(a)   **(b)**
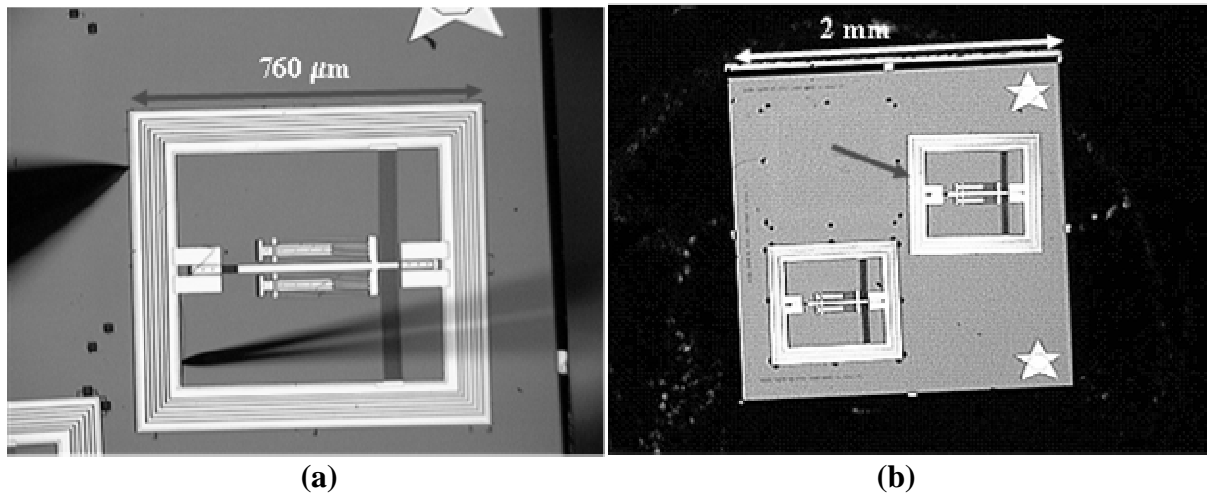
Figure 6.23: Digital images of the steps in releasing a LR250-8 laser microrobot for testing, with (a) illustrating the use of probes to break it free and position it and (b) illustrating the microrobot in the "launch" position the microrobot on PolyMUMPs chip surface.

6.6. Conclusion

This chapter discussed the experimental procedures and equipment used in electrically and optothermally characterizing the test actuators and microrobots. This chapter explained the experiments used to test the designs and concepts from Chapter 4 and the models in Chapter 5.

The post processing and release of PolyMUMPs chips was explained. The video capture equipment used in the collection of data was discussed. Electrical power and frequency testing of the test chevron actuators was discussed. The last section of this chapter discussed laser power and frequency testing used to characterize the optothermal actuators and the LR250-8 laser powered microrobot. The next chapter discusses the results of these experiments. Chapter 7 compares the experimental results with the predicted results from the models in Chapter 4.

6.7. Bibliography

[1]   Y. T. Cheng, Lin Liwei, Najafi Khalil, "Localized Silicon Fusion and Eutectic Bonding for MEMS Fabrication and Packaging," *Journal of Microelectromechanical Systems*, vol. 9, no. 1, pp. 4-14, March 2000.

[2]   P. E. Kladitis, *Self Assembly of Microstructures*, Masters Thesis Dissertation, Air Force Institute of Technology, 1997.

[3]   J. R. Caffey, *The Effects of Ionizing Radiation on Microelectromechanical Systems (MEMS) actuators: Electrostatic, Electrothermal, and Residual Stress,* Masters Thesis Dissertation, Air Force Institute of Technology, 2003.

7.   Results

This chapter presents the results of the experiments discussed in Chapter 6. These experimental results characterize the chevron bent beam actuators and the laser microrobot designs presented in Chapter 4. They are compared with and used to analysis the results of the models presented in Chapter 5. The results include characterization of each actuator for voltage and power versus deflection, frequency response, and optothermal operation.   The results characterizing the operation of the different microrobot parts are also presented.

Section 7.1 contains the results and analysis for measurements of test chevron actuators taken during electrothermal operation. The results of early designs are compared with the final designs. Then the results of the model are compared with experimental results in Section 7.2. The results and analysis for electrothermal frequency response is presented in Section 7.3. Section 7.4 presents the results and analysis of the optothermal model with experimental results. Section 7.5 presents optothermal actuator frequency response under laser illumination. Section 7.6 presents the validation evidence for the major parts of the microrobot, including the down thermal actuators and the conformal coated drive shaft housing.   Section 7.7 discusses the PolyMUMPs material reflectivity test.   The power losses in the optothermal laser heating paradigm are discussed in Section 7.8.

7.1. Experimental Electrothermal Actuation Results

This section discusses the early chevron actuator designs from the PolyMUMPs 57 (M57) run, and how they were improved for the final designs for the PolyMUMPs 58 (M58) test actuators and the final microrobot designs.   The PolyMUMPs 57 chevron actuators were designed from the literature before any equipment had been set up for laser testing; or any of the problems and challenges of laser illumination had been discovered or addressed. Consequently,

while they succeeded quite well as electrothermal actuators, they were failures as optothermal actuators. The reasons for this are discussed after a comparison of the PolyMUMPs 57 and 58 designs electrothermal operation.

Figure 7.1 shows digital images of the PolyMUMPs 58, 250 μm by 8-beam chevron test actuator under electrical test, with (a) being the pointer position at 0 volts, (b) being the pointer position showing a deflection of .5 μm at 1 volt and (c) showing a deflection of at 13 μm at 14 volts. The test pointers and measuring scales are displayed, showing how measured results were obtained for deflection of the actuators. Unfortunately, the M57 250 μm chevron test actuators all had their pointers break off due to a design flaw. The M58 250 μm chevron test actuators were able to obtain a maximum 13 μm of deflection at 14 volts, with a detectable 0.5 μm of deflection at one volt, or with 3.4 mW of power applied.

(a)   (b)

(c)
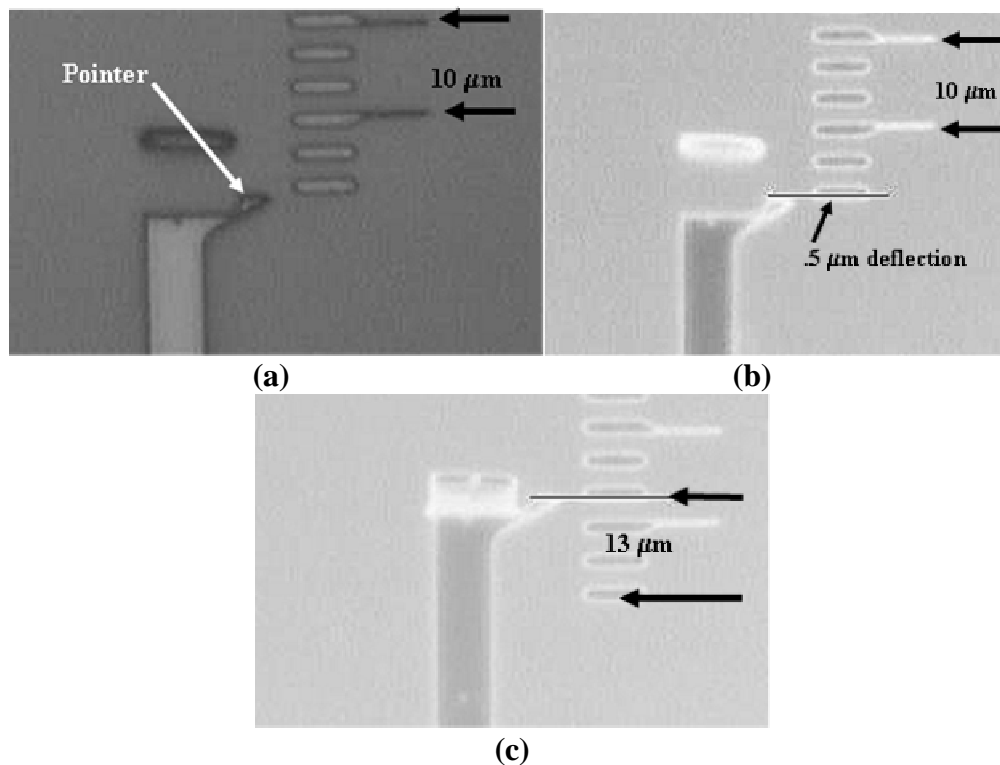
Figure 7.1: Digital images of the PolyMUMPs 58, 250 μm by 8-beam chevron test actuator under electrical test, with (a) being the pointer position at 0 volts, (b) being the pointer position showing a deflection of .5 μm at 1 volt and (c) showing a deflection of at 13 μm at 14 volts.

Figure 7.2 shows digital images of the PolyMUMPs 58 Chevron 350 μm by 16-beam chevron test actuator under electrical test, with (a) being the pointer position showing a barely discernable deflection of 0.25 μm at 1 volt and (b) showing a maximum deflection of at 16 μm at 16 volts. At 1 volt, or 9 mW of power applied, a deflection of 0.5 μm was observed. This compares with only 4.5 mW applied to obtain a deflection of 0.5 μm for the M57 350 μm chevron test actuators. This is because the M58 actuators had 16 beams acting as 16 parallel resistors, while the M57 designs had only 8 beams, or twice the resistance. However, despite the extra power required for electrothermal operation, the larger number of beams proved to be more effective for optothermal operation, as they provided more surface area for the light to illuminate and heat.

(a)   **(b)**
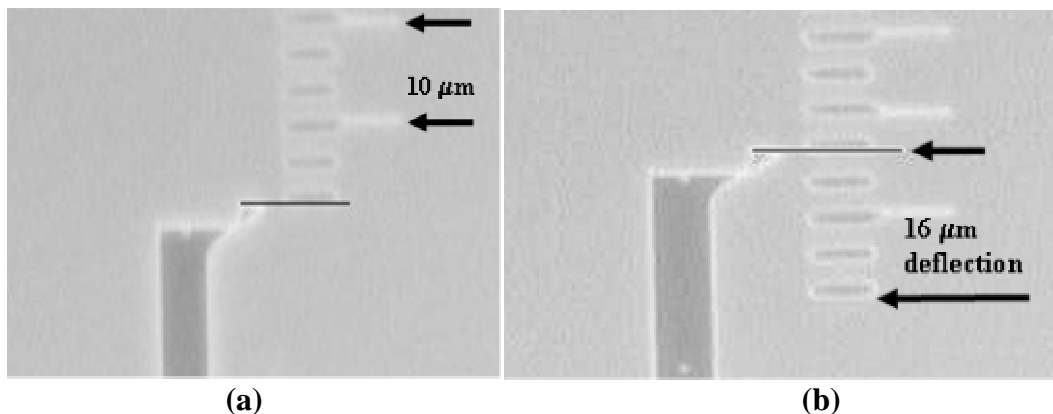
Figure 7.2: Digital images of the PolyMUMPs 58 Chevron 350 μm by 16-beam chevron test actuator under electrical test, with (a) being the pointer position showing a barely discernable deflection of .25 μm at 1 volt and (b) showing a maximum deflection of at 16 μm at 16 volts.

Figure 7.3 shows digital images of the PolyMUMPs 58 chevron 400 μm by 8-beam chevron test actuator under electrical test, with (a) being the pointer position showing a deflection of almost 1 μm at 1 volt and (b) showing a maximum deflection of at 17 μm at 18 volts. At 1 volt, or 2 mW of power applied, a deflection of 0.5 μm was observed. This compares with 3 mW applied to obtain a deflection of 0.5 μm for the M57 400 μm chevron test actuators. This reverses the trend seen in the 350 μm chevron test actuators. Even though the M58

actuators had 8 beams acting as 8 parallel resistors, while the M57 designs had only 4 beams, or twice the resistance, the M58 beams were much thinner (2.5 μm, versus 4 μm). Again, the larger number of beams proved more effective for optothermal operation, as they provided more surface area for the light to illuminate and heat.

Figure 7.4 is a plot showing the three PolyMUMPs 57 chevron test actuators' voltage versus deflection, under electrical test. The deflection versus voltage applied is nearly identical up to 12 Volts, despite having 4, 8, and 12 beams respectively, and being two different lengths. This uniformity is partially attributable to their thickness (3.5 or 4 μm). This thickness provided a stiffness that enforced more uniformity. As stated in the literature, the initial pre-bend angle of the actuators has a much greater effect on their actuation than other properties [1]. All the actuators in this research had a pre-bend angle of one degree.

(a)   **(b)**
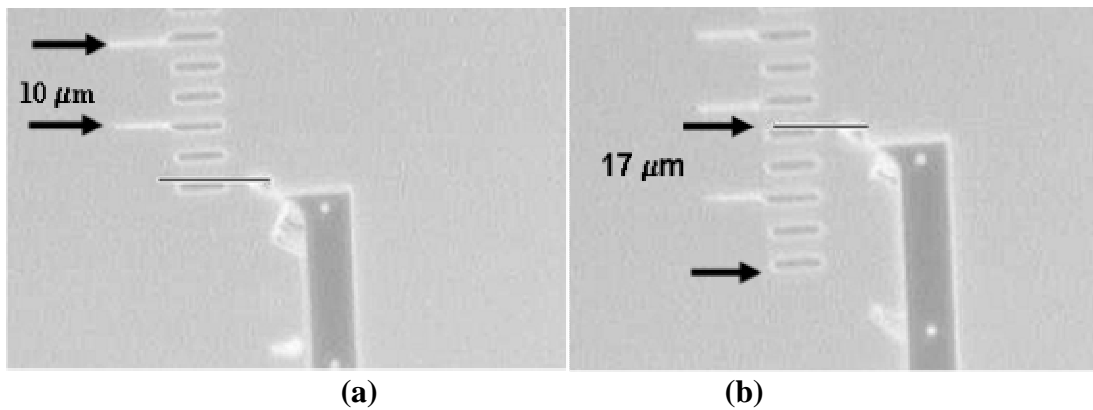
Figure 7.3: Digital images of the PolyMUMPs 58 chevron 400 μm by 8-beam chevron test actuator under electrical test, with (a) being the pointer position showing a deflection of almost 1 μm at 1 volt and (b) showing a maximum deflection of at 17 μm at 18 volts.
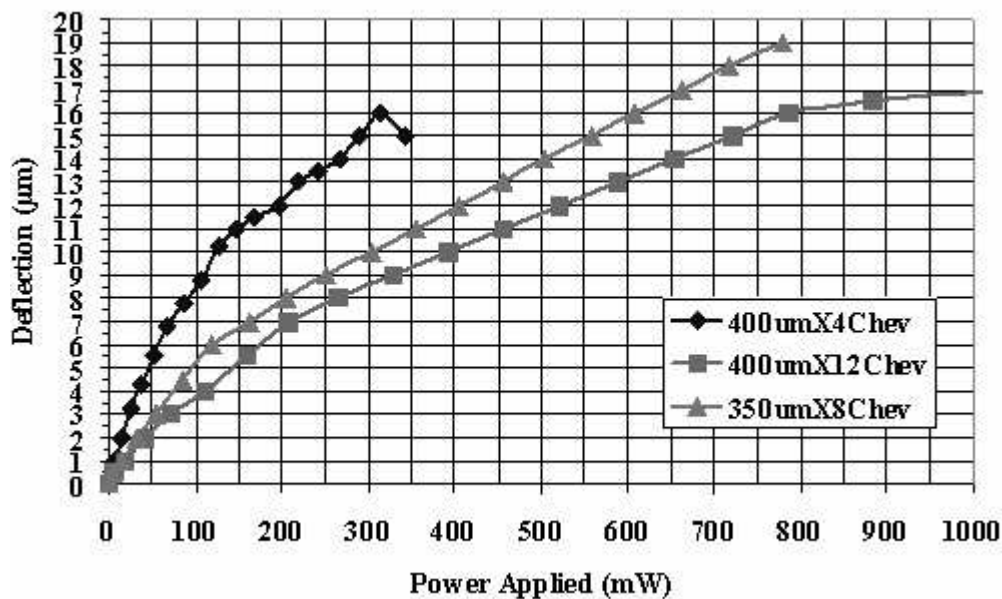
Figure 7.4: Plot showing the three PolyMUMPs 57 chevron test actuators' voltage versus deflection, under electrical test.

Figure 7.5 is a plot showing the three PolyMUMPs 58 chevron test actuators' voltage versus deflection, under electrical test. These actuators were all 2.5 μm in thickness, but varied in the number of arms and the length. The maximum deflection from any of the M58 actuators was 17 μm. The maximum amount of deflection from any of the M57 actuators was 19 μm. Two general design versus deflection trends were found. The first trend was that the longer the chevron arms, the more deflection it provided. This is expected since a longer length being heated provides more overall thermal expansion, thus more deflection. The second trend was that in multiple beam configurations (8 or more), combined with thicker arms (up to a point), can handle more power, thus provide more deflection.

However, at 10 volts all the test chevron actuators from both designs showed around 10 μm of deflection (within 10%). At 5 volts, all chevron actuators gave 4 μm of deflection (within 5%). Since these results were so close at low power, and the optothermal actuators were going

to be running on low power, this gave a large amount of design flexibility to custom design for

optothermal actuation purposes.
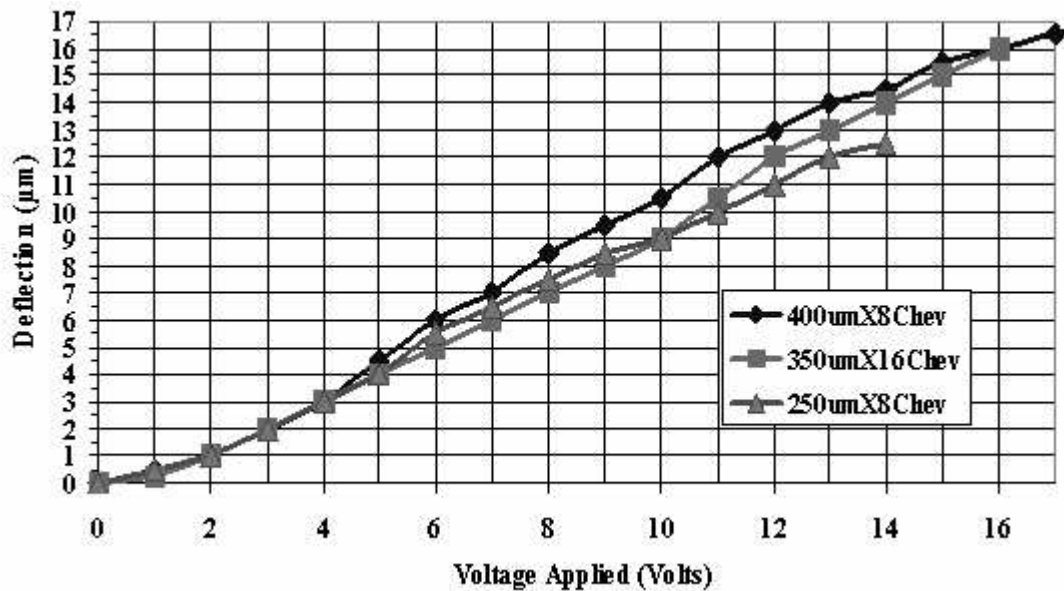
Figure 7.5: Plot showing the three PolyMUMPs 58 chevron test actuators' voltage versus deflection, under electrical test.

7.1.1. Power Consumption with Electrical Activation

Figure 7.6 is a plot showing the PolyMUMPs 57 test chevron actuators' power consumption versus deflection, under electrical testing. The M57 designs could handle more power and required more power for maximum deflection. The chevron design that was 400 μm long, 4 μm thick and had 12 beams required over one Watt of power. Figure 7.7 is a plot showing the PolyMUMPs 58 test chevron actuators' power consumption versus deflection, under electrical testing. The M58 designs did not need as much power to reach maximum deflection. The two designs that were finally chosen for the microrobots, the 400 μm by 8-beam, and the 250 μm by 8-beam, both had maximum deflection around 340 mW.

The more chevron arms there were, the more power was required to attain the same deflection, as shown with the 16 beam actuator in Figure 7.7 needing 650 mW to attain the same

14 µm of deflection as 240 mW attained on one of the 8 beam actuators. This shows that the

added beams added more stiffness to the structure of the whole actuator.
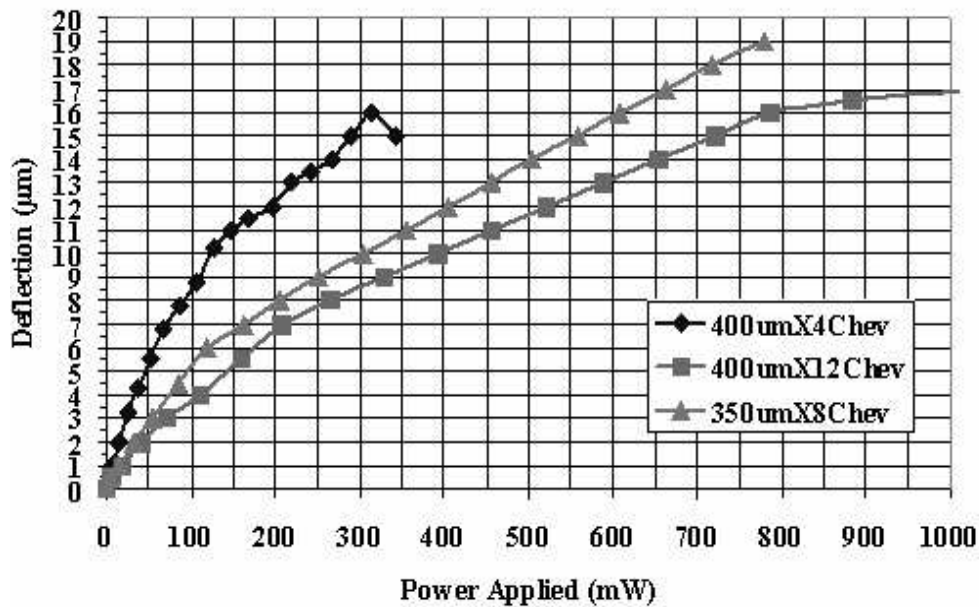
Figure 7.6: Plot showing the PolyMUMPs 57 test chevron actuators' power consumption versus deflection, under electrical testing.
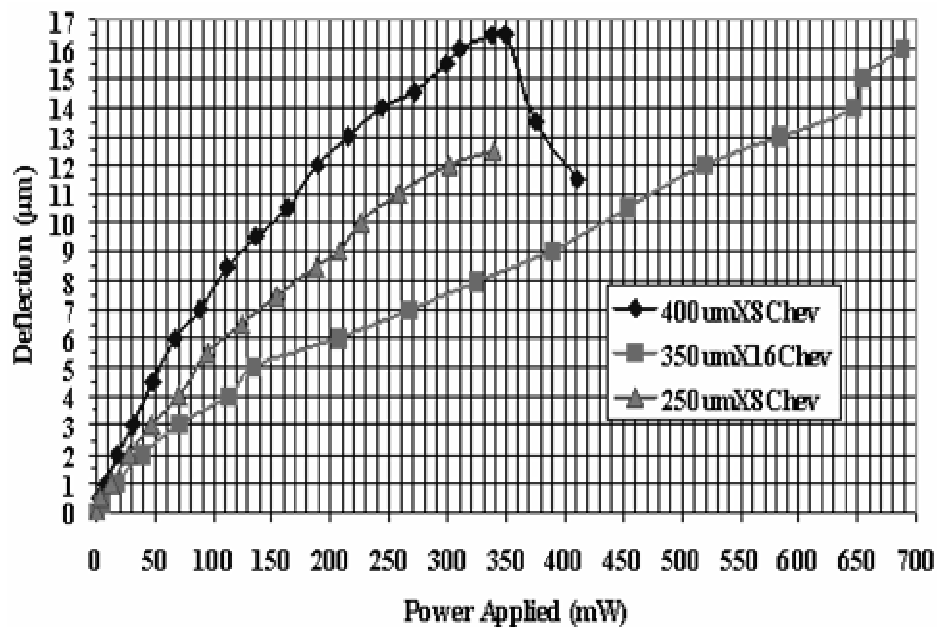
Figure 7.7: Plot showing the PolyMUMPs 58 test chevron actuators' power consumption versus deflection, under electrical testing.

The laser that was being used was rated for 45 mW at continuous power, and only a small part of that will actually heat the beams, so the lower power ends of the power-deflection charts were examined. Figure 7.8 is a plot showing the deflection of the three PolyMUMPs 57 chevron test actuators under electrical test at low power. Figure 7.9 is a plot showing the deflection of the three PolyMUMPs 58 chevron test actuators under electrical test at low power. The M57 400 μm by 4-beam design required 14 mW of power to reach 2 μm of deflection. The M58 400 μm by 8-beam design required 18 mW of power to reach same 2 μm of deflection. It was the original intent in this research to find a way to directly compare electrothermal actuation and optothermal actuation using power consumption. However, the comparison broke down at this poin, because the more beams an actuator had, the more parallel resistors it presents to an electrical power source, and the more power it consumes. However, an opposite effect happens with the optothermal actuators within the limits of the laser beam size. The more beam surface area that can be placed under the laser beam, the more power is absorbed and the more heating occurs.
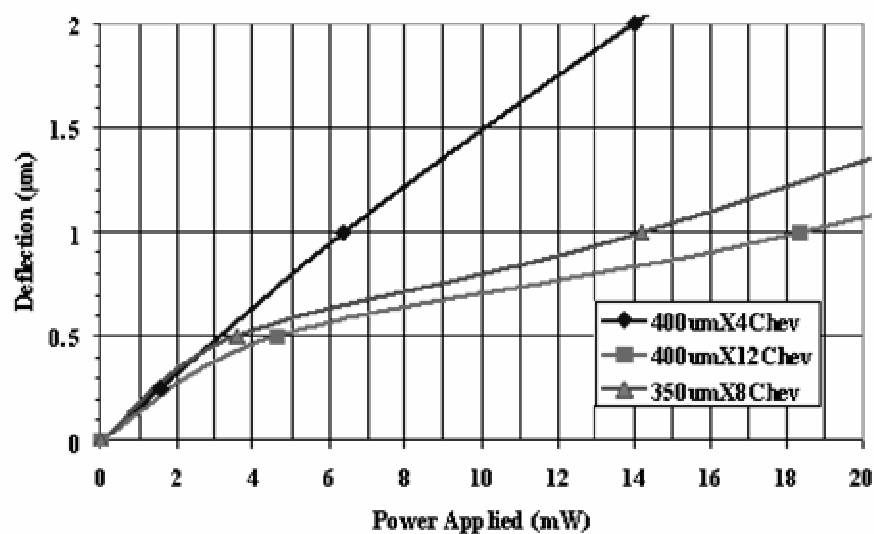
Figure 7.8: Plot showing the deflection of the three PolyMUMPs 57 chevron test actuators under electrical test at low power.
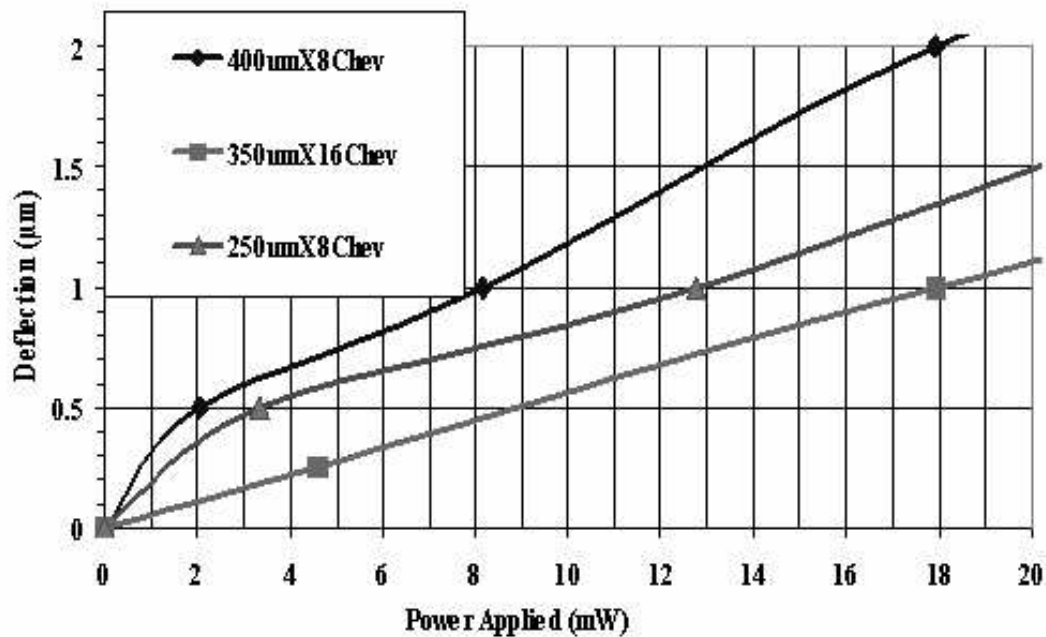
Figure 7.9: Plot showing the deflection of the three PolyMUMPs 58 chevron test actuators under electrical test at low power.

7.1.2. PolyMUMPs 58 Design Improvements

No visible or discernable actuation could be detected with a round laser dot with a size of 130 μm in radius powering the PolyMUMPs 57 actuators. The problems and reasons for this failure, and the improvements and optimizations made to the PolyMUMPs 58 designs to make them successful are given below in Table 7.1. Figure 7.10 is an illustration of the PolyMUMPs 57 chevron actuator design problems, with the number matching the rows in Table 7.1, which contain the explanation. The numbered problem/solution lines in Table 7.1 match the numbers in Figure 7.10.

Table 7.1: PolyMUMPs 57 Chevron Actuator Design Problems and Solutions.

Problem/Shortcoming	Solution/Optimization
(1.) Arms too thick (3.5 μm), too stiff:	New arms 2.5 μm thick, 3.5 μm tall
(2.) Too much space between arms (13 μm)	Reduce space to 2.5 μm
(3.) Not enough laser power absorbed	Add more arms, more surface area (increase from 4 to 8 arms)
(4.) Longer arms - greater deflection	400 μm arm length was best
(5.) Too much Laser on empty areas	Reduce beam dot size, change to ellipse dot
Note: these rows are explanations matching to the pertinent number in Figure 7.10.	
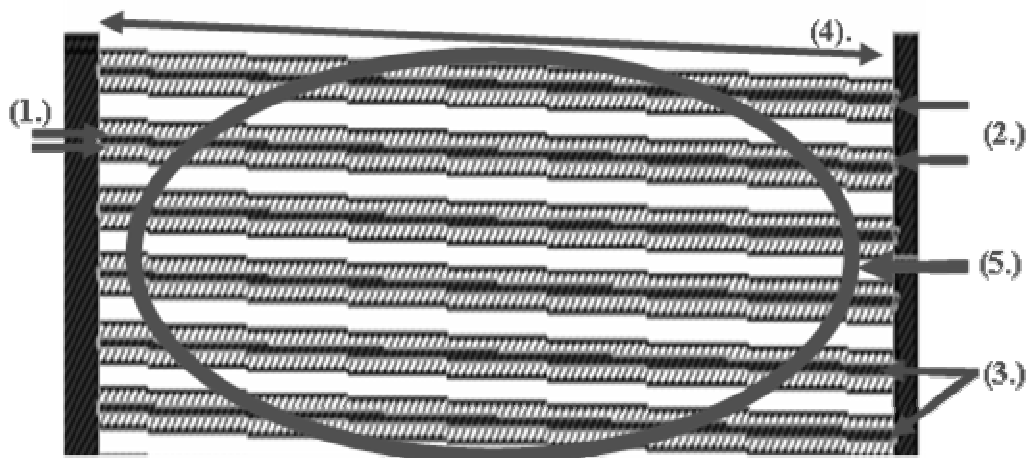
Figure 7.10: Illustration showing the PolyMUMPs 57 chevron actuator design problems, with the number matching the rows in Table 7.1, which contain the explanation.

Problem 1 was solved by thinning the arms, as seen in Figure 7.10 (1), providing more flexibility, and allowing more arms to be used. Problem 3 was solved by both reducing the space between the arms that wasted illuminating power, as seen in Figure 7.10 (2), and increasing the surface area by increasing the number of beams, as seen in Figure 7.10 (3). Increasing the beam length, as seen in Figure 7.10 (4), would also increase the deflection, but this was limited by the effective beam size, and the desire to miniaturize the microrobot as much as possible. The final optimization came in the form of the experimentation with the laser beam spot size. The original large circular spot size originally envision (260 μm in radius) turned out to deliver so little power that the heat power generated per meter^3, that was three orders of magnitude less than the resistive electrothermal heating at 1 mW. So after reworking the optothermal model and the

experimental laser setup, it was determined that a much smaller beam spot size, shaped like an ellipse, was more efficient. The combination of a large number of thin beams, closely packed together under a small intense elliptical laser beam provided sufficient heating for 2 μm of deflection, as will be discussed and shown in section 7.4.

7.2. Experimental Electrothermal Actuation Results versus Modeling

This section analyzes the results of the PolyMUMPs 58 chevron test actuator designs as compared to the model presented in Chapter 5. It also discusses the side experiments of the gold dots at eutectic temperature test and the resistivity tests to help validate the thermal part of the model. These deflection results are then compared to results available from the literature.

Figure 5.7 showed a plot illustrating the temperature distribution along a hot arm of an electrically powered 250 μm by 8-beam PolyMUMPs 58 chevron test actuator. In actual practice the 250 μm by 8-beam chevron actuator burnt out at 15 volts, so the top line is about 100 K low if compared to the normal melting temperature of polysilicon. However, when taking resistivity measurements to verify parts of the temperature dependant model, it was noticed that at high temperatures, the resistivity loses its near linear function and breaks down. The conclusion was drawn that this phenomenon could cause a catastrophic breakdown at a temperature lower than the actual melting point of silicon. If the other temperature dependant properties of the material changed unpredictably at high temperatures, and this was combined with the applied stress, it would explain why the model fails at high voltages/high temperatures. It would also lead to a possible prediction of catastrophic breakdown and burnout at a temperature below 1600 K. Figure 7.11 is a digital image of a polysilicon chevron actuator that is burnt out and oxidized after too much power has been applied. From the color of the burnt out actuators, it is possible that the polysilicon oxidized at a temperature below bulk melting point.
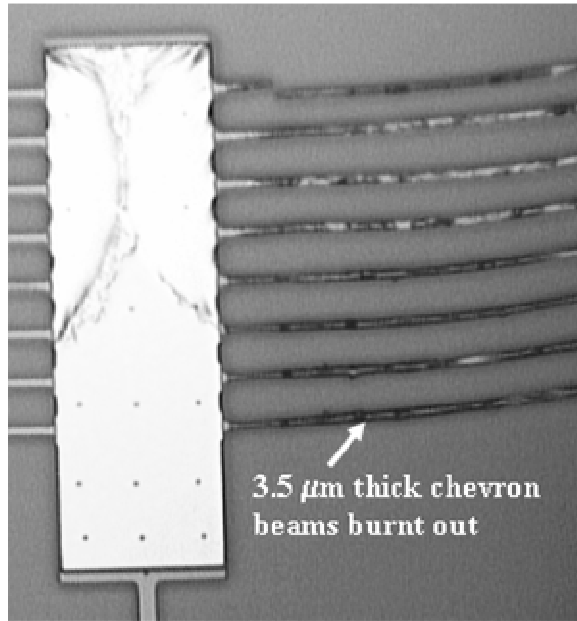
Figure 7.11: Digital image of a polysilicon chevron actuator that is burnt out and oxidized after too much power has been applied.

7.2.1. Temperature Dependant Resistivity

This section shows the results of the resistivity measurements, taken in the lab at the same time as the power versus deflection experiments. Figure 7.12 is a plot showing the temperature dependant resistivity in the arms of several electrically powered Polysilicon chevron actuators. The calculated resistivity (Calc_pe in Figure 7.12) used the value of resistivity of Poly1, as given on the MEMS run data sheet as a starting point and uses equation 5.39 to calculate its change with temperature [4]. Experiment number 1 (Exp 1 in Figure 7.12) was done with Poly2, which has a lower resistivity, so a lower curve was expected. Exp 2 and Exp 3 in Figure 7.12 were both done with 3.5 μm thick combined Poly1/Poly2 beams of different lengths. The combined Poly1/Poly2 resistivity was between the Exp 1 and the Calc_pe curves as expected. However, the catastrophic breakdown at higher temperatures mentioned in an earlier paragraph can be seen, especially in experiment 3, which was performed with thinner beams, causing the breakdown at an earlier voltage step. The measurements in Figure 7.12 were

actually taken as voltage versus resistivity; the equipment was not available to measure exact

temperatures at each voltage step. To illustrate the temperature dependence, the modeled

average temperatures corresponding to the voltage steps were used in Figure 7.12.
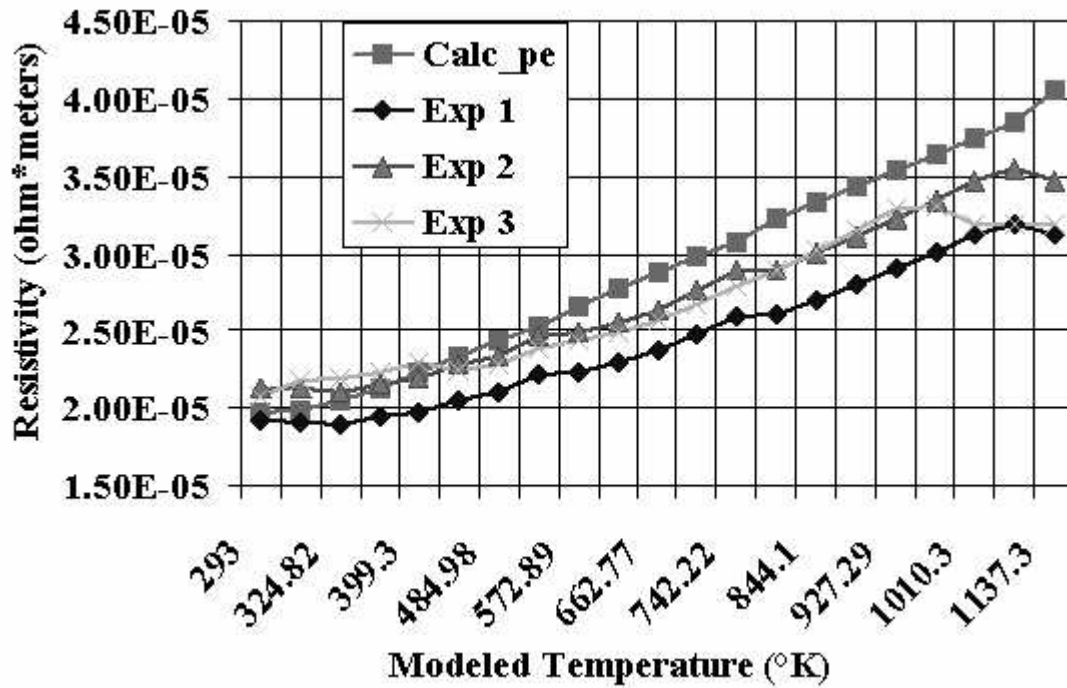
Figure 7.12: Plot showing the temperature dependant resistivity in the arms of several electrically powered Polysilicon chevron actuators.

7.2.2. Comparison of the Predicted Model and the Experimental Deflection

This section discusses a comparison of the predicted model deflection and the actual

experimental deflection. Figure 5.8 was a plot showing the model and experimental deflection of

electrically powered 250 μm by 8-beam PolyMUMPs 58 chevron test actuators. The

temperature dependant model for the 250 μm by 8-beam chevron actuators predicts results that

are very close to experimental results at lower voltages but slightly off at higher voltages. The

actuator burnt out at 15 volts. At voltages up to 10 volts, the model was within an average of

8.72% of the actual deflection.

Figure 7.13 is a plot showing the model and experimental deflection of electrically powered 350 μm by 16-beam PolyMUMPs 58 chevron test actuators. The temperature dependant model for the 350 μm by 16-beam chevron actuators was closest to the experimental results of the three model predictions. The actuator burnt out at 17 volts. At voltages up to 15 volts, the model was within an average of 1.68% of the actual deflection.
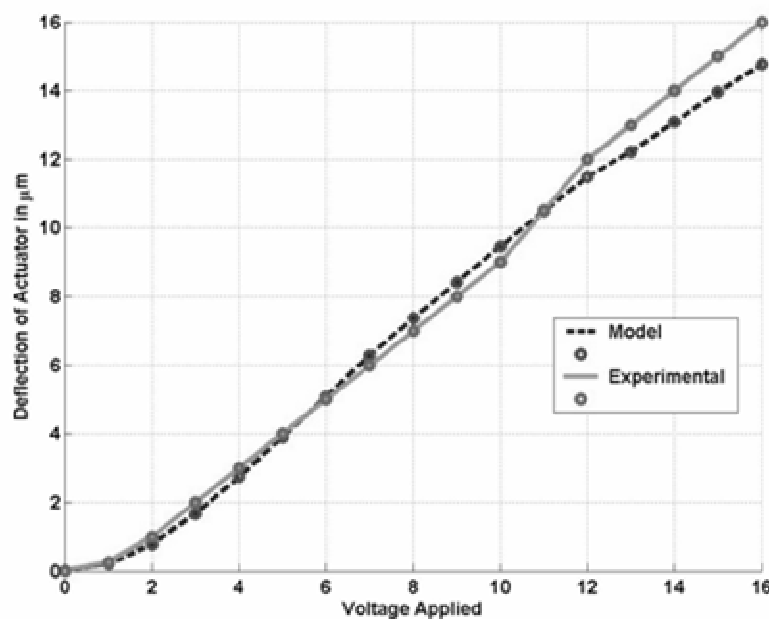
Figure 7.13: Plot showing the model and experimental deflection of electrically powered 350 μm by 16-beam PolyMUMPs 58 chevron test actuators.

Figure 7.14 is a plot showing the model and experimental deflection of electrically powered 400 μm by 8-beam PolyMUMPs 58 chevron test actuators. The temperature dependant model for the 400 μm by 8-beam chevron actuators has predicted results very close to experimental results, but slightly underestimates actual deflection at all voltages. The actuator burnt out at 21 volts. At voltages up to 15 volts, the model was within an average of 8.99% of the actual deflection.
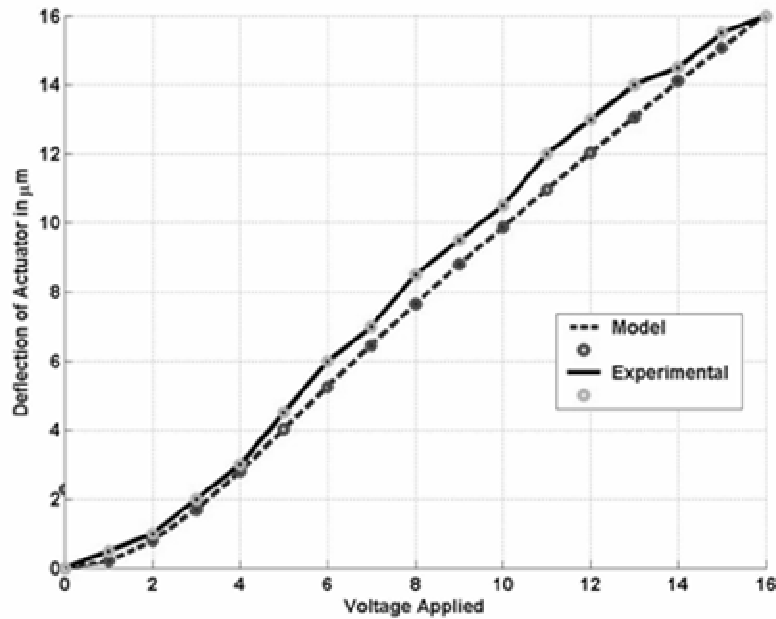
Figure 7.14: Plot showing the model and experimental deflection of electrically powered 400 μm by 8-beam PolyMUMPs 58 chevron test actuators.

7.2.3. Comparison with Results Obtained from Literature

Figure 7.15 shows the deflection Sinclair obtained from his chevron actuator designs [1]. It is provided for a comparison with designs and results obtained from literature and this research's experimental results. Figure 7.16 is a plot of the force and deflection Lai, et al. obtained for their chevron actuator designs [2]. Sinclair obtained approximately 10 μm of deflection for his actuators in Figure 7.15, with the same pre-bend length as used in this research. He cited one array of chevron actuators that had a maximum deflection of 14 μm. These actuators were fabricated with PolyMUMPs technology. Lai, et al. in 2004 were only able to obtain a deflection of 3 μm for an array with PolyMUMPs fabricated 150 μm long beams [2]. Que, et al. were able to obtain 5 μm of displacement at 180 mW of power, with silicon devices with 800 μm long, 13.9 μm wide, and 3.7 μm thick beams; fabricated with a non-PolyMUMPs technology. By comparison, the best actuator in this research was able to obtain a maximum

deflection of 19 μm. The best actuator in this research that was used also as an optothermal

actuator was able to obtain a maximum deflection of 17 μm.
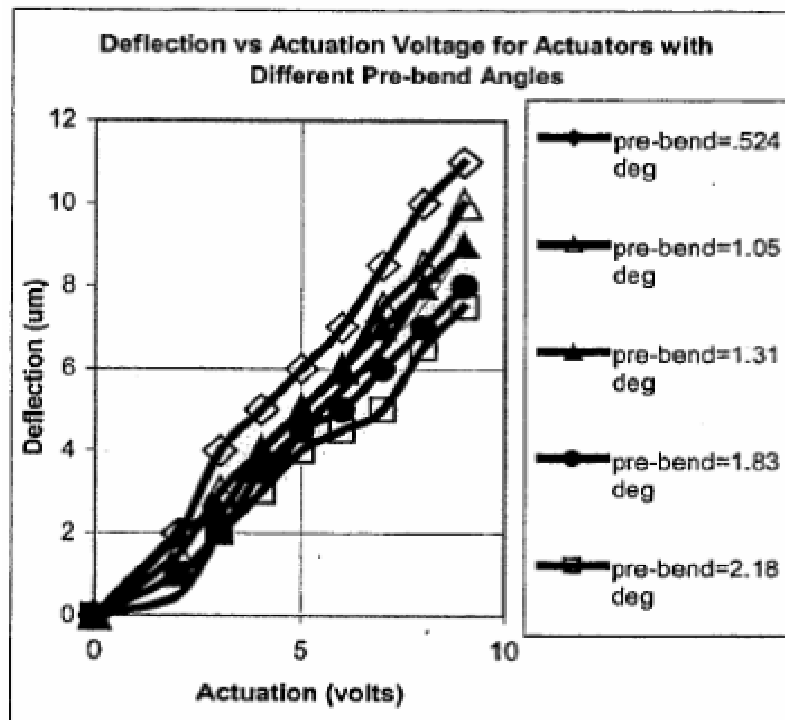
Figure 7.15: Plot showing the deflection Sinclair obtained from his chevron actuator designs [1].
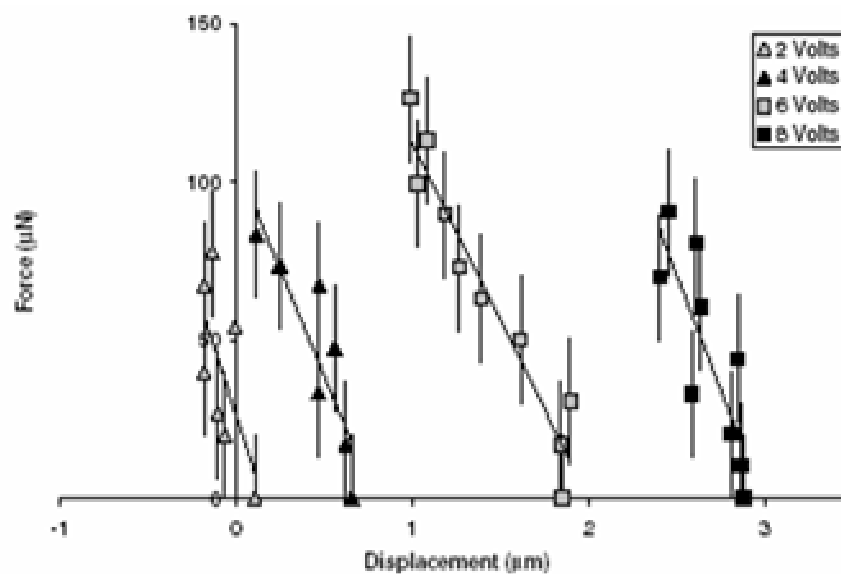
Figure 7.16: Plot of the force versus deflection Lai, et al. obtained for their 8 x 150 µm chevron actuator designs. [2].

7.3. Electrothermal Frequency Response

All the PolyMUMPs 58 test chevron actuators were tested for magnitude versus frequency response, as listed in chapter 6. Because the frame rate of the video capture system was 30 frames per second, this prevented most high frequency data from being recorded. After this was discovered during the testing, much experimentation was tried to find and observe deflection at higher frequencies. It was found that a high frequency test that was one to two Hz over or under of a multiple of the frame rate of 30 hertz provided observable recordable results, as it had the effect of slow motion freeze-framing the deflecting action. Also, it was found that measuring the vibration of the dimple dots was easier that observing the vibration of the tips. Figure 7.17 shows captured still digital video images from digital video of the effects of frequency on the magnitude of deflection, with (a) showing 8 μm of deflection at 61 Hz and (b) showing 2 μm of deflection at 2 kHz.

| **(a)** | **(b)** |
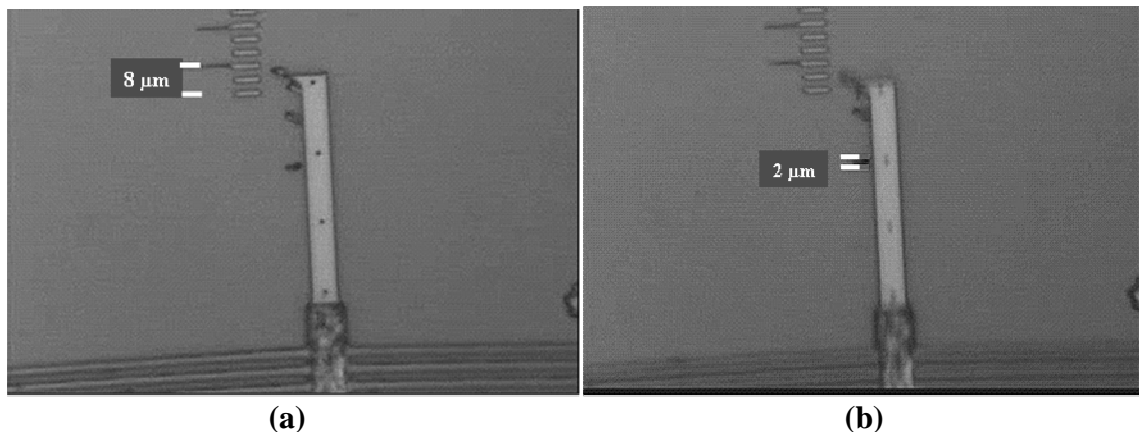
Figure 7.17: Captured still digital video images from digital video of the effects of frequency on the magnitude of deflection, with (a) showing 8 μm of deflection at 61 Hz and (b) showing 2 μm of deflection at 2 kHz.

The highest frequency with any detectable response for any test chevron actuator was 3.51 KHz. The 3 dB amplitude deflection frequency response point was 1.25 KHz for two of the three test actuators. By 2 KHz all the test chevron actuators had lost half of their original deflection. By 2.5 KHz, all actuators had lost two thirds to three fourth of their base deflection

amplitude, as can be seen below in Table 7.2, Test Chevron Frequency versus Magnitude Response. The first column in Table 7.2 shows the frequency at which deflection could be observed, despite the 30 Hz frame rate. The next three columns show the deflection for the listed actuators at the frequencies in column one.

Table 7.2: Test Chevron Frequency versus Magnitude Response.

	250 μm by 8-beam 4 Volt pp 2 Volt DC Bias	350 μm by 16-beam 5 Volt pp 2.5 Volt DC Bias	400 μm by 8-beam 5 Volt pp 2.5 Volt DC Bias
Test Frequency (Hertz)	Deflection (μm)	Deflection (μm)	Deflection (μm)
61	6	9	8
1020	4	7	6
1980	3	6	4
2511	2	3	2

Figure 7.18 is a plot showing the PolyMUMPs 58 test chevron frequency versus magnitude response from Table 7.4, with the 3 dB amplitude deflection point at 1.25 kHz and the half deflection point at 1.98 KHz.
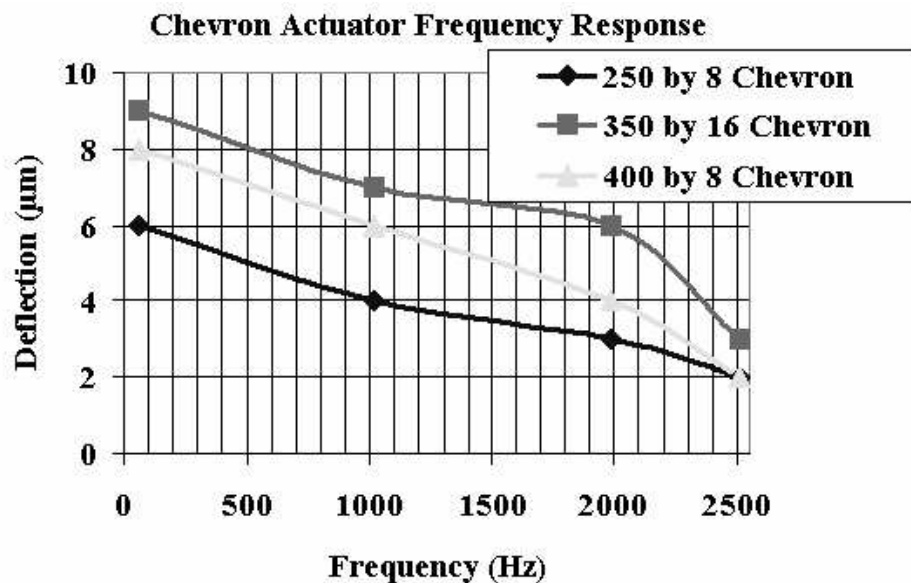
Figure 7.18: Plot showing the PolyMUMPs 58 test chevron frequency versus magnitude response from Table 7.4, with the 3 dB amplitude deflection point at 1.25 kHz and the half deflection point at 1.98 KHz.

7-18

The frequency response of the PolyMUMPs 58 test chevron actuators compares favorably with that found in the literature. Figure 7.19 is a plot of Que's bent beam actuator frequency versus magnitude response, with the 3 dB amplitude deflection point at 700 Hz [3]. By comparison, the 3 dB amplitude deflection point for the PolyMUMPs 58 test chevron actuators in this research was approximately 1.25 kHz.
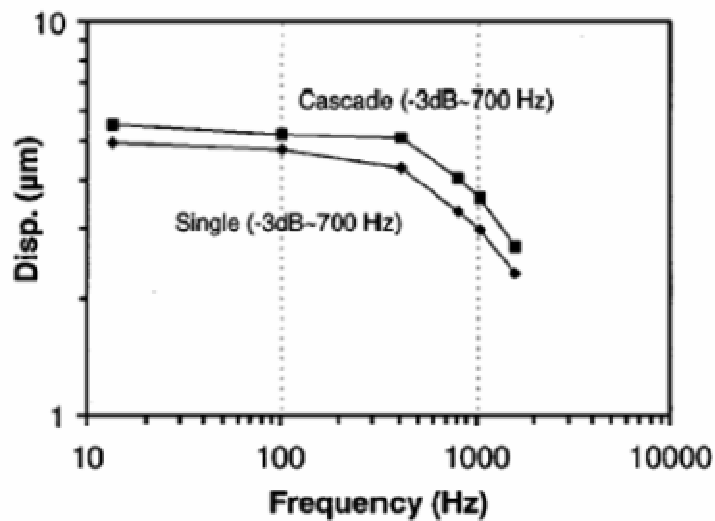
Figure 7.19: Plot of Que's bent beam actuator frequency versus magnitude response, with the 3 dB amplitude deflection point at 700 Hz [3].

7.4. Results and Analysis of the Optothermal Model with Experimental Results

The temperature dependant chevron actuator deflection model was adapted to predict deflection for optothermal actuation by substituting the laser heat generation $\dot{q}$ term for the current/resistive heating heat generation qdot term. Also, the model was adapted to different laser beam illumination and heating geometries. Figure 7.20 is a plot showing the model predicted deflection versus laser beam dot size with the beam asymmetrically heating one side of actuator. Experimental results showed approximately 2 µm of deflection at 60 mW of incident power and a 40 µm beam dot radius, while the model predicted between 1.4 and 1.8 μm of

deflection. The most efficient laser heating mode found was to concentrate the laser beam on one side of the actuator with asymmetrical heating.

The reason both 45 mW and 60 mW plots are provided is that the laser diode was rated for only 45 mW of continuous power or 60 mW of power at frequencies over 100 Hz, with a 50 percent duty cycle or less. The laser diode was being over driven at the 4 Hz testing frequency, but was somewhere between the 45 mW and 60 mW output range. The available test equipment could not obtain the power readings at other than continuous wave power.

One of the reasons the model underestimated the deflection was that all the properties used in the model were for pure crystal silicon. The actual material used was highly doped polysilicon. The non-crystalline structure may have provided more interactions with photons, allowing more heat generation.
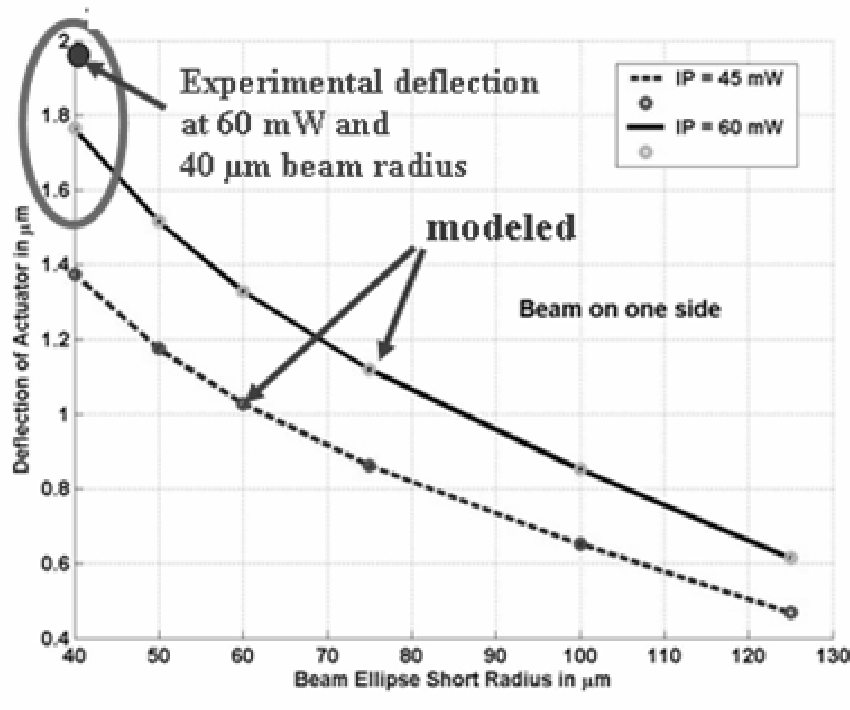
Figure 7.20: Plot showing the model predicted deflection versus laser beam dot size with the beam asymmetrical heating one side of actuator and giving almost 2 µm of deflection at 60 mW of incident power and a 40 µm beam dot radius.

7.4.1. Optothermal Experimental Problems

Unlike the video camera and capture system at the probe station used to capture deflection that gave very clear pictures, the camera and video capture system used at the laser test station gave grainy and unstable or shaky video, making digital video still capture pictures hard to read and hard to analyze. This was due in part to the laser flashes causing the video camera system to continuously try to self adjust its brightness compensation mechanism. Obtaining video tape from a digital VCR was completely impossible, as the laser reflection flashes video signal amplitude overcame the video synchronization signal amplitude, causing the video to have no recognizable sync pulse, and turn the video into a fuzzy blur. A multiple fix approach was finally hit upon. First, the laser beam was aligned and targeted at low ambient light from the microscope. Then, when actual deflection needed to be measured, a very bright microscope light was shown at maximum power on the chip. Also, the microscope focus point was moved so that the main area of the laser pulse was out of the picture. The combination of these two procedures overcame most of the laser reflective flashing. However, the light source introduced very bad vibration to the microscope and camera, and extensive adjustments had to be continuously made to isolate the light source fan vibration from the laser test table. These problems had to be overcome, because, unlike the probe station microscope under which the electrical testing was done, a person could not look directly through the microscope lens to observe operation, due to laser eye safety reasons. All operation had to be observed on video.

7.4.2. Observed Optothermal Deflection

Figure 7.21 shows captured still images from digital video showing the concentration of the laser dot for PolyMUMPs 58 test chevron actuator operation that produced 2 µm of

deflection, with (a) showing a 250 μm by 8-beam chevron, (b) showing a 350 μm by 16-beam chevron, (c) showing a 400 μm by 8-beam chevron, and (d) showing a laser dot focused on the center of the actuator. The approximately 2 μm measured deflection is observable. Figure 7.22 shows captured still images from digital video showing the magnitude of deflection caused by 60 mw laser with 40 μm diameter laser beam spot size asymmetrically illuminating one side of actuator, with (a) showing zero deflection with the laser off and (b) showing 2 μm of deflection at full power.

(a)　　　　　　　　　　　　　(b)

(c)　　　　　　　　　　　　　(d)
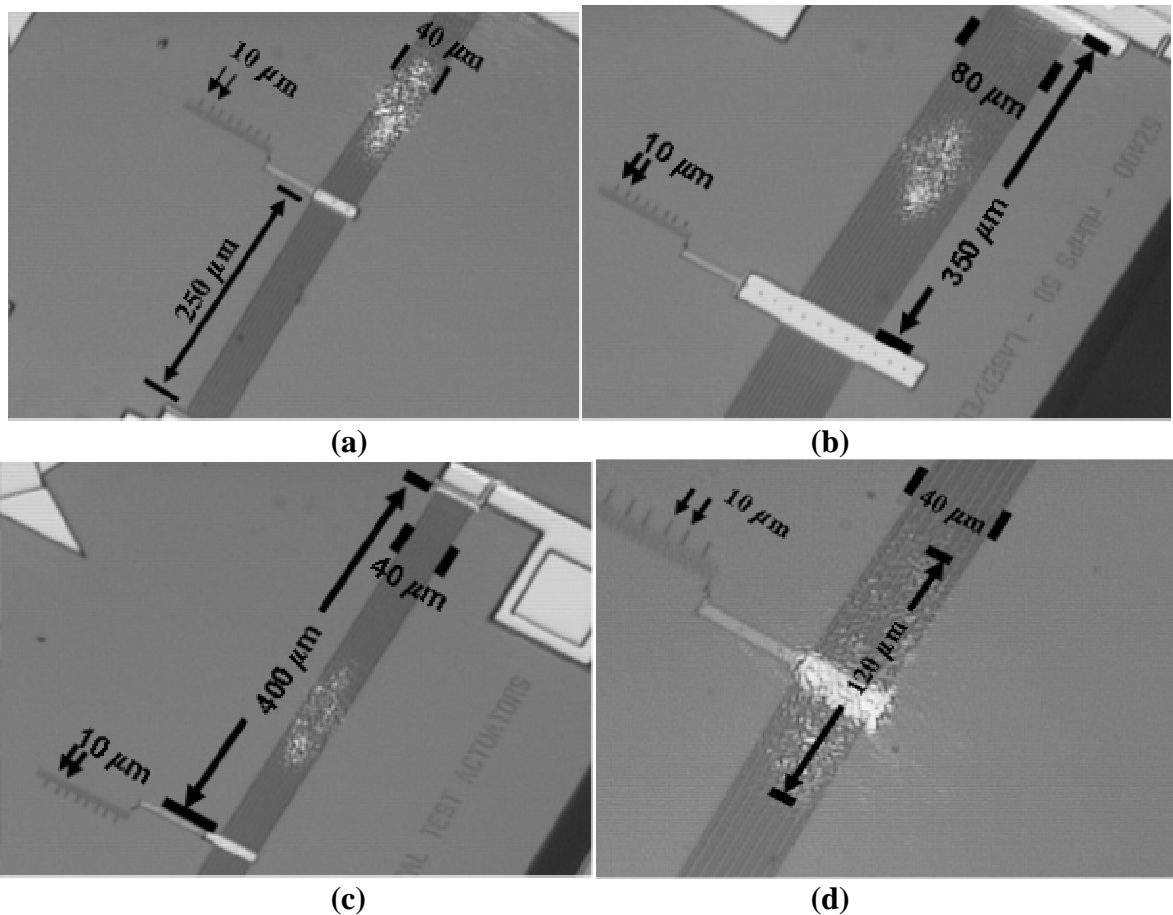
Figure 7.21: Captured still images from digital video showing the concentration of the laser dot for PolyMUMPs 58 test chevron actuator operation that produced 2 µm of deflection, with (a) showing a 250 μm by 8-beam chevron, (b) showing a 350 μm by 16-beam chevron, (c) showing a 400 μm by 8-beam chevron, and (d) showing a laser dot focused on the center of the actuator.

(a) **(b)**
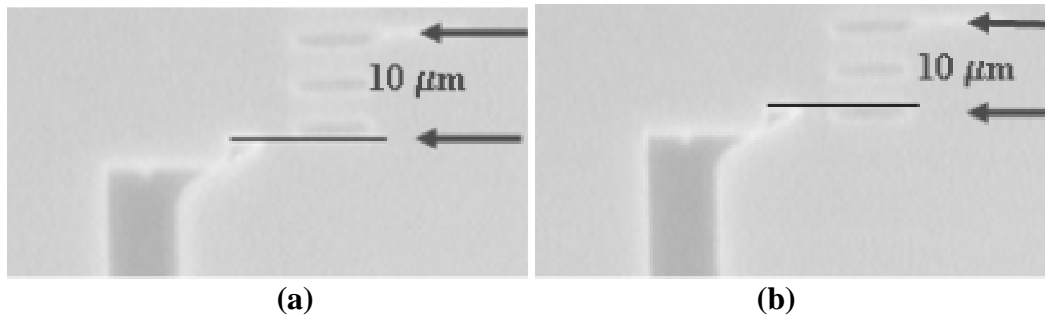
Figure 7.22: Captured still images from digital video showing the magnitude of deflection caused by 60 mw laser with 40 μm diameter laser beam spot size asymmetrically illuminating one side of actuator, with (a) showing zero deflection with the laser off and (b) showing 2 μm of deflection at full power.

7.5. Optothermal Actuator Frequency Response under Laser Illumination

The same frequency response tests used for the electrothermal test actuators were conducted using the laser on the optothermal actuators. However, the frequency response was much lower for the laser heated optothermal actuators than for the electrothermal actuators. The highest frequency with any discernable deflection was 481 Hz. The three dB amplitude point was approximately 121 Hz.

A series of tests performed on the type of signal generator wave-type that would create the best deflection. All the signal types were tried at 50 percent duty cycle. The best signal for maximum deflection with a laser turned was the square wave. The square wave was tested with different duty cycles and the 50% duty cycle was found to be the best signal for maximum deflection at higher frequencies (61 to 121 Hz). The maximum deflection of 2 μm was obtained with a square wave, a 50% duty cycle, at 31 Hz.

7.6. Validation of the Laser Microrobot Separate Parts

Because of the extreme reduction in size of the laser beam dot required to obtain sufficient heat generation, the laser microrobots were never able to move autonomously. This is because the chevron optothermal actuators and the down optothermal actuators were designed to

7-23

be actuated simultaneously with a large laser dot. However, each actuator was proven to work separately, and the conformal drive shaft housings were proven to work exceptionally well.

7.6.1. Microrobot Optothermal Chevron Actuators

Figure 7.27 shows captured still images from digital video, concatenated into a single digital image, of the LR250-8 laser microrobot being illuminated with a 60 mW, 40 µm radius, 4 Hz square-pulsed, laser beam and actuated by approximately 2µm. This was the LR250-8 microrobot with 200 μm down thermal actuators. These pictures are stills captured from digital video mpeg files recorded on a computer. The chevron actuators, illuminated asymmetrically on one side, were able to provide approximately 2 μm of rectilinear deflection to the drive shaft. Deflection of the drive shaft tip was noticeable up to 121 Hz. After 121 Hz, no discernable deflection could be observed.

The fact that the highest frequency with which deflection could be detected fell from 481 Hz with test actuators to 121 Hz with the microrobots can be attributed to two causes. The first is that all the attached hardware (multiple down thermal actuators and long drive shaft), add weight and slow down the structure. The second is the light friction that exists between the drive shafts and the conformal housings. Unfortunately, no separate test structures, with only chevron actuators, drive shafts and housing were fabricated, so these two effects could not be separated and quantified. However, since these housings bear no weight from the shaft, it is estimated that the friction between the shaft and housing is very small.
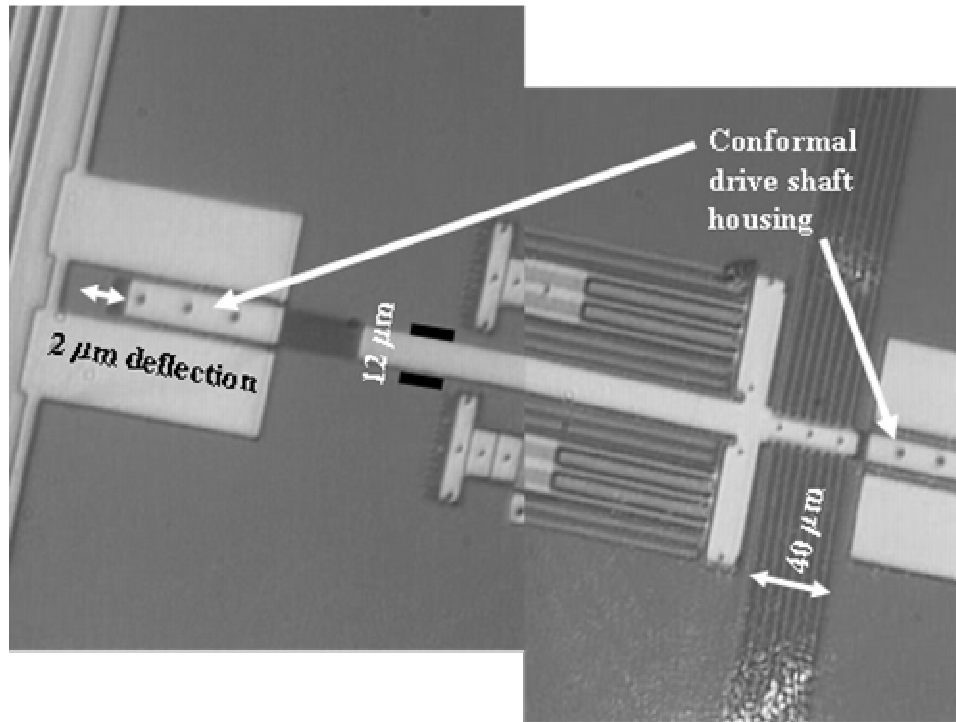
Figure 7.23: Captured still images from digital video, concatenated into a single digital image, of the LR250-8 laser microrobot being illuminated with a 60 mW, 40 µm radius, 4 Hz square-pulsed, laser beam and actuated by approximately 2µm.

7.6.2. Down Optothermal Actuators

The 200 μm down optothermal actuator had a flaw in the design layout that would not allow it to actuate. Figure 7.24 shows illustrations from L-Edit layouts depicting the problem with 200 μm down thermal actuator design on LR250-8 laser microrobot, with (a) showing a well designed 250 μm down thermal actuator and (b) showing a design flaw of a missing gap on the 200 μm down thermal actuator. Figure 7.25 shows an SEM micrograph depicting why the gap is needed for the down thermal actuators, as shown in Figure 7.24, to work. The 250 μm version of the down optothermal actuator was designed properly, as seen below in Figure 7.24 (a), and was used and tested on a larger microrobot. However, when that design was shortened to the 200 μm version (Figure 7.24 (b)), a critical gap in the Poly2, at the foot end, was left out, causing the whole actuator to fuse into one piece, instead of down actuating in two parts as seen

in Figure 7.25. The 250 μm version of the down optothermal actuator was tested, and although the amount of its deflection could not be measured with the available test equipment, the video shows it going in and out of focus as it is actuated. This demonstrated that it was changing distance from the microscope's focus length and thus proved it was actuating up and down. It was also asymmetrically heated, and showed side to side wiggling action, which was much easier to see on the video, for proof that they deflect under laser power.

(a)

(b)
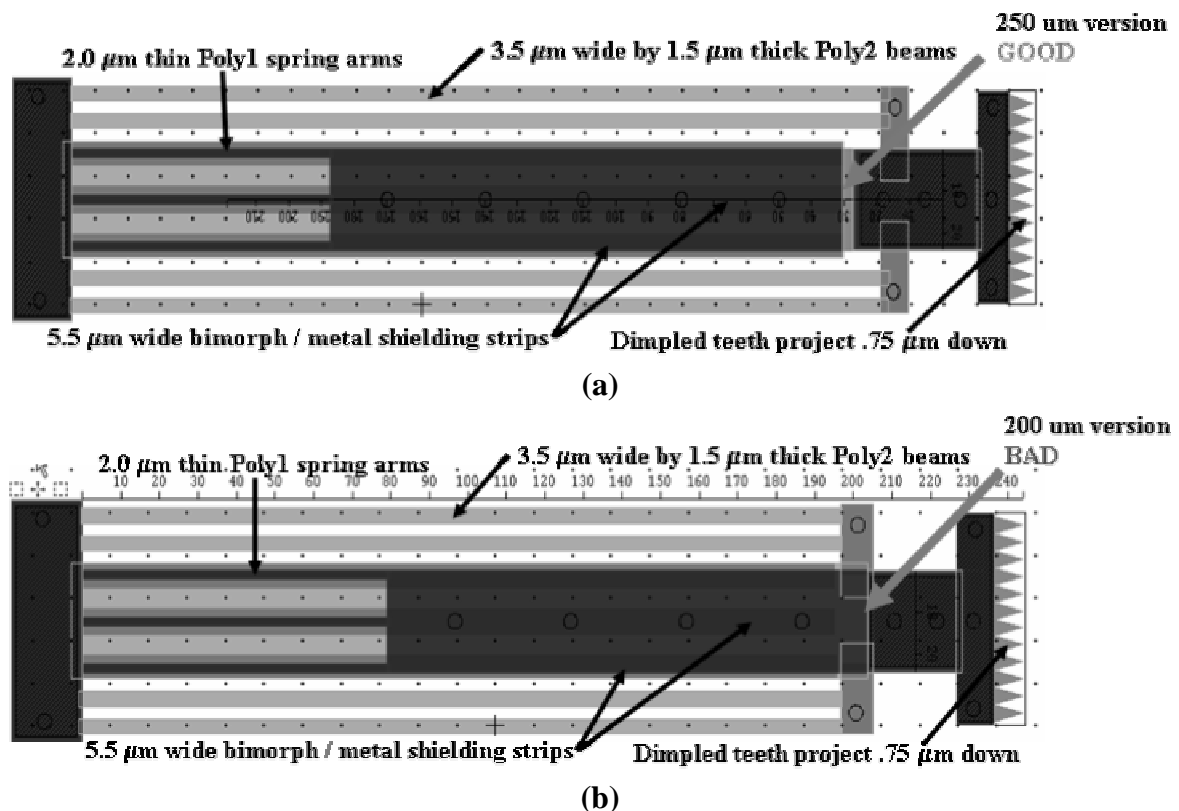
Figure 7.24: Illustrations from L-Edit layouts depicting the problem with 200 μm down thermal actuator design on LR250-8 laser microrobot, with (a) showing a well designed 250 μm down thermal actuator and (b) showing a design flaw of a missing gap on the 200 μm down thermal actuator.
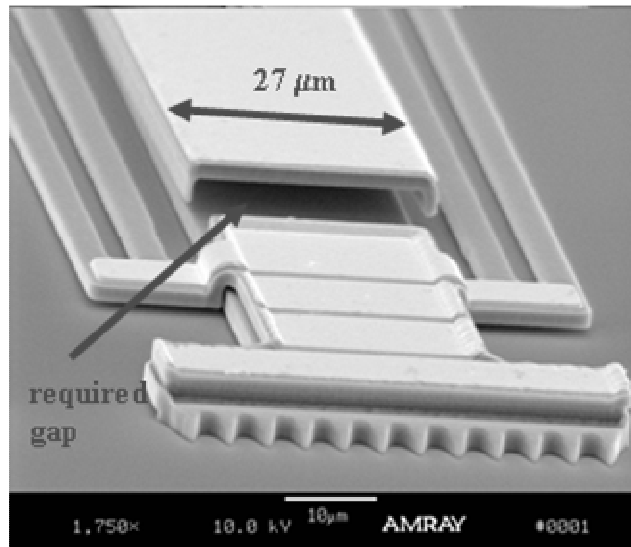
Figure 7.25: SEM micrograph depicting why the gap is needed for the down thermal actuators, as shown in Figure 7.24, to work.

7.6.3. Conformal Drive Shaft Housing

The conformal drive shaft housings performed exceptionally well. They were able to withstand over 24 μm of deflection from a probe that was providing a parallel force over 110 μm off center. Figure 7.26 has digital images showing the testing of the conformal drive shaft housing, with (a) showing a 12 μm wide drive shaft tip at rest, (b) showing a drive shaft tip extended by 14 μm, and (c) showing a 16 μm wide drive shaft tip extended by 24 μm using distinctly nonlinear actuation. Figure 7.27 has digital images showing the testing of the conformal drive shaft housing, with (a) showing an L-Edit layout depicting 16 μm wide drive shaft base and (b) showing the actual fabricated drive shaft base being extended by 24 μm. Figure 7.26 (c) in particular demonstrates the large moment force or torque that was placed on the drive shaft, yet it still remained inside the housing, providing rectilinear motion. The microrobots were attached to the substrate by 40, 2 μm by 10 μm strands, to keep the microrobot from washing away during release and handling. One particular video demonstrates that when the probe applied enough force against a stiff 24-beam chevron web to cause over 24 μm of

deflection, it also provided enough force to break all 40 strands and detach the microrobot from the substrate, without the drive shaft ever slipping out of its housing.

(a)

(b)

(c)
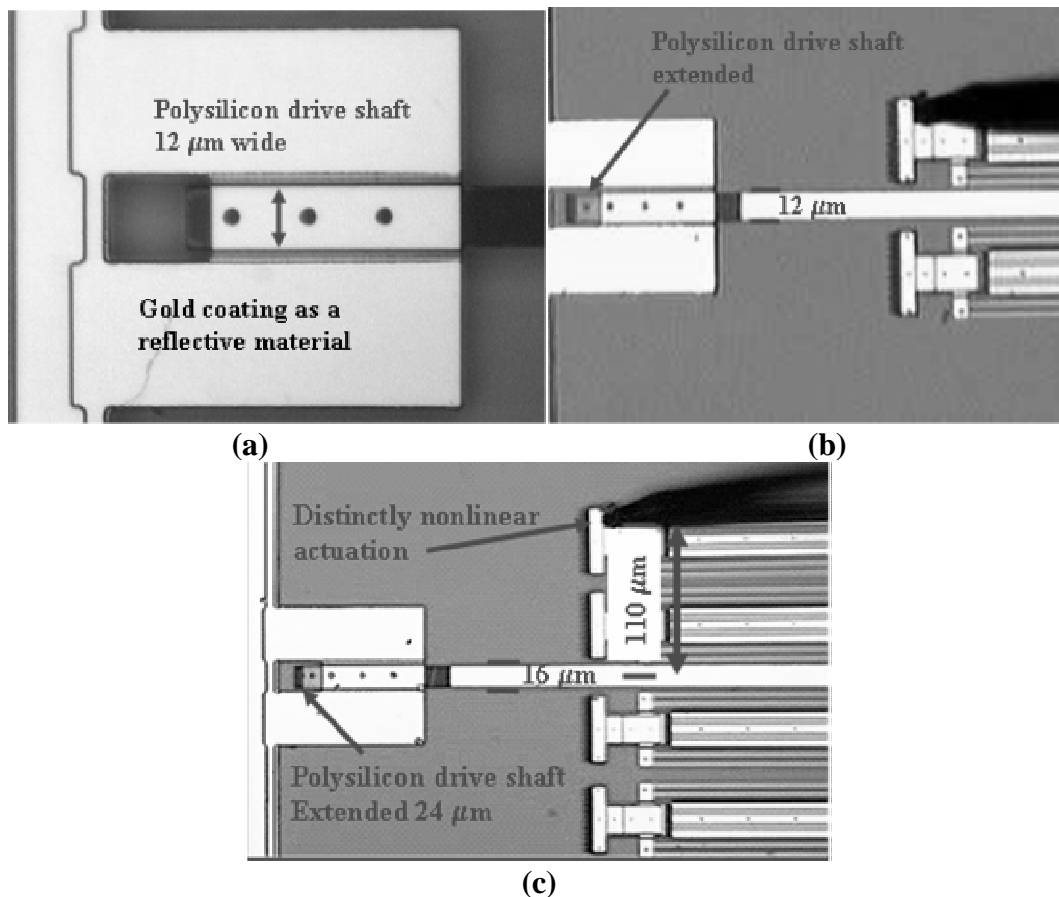
Figure 7.26: Digital images showing the testing of the conformal drive shaft housing, with (a) showing a 12 μm wide drive shaft tip at rest, (b) showing a drive shaft tip extended by 14 μm, and (c) showing a 16 μm wide drive shaft tip extended by 24 μm using distinctly nonlinear actuation.

(a)

(b)
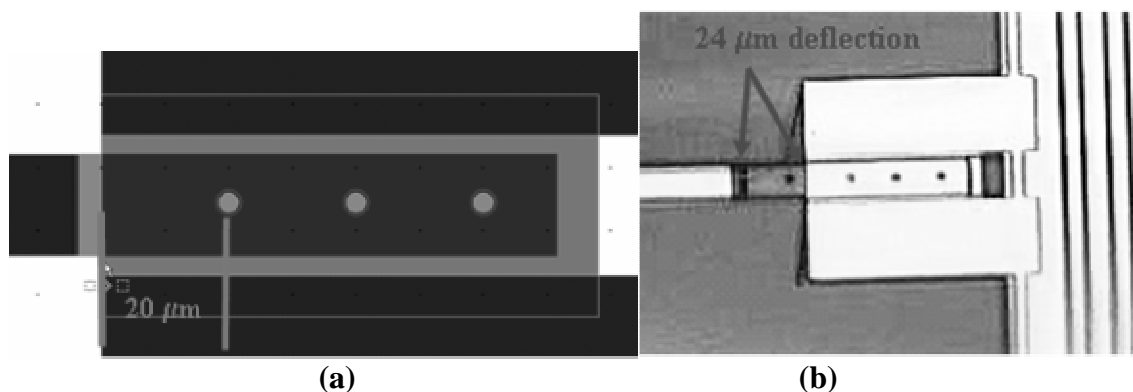
Figure 7.27: Digital images showing the testing of the conformal drive shaft housing, with (a) showing an L-Edit layout depicting 16 μm wide drive shaft base and (b) showing the actual fabricated drive shaft base being extended by 24 μm.

7.6.4. Lack of Autonomous Microrobot Movement

Unfortunately, microrobot to move autonomously was not achieved. The laser dot size reduction problem did not allow simultaneous actuation of the chevron and down optothermal actuators. There are also several other problems that need to be considered and fixed in future designs. The first one is to fix the design flaw in the 200 μm down optothermal actuator. The second is when the test chevron actuators were modeled and tested, and when the microrobot actuators were tested before release, the heated structures were 2 μm above the heat sink surface. The model predicted 1.8 μm of deflection at that height. However, when the microrobot was released and broken free from its constraints, the heated beams are now only 0.75 μm above the surface (the height of a dimple). Figure 7.28 is a plot showing the severe reduction in the magnitude of deflection (0.67 µm versus 1.8 µm) with the actuator situated only 0.75 μm above a surface acting as a heat sink, instead of 2 µm above the surface. This situation becomes worse if any part of the 5.5 μm thick frame becomes bent during release, and the heating beams on the actuators come in contact with the heat sinking substrate.
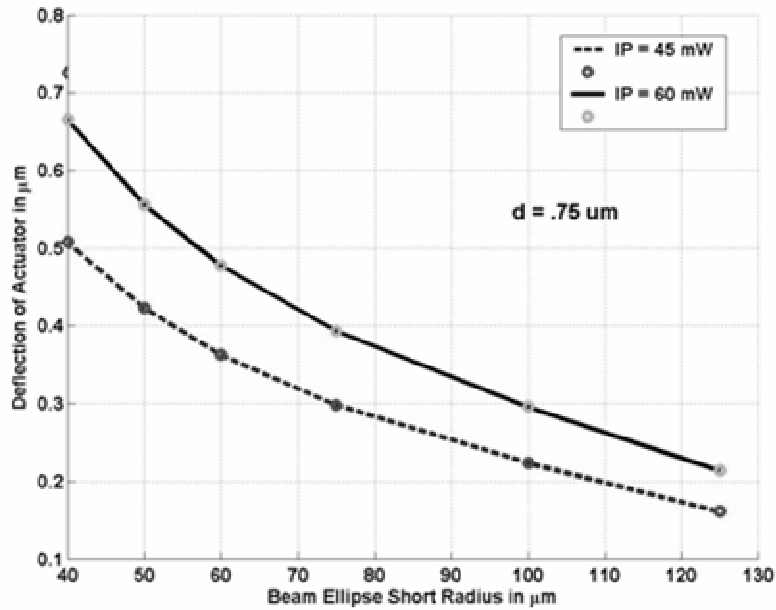
Figure 7.28: Plot showing the severe reduction in the magnitude of deflection (.67 μm versus 1.8 μm) with the actuator situated only .75 *μ*m above a surface acting as a heat sink instead of 2 μm above the surface.

7.7. PolyMUMPs Material Reflectivity Test

One final experiment was conducted to verify the model equations and the laser reflection and absorption theory discussed in chapter 3. The figures in chapter 3 were obtained for bulk crystal silicon and thick films of gold. These were used to approximate the effects of thin film highly doped polysilicon and thin film gold. Figure 7.29 shows digital images of the PolyMUMPs material reflectivity test, with (a) showing the illumination of the test chip with a laser and (b) showing the measured reflectivity (in percent) of PolyMUMPs materials. The beam angle for this test was conducted with the laser beam impinging the material surface at approximately a 45 degree angle. The reflectivity value of gold measured in the experiment was 87%. This was 7.45% lower than the estimated value of 94% obtained from the gold reflectivity table in the Handbook of Optics [5]. The standard reflectivity numbers given by King assume an incident beam normal to the surface, and this research used a beam reflecting at a 45 degree

angle, which could cause higher reflectivity. Also, part of this error may have come from the inability to capture all the reflected light with the small power meter head. See the scattering below in Figure 7.29 (a), as the beam scatters across the surface. The arrows show the angle of the incident beam and the scattering across the surface. The equations in chapter 3 show 80.22% of light being absorbed into bulk silicon, which leaves 19.78% being reflected. Poly1 and Poly2, which are highly doped polysilicon materials, showed a reflectivity of 24% and 25% respectively. This would indicate that the calculated reflectivity was about 5% off.

(a) **(b)**
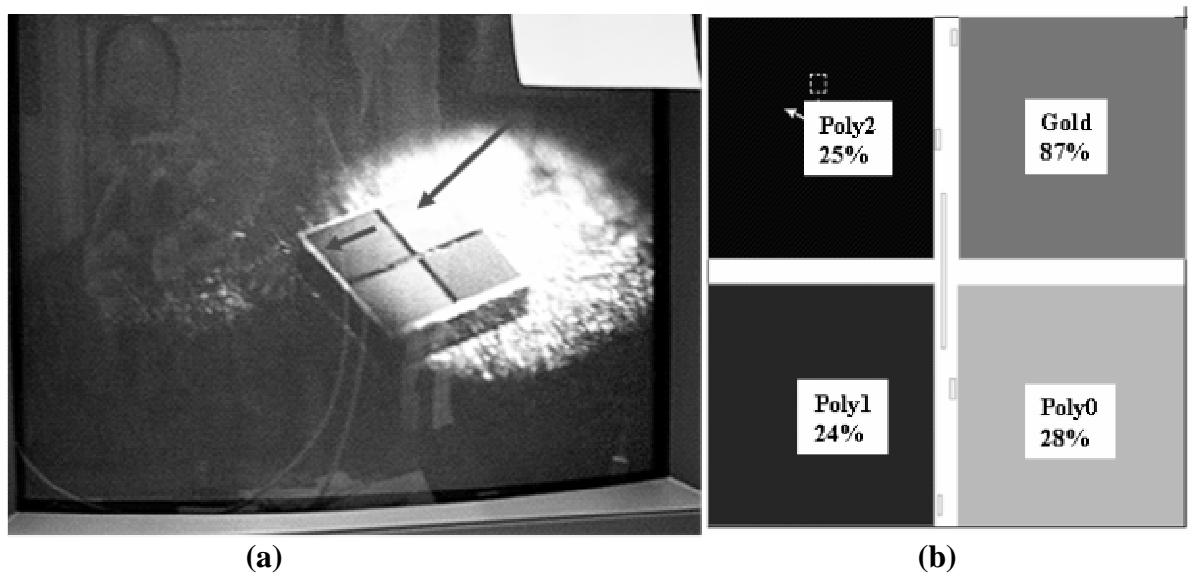
Figure 7.29: Digital images of the PolyMUMPs material reflectivity test, with (a) showing the illumination of the test chip with a laser and (b) showing the measured reflectivity (in percent) of PolyMUMPs materials.

7.8. Power Losses in the Optothermal Laser Heating Paradigm

One of the main problems in the whole optothermal laser heating paradigm was power losses at every step. A 29.7% power loss was measured through all the optics used to focus and direct the beam. Figure 7.30 is a photograph depicting the laser power loss from the laser optics beam focusing collimator lens, spatial filter, two inch magnifying lens and mirror. That means that if the laser was outputting 60 mW of power at the source (long arrow at right in Figure

7.30), then only 42 mW was reaching the target. If 25 % of that is being reflected, and only part

of that was hitting the actuator, and only a fraction of that is turned into heat, the bottom line was

that the maximum wattage actually being used to heat the actuator was approximately 15.6 mW.

This is according to the model and experimental loss results combined, and that was at a 40 μm

radius beam dot size with 60 mW of initial power. If this is compared with the electrical wattage

required in Figure 7.9, this gives slightly less than 2 μm of deflection, which is what the

experimental results proved.   If only 15.6 mW of power was actually heating the actuators, out

of the 60 mW output by the laser, the laser heating optothermal process was only 25.99%

efficient. According to the model, with a 29.7% loss to optics, a 200 mW laser yields about

52.199 mW of heating power. This would results in almost 4 μm of deflection at the 40 μm

beam dot size. At the beam dot size of radius 130 μm, with a 200 mW laser, one could still

expect a 1 μm deflection, but be able to actuate both the chevron actuators and the down thermal

actuators at the same time.
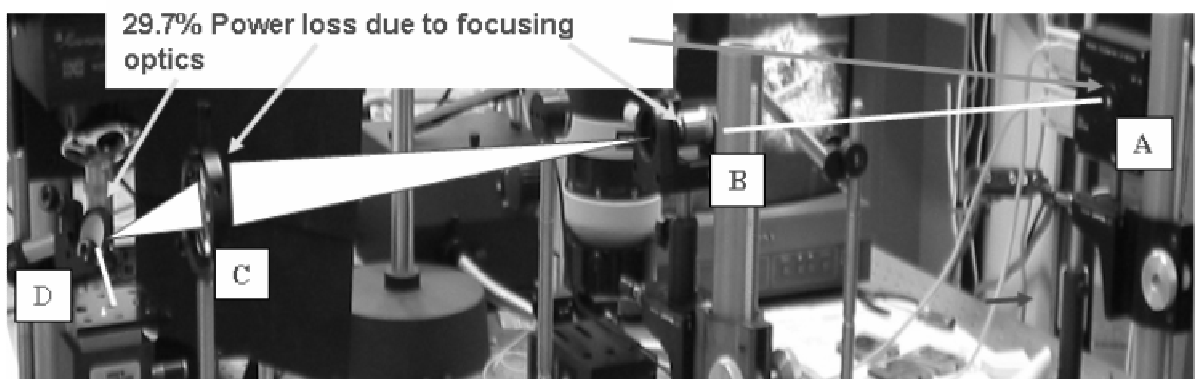
Figure 7.30: Photograph depicting the laser power loss from the laser optics beam focusing
collimator lens, spatial filter, two inch magnifying lens and mirror.

7.9. Conclusion

This chapter presented the results of the experiments discussed in Chapter 6. These

experimental results characterize the chevron bent beam actuators and the laser microrobot

designs presented in Chapter 4. They also compare with and match the results of the models presented in Chapter 5. The results included characterization of each actuator for voltage and power versus deflection, frequency response, and optothermal operation. The characterization and operation of the different microrobot parts is presented. The power losses in the optothermal laser heating paradigm are discussed.

Electrical testing of the test actuators proved the electrothermal model to be accurate within less than a 9% error. Electrothermal actuation provided a maximum deflection of 19 μm for the most successful chevron actuator. Frequency testing showed the chevron actuators provided excellent frequency response, with a 3 dB deflection loss at 1250 Hz.

The optothermal model predicted a 1.8 μm deflection, and approximately 2 μm of deflection was observed experimentally, using a 60 mW, square wave pulsed, .660 µm wavelength laser. Frequency testing showed the optothermal actuation provided much lower frequency response, with the highest frequency at which deflection could be observed was at 481 Hz.

Microrobot components were each demonstrated and verified separately. The most successful prototype microrobot design was the LR250-8. The LR250-8, with a size of 760 μm long by 710 μm wide, is a full order of magnitude smaller than the tiniest autonomous microrobot published to date.

The conformal drive shaft housing was successfully demonstrated, and ensured rectilinear motion with 24 μm of deflection, even with strong non-axial forces applied.

While the obtaining autonomous movement from the microrobots was not a success, many of the actuators and designs used in the parts were either new innovations or more

successful than those listed in the literature. The successes of this research will be summarized in the next chapter.

7.10. Bibliography

[1]   M. J. Sinclair, "A High Force Low Area MEMS Thermal Actuator," *2000 Inter Society Conference on Thermal Phenomena*, pp. 127-132, 2000.

[2]   Y. Lai, J. McDonald, M. Kujath and T. Hubbard, "Force, Deflection and Power Measurements of Toggled Microthermal Actuators", *Journal of Micromechanics and Microengineering*, Vol. 14, pp 49-56, 2004.

[3]   L. Que, J. Park, and Y. B. Gianchandani, "Bent-Beam Electrothermal Actuators-Part I: Single Beam and Cascaded Devices," *Journal of Microelectromechanical Systems*, Vol. 10, No. 2, pp. 247-254, June 2001.

[4]   http://www.memscap.com/memsrus/svcsdata.php.

[5]   M. Bass, *Handbook of Optics, Volume II, Devices, Measurements, and Properties,* New York, McGraw Hill, 1995.

8.   Conclusions

This chapter summarizes the results of this research. It compares the work accomplished with the original goals. Section 8.1 recapitulates the discussion of this research covered in Chapters 2 through 7. Section 8.2 discusses the results obtained. Contributions to the MEMS and scientific communities are listed in Section 8.3. Challenges encountered and proposed solutions to finish this particular research effort are discussed in Section 8.4. Directions for future work are proposed in Section 8.5.

8.1. Summary

Chapter 2 covered the background history on microrobots and some of the actuators that were used for microrobot motors. This background chapter covered what has been accomplished in the microrobotics field so far and listed a few possible microrobot applications. Microrobotic actuators and proposals for lasers as an actuation power source were reviewed. A summary of performance comparisons of existing small microrobots was given.

Chapter 3 briefly covered laser heating theory and discussed the wavelength and power of the laser to be used for this research. A brief description was given of the different reactions of a material to light impinging on a surface. The trade-off in parameters for reflectivity and absorption were discussed. The key concepts were actuator thickness and the amount of actuator surface area that can be placed in a small area to absorb the most laser power.

Chapter 4 presented the designs of electrothermal and optothermal actuators used in this research. Prototype microrobot designs based on optothermal actuators were also introduced. This chapter discussed the chevron actuators which could take the most advantage of the key concepts of close packed surface area to absorb the maximum amount of laser energy. The

details and principles of the basic wireless laser microrobot designs used in this research were presented. Alternate microrobot designs based on those same principles also discussed.

Chapter 5 introduced the models for single material optothermal chevron actuators. An electrothermal model was developed to predict temperature distribution, thermal expansion and deflection. This model was developed with five temperature dependant parameters, which were varied with temperature. An optothermal model was developed from the electrothermal model by substituting the laser heat generating term for the current/resistive qdot. These models enabled the prediction of the deflection of chevron actuators under electrothermal or optothermal actuation.

Chapter 6 discussed the experimental procedures and equipment that were used to electrically and optothermally characterize the test actuators and microrobots. The post processing and release of PolyMUMPs chips was explained. The video capture equipment used in the collection of data was discussed. Electrical power and frequency testing of the test chevron actuators wer expounded upon. The last section of this chapter discussed laser power and frequency testing used to characterize the optothermal actuators and the LR250-8 laser powered microrobot.

Chapter 7 demonstrated the results obtained from the research, and compared experimental results with the models from Chapter 5. These experimental results were used to characterize the chevron bent beam actuators and the laser microrobot designs presented in Chapter 4. The results included characterization of each actuator for voltage and power versus deflection, frequency response, and optothermal operation. The characterization and operation of the different microrobot parts is presented. The power losses in the optothermal laser heating paradigm were discussed.

While obtaining autonomous movement from the microrobots was not a success, many of the actuators and designs used in the parts were either new innovations or more successful than those listed in the literature.

8.2. Discussion of Results

The original ultimate goal in this research was "create a fully autonomous, wireless mobile microrobot". To that end, optothermal actuators were proposed; and the use of a laser to directly power the microrobot.

Optothermal actuators were modeled, designed, fabricated and tested. A temperature dependant thermal chevron actuator model was proposed, and electrothermal testing of the test actuators proved the model to be accurate within less than a 9% error. Electrothermal actuation provided a maximum deflection of 19 μm for the most successful chevron actuator. This model was then adapted to optothermal actuation using a laser for heating power. The model predicted a 1.8 μm deflection, and approximately 2 μm of deflection was observed experimentally, using a 60 mW, square wave pulsed, 0.660 µm wavelength laser.

Laser microrobots were designed using the optothermal actuators. Using multiple optothermal actuators to give a microrobot multiple degrees of freedom of movement was proposed and fabricated into the microrobot, but the components could only be demonstrated separately. Because movement of the microrobot was predicated on this multiple actuator movement concept, this research was never able to demonstrate autonomous movement of the microrobot, but was able to separately verify the designs of the separate components. The most successful prototype microrobot design was the LR250-8. The LR250-8, with a size of 760 μm long by 710 μm wide, is a full order of magnitude smaller than the tiniest autonomous

microrobot published to date. Some of the other advantages of the proposed microrobot design were wireless operation and the fact that no post-release assembly was required

The chevron optothermal actuators on the microrobot were demonstrated to provide approximately 2 μm of deflection to the drive shaft and the feet. In a separate test, the down optothermal actuators were shown to provide a small amount of down deflection, as demonstrated on video by moving in and out of focus under a microscope.

Finally, a conformal drive shaft was designed and fabricated. This drive shaft housing was very successful, and ensured rectilinear motion with 24 μm of deflection, even with strong distinctly off-axis forces applied.

8.3. Contributions to the MEMS and Scientific Communities

The following is a list of noteworthy contributions to the MEMS and scientific communities:

- Successfully demonstrated a new non-electronic paradigm for powering thermal actuators without wires.

- Successfully designed, modeled, fabricated and demonstrated laser heated optothermal actuators.

- Successfully demonstrated actuators that could be used in combination for providing multiple degrees of freedom of movement.

- Successfully demonstrated conformal drive shaft housings for long drive shafts. This housing limited movement in both the x and z directions, even with distinctly nonlinear forces applied to the shaft. This concept was much simpler to design and fabricate than existing designs that provide the same functionality.

- The electrothermal PolyMUMPs chevron actuators designed in this research provided distinctly improved performance in terms of both deflection and frequency response to those presently reported in the literature. Sinclair reported a maximum deflection of 14 μm [1]. This research produced a PolyMUMPs chevron actuator with an un-amplified maximum deflection of 19 μm. Que reported a 3 dB reduction in amplitude deflection of a chevron actuator at 700 Hz [2]. This research demonstrated a PolyMUMPs chevron actuator with a 3 dB amplitude deflection at 1250 Hz.

- A temperature dependant model of electrothermal actuators was successfully demonstrated that varied more properties with temperature than any model yet published, and proved very accurate at predicting deflection until the actuator was near burnout, at which point the predictions breaks down.

8.4. Challenges Encountered and Proposed Solutions

The major challenge that caused the most disappointment in this research was the inability to demonstrate autonomous movement of the microrobot. While all the actuators and parts were demonstrated to work, not enough power was available from the laser used to run them together as designed. The movement of the microrobot was predicated on the dual action of two actuators, one providing lateral movement, and one providing an up and down movement. This combined movement was to lift and push the microrobot at the same time. The laser power assumptions were based on literature describing damaging reflective thin film gold PolyMUMPs mirrors with only 9 mW of power. However, no mention was made of beam size, which greatly affects the power per area that can be applied. This designs used to obtain autonomous movement of a microrobot would have been more successful if the power per area consideration

had been more adequately explored. The LR250-8 microrobot was designed to work with a laser beam with a dot radius of 260 μm, which would have powered all actuators simultaneously. After considerable experimentation and re-deriving the optothermal model, it was found that a 40 μm radius dot size was needed to provide enough power per area to heat half of a chevron actuator to provide 2 μm of deflection. Under full electrical power this same actuator could provide 13 μm of deflection.

There are several sets of solutions available which could solve this problem, and provide the autonomous movement of the microrobot sought by this research. The first and most cost efficient solution would be to use a more powerful laser and a beam splitting optics setup. A 200 mW diode laser with the same .660 µm wavelength is available from Roithner Lasertechnik in Vienna, Austria. The beam could be split into two equal parts, both more powerful than the 45 to 60 mW laser diode used in this research. Two separate beams could illuminate the two separate actuators, providing the push and lift action needed to make the microrobot go. This laser diode could be driven by the same laser driver and diode cooler used in this research, so the only new equipment needed would be the beam splitter, and a second copy of the optics focusing hardware already used.

A 300 mW diode laser, also available from Roithner Lasertechnik, would be powerful enough to use a single dot size of 130 μm radius that could partially illuminate all actuators and still have enough power to drive them, with the chevron actuator still having enough power to provide 1.5 μm of deflection (according to the model). However, this diode would require a whole new rack of more expensive equipment to drive, cool and mount the laser diode.

A third idea would be to use the two 45 to 60 mW laser diodes already obtained, and use the dual beam driving concept outlined above. However, whole new rack of extra equipment

would be needed to drive, cool and mount the extra laser diode. It should be noted, that while lower frequency lasers would improve heating performance, laser diodes with power outputs above 45 mW were not readily available in frequencies below .660 µm. Frequencies above 700 nm would require a new fabrication process, because the maximum thickness provided by PolyMUMPs is 3.5 μm, and at frequencies above 700 nm, too much power would be lost to light passing through the actuators, unless thicker actuators could be fabricated.

Whichever of these increased power schemes is used, there are several suggested microrobot design optimizations that will make the actuators themselves more efficient. The first would be to test the design limits of the PolyMUMPs fabrication process, and place the chevron actuator beams only 2 μm apart. This would allow less laser power to be wasted. This would be combined with an increase in the number of chevrons from 8 to 12. This would provide much more surface area to absorb the laser power, without too much extra stiffness, as was encountered with the 16 and 24 beam chevrons.

Another optimization would be to reduce friction by shrinking the width of the long dimples used in the frame to provide the corrugated cardboard style stiffness effect used to stiffen the frame. These dimples also provide the surface area of the microrobot that rests on the "ground" when the microrobot is released. Too much of this surface area led to too much friction. There are 7 long dimples, each 5 μm wide, that go the length of each side of the frame. These should be reduced in size to the minimum width allowed by the fabrication rules (3 μm), and reduced in number from 7 to 5. The beams on the sides that are the direction the microrobot is designed to move are perpendicular to the movement, thus provide unwanted maximum resistance. These should also be reduced, as suggested above, and rotated 90 degrees so that

they present their thin side (3 μm) as resistance to movement, rather than their thick side (760 μm). This will also greatly reduce the frictional resistance the robot frame has.

8.5. Future Directions for this Research

There are several directions future research could take. The first would be to design and program a set of computer controlled mirrors that would allow the laser to follow the microrobot as it moved. The present crude equipment setup used a mirror with two hand-turned adjustment screws. The microrobot would only have moved far enough until the beam was no longer focused on the actuators enough to provide power for movement. The mirrors would have to be readjusted by hand until they were refocused on the actuators, and the laser power has to be turned down during that adjustment for eye safety reasons. It would be a very unwieldy process, to turn down the laser, hand adjust the two mirror screws to re-aim the beam, turn the laser back up, have the microrobot go a few microns in distance, then repeat the steps. Programmed computer controlled mirrors would be the perfect answer to continuous microrobot movement.

A second research direction would be to add more steering capabilities. The microrobot could possibly be steered by addressing the left or right down thermal actuators separately. A scheme such as adding extra actuators that would somehow be separately addressable with multiple laser beams would allow the microrobot's movement to be directed, especially if combined with computer controlled mirrors. As the microrobot is presently designed, it would go only one direction if it is only illuminated with one laser beam. Adding steering, or even the ability to reverse movement, would greatly increase the capabilities of this microrobot.

A final future direction for research would be for a continued reduction in size. Figure 8.1 is an L-Edit design layout of the 415 by 415 µm LR-150-12 microrobot, incorporating

several design optimizations; including twelve 150 µm long chevron actuator beams, placed only 2 µm apart. Smaller chevrons provide less deflection, but considering the fact the laser dot size is so small it cannot even cover half the length of the chevron beams on one side, as presently designed, such a size reduction could be accomplished without a significant loss in deflection.
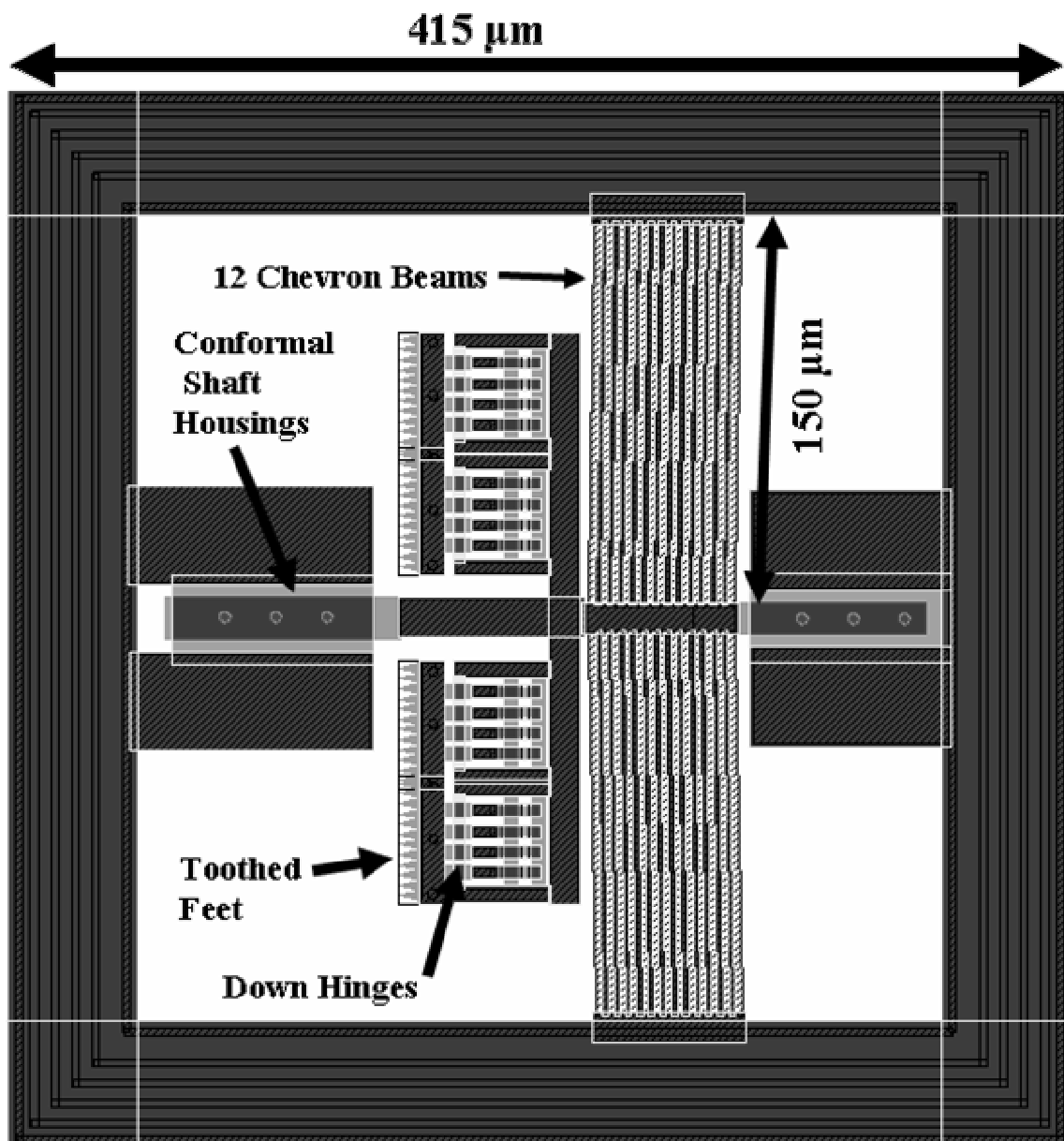
Figure 8.1: L-Edit design layout of the 415 by 415 μm LR-150-12 microrobot, incorporating several design optimizations; including twelve 150 μm long chevron actuator beams, placed only 2 μm apart.

8.6. Conclusion

These proposals conclude this research in optothermal actuators and laser microrobots. The MEMS microrobotics field is still in its infancy, and this research should be viewed as one of the many small stepping stones in the continuous search for the world's smallest autonomous robot. Many of the pieces, such as the combination of the drive shaft, conformal drive shaft housing, and chevron actuators have a great many possible applications for other MEMS machines. Hopefully this research will open up avenues for other creative minds to explore power scavenging and nontraditional ways of powering MEMS devices.

8.7. Bibliography

[1]   M. J. Sinclair, "A High Force Low Area MEMS Thermal Actuator," *2000 Inter Society Conference on Thermal Phenomena*, pp. 127-132, 2000.

[2]   L. Que, J. Park, and Y. B. Gianchandani, "Bent-Beam Electrothermal Actuators-Part I: Single Beam and Cascaded Devices," *Journal Of Microelectromechanical Systems*, Vol. 10, No. 2, pp. 247-254, June 2001.

APPENDIX A

This appendix provides large design layout pictures of all the PolyMUMPs designs submitted for fabrication during this research.
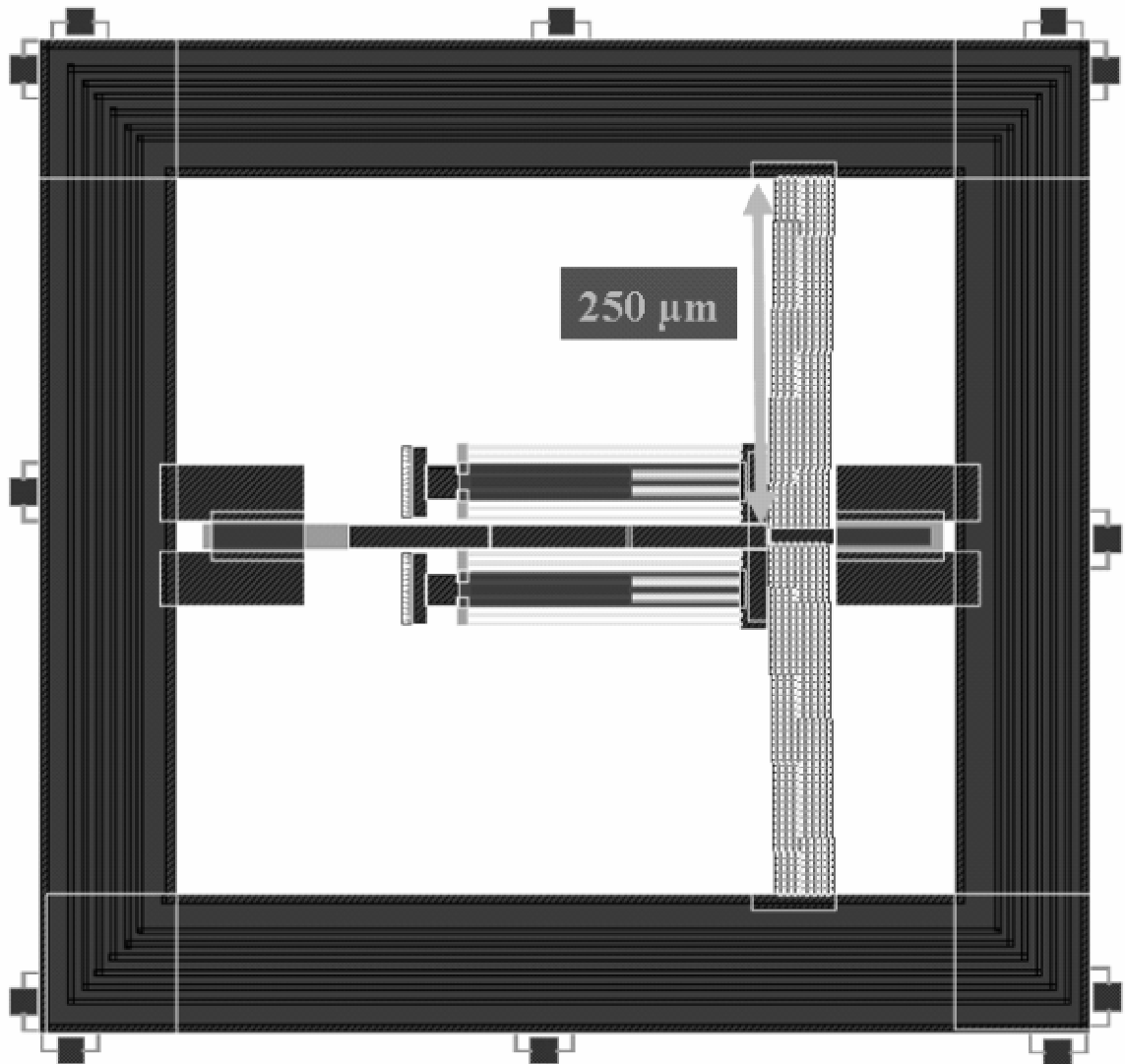
Figure A1.1: L-Edit layout showing the PolyMUMPs 58 microrobot design; the LR250-8 microrobot with a 760 by 710 µm size, 250 µm long chevron actuators with 8 chevron beams, and with two, 200 µm long down thermal actuators.
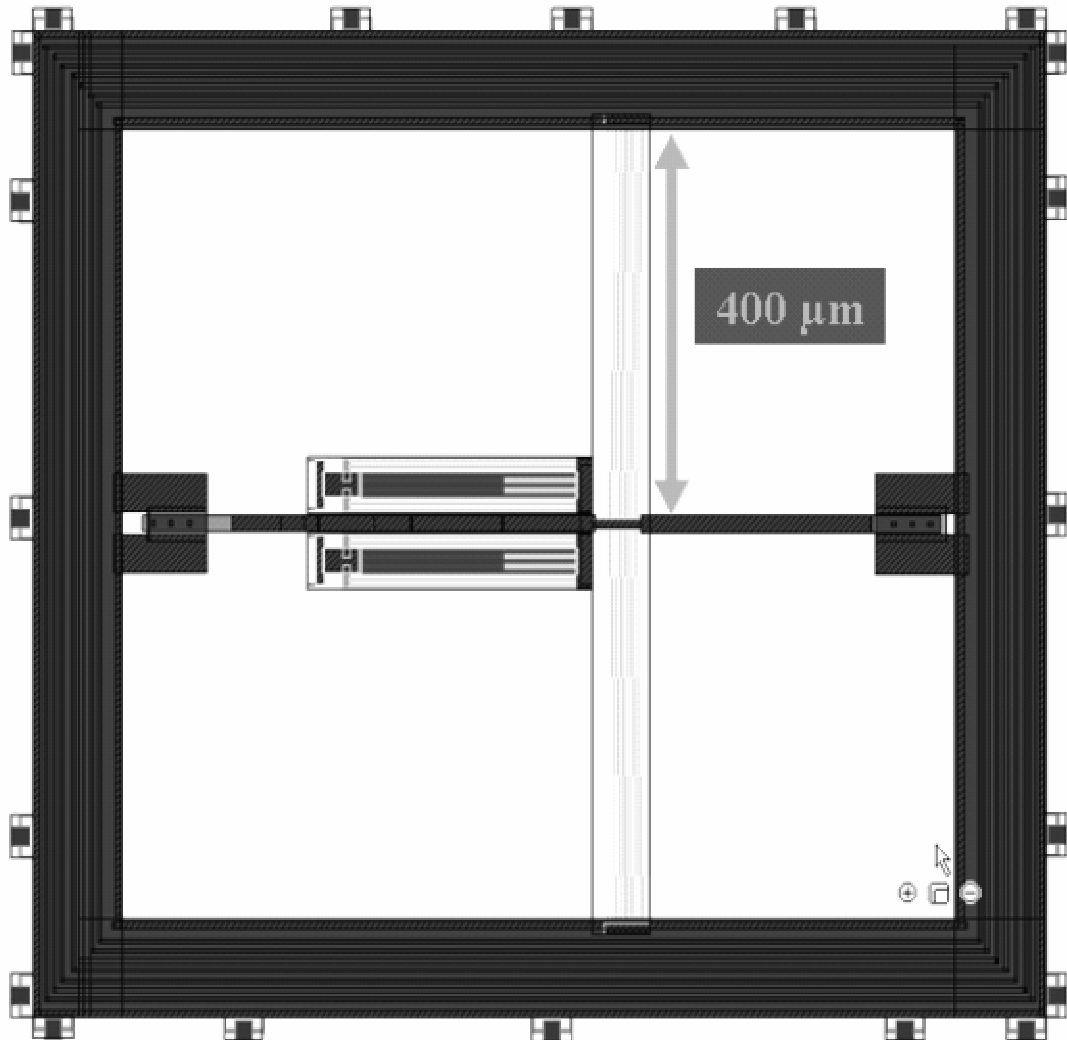
Figure A1.2: L-Edit layout showing the PolyMUMPs 58 microrobot design; the LR400-8 microrobot with a 990 by 1120 µm size, 400 µm long chevron actuators with 8 chevron beams, and with two, 250 µm long down thermal actuators.
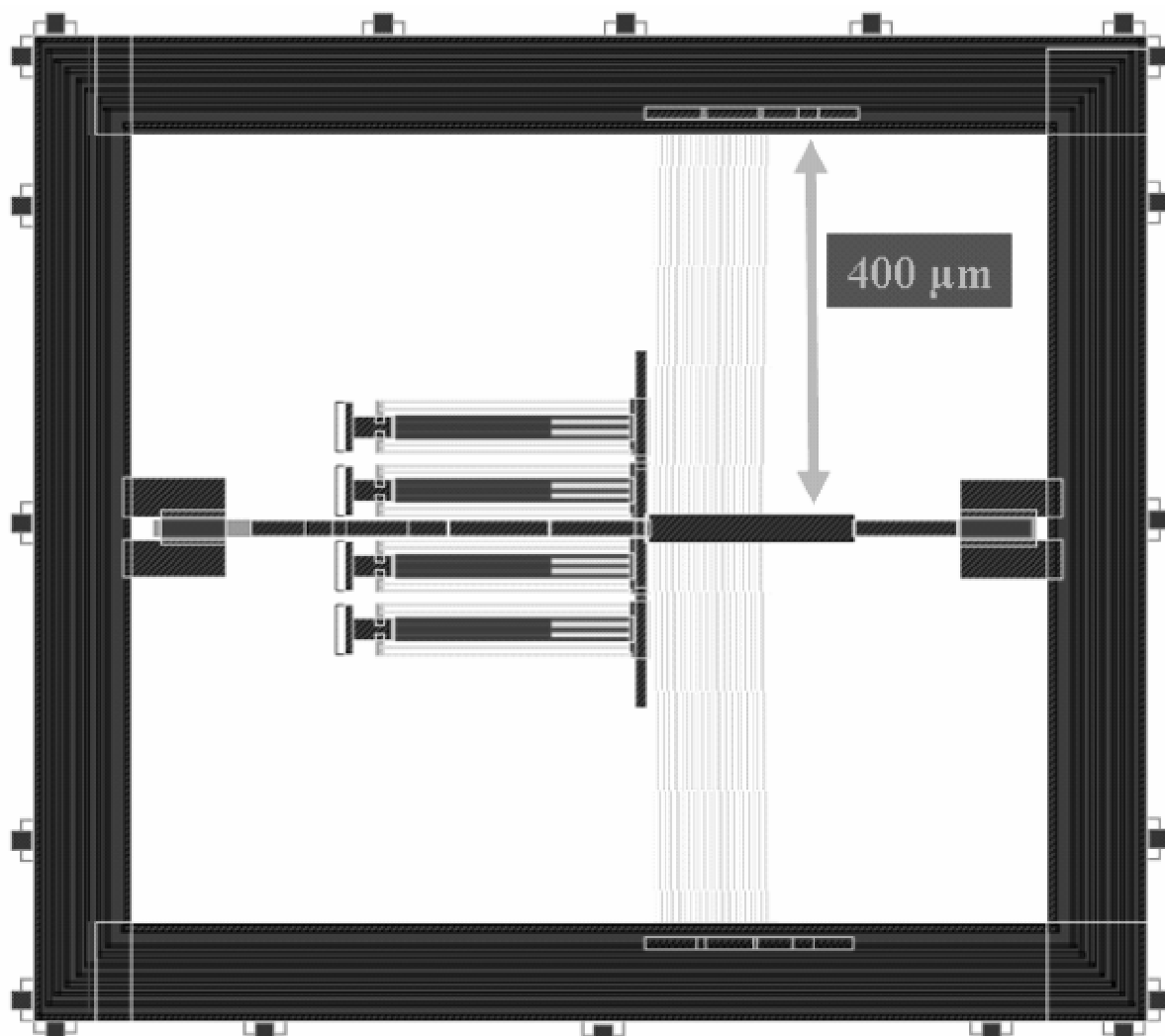
Figure A1.3: L-Edit layout showing the PolyMUMPs 58 microrobot design; the LR400 microrobot -24 with a 990 by 1120 µm size, 400 µm long chevron actuators with 24 chevron beams, and with four, 250 µm long down thermal actuators.
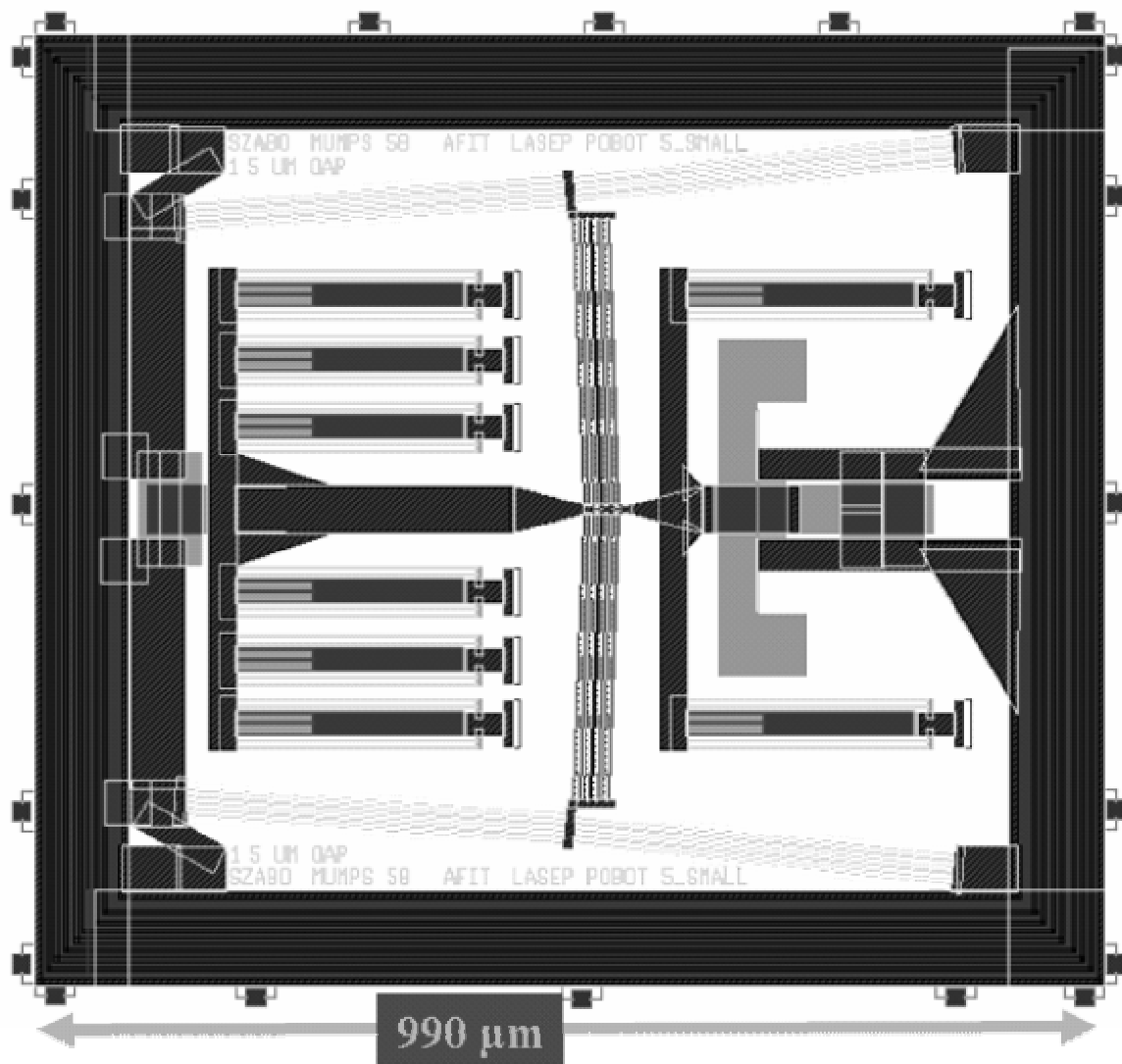
Figure A1.4: L-Edit layout showing the PolyMUMPs 58 microrobot design; the Cascade-LR400-8 microrobot with a 990 by 1120 µm size, 400 and 300 µm long chevron actuators with 8 and 4 chevron beams, and with eight, 250 µm long down thermal actuators.
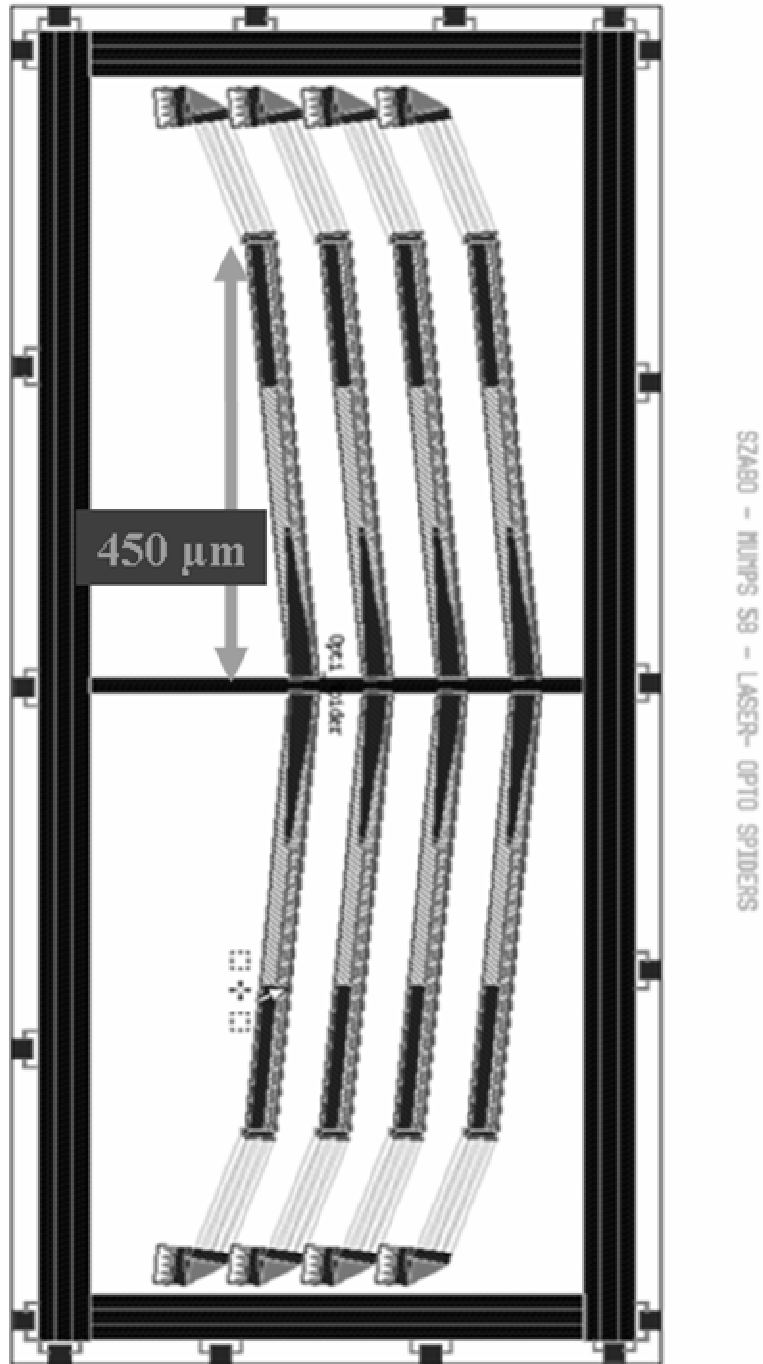
Figure A1.5: L-Edit layout showing the PolyMUMPs 58 microrobot design; the Laser Spider with a 1360 by 560 µm size, and 440 µm long, double hot arm actuators, and 200 µm long bimorph down thermal actuators mounted at the end of the double hot arm actuators.
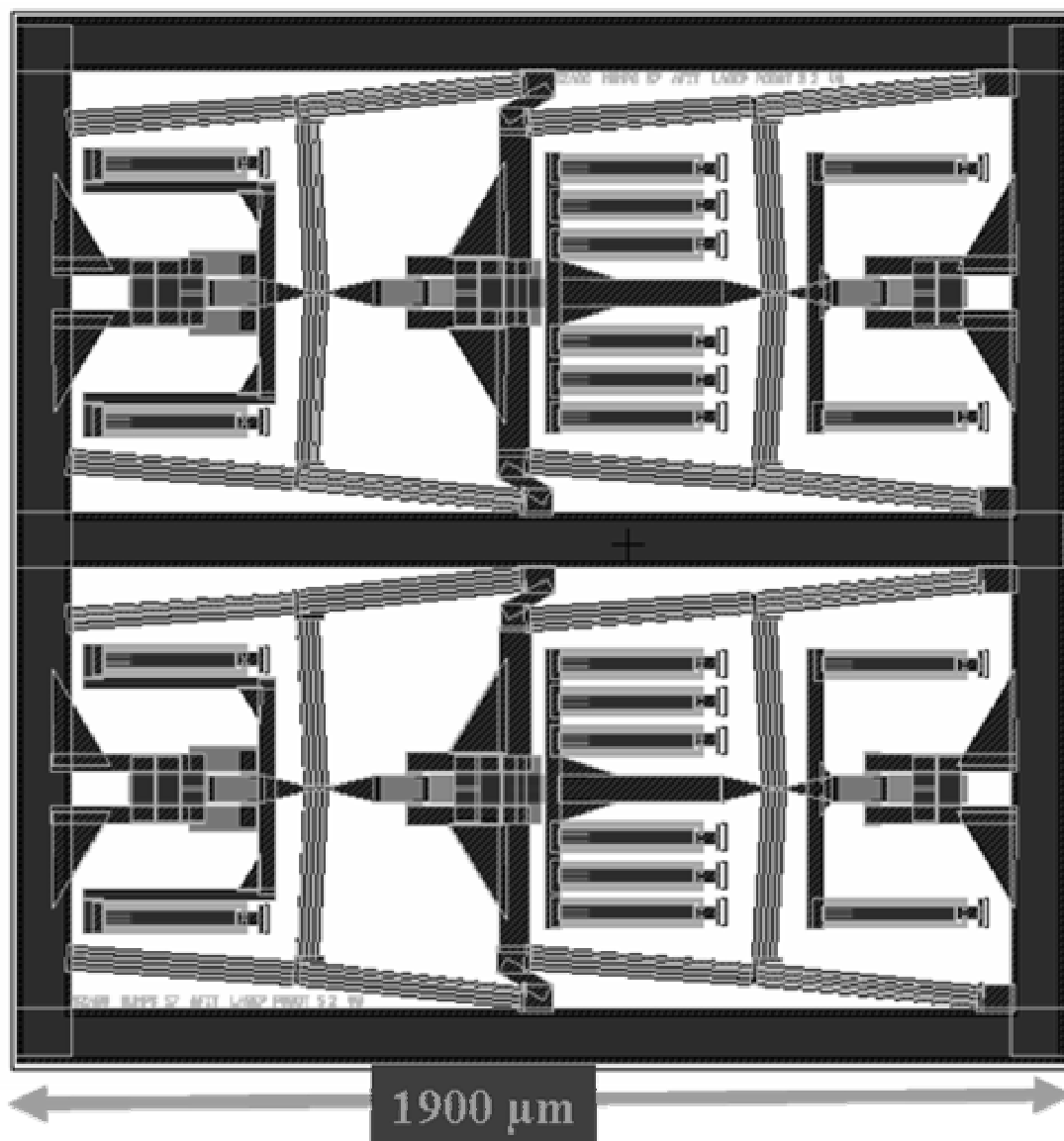
Figure A1.6: L-Edit layout showing the PolyMUMPs 57 microrobot design; a cascade-microrobot design with a 1900 by 1900 µm size, 400 and 300 µm long chevron actuators with 4 chevron beams, and with twenty, 250 µm long down thermal actuators.
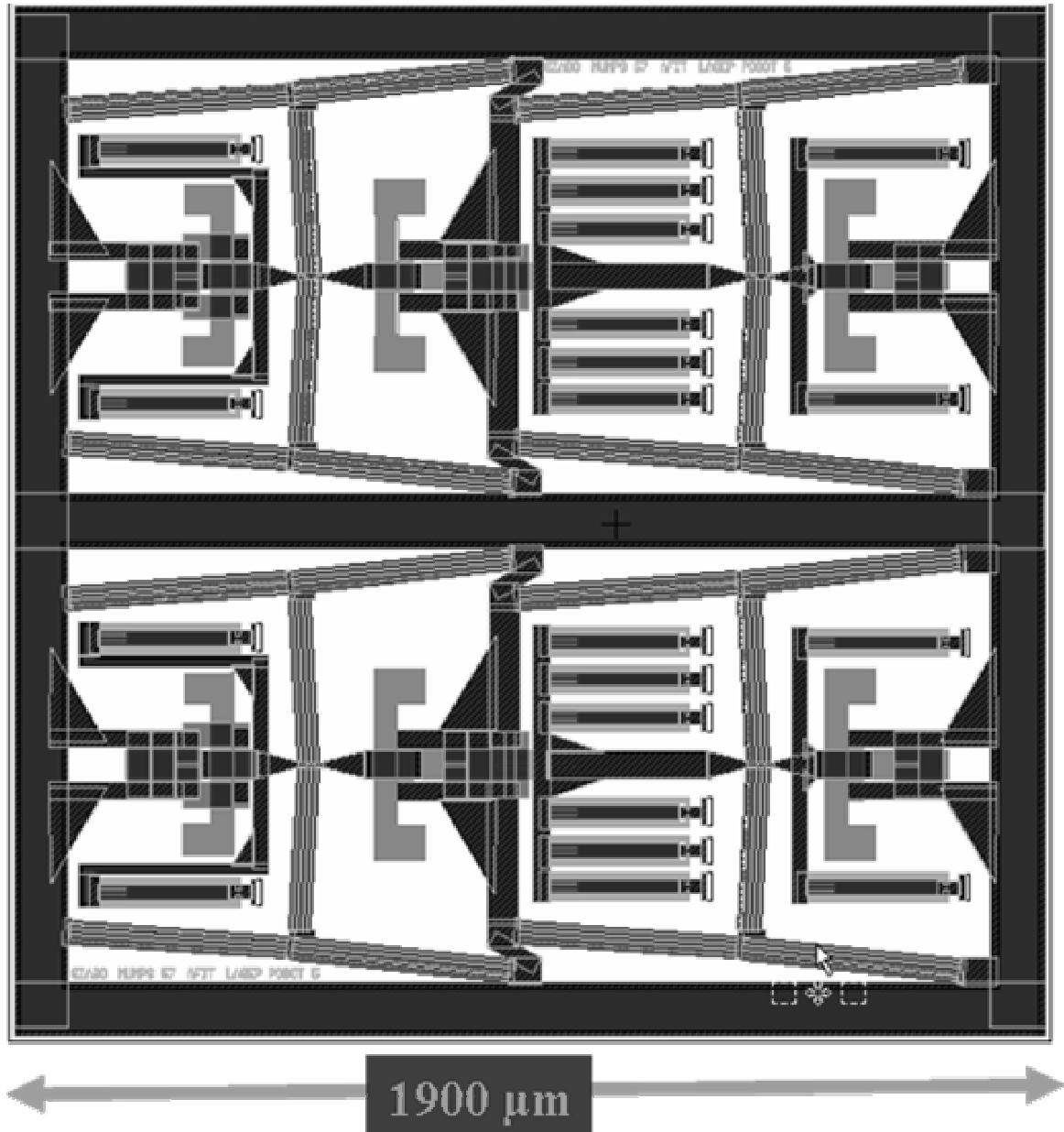
Figure A1.7: L-Edit layout showing the PolyMUMPs 57 microrobot design; a cascade-microrobot design with a 1900 by 1900 µm size, 400 and 300 µm long chevron actuators with 4 chevron beams, and with twenty, 250 µm long down thermal actuators. It also has detachable tabs for under-over drive shaft housings.
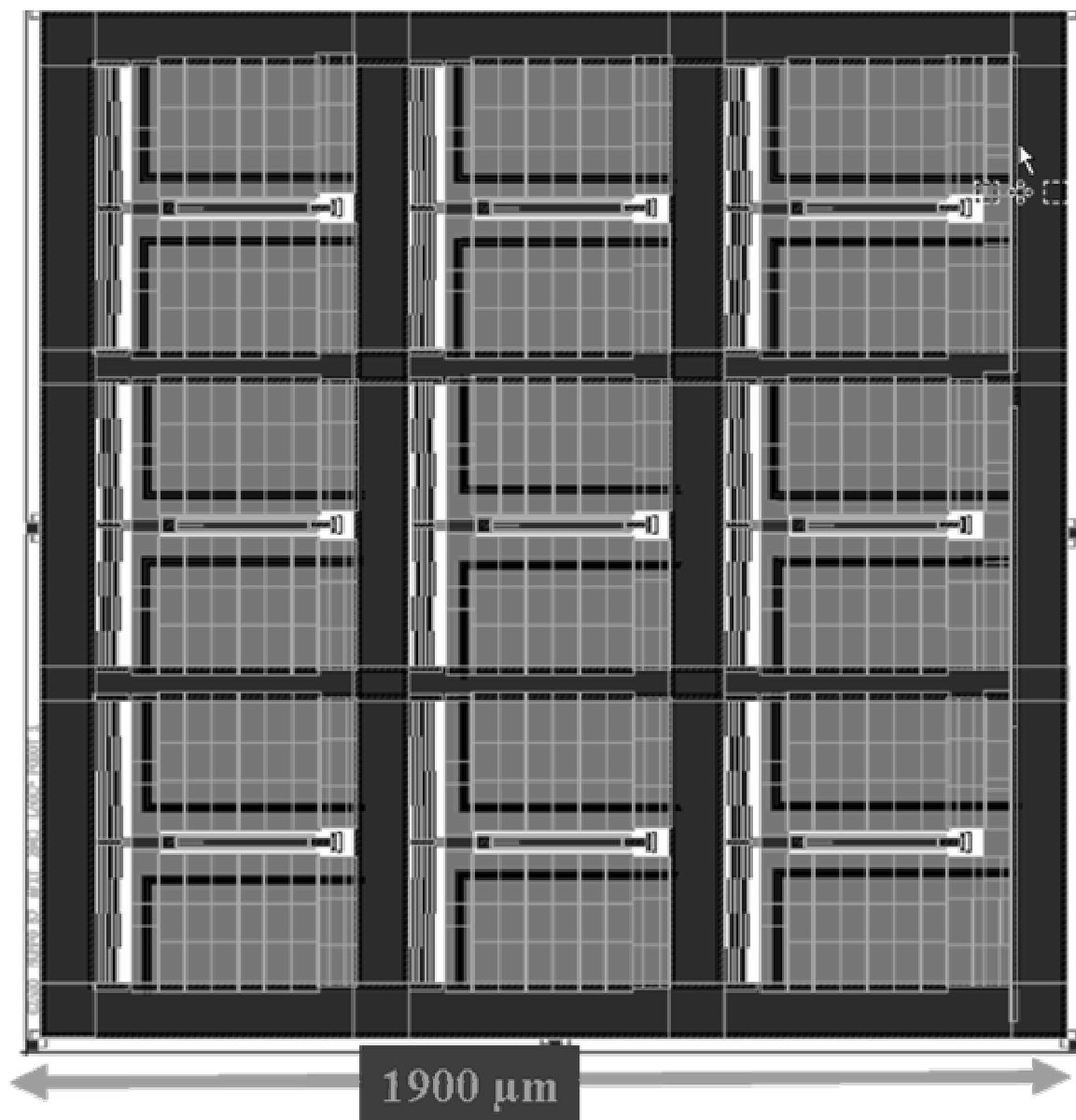
Figure A1.8: L-Edit layout showing the PolyMUMPs 57 microrobot design; an optothermal chevron microrobot design with a 1900 by 1900 µm size, 9, 250 µm long chevron actuators with 8 chevron beams, and with nine, 200 µm long down thermal actuators.
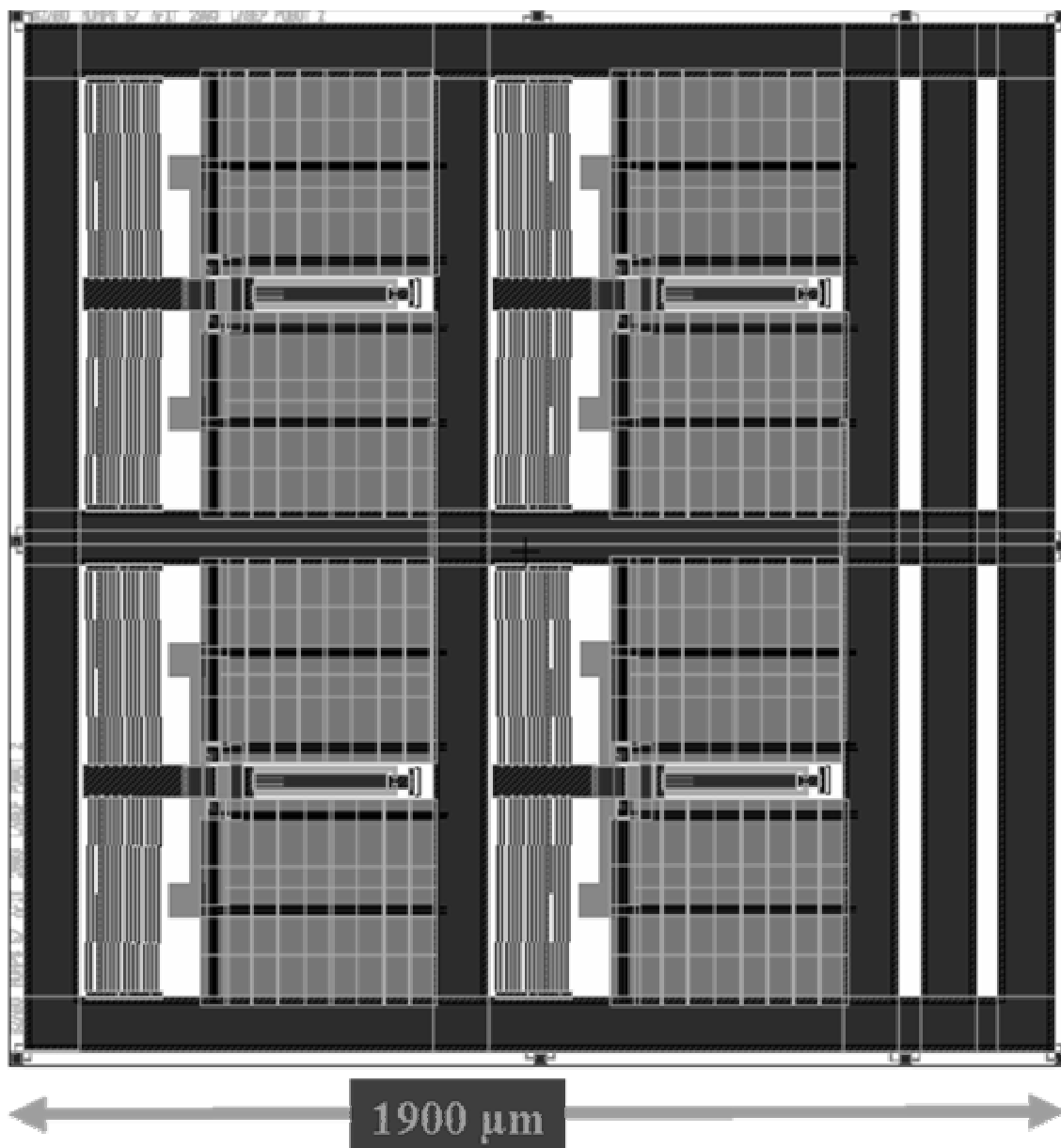
Figure A1.9: L-Edit layout showing the PolyMUMPs 57 microrobot design; an optothermal chevron microrobot design with a 1900 by 1900 µm size, four, 350 µm long chevron actuators with 16 chevron beams, and with four, 250 µm long down thermal actuators.

1900 μm
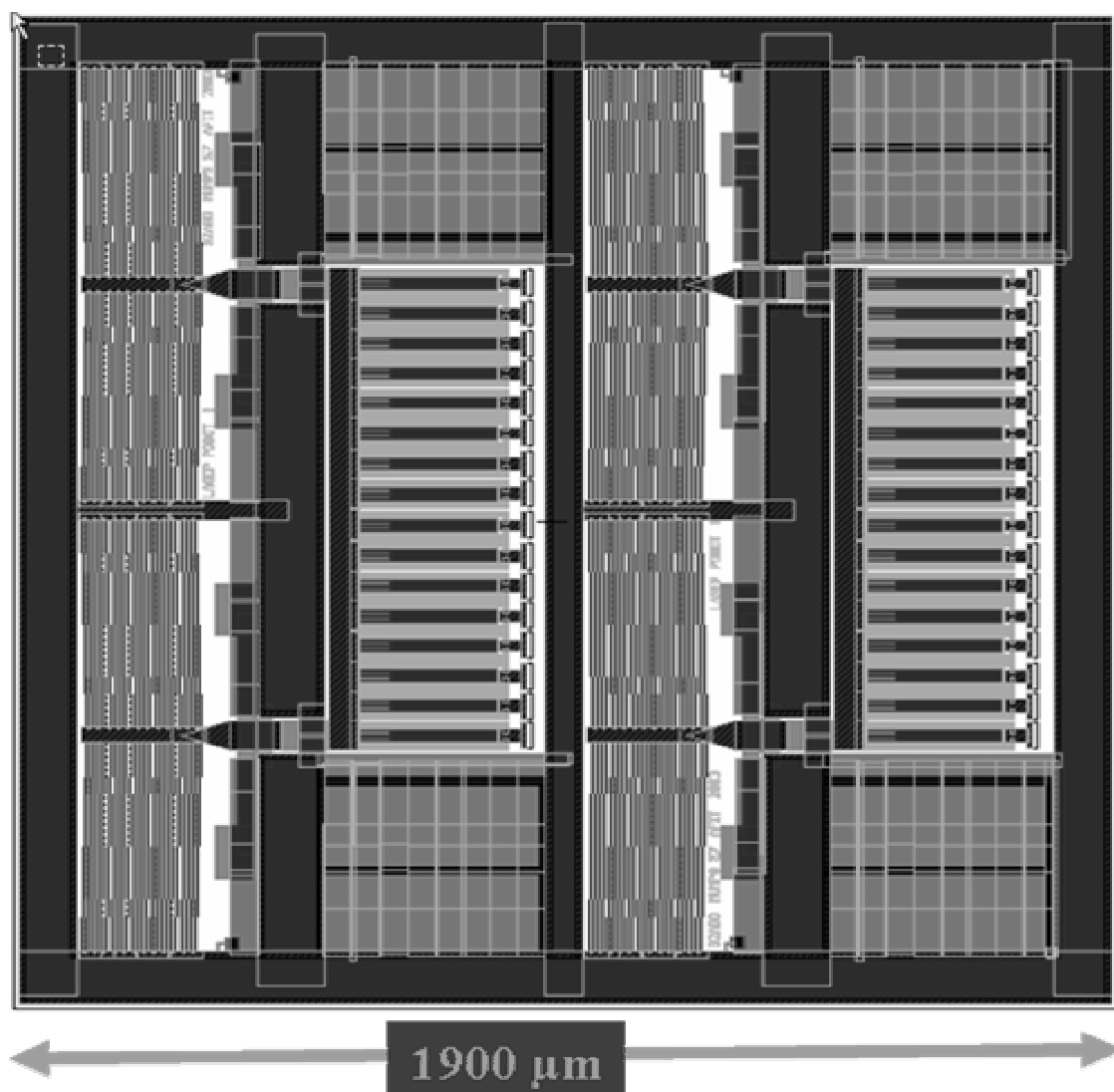
Figure A1.10: L-Edit layout showing the PolyMUMPs 57 microrobot design; an optothermal chevron microrobot design with a 1900 by 1900 μm size, 4, 400 μm long chevron actuators with 20 chevron beams, and with thirty-two, 250 μm long down thermal actuators.
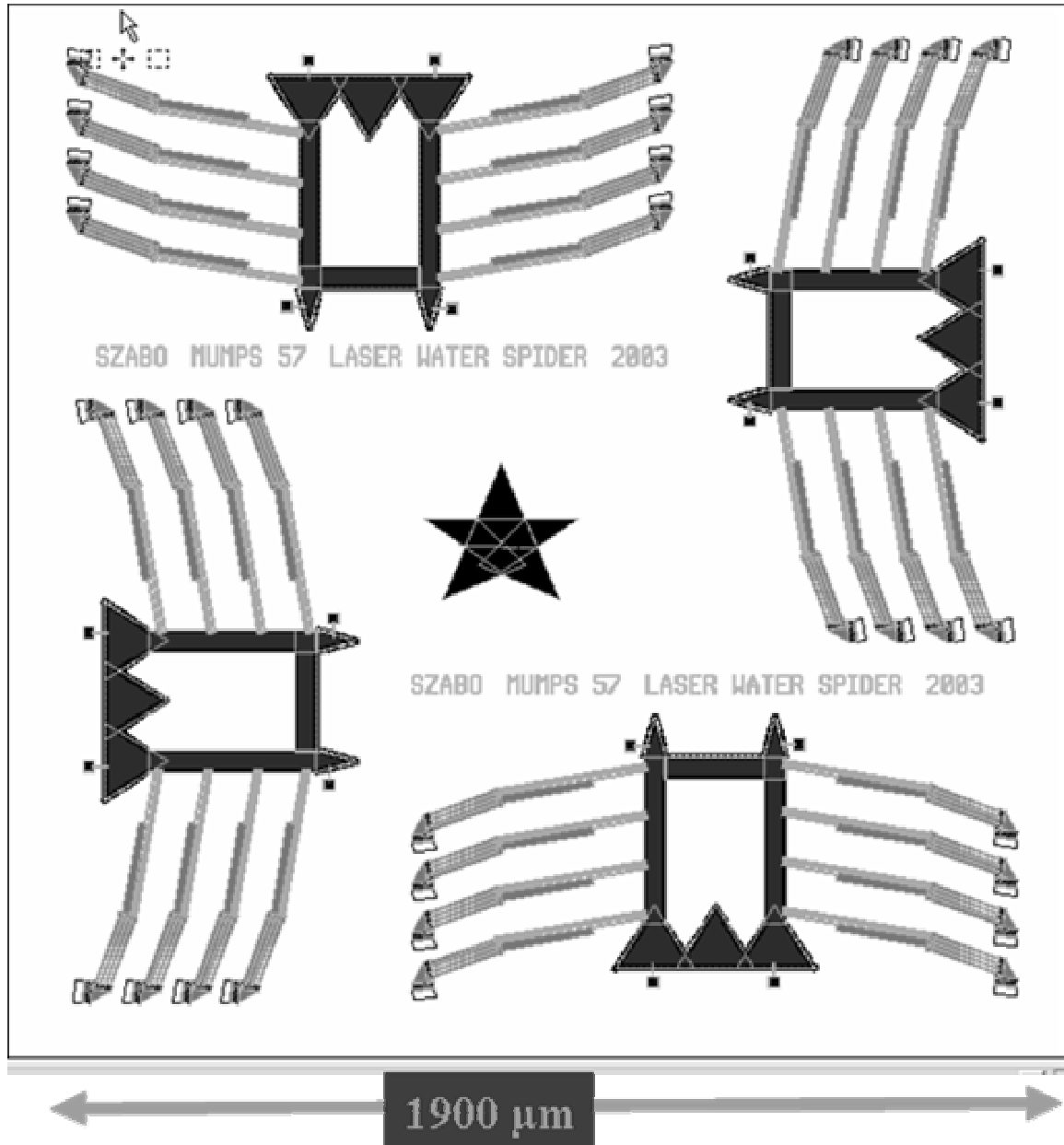
Figure A1.11: L-Edit layout showing the PolyMUMPs 57 microrobot design; the Laser Water Spider with a 1250 by 560 µm size, and eight, 250 µm long, double hot arm actuators, and 200 µm long bimorph down thermal actuators mounted at the end of the double hot arm actuators.
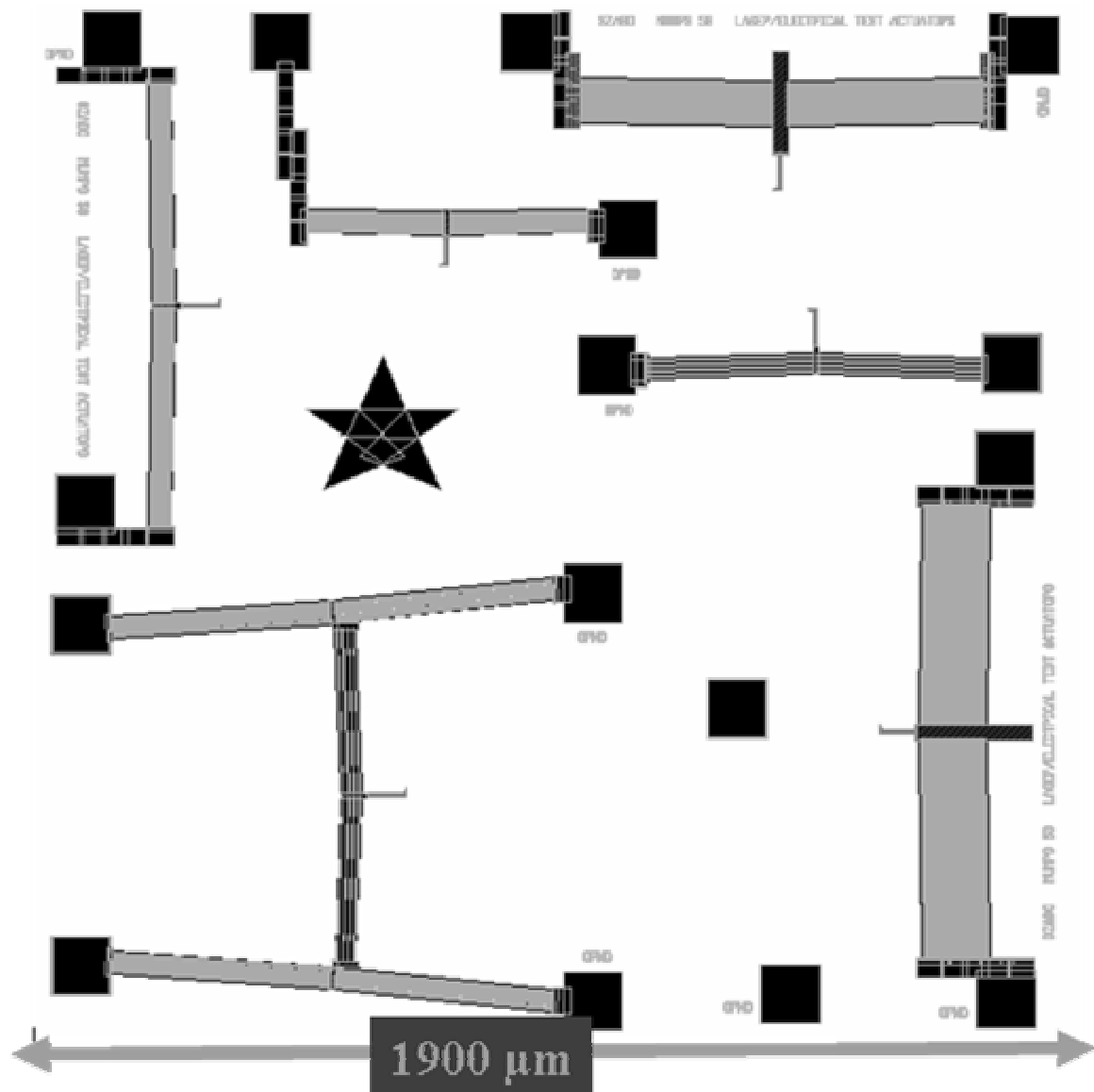
Figure A1.12: L-Edit layout showing the PolyMUMPs 58 test actuator design chip; with 250 µm long, 350 µm long, and 400 µm long chevron actuators with 8, 16 and 24 chevron beams. They can be tested both electrothermally and optothermally.
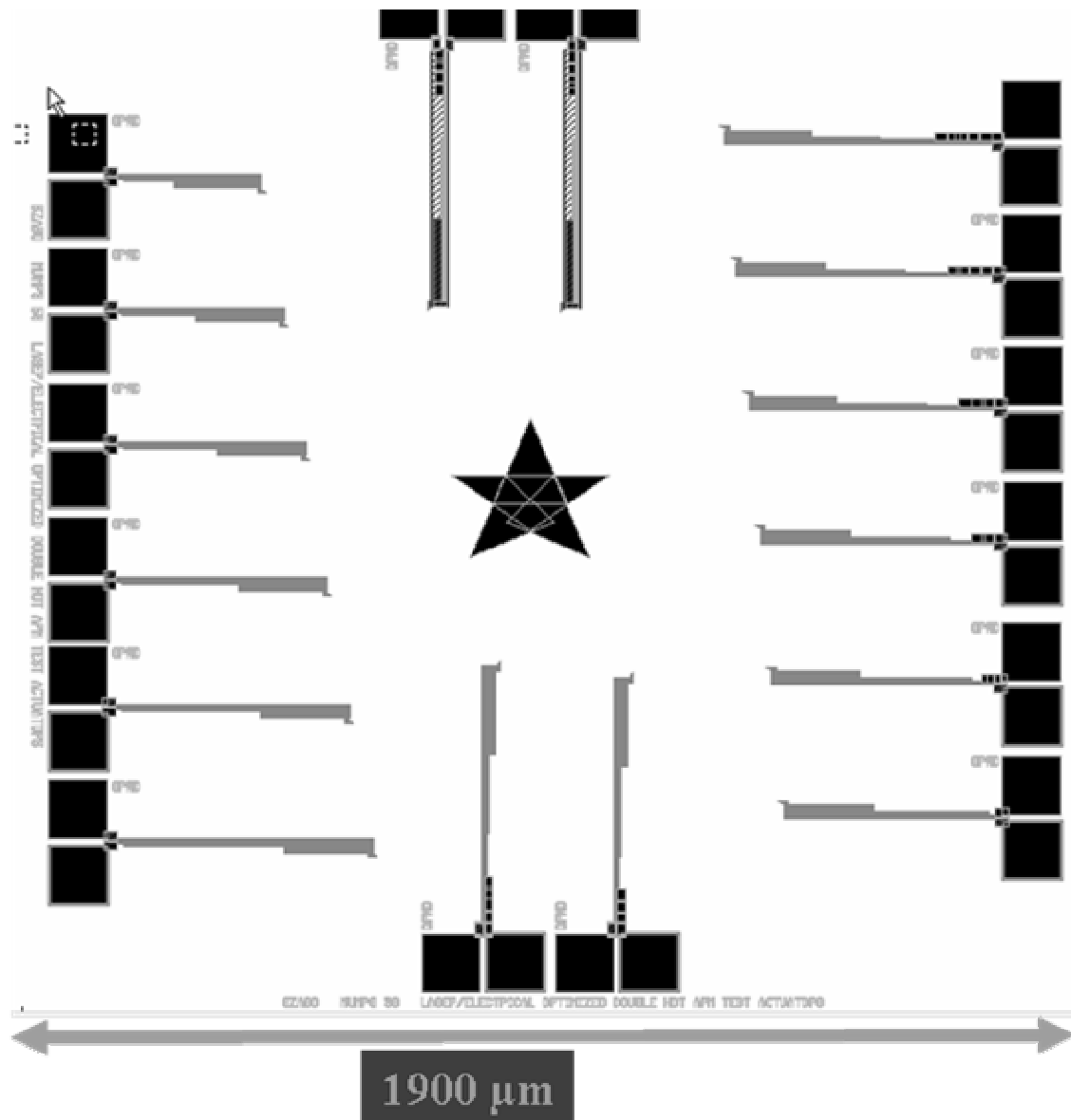
Figure A1.13: L-Edit layout showing the PolyMUMPs 58 test actuator design chip; with 250 µm, through 450 µm long double hot arm actuators. The ones at the top can be tested both electrothermally and optothermally.
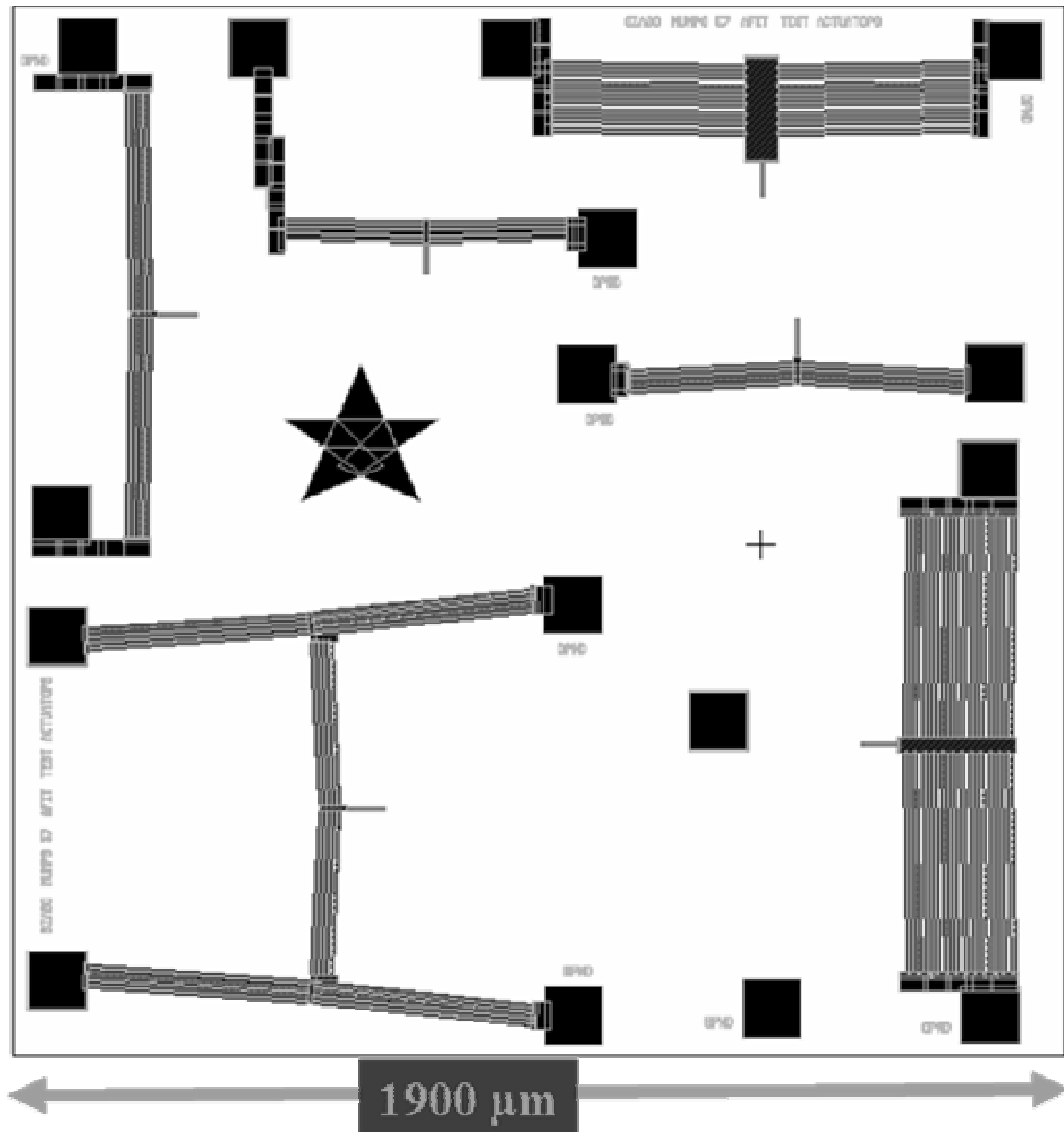
Figure A1.14: L-Edit layout showing the PolyMUMPs 57 test actuator design chip; with 250 µm, 350 µm, and 400 µm long chevron actuators with 4, 16 and 24 chevron beams. They can be tested both electrothermally and optothermally.
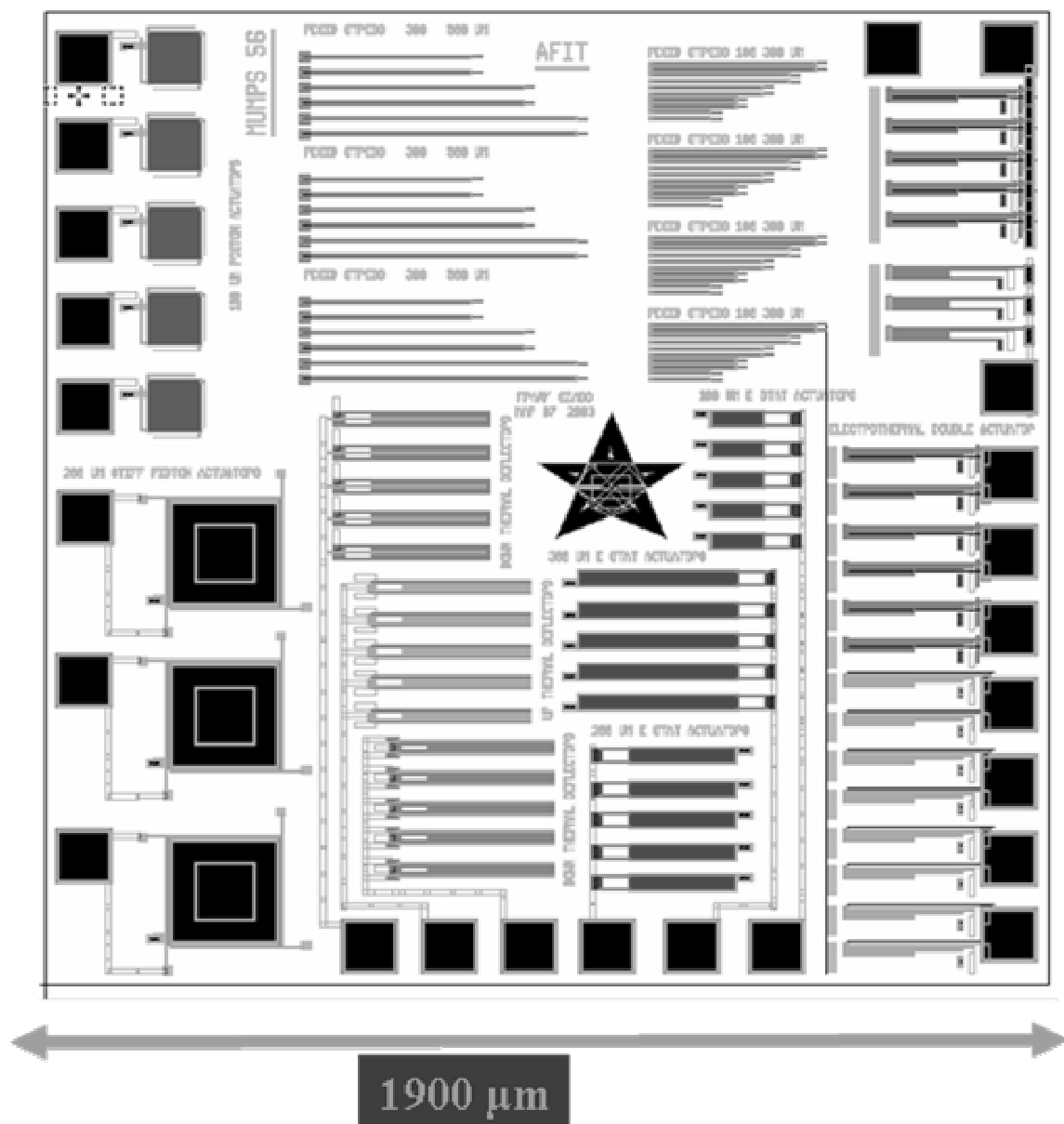
Figure A1.15: L-Edit layout showing the PolyMUMPs 56 test actuator design chip; with 250 µm long double hot arm actuators, up and down thermal actuators, gold dot tests double hot arm actuators, electrostatic actuators and residual stress structures. These residual stress structures were used in this research as calibration marks for aligning the laser beam dot size.
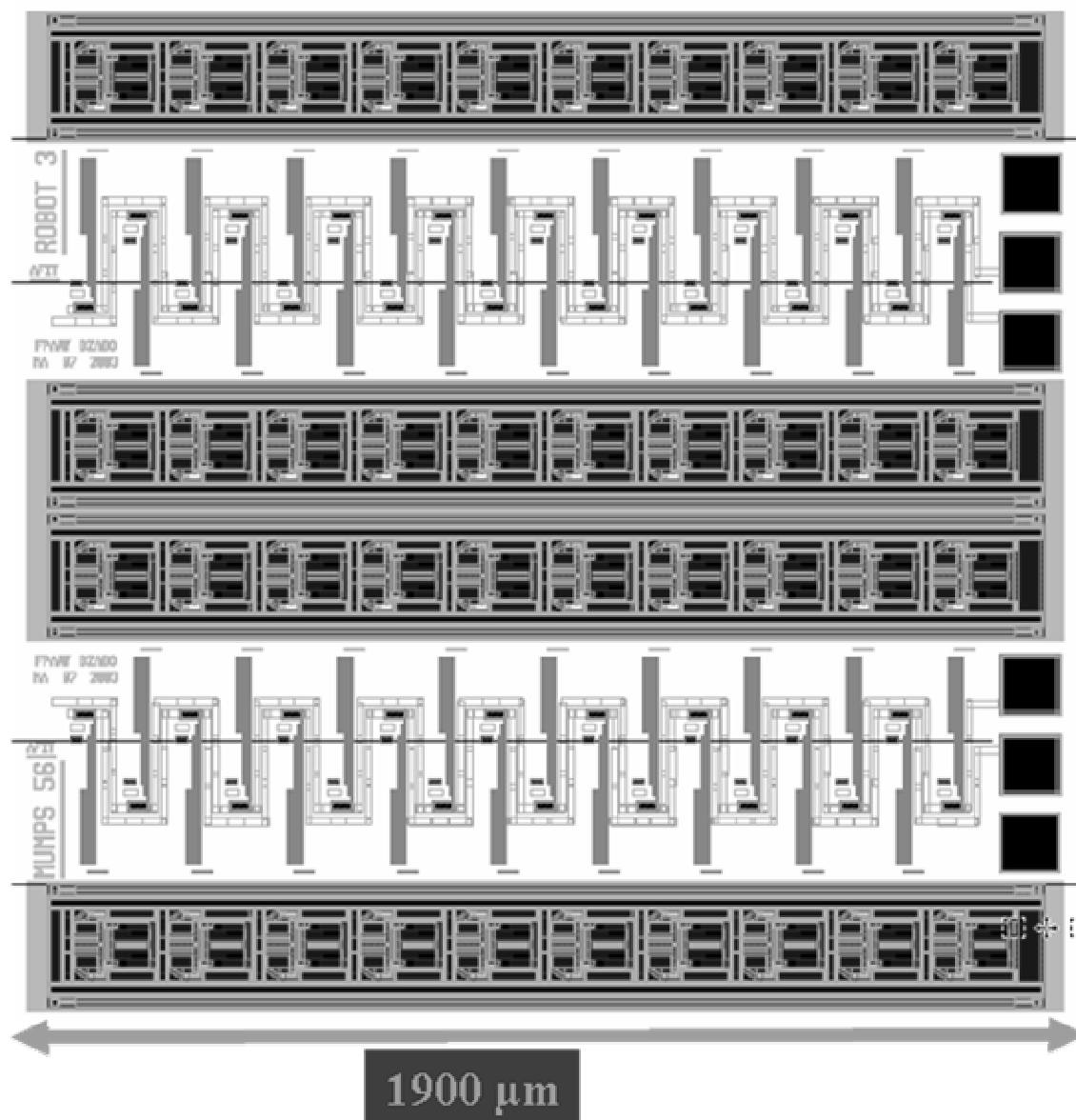
Figure A1.16: L-Edit layout showing the PolyMUMPs 56 microrobot design; with arrays of 250 µm long double hot arm actuators. These long sections are rows of ratcheting oars on a Nordic ski track structure, which is slid back and forth by the actuator arrays. This microrobot was meant to be turned upside down, so that the top you see here would actually be the bottom. The dark pads are for bonding attaching wires.

APPENDIX B

This appendix provides the MatLab code used during this research for the chevron

optothermal actuator model using an elliptical laser beam spot.

```
% SZABO THESIS MODEL -------- Chevron Hot Arm Actuator Laser Ellipse Beam Simulation
% SMSgt Szabo
% 17 Nov 03
% Revised: 27 Dec 03
% Revised: 14 Jan 04
% Version 2

clear all;
close all;
% EENG 777 ADVANCED MEMS -------- Laser Power mW/um^2 Calculations
% SMSgt Szabo
% 16 Oct 03
% Revised:
% Version 1
% % %%%%%%%%Laser Actuator M57 250 um, 4 chevrons, 3x3.5um^2
%%%%%%%%%%%%%%%%%%%%%%%%%%%%%%%%%%%%%%%%%
% N = 8;          %number of flexures
% Lp = 250.0e-6;   %flexure length  (in meters)
% width = 3e-6;         %width of flexure (in meters)
% % %%%%%%%%Laser Actuator M57 350 um, 8 chevrons, 3x3.5um^2
%%%%%%%%%%%%%%%%%%%%%%%%%%%%%%%%%%%%%%%%%
% N = 16;          %number of flexures
% Lp = 350.0e-6;   %flexure length  (in meters)
% width = 3.5e-6;        %width of flexure (in meters)
% % %%%%%%%%Laser Actuator M58 250 um, 8 chevrons, 2.5 x 3.5 um^2
%%%%%%%%%%%%%%%%%%%%%%%%%%%%%%%%%%%%%%%%%
% N = 16;          %number of flexures
% Lp = 250.0e-6;    %flexure length  (in meters)
% width = 2.5e-6;       %width of flexure (in meters)
%
% % %%%%%%%%Laser Actuator M58 210 um, 8 chevrons, 2.5 x 3.5 um^2
%%%%%%%%%%%%%%%%%%%%%%%%%%%%%%%%%%%%%%%%%
% N = 16;          %number of flexures
% Lp = 90.0e-6;    %flexure length  (in meters)
% width = 2.5e-6;       %width of flexure (in meters)
% % %%%%%%%%Laser Actuator 400 um, 8 chevrons, 25x3.5um^2
%%%%%%%%%%%%%%%%%%%%%%%%%%%%%%%%%%%%%%%%%
N = 16;          %number of flexures
Lp = 400.0e-6;   %flexure length
width = 2.5e-6;        %width of flexure (in meters)
% Ap = 12.25e-12;  %Cross Sectional Area
% Sp = 33600e-12;   %um^2  Surface Area Polysilicon
% Sg = 5747.5e-12;  %um^2  Surface Area Gold
th = 3.5e-6;        % structural thickness, Poly1 and Poly2 combined (meters {um})
Lambda = .660;       %Wavelength in um
alpha = 463e3;        % (4.63e3 cm-1) absorption coefficient, from figure 5, Sze text, page 287, (meters)

% Lambda = .632;        %Wavelength in um
% alpha = 563e3;        % (5.63e3 cm-1) absorption coefficient, from figure 5, Sze text, page 287, (meters)

Eg = 1.24 / Lambda;    %Energy Bandgap (in eV) as a function of Wavelength in um
EgSil = 1.12;        % Bandgap of Silicon (in eV)

IP = [45 60 200]*1e-3; %Incident photon power in Watts
%%%%% with 29.7% power loss due to optics
% IP = [(45*(1-.297)) (60*(1-.297)) (300*(1-.297))]*1e-3; %Incident photon power in Watts

Beam_radius1 = [250 200 150 120 100 80]*1e-6;      % Ellipse Laser Beam LONG Radius
```

```
Beam_radius2 = Beam_radius1./2;      % Ellipse Laser Beam SHORT Radius

if (Lp < 250e-6)      %%%prevent divide by zero errors
Beam_radius1(1) = Lp;
end
if (Lp < 130e-6)
Beam_radius1(1) = Lp;
Beam_radius1(2) = Lp;
end
if (Lp < 100e-6)
Beam_radius1(1) = Lp;
Beam_radius1(2) = Lp;
Beam_radius1(3) = Lp;
end


%%%%%%%%%%%%%%%%%%%%%%%%%%%%%%%%%%%%%%%%%%%%%%%%%%%%%%
%%%%%%

%%%%%%%%Calc percent of photon energy converted to heat%%%%%%%%%%%%%%%%%%%%%%%
PerHeat =  (Eg - EgSil)/Eg;    % percent photon energy converted to heat per second (Percent)

%%%%%%%%Calc incident photon energy converted to heat per second %%%%%%%%%%%%%%%%%%%%%%
  for (ii = 1:length(IP));


  PEabs(ii) = IP(ii).*( 1 - exp(-alpha .* th));   %photon energy absorbed per second (in Watts)

  Pabs(ii) = PEabs(ii) * PerHeat;                % Power absorbed in material as heat

   for (jj = 1:length(Beam_radius1));

       Beam_Area(jj) = pi * (Beam_radius1(jj))*(Beam_radius2(jj));       % area of laser beam ELLIPSE to calc Power

       Power_Per_Area(ii,jj) = Pabs(ii) ./ Beam_Area(jj);       % Heating Power per area

       SA_Actuator1(jj) = N * (Beam_radius1(jj)*1.5) * (width + th);     %Surface Area of Actuator absorbing photon energy/heat

       SA_Actuator2(jj) = N * (Beam_radius1(jj)) * width;      %Top Surface Area of Actuator absorbing photon energy/heat

       Pabs_Act(ii,jj) = Power_Per_Area(ii,jj) .* SA_Actuator1(jj);   %Actual Heat power absorbed by actuators

       qdot_Laser(ii,jj) =  Pabs_Act(ii,jj)./(SA_Actuator2(jj)*th);   %heat power generated in watts/m^3
end
end


%%%%%%%%%%%%%%%%%%%%%%%%%%%%%%%%%%%%%%%%%%%%%%%%%%%%%%%
%%%%%%%%%%%%%%%%%
% Definition of constants
%%%%%%%%%%%%%%%%%%%%%%%%%%%%%%%%%%%%%%%%%%%%%%%%%%%%%%%
%%%%%%%%%%%%%%%%%%
for (ll = 1:length(IP))
for (kk = 1:length(Beam_radius2))
% %double hot arm, Poly1Poly2
w = [width, width, (20.0*1e-6), width, width];
  %%%%% effective Thermal width of T_hot_arm1p1 T_hot_arm1p2 T_center_piece T_hot_arm2p1 T_hot_arm2p2, in um
wp = [width, width, (20.0*1e-6), width, width];
  %%%%% Physical width of T_hot_arm1p1 T_hot_arm1p2 T_center_piece T_hot_arm2p1 T_hot_arm2p2, in um

%%%Final Comparison of Original and Poly1Poly2 Fully Optimized Models
Code%%%%%%%%%%%%%%%%%%%%%%%%%%%%%%%%%%%%%%%%%%%%%%%%%%%%%%%
% Lv = [.1, 350, 35, 350, .1]*1e-6;
%     % effective Thermal Length of T_hot_arm1p1 T_hot_arm1p2 T_center_piece T_hot_arm2p1 T_hot_arm2p2; in um
% Lpv = [.1, 350, 350, .1]*1e-6;
%     % Physical Length of (T_hot_arm1p1 T_hot_arm1p2 T_center_piece T_hot_arm2p1 T_hot_arm2p2; in um


Lv = [(Lp - Beam_radius1(kk)), (Beam_radius1(kk) ), 20e-6, (Beam_radius1(kk) ), (Lp - Beam_radius1(kk))];
   % effective Thermal Length of T_hot_arm1p1 T_hot_arm1p2 T_center_piece T_hot_arm2p1 T_hot_arm2p2; in um
```

B2

```
Lpv = [(Lp  - Beam_radius1(kk)), (Beam_radius1(kk) ), 20e-6, (Beam_radius1(kk) ), (Lp  - Beam_radius1(kk))];
   % Physical Length of T_hot_arm1p1  T_hot_arm1p2  T_center_piece  T_hot_arm2p1  T_hot_arm2p2; in um

   %%%%Final Comparison of Original and Poly1Poly2 Fully Optimized Models
Code%%%%%%%%%%%%%%%%%%%%%%%%%%%%%%%%%%%%%%%%%%%%%%%%%%%%%%%%%%

d = 2.00e-6;                % Poly 1   distance of structure from substrate in um
% d = .75e-6;                  % released microrobot  actuattors distance of structure from substrate in um


T0 = 293;                % substrate Temp in degrees K (20 deg C)

%%%%%%%%%%%%%%%%%%%%%%%%%%%%%%%%%%%%%%%%%%%%%%%%%%%%%%%%%%
%%%%%%%%%%%%%%%%%%%%%
% MUMPS AND OTHER MATERIAL PROPERTIES
%%%%%%%%%%%%%%%%%%%%%%%%%%%%%%%%%%%%%%%%%%%%%%%%%%%%%%%%%%
%%%%%%%%%%%%%%%%%%%%%

t_poly1 = 2.0e-6;           % thickness of polysilicon 1 in um (MUMPS data sheet run 56)
t_poly2 = 1.5e-6;           % thickness of polysilicon 2 in um (MUMPS data sheet run 56)
t_poly1poly2 = 3.5e-6;       % thickness of polysilicon 1 in um (MUMPS data sheet run 56)

%%%%%%%%%%%%%%% change for material thickness%%%%%%%%%%%
% t = t_poly1;
% t = t_poly2;
t = t_poly1poly2;

t_gold = .5e-6;             % thickness of gold in um         (MUMPS data sheet run 56)
t_dimple = .75e-6;           % thickness of gold in um         (POLYMUMPS Handbook)

d1 = 2.00e-6;              % distance of Poly1 structure from substrate in um (MUMPS data sheet run 56)
d2 = 2.75e-6;              % distance of Poly2 structure from substrate in um (MUMPS data sheet run 56)

a_poly1 = 2.33e-6;           % coefficient of thermal expansion poly1 in K^-1 (2.33 Kovacks page 558)
a_poly2 = 2.33e-6;           % coefficient of thermal expansion poly2 in K^-1 (2.33 Kovacks page 558)
a_gold = 14.2e-6;            % coefficient of thermal expansion gold in K^-1  (14.2 Kovacks page 558)

E_poly1 = 169e9;            % Young's Modulus for poly in GPa  (Kovacks page 201)
E_poly2 = 169e9;            % Young's Modulus for poly in GPa  (Kovacks page 201)
E_gold = 80e9;             % Young's Modulus for Thin Film gold in GPa
                % http://www.allmeasures.com/Formulae/static/formulae/youngs_modulus/16.htm
                % http://www.memsnet.org/material/polysiliconfilm/
                % http://www.memsnet.org/material/goldaufilm/

r_poly1 = .22;             % Poisson's Ratio for poly1 unitless  (Kovacks page 201)
r_poly2 = .22;             % Poisson's Ratio for poly2 unitless  (Kovacks page 201)
r_gold = .44;              % Poisson's Ratio for Gold in unitless
                % http://www.webelements.com/webelements/elements/text/Au/phys.html

s_poly1 = -14.582e6;         % residual stress for poly1 Mpa  (MUMPS data sheet run 56)
s_poly2 = -14.364e6;         % residual stress for poly2 Mpa  (MUMPS data sheet run 56)
s_gold = 23.65e6;           % residual stress for gold Mpa   (MUMPS data sheet run 56)

T0_rel = 300;             % substrate Temp at release in degrees K (30 deg C)
T0_fab = 400;             % ASSUMED substrate Temp at deposition in degrees K (100 deg C)

Kgold = 318;              % Thermal Conductivity of gold in W/m*degK (Kovacks page 558)
KNitr = 16;               % Thermal Conductivity of Nitride in W/m*degK (Kovacks page 558)
Kpoly1 = 34;              % Thermal Conductivity of polysilicon in W/m*degK (Kovacks page 558)
% Kpoly = 31;              %class values to test code
% Kair = .039;             % Thermal Conductivity of air in W/m*degK
 Kair = .026;             % Thermal Conductivity of air in W/m*degK @ 300 deg K
                % http://www.hukseflux.com/thermal%20conductivity/thermal.htm
% Kair = .0681;            % average Thermal Conductivity of air in W/m*degK at Top  deg K
                % http://users.wpi.edu/~ierardi/FireTools/air_prop.html

eps0 = 8.85418e-12;         % Permeativity of free space F/m (Semiconductor Devices, Sze, page 536)
epsr_A = 1.0006;            % Dielectric Constant of air (unitless) (Advanced Engineering Elctromagnetics, Balanis, page 50)
epsr_N = 7.5;              % Dielectric Constant of Nitride (unitless) 6-9 (RF MEMS, Rebiez, pages 474-476)
```

```
%pe_poly1 = 2.3e-5;              % resistivity poly1 in ohm-m  %class values to test code
%pe_poly2 = 3.22e-5;             % resistivity poly2 in ohm-m  (MUMPS data sheet run 51)
pe_poly1 = 1.97e-5;             % resistivity poly1 in ohm-m  (MUMPS data sheet run 56)
%pe_poly2 = 2.49e-5;             % resistivity poly2 in ohm-m  (MUMPS data sheet run 56)

pe_temp_const = 1.25e-3;        % Temperature dependance of resistivity constant C-1

%%%%%%%%%%%%%%%%%%%%%%%%%%%%%%%%%%%%%%%%%%%%%%%%%%%%%%%%%%%%
%%%%%%%%%%%%%%%%%%%%%%%%
% Calculation and plotting of  Hot Arm Actuator due to stepping voltages and Temps
%%%%%%%%%%%%%%%%%%%%%%%%%%%%%%%%%%%%%%%%%%%%%%%%%%%%%%%%%%%%
%%%%%%%%%%%%%%%%%%%%%%%%
a_poly1_t = zeros(25,1);        % initialize
a_poly1_t(1) = a_poly1;         % initialize

% Vo_step = [0 1 2 3 4 5 6 7 8 9 10 11 12 13 14 15 16 17 18 19 20 21 22 23 24];     % Applied STEPPING voltage in Volts

%% Top_step = [293 301.27     324.82      358.23      399.3       440.33      484.98      522.41      572.89      620.54      662.77
              703.42      742.22...
%    800.32          844.1       883.86      927.29      969.53      1010.3      1054.8      1137.30 144 144 144 144 144 144];

Top_step = [295.58   300.37   303.78   307.67   314.4   328.35];
% Top_step = [295.87301.28   305.15   309.52   317.02   332.1];


Top = Top_step(kk);

%
%%%%%%%%%%%%%%%%%%%%%%%%%%%%%%%%%%%%%%%%%%%%%%%%%%%%%%%%%%%%
%%%%%%%%%%%%%%%%%%%%%%%%
% initialize vectors and matrices

Amatrix = zeros(10,10);           % initialize A matrix
Cvector = zeros(10,1);            % initialize integration constants vector
Fvector = zeros(10,1);           % initialize Forcing values vector
K_master_stiffness = zeros(15,15);  % initialize master stiffness matrix
R_vector = zeros(15,1);          % initialize master FORCE/MOMENT Resultant vector
D_vector = zeros(15,1);          % initialize master Displacement(x,y,theta) vector
Flex_matrix = zeros(6,6);
d_L_vector = zeros(6,1);
X_vector = zeros(6,1);


%%%%%%%%%%%%%%%%%%%%%%%%%%%%%%%%%%%%%%%%%%%%%%%%%%%%%%%%%%%%
%%%%%%%%%%%%%%%%%%%%%%%%
% Temperature Dependencies
%%%%%%%%%%%%%%%%%%%%%%%%%%%%%%%%%%%%%%%%%%%%%%%%%%%%%%%%%%%%
%%%%%%%%%%%%%%%%%%%%%%%%

pe_poly_t = pe_poly1 * (1 + (pe_temp_const * (Top-T0)));   % Huang and Lee page 66
                %%%%%% average resistivity of poly in W/m*degK at Top in deg K
pe_poly12_tv(ii) = pe_poly_t;

Kair_t = 1.5207E-11*Top^3 - 4.8574E-08*Top^2 + 1.0184E-04*Top - 3.9333E-04;

Kair_tv(ii) = Kair_t;         % average Thermal Conductivity of air in W/m*degK at Top in deg K
                    % http://users.wpi.edu/~ierardi/FireTools/air_prop.html
%   Kair_tv(ii) = .026;

% KpolyT(ii) = 41 - 1.06*(ii-1);     % Poly1 Thermal conductivity Dong Yan, Amir Khajepour and Raafat Mansour page 315:
kp=41×10^6
KpolyT(ii) = 41 - .66*(ii-1);    % Poly2 Thermal conductivity Dong Yan, Amir Khajepour and Raafat Mansour page 315:
kp=41×10^6
Kpoly_t = KpolyT(ii);           % This value ranges between these two values to show temperature dependence
                % Materials Handbook for Hybrid Microelectronics by King
                % shows Therm Cond decreases almost linearly in the temp range of 300 to 1700 deg K
                % and ranging down to a value of 25 at 1400 deg K
% a_poly1_t(ii) = ((3.725*(1-exp(-5.88e-3*(Top-246)))+5.548e-4*Top)*1e-6);
%a_poly1_t(ii) = (((3.725*(1-exp(-5.88e-3*(Top-124))))+5.548e-4*Top)*1e-6);
a_poly1_t(ii) = (((3.725*(1-exp(-5.88e-3*(Top-144))))+5.548e-4*Top)*1e-6);
```

```
                        % from "Average power control and positioning of polysilicon thermal actuators"
                        % by Butler, Bright, and Cowan page 95
% a_poly1_t(ii) = a_poly1;

% E_poly1T(ii)=((-2.35e-2*Top) + 176)*1e9;   % Poly1 Poly 2 line fitting equation from ranging from 169 to 140
E_poly1T(ii)=((-3.40e-2*Top) + 179)*1e9;   %Poly1+2 line fitting equation from ranging from 169 to 140

E_poly1 = E_poly1T(ii);              % This value ranges between these two values to show temperature dependence
                        % Materials Handbook for Hybrid Microelectronics by King
                        % shows Therm Cond decreases almost linearly in the temp range of 300 to 1700 deg K
                        % and ranging down to a value of 140 at 1400 deg K ;%


%%%%%%%%%%%%%%%%%%%%%%%%%%%%%%%%%%%%%%%%%%%%%%%%%%%%%%%%%%%%%%
%%%%%%%%%%%%%%%%%%%%%%%%
% Calculation of Variables
%%%%%%%%%%%%%%%%%%%%%%%%%%%%%%%%%%%%%%%%%%%%%%%%%%%%%%%%%%%%%%
%%%%%%%%%%%%%%%%%%%%%%

% Per = w;                % Perimeter of cross section for conduction in um, set to width for intial analysis
% Per = [w(1) + .5*t, w(2) + .5*t, w(3) + t, w(4), w(5), w(6)];
Per = [w(1) + t, w(2) + t, w(3) + 2*t, w(4) + t, w(5) + t];
                        % Perimeter of cross section for conduction in um, set to width + 2*(t/4) for intial analysis
h = [Kair_tv(ii)/d, Kair_tv(ii)/d, Kair_tv(ii)/d, Kair_tv(ii)/d, Kair_tv(ii)/d];
                        % heat transfer coefficient
Acs = w.*t;                % cross sectional area in um
          % Area cs of (1)hot arm 1, (2)short piece 1, (3)hot arm 2, (4)short piece 2, (5)cold arm, (6)flexor; in um
%R = pe_poly_t.*Lv./Acs;        % Resistance of (1)hot arm 1, (2)short piece 1, (3)hot arm 2; in ohms
% I = Vo./(R(1)+R(2)+R(4)+R(5));                % Current in mA in (1)hot arm 1, (2)short piece 1, (3)hot arm 2
% qdot1 = ((I^2.*pe_poly_t)./(Acs.^2));
                        % heat generated by current per volume Watts/m^3, (1)hot arm 1, (2)short piece 1, (3)hot arm 2

%%%%%%%%%%%%%%%%%%%%%%%%%%%% Laser Generated Qdot
qdot1(1) = .1259e3;   %%%some small number so as not to get a divide by zero error
qdot1(2) = qdot_Laser(ll,kk);
qdot1(3) = .1259e3;
qdot1(4) = qdot_Laser(ll,kk);
qdot1(5) = .1259e3;

qdot_pwr(ii) = qdot1(2);

Ga = sqrt((h.*Per)./(Kpoly_t.*Acs));  % Gamma combination of variables, (1)hot arm, (2)short piece, (3)cold arm, (4)flexor;
Ep1 = (((qdot1.*Acs)./(h.*Per)) + T0); % Epsilon combination of variables, (1)hot arm 1, (2)short piece 1, (3)hot arm 2
Ep = [Ep1(1), Ep1(2), Ep1(3), Ep1(4), Ep1(5)];
li = [Lv(1), Lv(1)+Lv(2), Lv(1)+Lv(2)+Lv(3), Lv(1)+Lv(2)+Lv(3)+Lv(4), Lv(1)+Lv(2)+Lv(3)+Lv(4)+Lv(5)];
                        %adding up lengths for cumulative lengths at each boundary

Im = wp.^3 * (t / 12);        % Area moment of inertia for a rectangle

%%%%%%%%%%%%%%%%%%%%%%%%%%%%%%%%%%%%%%%%%%%%%%%%%%%%%%%%%%%%%%
%%%%%%%%%%%%%%%%%%%%%%%
%Calculate and Plot Temperature Distribution
%%%%%%%%%%%%%%%%%%%%%%%%%%%%%%%%%%%%%%%%%%%%%%%%%%%%%%%%%%%%%%
%%%%%%%%%%%%%%%%%%%%%%

%Forcing values vector
Fvector = [T0-Ep(1), Ep(2)-Ep(1), Ep(3)-Ep(2), Ep(4)-Ep(3), Ep(5)-Ep(4), T0-Ep(5), 0,0,0,0];

%Populate A matrix row by row
Amatrix(1,:) = [1,1,0,0,0,0,0,0,0,0];
Amatrix(2,:) = [exp(Ga(1)*li(1)), exp(-Ga(1)*li(1)), -exp(Ga(2)*li(1)), -exp(-Ga(2)*li(1)),  0,0,0,0,0,0];
Amatrix(3,:) = [0,0,exp(Ga(2)*li(2)), exp(-Ga(2)*li(2)), -exp(Ga(3)*li(2)), -exp(-Ga(3)*li(2)),  0,0,0,0];
Amatrix(4,:) = [0,0,0,0,exp(Ga(3)*li(3)), exp(-Ga(3)*li(3)), -exp(Ga(4)*li(3)), -exp(-Ga(4)*li(3)),0,0];
Amatrix(5,:) = [0,0,0,0,0,0,exp(Ga(4)*li(4)), exp(-Ga(4)*li(4)), -exp(Ga(5)*li(4)), -exp(-Ga(5)*li(4))];
Amatrix(6,:) = [0,0,0,0,0,0,0,0,exp(Ga(5)*li(5)), exp(-Ga(5)*li(5))];
Amatrix(7,:) = [Acs(1)*Ga(1)*exp(Ga(1)*li(1)),-Acs(1)*Ga(1)*exp(-Ga(1)*li(1)),...
      -Acs(2)*Ga(2)*exp(Ga(2)*li(1)),Acs(2)*Ga(2)*exp(-Ga(2)*li(1)),0,0,0,0,0,0];
Amatrix(8,:) = [0,0,Acs(2)*Ga(2)*exp(Ga(2)*li(2)),-Acs(2)*Ga(2)*exp(-Ga(2)*li(2)),...
      -Acs(3)*Ga(3)*exp(Ga(3)*li(2)),Acs(3)*Ga(3)*exp(-Ga(3)*li(2)),0,0,0,0];
Amatrix(9,:) = [0,0,0,0,Acs(3)*Ga(3)*exp(Ga(3)*li(3)),-Acs(3)*Ga(3)*exp(-Ga(3)*li(3)),...
      -Acs(4)*Ga(4)*exp(Ga(4)*li(3)),Acs(4)*Ga(4)*exp(-Ga(4)*li(3)),0,0];
```

```matlab
Amatrix(10,:) = [0,0,0,0,0,0, Acs(4)*Ga(4)*exp(Ga(4)*li(4)),-Acs(4)*Ga(4)*exp(-Ga(4)*li(4)),...
    -Acs(5)*Ga(5)*exp(Ga(5)*li(4)),Acs(5)*Ga(5)*exp(-Ga(5)*li(4))];


% solve for integration constants
Cvector = inv(Amatrix)*Fvector';
C = Cvector;    %rename to shorten next set of equations

% solve for Temperature Distribution in original equations

%First set up x point vectors for plotting
x1 = linspace(0,li(1),Lv(1)/1e-8);   %sets up number of points to plot in x dir  (1)hot arm 1p1
x2 = linspace(li(1),li(2),Lv(2)/1e-8);   %sets up number of points to plot in x dir  (2)hot arm 1p2
x3 = linspace(li(2),li(3),Lv(3)/1e-8);   %sets up number of points to plot in x dir  (3)center piece
x4 = linspace(li(3),li(4),Lv(4)/1e-8);   %sets up number of points to plot in x dir  (4)hot arm 2p1
x5 = linspace(li(4),li(5),Lv(5)/1e-8);   %sets up number of points to plot in x dir  (4)hot arm 2p2

% solve for Temperature Distribution in original equations using calcualted constants
T_hot_arm1p1 = C(1)*exp(Ga(1).*x1) + C(2)*exp(-Ga(1).*x1) + Ep(1);
T_hot_arm1p2 = C(3)*exp(Ga(2).*x2) + C(4)*exp(-Ga(2).*x2) + Ep(2);
T_center_piece = C(5)*exp(Ga(3).*x3) + C(6)*exp(-Ga(3).*x3) + Ep(3);
T_hot_arm2p1 = C(7)*exp(Ga(4).*x4) + C(8)*exp(-Ga(4).*x4) + Ep(4);;
T_hot_arm2p2 = C(9)*exp(Ga(5).*x5) + C(10)*exp(-Ga(5).*x5) + Ep(5);


%Concatinate data points for plotting
T_actuator = [T_hot_arm1p1  T_hot_arm1p2  T_center_piece  T_hot_arm2p1 T_hot_arm2p2];
 Tck2(ii) = mean(T_hot_arm1p2);                % check operating temperature steps

%set up T_actuator points for plotting
xT = linspace(0,li(5),length(T_actuator))./1e-6;   %sets up points to plot in x (in um) dir for T_actuator


%%%%%%Plot Temp for length of hot arm actuator
%

if (ll == 2)

    if (kk == 1)
    figure;        %%%%%%%comment out to add plot lines

    plot(xT,T_actuator,'b','LineWidth',3); %%%%%%%%%%%%%%%%%b,g,r,c,m  k= black
    axis off;
    title( [num2str(Lp*1e6) ' um x ' num2str(N/2) ' Chevron Ellipse Laser Actuator Sim, Temp
Distribution'],'fontsize',14,'fontweight','bold');
    axes('fontsize',12,'fontweight','bold');
    grid on;
    xlabel('x Position Along Actuator in \mum','fontsize',12,'fontweight','bold');
    ylabel('Temperature in degrees K (\circK)','fontsize',12,'fontweight','bold');
    hold on;
    plot(xT,T_actuator,'b','LineWidth',3); %%%%%%%%%%%%%%%%b,g,r,c,m  k= black
end

if (kk == 2)
    plot(xT,T_actuator,'g','LineWidth',3); %%%%%%%%%%%b,g,r,c,m k= black
end
if (kk == 3)
    plot(xT,T_actuator,'r','LineWidth',3); %%%%%%%%%%%%%b,g,r,c,m k= black
end
if (kk == 4)
    plot(xT,T_actuator,'k','LineWidth',3); %%%%%%%%%%%b,g,r,c,m k= black
end
if (kk == 5)
    plot(xT,T_actuator,'c','LineWidth',3); %%%%%%%%%%%b,g,r,c,m k= black
end
if (kk == 6)
    plot(xT,T_actuator,'m','LineWidth',3); %%%%%%%%%%b,g,r,c,m k= black
end
end
```

```
 legend(['Beam short radius = ' num2str(Beam_radius2(1)*1e6) '\mum'], ['Beam short radius = ' num2str(Beam_radius2(2)*1e6)
'\mum'], ...
    ['Beam short radius = ' num2str(Beam_radius2(3)*1e6) '\mum'], ['Beam short radius = ' num2str(Beam_radius2(4)*1e6) '\mum'], ...
    ['Beam short radius = ' num2str(Beam_radius2(5)*1e6) '\mum'], ['Beam short radius = ' num2str(Beam_radius2(6)*1e6) '\mum'],...
    ['IP = ' num2str(IP(2)*1e3) ' mW'],0);

% %
%
%%%%%%%%%%%%%%%%%%%%%%%%%%%%%%%%%%%%%%%%%%%%%%%%%%%
%%%%%%%%%%%%%%%%%%%%%%%
% %Calculate the Delta Change in Length and Force Vectors due to Thermal Expansion
%
%%%%%%%%%%%%%%%%%%%%%%%%%%%%%%%%%%%%%%%%%%%%%%%%%%%
%%%%%%%%%%%%%%%%%%%%%%%

%Use average temperature in each section to find the thermal expansion
T_hot_arm1p1_av = sum(T_hot_arm1p1)/length(T_hot_arm1p1);
T_hot_arm1p2_av = sum(T_hot_arm1p2)/length(T_hot_arm1p2);
T_center_piece_av = sum(T_center_piece)/length(T_center_piece);
T_hot_arm2p1_av = sum(T_hot_arm2p1)/length(T_hot_arm2p1);
T_hot_arm2p2_av = sum(T_hot_arm2p2)/length(T_hot_arm2p2);

T_actuator_av = [T_hot_arm1p1_av T_hot_arm1p2_av T_center_piece_av T_hot_arm2p1_av T_hot_arm2p2_av];

T_hot_arm1_av_step(ll,kk) = T_hot_arm1p2_av;

%calc d_length vector and force_vector
    for i=1:length(T_actuator_av)
        d_length(i) = Lpv(i) * a_poly1_t(ii) *  (T_actuator_av(i) - T0); % length of piece * TCE * Avg change in Temp
        force_vector(i) = E_poly1 * Acs(i) * d_length(i) / Lpv(i); % Young's * cross sectional area * delta length / length
    end

%%%%%%%%%%%%%%%%%%%%%%%%%%%%%%%%%%%%%%%%%%%%%%%%%%%
%%%%%%%%%%%%%%%%%%%%%%%
%Calculate Global Flexibility Matrix
%%%%%%%%%%%%%%%%%%%%%%%%%%%%%%%%%%%%%%%%%%%%%%%%%%%
%%%%%%%%%%%%%%%%%%%%%%%

L1 = Lpv(1) + Lpv(2);

dL1(ll) = d_length(1) + d_length(2);




%%%%%%%%%%%%%%%%%%%%%%%%%%%%%%%%%%%%%%%%%%%%%%
% CALCULATE Moments and Forces
deg = 1;  %angle of chevrons in degrees
ang = deg * pi/180;  %angle of chevrons in radians
defl = sqrt((L1^2) + 2*L1*dL1(ll) - (L1*(cos(ang)))^2) - L1*sin(ang);  %(1/(E_poly1*Im(1))) *
deflection(ll,kk) = defl;
dum(kk) = (1/(E_poly1*Im(1)));
end
end  %%%% master loop for stepping voltages
%
%%%%%%%%%%%%%%%%%%%%%%%%%%%%%%%%%%%%%%%%%%%%%%%%%%%
%%%%%%%%%%%%%%%%%%%%%
% %Plot Deflection of hot arm actuator
%
 for (ll = 1:length(IP));
if (ll == 1)
    figure;        %comment out to add plot lines
    plot(Beam_radius2/1e-6,deflection(ll,:)/1e-6,'b',Beam_radius2/1e-6,deflection(ll,:)/1e-6,'ro','LineWidth',3); %b,g,r k= black
    axis off;
    axes('fontsize',12,'fontweight','bold');
    grid on;
    title([num2str(Lp*1e6) ' um x ' num2str(N/2) ' Chevron Ellipse Laser Actuator Simulation,
Deflection'],'fontsize',14,'fontweight','bold');
    xlabel('Beam Ellipse Short Radius in \mum','fontsize',12,'fontweight','bold');
    ylabel('Deflection of Actuator in \mum','fontsize',12,'fontweight','bold');
    hold on;
```

```matlab
    plot(Beam_radius2/1e-6,deflection(ll,:)/1e-6,'b',Beam_radius2/1e-6,deflection(ll,:)/1e-6,'ro','LineWidth',3); %b,g,r k= black
    hold on;
end

if (ll == 2)
  plot(Beam_radius2/1e-6,deflection(ll,:)/1e-6,'k',Beam_radius2/1e-6,deflection(ll,:)/1e-6,'co','LineWidth',3);
end

% if (ll == 3)
%   plot(Beam_radius2/1e-6,deflection(ll,:)/1e-6,'g',Beam_radius2/1e-6,deflection(ll,:)/1e-6,'mo','LineWidth',3);
% end
end
legend(['IP = ' num2str(IP(1)*1e3) ' mW'],[' '],['IP = ' num2str(IP(2)*1e3) ' mW'],...
    [' '],0);




 for (ii = 1:length(IP));
 if (ii==1)
   figure;       %comment out to add plot lines
   plot(Beam_radius2(1,:)*1e6,qdot_Laser(ii,:),'b',Beam_radius2(ii,:)*1e6,qdot_Laser(ii,:),'ro','LineWidth',3);
                 %b,g,r,c,m  k= black
   axis off;
   title('Qdot vs Laser Beam Ellipse Short Radius','fontsize',14,'fontweight','bold');
   axes('fontsize',12,'fontweight','bold');
   grid on;
   xlabel('Laser Beam Ellipse Short Radius (um)','fontsize',12,'fontweight','bold');
   ylabel('Qdot (Watts/m^3)','fontsize',12,'fontweight','bold');
   hold on;
   plot(Beam_radius2(1,:)*1e6,qdot_Laser(ii,:),'b',Beam_radius2(ii,:)*1e6,qdot_Laser(ii,:),'ro','LineWidth',3);
                 %b,g,r,c,m  k= black;
   hold on;
end

if (ii == 2)
   plot(Beam_radius2(1,:)*1e6,qdot_Laser(ii,:),'k',Beam_radius2(1,:)*1e6,qdot_Laser(ii,:),'mo','LineWidth',3);
          %b,g,r,c,m k= black
end
% if (ii == 3)
%   plot(Beam_radius2(1,:)*1e6,qdot_Laser(ii,:),'g',Beam_radius2(1,:)*1e6,qdot_Laser(ii,:),'co','LineWidth',3);
%             %b,g,r,c,m k= black
% end


 legend(['IP = ' num2str(IP(1)*1e3) ' mW'],[' '],['IP = ' num2str(IP(2)*1e3) ' mW'],[' '],0);

end%
 hold off;

end
```

APPENDIX C

This appendix provides the MatLab code used during this research for the chevron

electrothermal actuator model.

```
% SZABO THESIS MODEL -------- Chevron Electrothermal Hot Arm Actuator Simulation
% SMSgt Szabo
% 17 Nov 03
% Version 1

clear all;
close all;
%%%%%%%%%%%%%%%%%%%%%%%%%%%%%%%%%%%%%%%%%%%%%%%%%%%%%%%%%%%
%%%%%%%%%%%%%%%%
% Definition of constants
%%%%%%%%%%%%%%%%%%%%%%%%%%%%%%%%%%%%%%%%%%%%%%%%%%%%%%%%%%%
% %double hot arm, Poly1Poly2
% w = [3.5, 3.5, 15.0, 3.5, 3.5]*1e-6;
%    %%%% effective Thermal width of (1)hot arm 1, (2)short piece 1, (3)hot arm 2, in um
% wp = [3.5, 3.5, 15.0, 3.5, 3.5]*1e-6;
%    %%%%% Physical width of (1)hot arm 1, (2)short piece 1, (3)hot arm 2,  in um
% % % %double hot arm, Poly1Poly2
% %double hot arm, Poly1Poly2
w = [2.5, 2.5, 15.0, 2.5, 2.5]*1e-6;
   %%%% effective Thermal width of (1)hot arm 1, (2)short piece 1, (3)hot arm 2, in um
wp = [2.5, 2.5, 15.0, 2.5, 2.5]*1e-6;
   %%%%% Physical width of (1)hot arm 1, (2)short piece 1, (3)hot arm 2,  in um


% % %double hot arm, Poly1Poly2
%%%Final Comparison of Original and Poly1Poly2 Fully Optimized Models
Code%%%%%%%%%%%%%%%%%%%%%%%%%%%%%%%%%%%%%%%%%%%%%%%%%%%%%%
% Lv = [.1, 350, 35, 350, .1]*1e-6;
%    % effective Thermal Length of (1)hot arm 1, (2)short piece 1, (3)hot arm 2, (4)short piece 2, (5)cold arm, (6)flexor; in um
% Lpv = [.1, 350, 35, 350, .1]*1e-6;
%    % Physical Length of (1)hot arm 1, (2)short piece 1, (3)hot arm 2, (4)short piece 2, (5)cold arm, (6)flexor; in um
% Lv = [340, 60, 35, 60, 340]*1e-6;
%    % effective Thermal Length of (1)hot arm 1, (2)short piece 1, (3)hot arm 2, (4)short piece 2, (5)cold arm, (6)flexor; in um
% Lpv = [340, 60, 35, 60, 340]*1e-6;
%    % Physical Length of (1)hot arm 1, (2)short piece 1, (3)hot arm 2, (4)short piece 2, (5)cold arm, (6)flexor; in um

%%%M58 250x8
Lv = [249, 1, 25, 1, 249]*1e-6;
   % effective Thermal Length of (1)hot arm 1, (2)short piece 1, (3)hot arm 2, (4)short piece 2, (5)cold arm, (6)flexor; in um
Lpv = [249, 1, 25, 1, 249]*1e-6;
   % Physical Length of (1)hot arm 1, (2)short piece 1, (3)hot arm 2, (4)short piece 2, (5)cold arm, (6)flexor; in um

%%%%%M58 350x16
% Lv = [349, 1, 25, 1, 349]*1e-6;
%    % effective Thermal Length of (1)hot arm 1, (2)short piece 1, (3)hot arm 2, (4)short piece 2, (5)cold arm, (6)flexor; in um
% Lpv = [349, 1, 25, 1, 349]*1e-6;
%    % Physical Length of (1)hot arm 1, (2)short piece 1, (3)hot arm 2, (4)short piece 2, (5)cold arm, (6)flexor; in um

%%%M58 400x8
% Lv = [399, 1, 25, 1, 399]*1e-6;
%    % effective Thermal Length of (1)hot arm 1, (2)short piece 1, (3)hot arm 2, (4)short piece 2, (5)cold arm, (6)flexor; in um
% Lpv = [399, 1, 25, 1, 399]*1e-6;
%    % Physical Length of (1)hot arm 1, (2)short piece 1, (3)hot arm 2, (4)short piece 2, (5)cold arm, (6)flexor; in um

   %%%Final Comparison of Original and Poly1Poly2 Fully Optimized Models
Code%%%%%%%%%%%%%%%%%%%%%%%%%%%%%%%%%%%%%%%%%%%%%%%%%%%%%%

d = 2.00e-6;                   % Poly 1   distance of structure from substrate in um
```

```
T0 = 293;                   % substrate Temp in degrees K (20 deg C)

%%%%%%%%%%%%%%%%%%%%%%%%%%%%%%%%%%%%%%%%%%%%%%%%%%%%%%%%%%%%
%%%%%%%%%%%%%%%%%%%%%%%%
% MUMPS AND OTHER MATERIAL PROPERTIES
%%%%%%%%%%%%%%%%%%%%%%%%%%%%%%%%%%%%%%%%%%%%%%%%%%%%%%%%%%%%
%%%%%%%%%%%%%%%%%%%%%%%

t_poly1 = 2.0e-6;           % thickness of polysilicon 1 in um (MUMPS data sheet run 56)
t_poly2 = 1.5e-6;           % thickness of polysilicon 2 in um (MUMPS data sheet run 56)
t_poly1poly2 = 3.5e-6;      % thickness of polysilicon 1 in um (MUMPS data sheet run 56)

%%%%%%%%%%%%%%% change for material thickness%%%%%%%%%%
% t = t_poly1;
% t = t_poly2;
t = t_poly1poly2;

t_gold = .5e-6;             % thickness of gold in um        (MUMPS data sheet run 56)
t_dimple = .75e-6;          % thickness of gold in um        (POLYMUMPS Handbook)

d1 = 2.00e-6;               % distance of Poly1 structure from substrate in um (MUMPS data sheet run 56)
d2 = 2.75e-6;               % distance of Poly2 structure from substrate in um (MUMPS data sheet run 56)

a_poly1 = 2.33e-6;          % coefficient of thermal expansion poly1 in K^-1 (2.33 Kovacs page 558)
a_poly2 = 2.33e-6;          % coefficient of thermal expansion poly2 in K^-1 (2.33 Kovacs page 558)
a_gold = 14.2e-6;           % coefficient of thermal expansion gold in K^-1  (14.2 Kovacs page 558)

E_poly1 = 169e9;            % Young's Modulus for poly in GPa  (Kovacks page 201)
E_poly2 = 169e9;            % Young's Modulus for poly in GPa  (Kovacks page 201)
E_gold = 80e9;              % Young's Modulus for Thin Film gold in GPa
                % http://www.allmeasures.com/Formulae/static/formulae/youngs_modulus/16.htm
                % http://www.memsnet.org/material/polysiliconfilm/
                % http://www.memsnet.org/material/goldaufilm/

r_poly1 = .22;              % Poisson's Ratio for poly1 unitless  (Kovacks page 201)
r_poly2 = .22;              % Poisson's Ratio for poly2 unitless  (Kovacks page 201)
r_gold = .44;               % Poisson's Ratio for Gold in unitless
                % http://www.webelements.com/webelements/elements/text/Au/phys.html

s_poly1 = -14.582e6;        % residual stress for poly1 Mpa  (MUMPS data sheet run 56)
s_poly2 = -14.364e6;        % residual stress for poly2 Mpa  (MUMPS data sheet run 56)
s_gold = 23.65e6;           % residual stress for gold Mpa   (MUMPS data sheet run 56)

T0_rel = 300;               % substrate Temp at release in degrees K (30 deg C)
T0_fab = 400;               % ASSUMED substrate Temp at deposition in degrees K (100 deg C)

Kgold = 318;                % Thermal Conductivity of gold in W/m*degK (Kovacks page 558)
KNitr = 16;                 % Thermal Conductivity of Nitride in W/m*degK (Kovacks page 558)
Kpoly1 = 34;                % Thermal Conductivity of polysilicon in W/m*degK (Kovacks page 558)
% Kpoly = 31;               %class values to test code
% Kair = .039;              % Thermal Conductivity of air in W/m*degK
 Kair = .026;               % Thermal Conductivity of air in W/m*degK @ 300 deg K
                % http://www.hukseflux.com/thermal%20conductivity/thermal.htm
% Kair = .0681;             % average Thermal Conductivity of air in W/m*degK at Top  deg K
                % http://users.wpi.edu/~ierardi/FireTools/air_prop.html

eps0 = 8.85418e-12;         % Permeativity of free space F/m (Semiconductor Devices, Sze, page 536)
epsr_A = 1.0006;            % Dielectric Constant of air (unitless) (Advanced Engineering Elctromagnetics, Balanis, page 50)
epsr_N = 7.5;               % Dielectric Constant of Nitride (unitless) 6-9 (RF MEMS, Rebiez, pages 474-476)

%pe_poly1 = 2.3e-5;         % resistivity poly1 in ohm-m  %class values to test code
%pe_poly2 = 3.22e-5;        % resistivity poly2 in ohm-m   (MUMPS data sheet run 51)
pe_poly1 = 1.97e-5;         % resistivity poly1 in ohm-m  (MUMPS data sheet run 56)
%pe_poly2 = 2.49e-5;        % resistivity poly2 in ohm-m   (MUMPS data sheet run 56)

pe_temp_const = 1.25e-3;    % Temperature dependance of resistivity constant C-1

%%%%%%%%%%%%%%%%%%%%%%%%%%%%%%%%%%%%%%%%%%%%%%%%%%%%%%%%%%%%
%%%%%%%%%%%%%%%%%%%%%%%
% Calculation and plotting of  Hot Arm Actuator due to stepping voltages and Temps
```

C2

```
%%%%%%%%%%%%%%%%%%%%%%%%%%%%%%%%%%%%%%%%%%%%%%%%%%%%%%%%
%%%%%%%%%%%%%%%%%%%%%%%
a_poly1_t = zeros(25,1);        % initialize
a_poly1_t(1) = a_poly1;         % initialize

Vo_step = [0 1 2 3 4 5 6 7 8 9 10 11 12 13 14 15 16 17 18 19 20 21 22 23 24];     % Applied STEPPING voltage in Volts
% Top_step = [293    306.73 345.66 399.67 460.69 518.78 586.4 651.23 722.78 788.86 878.56 952.13 1041.7 1149.9 1250 1345.5];
                    % Applied STEPPING Average Operating Temperature in deg K
                    % values taken from the mean temp at each level, with Top =
                    % average 900 deg K for all steps

% Top_step = [293 305.56      338.18      384.56      440.54      502.5       564.31      627.32 705.2        776.84      842.47...
%             911.14  996.75      1071.9      1142.9      1223.7];    %%%Poly1

% Top_step = [293     299.48      317.97      345.6       379.65      420.44      461.75      508.95      543.98      575.96      620.19...
%       654.96      695.99      736.77      776.5       814.81      842.74      868.93      894.73      925.97      952.07      996.78
%             1037.9...
%       1084.4      1131.8];    %%%Poly12
%

%%%400x8
% Top_step = [293     299.87      318.68      345.52      376.71      408.98      442.34      473.73      510.76      550.09      582.73
%             620.74...
%       654.58      688.11      721.85      756.12      797.94      841.35      885.29      924.39      968.02      993.5       1021.6
%             1043.6      1063.9];

% Top_step = [293     300.54      321.67      352.58      390.2       435.34      481.77      537.81      586.99      633.39      690.19
%             735.36...
%       779.91      823.24      861.59      903.83      935.57      968.21      999.62      1039        1073.9      1073.9      1073.9
%             1073.9      1073.9];

% Top_step = [293     300.45      321.19      351.13      386.81      427.7       468.8       514.45      556.99      598.68      643.14
%             683.4       721.45...
%       758.64      793.44      830.31      865.92      902.83      939.52      977.56      1015.9      1015.9 1015.9 1015.9 1015.9];

%%%250x8,
Top_step = [293     301.27      324.82      358.23      399.3       440.33      484.98      522.41      572.89      620.54      662.77
            703.42      742.22...
   800.32   844.1       883.86      927.29      969.53      1010.3      1054.8      1137.30 144 144 144 144 144 144];




for ii=1:length(Vo_step)
  Vo = Vo_step(ii);               % vary voltage in steps
  Top = Top_step(ii);     % vary operating temperature in steps
  Top_2(ii) = T0;

%%%%%%%%%%%%%%%%%%%%%%%%%%%%%%%%%%%%%%%%%%%%%%%%%%%%%%%%
%%%%%%%%%%%%%%%%%%%%%%%%%
% initialize vectors and matrices

Amatrix = zeros(10,10);             % initialize A matrix
Cvector = zeros(10,1);              % initialize integration constants vector
Fvector = zeros(10,1);              % initialize Forcing values vector
K_master_stiffness = zeros(15,15);  % initialize master stiffness matrix
R_vector = zeros(15,1);             % initialize master FORCE/MOMENT Resultant vector
D_vector = zeros(15,1);             % initialize master Displacement(x,y,theta) vector
Flex_matrix = zeros(6,6);
d_L_vector =  zeros(6,1);
X_vector = zeros(6,1);

%%%%%%%%%%%%%%%%%%%%%%%%%%%%%%%%%%%%%%%%%%%%%%%%%%%%%%%%
%%%%%%%%%%%%%%%%%%%%%%%%%
% Temperature Dependencies
%%%%%%%%%%%%%%%%%%%%%%%%%%%%%%%%%%%%%%%%%%%%%%%%%%%%%%%%
%%%%%%%%%%%%%%%%%%%%%%%%%

pe_poly_t = pe_poly1 * (1 + (pe_temp_const * (Top-T0)));   % Huang and Lee page 66
                %%%%%% average resistivity of poly in W/m*degK at Top in deg K
```

C3

```
pe_poly12_tv(ii) = pe_poly_t;

% pe_poly12_tv = [33.86157895 36.13995752 36.34367768 37.03255842 37.84222111 38.00394 38.97457108 38.94010263...
%        40.13925865 41.64070024 42.33334485 44.03666727 45.92960585 47.86738405 50.14619883 51.96696739...
%        54.23653772 56.2655355 58.28861455 59.79985355 61.40350877 1 1 1 1 1 1 1 ]*1e-6;
% pe_poly_t =  pe_poly12_tv(ii)/1.85;

Kair_t = 1.5207E-11*Top^3 - 4.8574E-08*Top^2 + 1.0184E-04*Top - 3.9333E-04;

Kair_tv(ii) = Kair_t;          % average Thermal Conductivity of air in W/m*degK at Top in deg K
                    % http://users.wpi.edu/~ierardi/FireTools/air_prop.html
%    Kair_tv(ii) = .026;

% KpolyT(ii) = 41 - 1.06*(ii-1);     % Poly1 Thermal conductivity Dong Yan, Amir Khajepour and Raafat Mansour page 315:
kp=41×10^6
KpolyT(ii) = 41 - .66*(ii-1);     % Poly2 Thermal conductivity Dong Yan, Amir Khajepour and Raafat Mansour page 315:
kp=41×10^6
Kpoly_t = KpolyT(ii);          % This value ranges between these two values to show temperature dependence
                    % Materials Handbook for Hybrid Microelectronics by King
                    % shows Therm Cond decreases almost linearly in the temp range of 300 to 1700 deg K
                    % and ranging down to a value of 25 at 1400 deg K
% a_poly1_t(ii) = ((3.725*(1-exp(-5.88e-3*(Top-246)))+5.548e-4*Top)*1e-6);
%a_poly1_t(ii) = (((3.725*(1-exp(-5.88e-3*(Top-124))))+5.548e-4*Top)*1e-6);
a_poly1_t(ii) = (((3.725*(1-exp(-5.88e-3*(Top-144))))+5.548e-4*Top)*1e-6);

                    % from "Average power control and positioning of polysilicon thermal actuators"
                    % by Butler, Bright, and Cowan page 95
% a_poly1_t(ii) = a_poly1;

% E_poly1T(ii)=((-2.35e-2*Top) + 176)*1e9;   % Poly1 Poly 2 line fitting equation from ranging from 169 to 140
E_poly1T(ii)=((-3.40e-2*Top) + 179)*1e9;   %Poly1+2 line fitting equation from ranging from 169 to 140

E_poly1 = E_poly1T(ii);          % This value ranges between these two values to show temperature dependence
                    % Materials Handbook for Hybrid Microelectronics by King
                    % shows Therm Cond decreases almost linearly in the temp range of 300 to 1700 deg K
                    % and ranging down to a value of 140 at 1400 deg K ;%


%%%%%%%%%%%%%%%%%%%%%%%%%%%%%%%%%%%%%%%%%%%%%%%%%%%%%%%%%%%%%%%%%%%
%%%%%%%%%%%%%%%%%%%%%%%%%%
% Calculation of Variables
%%%%%%%%%%%%%%%%%%%%%%%%%%%%%%%%%%%%%%%%%%%%%%%%%%%%%%%%%%%%%%%%%%%
%%%%%%%%%%%%%%%%%%%%%%%%%

% Per = w;              % Perimeter of cross section for conduction in um, set to width for intial analysis
% Per = [w(1) + .5*t, w(2) + .5*t, w(3) + t, w(4), w(5),  w(6)];
Per = [w(1) + t, w(2) + t, w(3) + 2*t, w(4) + t, w(5) + t];
                    % Perimeter of cross section for conduction in um, set to width + 2*(t/4) for intial analysis
% Per = w + t;          % Perimeter of cross section for conduction in um, set to width + 2*(t/2) for intial analysis
% Per = w + 2 * t;      % Perimeter of cross section for conduction in um, set to width + 2 * t for intial analysis
% Per = 2*w + 2*t;      % Perimeter of cross section for conduction in um, set to 2*width + 2*(t) for intial analysis
        % Perimeter of (1)hot arm 1, (2)short piece 1, (3)hot arm 2, (4)short piece 2, (5)cold arm, (6)flexor; in um
h = [Kair_tv(ii)/d, Kair_tv(ii)/d, Kair_tv(ii)/d, Kair_tv(ii)/d, Kair_tv(ii)/d];
                    % heat transfer coefficient
Acs = w.*t;              % cross sectional area in um
        % Area cs of (1)hot arm 1, (2)short piece 1, (3)hot arm 2, (4)short piece 2, (5)cold arm, (6)flexor; in um
R = pe_poly_t.*Lv./Acs;        % Resistance of (1)hot arm 1, (2)short piece 1, (3)hot arm 2; in ohms
I = Vo./(R(1)+R(2)+R(4)+R(5));          % Current in mA in (1)hot arm 1, (2)short piece 1, (3)hot arm 2
qdot1 = ((I^2.*pe_poly_t).*(Acs.^2));
                % heat generated by current per volume Watts/m^3, (1)hot arm 1, (2)short piece 1, (3)hot arm 2
% qdot1(1) = .1259e3;          % heat generated in (4)short piece 2, (5)cold arm, (6)flexor
% qdot1(3) = .1259e3;
% qdot1(5) = .1259e3;

qdot_pwr(ii) = qdot1(2);

Ga = sqrt((h.*Per)./(Kpoly_t.*Acs));  % Gamma combination of variables, (1)hot arm, (2)short piece, (3)cold arm, (4)flexor;
Ep1 = (((qdot1.*Acs)./(h.*Per)) + T0);  % Epsilon combination of variables, (1)hot arm 1, (2)short piece 1, (3)hot arm 2
Ep = [Ep1(1), Ep1(2), Ep1(3), Ep1(4), Ep1(5)];
li = [Lv(1), Lv(1)+Lv(2), Lv(1)+Lv(2)+Lv(3), Lv(1)+Lv(2)+Lv(3)+Lv(4), Lv(1)+Lv(2)+Lv(3)+Lv(4)+Lv(5)];
                    %adding up lengths for cumulative lengths at each boundary
```

C4

```
Im = wp.^3 * (t / 12);          % Area moment of inertia for a rectangle

%%%%%%%%%%%%%%%%%%%%%%%%%%%%%%%%%%%%%%%%%%%%%%%%%%%%%%%%%%%%%%%%%
%%%%%%%%%%%%%%%%%%%%%%%%%
%Calculate and Plot Temperature Distribution
%%%%%%%%%%%%%%%%%%%%%%%%%%%%%%%%%%%%%%%%%%%%%%%%%%%%%%%%%%%%%%%%%
%%%%%%%%%%%%%%%%%%%%%%%%

%Forcing values vector
Fvector = [T0-Ep(1), Ep(2)-Ep(1), Ep(3)-Ep(2), Ep(4)-Ep(3), Ep(5)-Ep(4), T0-Ep(5), 0,0,0,0];

%Populate A matrix row by row
Amatrix(1,:) = [1,1,0,0,0,0,0,0,0,0];
Amatrix(2,:) = [exp(Ga(1)*li(1)), exp(-Ga(1)*li(1)), -exp(Ga(2)*li(1)), -exp(-Ga(2)*li(1)), 0,0,0,0,0,0];
Amatrix(3,:) = [0,0,exp(Ga(2)*li(2)), exp(-Ga(2)*li(2)), -exp(Ga(3)*li(2)), -exp(-Ga(3)*li(2)), 0,0,0,0];
Amatrix(4,:) = [0,0,0,0,exp(Ga(3)*li(3)), exp(-Ga(3)*li(3)), -exp(Ga(4)*li(3)), -exp(-Ga(4)*li(3)),0,0];
Amatrix(5,:) = [0,0,0,0,0,0,exp(Ga(4)*li(4)), exp(-Ga(4)*li(4)), -exp(Ga(5)*li(4)), -exp(-Ga(5)*li(4))];
Amatrix(6,:) = [0,0,0,0,0,0,0,0,exp(Ga(5)*li(5)), exp(-Ga(5)*li(5))];
Amatrix(7,:) = [Acs(1)*Ga(1)*exp(Ga(1)*li(1)),-Acs(1)*Ga(1)*exp(-Ga(1)*li(1)),...
     -Acs(2)*Ga(2)*exp(Ga(2)*li(1)),Acs(2)*Ga(2)*exp(-Ga(2)*li(1)),0,0,0,0,0,0];
Amatrix(8,:) = [0,0,Acs(2)*Ga(2)*exp(Ga(2)*li(2)),-Acs(2)*Ga(2)*exp(-Ga(2)*li(2)),...
     -Acs(3)*Ga(3)*exp(Ga(3)*li(2)),Acs(3)*Ga(3)*exp(-Ga(3)*li(2)),0,0,0,0];
Amatrix(9,:) = [0,0,0,0,Acs(3)*Ga(3)*exp(Ga(3)*li(3)),-Acs(3)*Ga(3)*exp(-Ga(3)*li(3)),...
     -Acs(4)*Ga(4)*exp(Ga(4)*li(3)),Acs(4)*Ga(4)*exp(-Ga(4)*li(3)),0,0];
Amatrix(10,:) = [0,0,0,0,0,0, Acs(4)*Ga(4)*exp(Ga(4)*li(4)),-Acs(4)*Ga(4)*exp(-Ga(4)*li(4)),...
     -Acs(5)*Ga(5)*exp(Ga(5)*li(4)),Acs(5)*Ga(5)*exp(-Ga(5)*li(4))];


% solve for integration constants
Cvector = inv(Amatrix)*Fvector';
C = Cvector;    %rename to shorten next set of equations

% solve for Temperature Distribution in original equations

%First set up x point vectors for plotting
x1 = linspace(0,li(1),Lv(1)/1e-8);   %sets up number of points to plot in x dir  (1)hot arm 1p1
x2 = linspace(li(1),li(2),Lv(2)/1e-8);   %sets up number of points to plot in x dir  (2)hot arm 1p2
x3 = linspace(li(2),li(3),Lv(3)/1e-8);   %sets up number of points to plot in x dir  (3)center piece
x4 = linspace(li(3),li(4),Lv(4)/1e-8);   %sets up number of points to plot in x dir  (4)hot arm 2p1
x5 = linspace(li(4),li(5),Lv(5)/1e-8);   %sets up number of points to plot in x dir  (4)hot arm 2p2

% solve for Temperature Distribution in original equations using calcualted constants
T_hot_arm1p1 = C(1)*exp(Ga(1).*x1) + C(2)*exp(-Ga(1).*x1) + Ep(1);
T_hot_arm1p2 = C(3)*exp(Ga(2).*x2) + C(4)*exp(-Ga(2).*x2) + Ep(2);
T_center_piece = C(5)*exp(Ga(3).*x3) + C(6)*exp(-Ga(3).*x3) + Ep(3);
T_hot_arm2p1 = C(7)*exp(Ga(4).*x4) + C(8)*exp(-Ga(4).*x4) + Ep(4);;
T_hot_arm2p2 = C(9)*exp(Ga(5).*x5) + C(10)*exp(-Ga(5).*x5) + Ep(5);


%Concatinate data points for plotting
T_actuator = [T_hot_arm1p1  T_hot_arm1p2  T_center_piece  T_hot_arm2p1 T_hot_arm2p2];
 Tck2(ii) = mean(T_hot_arm1p2);            % check operating temperature steps

%set up T_actuator points for plotting
xT = linspace(0,li(5),length(T_actuator))./1e-6;   %sets up points to plot in x (in um) dir for T_actuator


%Plot Temp for length of hot arm actuator

if (ii == 1)
   figure;       %%%%%%comment out to add plot lines

   plot(xT,T_actuator,'b','LineWidth',3); %%%%%%%%%%%%%b,g,r,c,m  k= black
   axis off;
   title('250 um x 8 Chevron Actuator Sim, Temp. Distro','fontsize',14,'fontweight','bold');
   axes('fontsize',12,'fontweight','bold');
   grid on;
   xlabel('x Position Along Actuator in \mum','fontsize',12,'fontweight','bold');
   ylabel('Temperature in degrees K (\circK)','fontsize',12,'fontweight','bold');
```

C5

```
    hold on;
    plot(xT,T_actuator,'b','LineWidth',3); %%%%%%%%%%%%%%b,g,r,c,m  k= black
end

if (ii == 3)
    plot(xT,T_actuator,'g','LineWidth',3); %%%%%%%%%b,g,r,c,m k= black
end
if (ii == 5)
   plot(xT,T_actuator,'r','LineWidth',3); %%%%%%%%%%%b,g,r,c,m k= black
end
if (ii == 7)
    plot(xT,T_actuator,'k','LineWidth',3); %%%%%%%%%b,g,r,c,m k= black
end
if (ii == 9)
    plot(xT,T_actuator,'c','LineWidth',3); %%%%%%%%%b,g,r,c,m k= black
end
if (ii == 11)
    plot(xT,T_actuator,'m','LineWidth',3); %%%%%%%%%b,g,r,c,m k= black
end
if (ii == 13)
    plot(xT,T_actuator,'y','LineWidth',3); %%%%%%%%%b,g,r,c,m k= black
end
if (ii == 14)
    plot(xT,T_actuator,'b','LineWidth',3); %%%%%%%%%b,g,r,c,m k= black
end
if (ii == 15)
    plot(xT,T_actuator,'g','LineWidth',3); %%%%%%%%%b,g,r,c,m k= black
end
if (ii == 16)
   plot(xT,T_actuator,'r','LineWidth',3); %%%%%%%%%b,g,r,c,m k= black
end
if (ii == 17)
    plot(xT,T_actuator,'k','LineWidth',3); %%%%%%%%%b,g,r,c,m k= black
end
% if (ii == 18)
%    plot(xT,T_actuator,'c','LineWidth',3); %%%%%%%%%b,g,r,c,m k= black
% end
% if (ii == 19)
%    plot(xT,T_actuator,'m','LineWidth',3); %%%%%%%%%b,g,r,c,m k= black
% end
% if (ii == 20)
%    plot(xT,T_actuator,'y','LineWidth',3); %%%%%%%%%b,g,r,c,m k= black
% end
 legend(['V = ' num2str(Vo_step(1)) ' Volts'],['V = ' num2str(Vo_step(3)) ' Volts'],['V = ' num2str(Vo_step(5)) ' Volts'],...
    ['V = ' num2str(Vo_step(7)) ' Volts'],   ['V = ' num2str(Vo_step(9)) ' Volts'],['V = ' num2str(Vo_step(11)) ' Volts'],...
    ['V = ' num2str(Vo_step(13)) ' Volts'],   ['V = ' num2str(Vo_step(14)) ' Volts'],['V = ' num2str(Vo_step(15)) ' Volts'],...
    ['V = ' num2str(Vo_step(16)) ' Volts'],   ['V = ' num2str(Vo_step(17)) ' Volts'],0);

 %['V = ' num2str(Vo_step(18)) ' Volts'],...
 %    ['V = ' num2str(Vo_step(19)) ' Volts'],['V = ' num2str(Vo_step(20)) ' Volts']
 %
%%%%%%%%%%%%%%%%%%%%%%%%%%%%%%%%%%%%%%%%%%%%%%%%%%%%%%%%%%%%
%%%%%%%%%%%%%%%%%%%%%%
% %Calculate the Delta Change in Length and Force Vectors due to Thermal Expansion
%
%%%%%%%%%%%%%%%%%%%%%%%%%%%%%%%%%%%%%%%%%%%%%%%%%%%%%%%%%%%%
%%%%%%%%%%%%%%%%%%%%%%

%Use average temperature in each section to find the thermal expansion
T_hot_arm1p1_av = sum(T_hot_arm1p1)/length(T_hot_arm1p1);
T_hot_arm1p2_av = sum(T_hot_arm1p2)/length(T_hot_arm1p2);
T_center_piece_av = sum(T_center_piece)/length(T_center_piece);
T_hot_arm2p1_av = sum(T_hot_arm2p1)/length(T_hot_arm2p1);
T_hot_arm2p2_av = sum(T_hot_arm2p2)/length(T_hot_arm2p2);

T_actuator_av = [T_hot_arm1p1_av T_hot_arm1p2_av T_center_piece_av T_hot_arm2p1_av T_hot_arm2p2_av];

T_hot_arm1_av_step(ii) = T_hot_arm1p2_av;

%calc d_length vector and force_vector
```

```matlab
    for i=1:length(T_actuator_av)
        d_length(i) = Lpv(i) * a_poly1_t(ii) *  (T_actuator_av(i) - T0); % length of piece * TCE * Avg change in Temp
        force_vector(i) = E_poly1 * Acs(i) * d_length(i) / Lpv(i); % Young's * cross sectional area * delta length / length
    end

%%%%%%%%%%%%%%%%%%%%%%%%%%%%%%%%%%%%%%%%%%%%%%%%%%%%%%%%%%%%
%%%%%%%%%%%%%%%%%%%%%%%%%%%
%Calculate Global Flexibility Matrix
%%%%%%%%%%%%%%%%%%%%%%%%%%%%%%%%%%%%%%%%%%%%%%%%%%%%%%%%%%%%
%%%%%%%%%%%%%%%%%%%%%%%%%%%

L1 = Lpv(1) + Lpv(2);

dL1 = d_length(1) + d_length(2);


%%%%%%%%%%%%%%%%%%%%%%%%%%%%%%%%%%%%%%%%%%%%%%%
% CALCULATE Moments and Forces
deg = 2;  %angle of chevrons in degrees
ang = deg * pi/180;  %angle of chevrons in radians
defl = sqrt((L1^2) + 2*L1*dL1 - (L1*(cos(ang)))^2) - L1*sin(ang);  %(1/(E_poly1*Im(1))) *
deflection(ii) = defl;
dum(ii) = (1/(E_poly1*Im(1)));

end   %%%% master loop for stepping voltages
%
%%%%%%%%%%%%%%%%%%%%%%%%%%%%%%%%%%%%%%%%%%%%%%%%%%%%%%%%%%%%%
%%%%%%%%%%%%%%%%%%%%
% %Plot Deflection of hot arm actuator
%

    figure;         %comment out to add plot lines
    plot(Vo_step,deflection/1e-6,'b',Vo_step,deflection/1e-6,'ro','LineWidth',3); %b,g,r k= black
    axis off;
    axes('fontsize',12,'fontweight','bold');
    grid on;
    title('250 um x 8 Chevron Actuator Sim, Deflection','fontsize',14,'fontweight','bold');
    xlabel('Voltage Applied','fontsize',12,'fontweight','bold');
    ylabel('Deflection of Actuator in \mum','fontsize',12,'fontweight','bold');
    hold on;
    plot(Vo_step,deflection/1e-6,'b',Vo_step,deflection/1e-6,'ro','LineWidth',3); %b,g,r k= black
    hold on;
% deflection_Coventorware = [0.38,1.04,2.05,3.45,5.3,7.67,10.6]*1e-6;
% plot(Vo_step,deflection_Coventorware,'g',Vo_step,deflection_Coventorware,'mo','LineWidth',3); %b,g,r k= black

%%%%%400x4 um
% deflection_Measured = [0 0.25 1 2 3.25 4.25 5.5 6.75 7.75 8.75 10.25 11 11.5 12 13 13.5 14 15 16 15 15 0 0 0];
% plot(Vo_step,deflection_Measured,'k',Vo_step,deflection_Measured,'co','LineWidth',3); %b,g,r k= black

%%%%%350x8 um
% deflection_Measured = [0 0.5 1 2 3 4.5 6 7 8 9 10 11 12 13 14 15 16 17 18 19 0 0 0 0];
% plot(Vo_step,deflection_Measured,'k',Vo_step,deflection_Measured,'co','LineWidth',3); %b,g,r k= black

%%%%%M58 250x8 um
% deflection_Measured = [0 0.5 1 2 3 4 5.5 6.5 7.5 8.5 9 10 11 12 12.5 0 0 0 0 0 0 0 0 0];
% plot(Vo_step,deflection_Measured,'k',Vo_step,deflection_Measured,'co','LineWidth',3); %b,g,r k= black
% legend(['Model'], [' '], ['Experimental'],[' '],0);

% %%%%%M58 350x16 um
% deflection_Measured = [0 0.25 1 2 3 4 5 6 7 8 9 10.5 12 13 14 15 16 0 0 0 0 0 0 0];
% plot(Vo_step,deflection_Measured,'g',Vo_step,deflection_Measured,'mo','LineWidth',3); %b,g,r k= black
% legend(['Model'], [' '], ['Experimental'],[' '],0);

%%%%%M58 400x8 um
deflection_Measured = [0 0.5 1 2 3 4.5 6 7 8.5 9.5 10.5 12 13 14 14.5 15.5 16 16.5 16.5 13.5 11.5 0 0 0];
plot(Vo_step,deflection_Measured,'k',Vo_step,deflection_Measured,'co','LineWidth',3); %b,g,r k= black
 legend(['Model'], [' '], ['Experimental'],[' '],0);
```

		REPORT DOCUMENTATION PAGE			*Form Approved* *OMB No. 074-0188*

The public reporting burden for this collection of information is estimated to average 1 hour per response, including the time for reviewing instructions, searching existing data sources, gathering and maintaining the data needed, and completing and reviewing the collection of information. Send comments regarding this burden estimate or any other aspect of the collection of information, including suggestions for reducing this burden to Department of Defense, Washington Headquarters Services, Directorate for Information Operations and Reports (0704-0188), 1215 Jefferson Davis Highway, Suite 1204, Arlington, VA 22202-4302. Respondents should be aware that notwithstanding any other provision of law, no person shall be subject to an penalty for failing to comply with a collection of information if it does not display a currently valid OMB control number.
PLEASE DO NOT RETURN YOUR FORM TO THE ABOVE ADDRESS.

1. REPORT DATE *(DD-MM-YYYY)* 23-03-2004	2. REPORT TYPE **Master's Thesis**	3. DATES COVERED *(From – To)* Aug 2003 – Mar 2004

4. TITLE AND SUBTITLE DEMONSTRATING OPTOTHERMAL ACTUATORS FOR AN AUTONOMOUS MEMS MICROROBOT	5a. CONTRACT NUMBER
	5b. GRANT NUMBER
	5c. PROGRAM ELEMENT NUMBER
6. AUTHOR(S) Szabo, Francis R., SMSgt, USAF	5d. PROJECT NUMBER
	5e. TASK NUMBER
	5f. WORK UNIT NUMBER

7. PERFORMING ORGANIZATION NAMES(S) AND ADDRESS(S) Air Force Institute of Technology Graduate School of Engineering and Management (AFIT/EN) 2950 Hobson Way Street, Building 640 WPAFB OH 45433-7765	8. PERFORMING ORGANIZATION REPORT NUMBER AFIT/GE/ENG/04-23

9. SPONSORING/MONITORING AGENCY NAME(S) AND ADDRESS(ES) Capt. Paul Kladitis, PhD. AETC/AFIT/ENG Graduate School of Engineering and Management 2950 Hobson Way Street, Building 640 WPAFB OH 45433-7765 937-255-3636 ext. 4595	10. SPONSOR/MONITOR'S ACRONYM(S)
	11. SPONSOR/MONITOR'S REPORT NUMBER(S)

12. DISTRIBUTION/AVAILABILITY STATEMENT
   APPROVED FOR PUBLIC RELEASE; DISTRIBUTION UNLIMITED.

13. SUPPLEMENTARY NOTES

14. ABSTRACT
There are numerous applications for microrobots which are beneficial to the Air Force. However, the microrobotics field is still in its infancy, and will require extensive basic research before these applications can be fielded. The biggest hurdle to be solved, in order to create autonomous microrobots, is generating power for their actuator engines. Most present actuators require orders of magnitude more power than is presently available from micropower sources. To enable smaller microrobots, this research proposed a simplified power concept that eliminates the need for on-board power supplies and control circuitry by using actuators powered wirelessly from the environment. This research extended the basic knowledge of methods required to power Micro-Electro-Mechanical Systems (MEMS) devices and reduce MEMS microrobot size. This research demonstrated optothermal actuators designed for use in a wirelessly propelled autonomous MEMS microrobot, without the need of an onboard power supply, through the use of lasers to directly power micrometer scale silicon thermal actuators. Optothermal actuators, intended for use on a small MEMS microrobot, were modeled, designed, fabricated and tested, using the PolyMUMPs silicon-metal chip fabrication process. Prototype design of a MEMS polysilicon-based microrobot, using optothermal actuators, was designed, fabricated and tested. Each of its parts was demonstrated to provide actuation using energy from an external laser. The optothermal actuators provided 2 µm of deflection to the microrobot drive shaft, with 60 mW of pulsed laser power. The results of these experiments demonstrated the validity of a new class of wireless silicon actuators for MEMS devices, which are not directly dependant on electrical power for actuation. The experiments also demonstrated a potentially viable design that could be used to propel the world's smallest autonomous MEMS microrobot.

15. SUBJECT TERMS
   Micro-Electro-Mechanical Systems, MEMS, microrobot, optothermal actuators, and laser heating.

16. SECURITY CLASSIFICATION OF:			17. LIMITATION OF ABSTRACT	18. NUMBER OF PAGES	19a. NAME OF RESPONSIBLE PERSON Capt. Paul E. Kladitis, Ph.D. (ENG)
a. REPORT	b. ABSTRACT	c. THIS PAGE	UU	230	19b. TELEPHONE NUMBER *(Include area code)* 937-255-3636 ext. 4595; e-mail: Paul.Kladitis @afit.edu
U	U	U			

Standard Form 298 (Rev. 8-98)
Prescribed by ANSI Std. Z39-18